

JOANNA IRINA ZAITSEVA-KINNEBERG

PHOTOCAGES FOR TIME-RESOLVED X-RAY  
CRYSTALLOGRAPHY



PHOTOCAGES FOR TIME-RESOLVED X-RAY  
CRYSTALLOGRAPHY

JOANNA IRINA ZAITSEVA-KINNEBERG

Department of Chemistry  
Faculty of Mathematics, Informatics and Natural Sciences  
University of Hamburg

September 2024 – publication edition

Joanna Irina Zaitseva-Kinneberg: *Photocages for time-resolved X-ray crystallography*, Doktor rerum naturalium (Dr. rer. nat.), © 2024.  
This work is licensed under CC BY 4.0. To view a copy of this license, visit <https://creativecommons.org/licenses/by/4.0/>.

**SUPERVISORS:**

Prof. Dr. Arwen R. Pearson

Prof. Dr. Henning Tidow

**LOCATION:**

Hamburg

**TIME FRAME OF LABORATORY WORK:**

Oct 2015 – Nov 2019

**EXAMINATION EDITION SUBMITTED:**

December 2021

**EXAMINATION PASSED:**

13.03.2020

To Arwen  
for your enduring patience, kindness, and acceptance

To Thoth  
for all learning, reckoning and writing are yours,  
and I could not write this without first reading



## FOREWORD

---

In editing this for publication, my goal has been largely to streamline the aesthetics, improve readability, and make things consistent. I hope I've succeeded with this.

### ACKNOWLEDGMENTS TO THE PUBLICATION EDITION

I want to thank Jacquie Hansen for prompting me to get a plan together to publish within my deadline, and keeping an eye on me to make sure I stick to it. I'm also very grateful to David Damerell for proofreading a recent draft of the thesis, it seems your fondness of Oxford commas has rubbed off on me.

I'm also extremely grateful to Uta Fischer and others at the Department of Chemistry for their help and patience with my many extensions and administrative queries. Thank you so much.

The original acknowledgements from the examination edition have been preserved, with some updates to reflect title changes. Additionally, a note was added regarding the translation of the Abstract into German.



## ACKNOWLEDGMENTS

---

First and foremost I would like to thank my ex-wife, Camilla Dahlberg Bech. She took care of every aspect of our lives while I was lost in the deep, dark thesis hole. I could not have done it without her.

Secondly, I owe a deep debt of gratitude to Dr. Helen “Mary Floggins” Ginn. You locked me in the thesis hole, chained me to my desk, and wouldn’t let me out until I’d finished writing. Thanks!

I am grateful to my supervisor, Prof. Dr. Arwen Pearson, for giving me this chance to do science and write a thesis about it. What were you thinking? I hope this thesis makes you proud, and that you feel it was a good decision!

I want to thank many colleagues and students, many of whom became great friends, who’ve made life more fun during my time as a PhD student: Anke Puchert, Dr. Maria “Maraki” Kokkinidou, Dr. Yunyun Gao, Dr. Henry Giesler, Dr. Diogo Melo, Dr. Marta Sans, Dr. Briony Yorke, Dr. Diana Monteiro, Dr. Stephan Niebling, Dr. Maria “Masha” Naumova, Dana Komadina, Dr. Simon Bittmann, Dr. Michael Agthe, Dr. Sam Horrell, Susanne Meier, Elena Kornilova, Heike Burmeister, Prof. Dr. Nils Huse, Dr. Matthias Ruppert, Dr. Christoph Testud, Dr. Miguel Ochmann, Niko Höppel, Dr. Brandon Seychell, Dr. Caitlin Hatton, Jannik Strauss, Dr. Julian Czajor, James Gowdy, Dr. Anna Schepers, Owen Tuck, Phuong-Hien Van, Theresa Bock and Maxim Heinrich.

In particular, I want to thank again those close friends with whom I shared good times, who cheered me up when I was sad or frustrated, and invested their emotional labour in me: Anke, Christoph, Maraki, Miguel, Yunyun, Masha and Helen. I love you all.

Dr. Stephan Niebling translated the Abstract of this thesis into German.

I want to thank my collaborators in Potsdam: Prof. Dr. Henrike M. Müller-Werkmeister and Yannik Pfeifer. Your email correspondence made my life in Hamburg much more exciting and eventually provided crucial data for our paper in RSC Advances.

Finally, I acknowledge funding from the Hamburg Centre for Ultrafast Imaging (currently CUI: Advanced Imaging of Matter), an Excellence Cluster of the Deutsche Forschungsgemeinschaft (German Research Foundation).



## PUBLICATIONS

---

- [1] Joanna I. Zaitseva-Kinneberg et al. In: *RSC Adv.* 9 (15 2019), pp. 8695–8699. doi: [10.1039/C9RA00968J](https://doi.org/10.1039/C9RA00968J).



## ZUSAMMENFASSUNG

---

Die zeitaufgelöste Röntgenkristallographie ist ein aufstrebendes Forschungsgebiet, das die Vorteile der jüngsten Fortschritte in der Detekortertechnologie und der hochbrillanten Röntgenquellen von Synchrotrons und Freie-Elektronen-Lasern nutzt. Herausfordernd ist dabei die Anpassung der makromolekularen Kristallographie an einen zeitaufgelösten Experimentiermodus, dessen Hauptforschungsschwerpunkte unter anderem darin liegen, wie die Reaktion im Kristall ausgelöst werden kann. Ein Ansatz zur schnellen und genauen Reaktionsinitiierung im Kristall ist die Bestrahlung der Probe mit Laserlicht. Jedoch reagieren die meisten Proteine nicht von Natur aus auf diese Lichtanregung. Dies kann durch die Einführung von photolysierbaren Verbindungen, sogenannten Photocaging-Gruppen, in das Protein oder sein Substrat erreicht werden. Daher ist es wichtig, neue Photocagetypen für den Einsatz in der zeitaufgelösten Strukturbiologie zu erzeugen und zu charakterisieren. In diesem Projekt wurden eine Reihe von  $\alpha$ -Carboxynitrobenzyl-Photocages synthetisiert und mit L-Aspartat verbunden. Die caged-Aspartatverbindungen waren wasserlöslich, mit hydrolytischen Halbwertszeiten von 10 – 29 h, die sie für eine Reihe von biologischen Anwendungen geeignet erscheinen lassen. Die Quantenausbeute der Aspartatfreisetzung lag zwischen 0,05 und 0,14.  $\alpha$ -Carboxynitrobenzyle sind chiral, und ihre Kopplung an L-Aspartat führt bei Verwendung eines Racemats zu einem diastereomeren Gemisch. Einige enantioselektive Routen wurden vorgeschlagen, scheiterten aber letztlich. Stattdessen wird die chirale Auflösung, anstatt chiraler Kontrolle, als ein Weg für zukünftige Arbeiten präsentiert. Mit der zeitaufgelösten UV-Vis-Spektroskopie wurde die Kinetik der  $\alpha$ -Carboxynitrobenzyl-Photoreaktionen untersucht. Wichtige Acil-Nitro-Zwischenprodukte wurden mit Zeitkonstanten von 1 – 10  $\mu$ s oder 1 ms, abhängig von den aromatischen Substituenten, beobachtet. Sub-Nanosekunden-Transienten von 450 fs und 1 ps wurden für  $\alpha$ -Carboxy-6-nitropiperonylazetat beobachtet, die auf Schwingungsrelaxation bzw. die  $S_1$ -Lebensdauer zurückzuführen sind.



## ABSTRACT

---

Time-resolved X-ray crystallography is an emerging research field that takes advantage of recent developments in detector technology and high-brilliance X-ray sources from synchrotrons and X-ray free-electron lasers. Adapting macromolecular crystallography to a time-resolved experimental mode is challenging, with reaction initiation *in crystallo* a key element that must be addressed. One approach that allows for rapid and accurate triggering of a reaction within a crystal uses laser light irradiation. However, most proteins may not inherently respond to light-initiation. This can be addressed by the introduction of photocaging groups into either the protein or its substrate. Therefore, it is important to both generate and characterise new photocage types for application in time-resolved structural biology. In this project, a number of  $\alpha$ -carboxynitrobenzyl photocages were synthesised and joined to L-aspartate. The caged aspartates were water soluble, with hydrolytic half-lives of 10 – 29 h, making them suitable for a range of biological applications. The quantum yields of aspartate release ranged from 0.05 to 0.14.  $\alpha$ -Carboxynitrobenzyls are chiral, and their coupling to L-aspartate results in a diastereomeric mixture if a racemate is used. Some enantioselective routes were proposed but failed. Chiral resolution, rather than chiral control, is suggested as an avenue for future work. Time-resolved UV-Vis spectroscopy was used to investigate the kinetics of the  $\alpha$ -carboxynitrobenzyl photoreactions. Key *aci*-nitro intermediates were observed with time constants of 1 – 10  $\mu$ s or 1 ms, depending on the aromatic substituents. Subnanosecond transients were observed for  $\alpha$ -carboxy-6-nitropiperonyl acetate: 450 fs and 1 ps, attributed to vibrational relaxation and  $S_1$  lifetime, respectively.



## CONTENTS

---

|       |  |    |
|-------|--|----|
| 1     | Introduction   | 1  |
| 1.1   | Triggering methods   | 2  |
| 1.1.1 | Photoswitches  | 3  |
| 1.1.2 | Photocages   | 3  |
| 1.1.3 | Reaction initiation using a photocage  | 5  |
| 1.1.4 | Sample response  | 7  |
| 1.2   | Topics discussed in this thesis  | 9  |
| 2     | $\alpha$ -Carboxynitrobenzyl photocages  | 11 |
| 2.1   | Introduction   | 11 |
| 2.2   | Synthesis  | 13 |
| 2.2.1 | Synthesis of $\alpha$ -hydroxyacids  | 13 |
| 2.2.2 | Attempted selective protection of the carboxyl group                                   | 18 |
| 2.2.3 | Synthesis of <i>tert</i> -butyl <i>O</i> -acetyl 2-nitromandelates                     | 25 |
| 2.2.4 | Carbodiimide ester condensation  | 26 |
| 2.2.5 | Global deprotection of <i>N</i> -Boc and <i>tert</i> -butyl groups                     | 29 |
| 2.2.6 | Synthetic summary  | 30 |
| 2.3   | Characterisation   | 32 |
| 2.3.1 | Aqueous stability  | 32 |
| 2.3.2 | Quantum yields   | 33 |
| 2.3.3 | Absorption properties  | 39 |
| 2.3.4 | Photocleavage times  | 40 |
| 2.3.5 | Radiation damage   | 41 |
| 2.4   | Conclusions and future work  | 44 |
| 3     | Asymmetric synthesis of $\alpha$ -carboxynitropiperonyl photocages                     | 45 |
| 3.1   | Introduction   | 46 |
| 3.1.1 | Aims   | 47 |
| 3.2   | Late installation of chiral centre   | 48 |
| 3.2.1 | Dess-Martin oxidation of <i>tert</i> -butyl $\alpha$ -carboxy-6-nitropiperonyl alcohol | 48 |
| 3.2.2 | Corey-Bakshi-Shibata reduction   | 49 |
| 3.2.3 | Ruthenium catalysed asymmetric transfer hydrogenation                                  | 52 |
| 3.3   | Early installation of chiral centre  | 56 |
| 3.3.1 | Asymmetric addition reactions with trimethylsilyl cyanide                              | 56 |
| 3.3.2 | Use of the chiral pool   | 61 |
| 3.3.3 | Chiral resolution  | 62 |
| 3.3.4 | Conclusions and future work  | 62 |
| 4     | Nitrobenzyl photocleavage reaction mechanisms  | 65 |
| 4.1   | Introduction   | 66 |

|       |   |     |
|-------|---|-----|
| 4.1.1 | Nitrobenzyl methyl ethers and caged ATP   | 66  |
| 4.1.2 | Photochemistry of 2-nitrotoluene  | 69  |
| 4.1.3 | Carboxynitrobenzyl photocages   | 69  |
| 4.1.4 | Aims  | 72  |
| 4.2   | Methods   | 73  |
| 4.2.1 | Computational methods   | 73  |
| 4.2.2 | Experimental methods  | 76  |
| 4.3   | Results & Discussion  | 84  |
| 4.3.1 | Observing <i>aci</i> -nitro intermediates   | 84  |
| 4.3.2 | Femtosecond transient absorption spectroscopy   | 89  |
| 4.3.3 | Density functional theory calculations  | 91  |
| 4.4   | Conclusions   | 100 |
| 4.5   | Future work   | 102 |
| 5     | Conclusions   | 103 |
| 5.1   | $\alpha$ -Carboxynitrobenzyl photocages   | 104 |
| 5.2   | 4-Hydroxyphenacyl photocages  | 105 |
| 5.3   | Summary   | 107 |
| 6     | Synthetic procedures  | 109 |
| 6.1   | General methods   | 110 |
| 6.2   | 2-Nitromandelic acid  | 112 |
| 6.3   | 6-Nitropiperonal cyanohydrin  | 113 |
| 6.4   | <i>tert</i> -Butyl 2-nitromandelate   | 114 |
| 6.5   | <i>tert</i> -Butyl $\alpha$ -carboxy-6-nitropiperonyl alcohol   | 115 |
| 6.6   | TMSCN addition to aldehydes   | 116 |
| 6.7   | Hydrolysis of trimethylsilyl cyanohydrins   | 118 |
| 6.8   | Acetylation of hydroxyacids   | 120 |
| 6.9   | <i>tert</i> -Butyl ester protection   | 122 |
| 6.10  | Deacetylation   | 124 |
| 6.11  | Coupling to L-Aspartate   | 126 |
| 6.12  | Deprotection of <i>N</i> -Boc and <i>tert</i> -Butyl Esters   | 129 |
| 6.13  | Mosher's ester protocol A   | 131 |
| 6.14  | Mosher's ester protocol B   | 132 |
| 6.15  | <i>tert</i> -Butyloxycarbonyl 6-nitropiperonyl ketone   | 133 |
| 6.16  | <i>tert</i> -Butyl $\alpha$ -carboxy-6-nitropiperonyl alcohol<br>via Corey-Bakshi-Shibata catalysis     | 134 |
| 6.17  | Attempted asymmetric reduction<br>with ruthenium catalyst   | 135 |
| 6.18  | Methyl $\alpha$ -carboxy-6-nitropiperonyl alcohol   | 136 |
| 6.19  | Methyloxycarbonyl 6-nitropiperonyl ketone   | 137 |
| 6.20  | Methyl $\alpha$ -carboxy-6-nitropiperonyl alcohol<br>via Corey-Bakshi-Shibata catalysis                 | 138 |
| 6.21  | Uncatalysed TMSCN addition to 6-nitropiperonal in<br>CH <sub>2</sub> Cl <sub>2</sub>                    | 139 |
| 6.22  | TMSCN addition to 6-nitropiperonal<br>catalysed by L-DIPT and Ti(O <sup><i>i</i></sup> Pr) <sub>4</sub> | 140 |

|      |  |     |
|------|--|-----|
| 6.23 | Titanium dichloride complex<br>with ( <i>R,R</i> )-Jacobsen's ligand | 141 |
| 6.24 | Dimer complex of titanium<br>and ( <i>R,R</i> )-Jacobsen's ligand    | 142 |
| 6.25 | Crystallisation of diastereomeric salts                              | 143 |

|  |                                      |     |
|--|--------------------------------------|-----|
|  | Bibliography                         | 145 |
|  | Appendix I: hazardous chemicals used | 151 |
|  | Appendix II: novel spectra           | 157 |
|  | Appendix III: published spectra      | 159 |
|  | Appendix IV: Python scripts          | 181 |

## ABBREVIATIONS

---

|                    |   |
|--------------------|---|
| ADC(2)             | second-order algebraic diagrammatic construction                                |
| ATP                | adenosine triphosphate  |
| B <sub>3</sub> LYP | Becke's three-parameter exchange with Lee, Yang & Parr's correlation functional |
| 4-Br-CNB           | 4-bromo- $\alpha$ -carboxynitrobenzyl   |
| CASSCF             | complete active space self-consistent field                                     |
| CBS                | Corey-Bakshi-Shibata  |
| C <sub>m</sub>     | coumarinyl  |
| CI                 | conical intersection  |
| CNB                | $\alpha$ -carboxynitrobenzyl  |
| CNP                | $\alpha$ -carboxynitropiperonyl   |
| COSMO              | conductor-like screening model  |
| COSY               | correlation spectroscopy  |
| CPM                | cross-phase modulation  |
| DCC                | <i>N,N'</i> -dicyclohexylcarbodiimide   |
| DCU                | dicyclohexylurea  |
| DFA                | density functional approximation  |
| DFT                | density functional theory   |
| DMAP               | 4-(dimethylamino)-pyridine  |
| DMP                | Dess-Martin periodinane   |
| DMSO               | dimethyl sulfoxide  |
| EDC·HCl            | 1-ethyl-3-(3-dimethylaminopropyl)carbodiimide hydrochloride                     |
| ESI                | electrospray ionisation   |
| ESRF               | European Synchrotron Radiation Facility   |
| FA                 | formic acid   |
| fs-TAS             | femtosecond transient absorption spectroscopy                                   |
| fs-SR              | femtosecond stimulated Raman  |
| FTIR               | fourier transform infrared  |
| FWHM               | full width half maximum   |
| GTP                | guanosine-5'-triphosphate   |
| HAT                | hydrogen atom transfer  |
| HPLC               | high-performance liquid chromatography  |

|        |   |
|--------|---|
| HMBC   | heteronuclear multiple-bond coherence spectroscopy  |
| HOMO   | highest occupied molecular orbital                  |
| HRMS   | high-resolution mass spectrometry                   |
| HSQC   | heteronuclear single quantum coherence spectroscopy |
| IC     | internal conversion                                 |
| ICCD   | intensified charge-coupled device                   |
| IR     | infrared  |
| ISC    | intersystem crossing                                |
| ISTD   | internal standard                                   |
| LED    | light-emitting diode                                |
| LFP    | laser flash photolysis                              |
| LUMO   | lowest unoccupied molecular orbital                 |
| MALDI  | matrix-assisted laser desorption/ionisation         |
| MNB    | $\alpha$ -methyl-2-nitrobenzyl                      |
| MS     | mass spectrometry                                   |
| 4-HP   | 4-hydroxyphenacyls                                  |
| NB     | 2-nitrobenzyl                                       |
| 2-NT   | 2-nitrotoluene                                      |
| ns-LFP | nanosecond laser flash photolysis                   |
| Nd:YAG | neodymium-doped yttrium aluminium garnet            |
| NMR    | nuclear magnetic resonance                          |
| ODR    | orthogonal diagonal regression                      |
| OPA    | optical parametric amplifier                        |
| PES    | potential energy surface                            |
| PMT    | photomultiplier tube                                |
| PVDF   | polyvinylidene fluoride                             |
| RASSCF | restricted active space self-consistent field       |
| RSE    | radical stabilisation energy                        |
| SCF    | self-consistent field                               |
| TAS    | transient absorption spectroscopy                   |
| TBTA   | <i>tert</i> -butyl 2,2,2-trichloroacetimidate       |
| TDDFT  | time-dependent DFT                                  |
| TFA    | trifluoroacetic acid                                |
| TLC    | thin-layer chromatography                           |
| TMS    | trimethylsilyl                                      |
| TMSCN  | trimethylsilyl cyanide                              |

|                     |  |
|---------------------|--|
| ToF                 | time of flight                         |
| TRX                 | time-resolved X-ray crystallography    |
| TS                  | transition state                       |
| TRVS                | time-resolved vibrational spectroscopy |
| TVS                 | transient vibrational spectroscopy     |
| UB <sub>3</sub> LYP | unrestricted B <sub>3</sub> LYP        |
| UV                  | ultraviolet                            |
| Vis                 | visible                                |
| VR                  | vibrational relaxation                 |
| XUV                 | extreme ultraviolet                    |
| XEOL                | X-ray excited optical luminescence     |
| XFEL                | X-ray free electron laser              |

## CHEMICAL NAMES

| SHORT             | LONG  | IUPAC  |
|-------------------|---|--|
| ABDD              | (4 <i>R</i> ,5 <i>R</i> )-5-amino-4-(4'-biphenyl)-2,2-dimethyl-1,3-dioxan |  |
| Ac                | Acetyl  |  |
| AcOH              | Acetic acid   |  |
| Ac <sub>2</sub> O | Acetic anhydride  |  |
| ADPD              | (4 <i>S</i> ,5 <i>S</i> )-5-amino-2,2-dimethyl-4-phenyl-1,3-dioxan        |  |
| L-Asp             | L-Aspartate   | (2 <i>S</i> )-2-Amino-butanedioic acid   |
| ATP               | Adenosine 5'-(tetrahydrogen triphosphate)                                 |  |
| Boc               | <i>tert</i> -Butyloxy-carbonyl  |  |
| <b>4-Br-2-NBA</b> | 4-Bromo-2-nitrobenzaldehyde   |  |
| <sup>t</sup> Bu   | <i>tert</i> -Butyl  |  |
| <sup>t</sup> BuOH | <i>tert</i> -Butanol  |  |
| R-CBS             | ( <i>R</i> )-2-Methyl-CBS-oxazaborolidine                                 | (3 <i>aR</i> )-1-Methyl-3,3-diphenyl-tetrahydro-1 <i>H</i> ,3 <i>H</i> -pyrrolo[1,2- <i>c</i> ][1,3,2]-oxazaborole |
| <b>CANB-OH</b>    | $\alpha$ -Carboxamido-2-nitrobenzyl alcohol                               | 2-Nitrophenyl-(carboxamido)-methanol   |
| Cm                | Coumarin-4-yl-methyl  | 2 <i>H</i> -Chromen-2-one-4-yl-methyl  |
| <b>CNB</b>        | $\alpha$ -Carboxy-2-nitrobenzyl   | 2-Nitrophenyl-(carboxy)methyl  |
| <b>CNB-OH</b>     | $\alpha$ -Carboxy-2-nitromandelic acid                                    | 2-Nitrophenyl-(hydroxy)acetic acid   |

|                   |  |   |
|-------------------|--|---|
| CNP               | $\alpha$ -Carboxy-6-nitropiperonyl                           | 1,3-Benzodioxol-5-yl-(carboxy)methyl  |
| CNP-OH            | $\alpha$ -Carboxy-6-nitropiperonyl alcohol                   | 1,3-Benzodioxol-5-yl-(hydroxy)acetic acid   |
| CNPK              | Carboxyl 6-nitropiperonyl ketone                             | 2-(1,3-Benzodioxol-5-yl)-2-oxoacetic acid   |
| DIPEA             | <i>N,N</i> -Diisopropylethylamine                            | <i>N</i> -Ethyl- <i>N</i> -(propan-2-yl)propan-2-amine  |
| DIPT              | Diisopropyl tartrate   | Dipropan-2-yl 2,3-dihydroxybutanedioate   |
| DMP               | Dess-Martin periodinane                                      | 3-Oxo-1 $\lambda^5$ ,2-benziodoxole-1,1,1(3 <i>H</i> )-triyl triacetate                         |
| DCC               | <i>N,N'</i> -Dicyclohexylcarbodiimide                        | <i>N,N'</i> -Dicyclohexylmethanediimine   |
| DCU               | <i>N,N'</i> -Dicyclohexylurea                                |   |
| DMAP              | 4-Dimethylaminopyridine                                      | <i>N,N</i> -Dimethylpyridin-4-amine   |
| DMSO              | Dimethyl sulfoxide   |   |
| EDC·HCl           | 1-Ethyl-3-(3-dimethylaminopropyl)-carbodiimide hydrochloride | 3-[[ <i>N</i> -(Ethylimino)methylidene]amino]- <i>N,N</i> -dimethylpropan-1-amine hydrochloride |
| Et                | Ethyl  |   |
| Et <sub>2</sub> O | Diethyl ether  | Ethoxyethane  |
| EtOAc             | Ethyl acetate  |   |
| EtOH              | Ethanol  |   |
| Et <sub>3</sub> N | Triethylamine  | <i>N,N</i> -Diethylethanamine   |
| FA                | Formic acid  |   |
| GTP               | Guanosine triphosphate                                       | Guanosine 5'-(tetrahydrogen triphosphate)   |

|             |  |  |
|-------------|--|--|
| Hexanes     | Hexane, mixture of isomers                     | Hexane<br>2-Methylpentane<br>3-Methylpentane<br>2,3-Dimethylbutane<br>2,2-Dimethylbutane |
| 4-HP        | 4-Hydroxyphenacyl                              | 1-(4-Hydroxyphenyl)ethan-1-one-2-yl  |
| Me          | Methyl   |  |
| MeCN        | Acetonitrile                                   |  |
| MeOH        | Methanol                                       |  |
| MNB         | $\alpha$ -Methyl-2-nitrobenzyl                 | 1-(2-Nitrobenzyl)eth-1-yl  |
| MTPA        | Mosher's acid                                  | 3,3,3-Trifluoro-2-methoxy-2-phenylpropanoic acid   |
| MTPA-Cl     | Mosher's acid chloride                         | 3,3,3-Trifluoro-2-methoxy-2-phenylpropanoyl chloride                                     |
| 2-NB        | 2-Nitrobenzyl                                  |  |
| 2-NBA       | 2-Nitrobenzaldehyde                            |  |
| 2-NBA-HCN   | 2-Nitrobenzaldehyde cyanohydrin                | 2-Hydroxy-2-(2-nitrophenyl)acetonitrile  |
| 2-NBA-TMSCN | 2-Nitrobenzaldehyde trimethylsilyl cyanohydrin | 2-(2-Nitrophenyl)-2-trimethylsilyloxyacetonitrile  |
| 6-NPA       | 6-Nitropiperonal                               | 6-Nitro-1,3-benzodioxole-5-carbaldehyde  |
| 6-NPA-TMSCN | 6-Nitropiperonal trimethylsilyl cyanohydrin    | 2-(6-Nitro-1,3-benzodioxol-5-yl)-2-trimethylsilyloxyacetonitrile                         |
| 2-NT        | 2-Nitrotoluene                                 |  |
| Ph          | Phenyl   |  |

|   |  |  |
|---|--|--|
| Ph(CO)CO <sub>2</sub> H                   | Phenylglyoxylic acid   | Oxo(phenyl)acetic acid   |
| <i>i</i> Pr                               | Isopropyl  |  |
| <i>i</i> PrOH                             | Isopropanol  | Propan-2-ol  |
| <b>Salen</b>                              | ( <i>R,R</i> )-Jacobsen's ligand   | ( <i>R,R</i> )-(-)- <i>N,N'</i> -Bis-(3,5-di- <i>tert</i> -butyl-salicylidene)-1,2-cyclohexane-diamine   |
| SiO <sub>2</sub>                          | Silica gel   |  |
| TBTA                                      | <i>tert</i> -Butyl 2,2,2-trichloroacetimidate  | <i>tert</i> -Butyl 2,2,2-trichloroethanimidate   |
| TFA                                       | Trifluoroacetic acid   |  |
| THF                                       | Tetrahydrofuran  | Oxolane  |
| Ti(O <sup><i>i</i></sup> Pr) <sub>4</sub> | Titanium isopropoxide  |  |
| TMSCN                                     | Trimethylsilyl cyanide   | Trimethylsilane-carbonitrile   |
| TsDPEN                                    | <i>N</i> -tosyl-1,2-diphenyl-1,2-ethylenediamine   | <i>N</i> -toluenesulfonyl-1,2-diphenyl-1,2-ethylenediamine   |
| RuCl-[( <i>S,S</i> )-TsDPEN]-<br>(Mes)    | RuCl[( <i>S,S</i> )- <i>N</i> -Tosyl-1,2-diphenyl-1,2-ethylene-diamine]-<br>(mesitylene) | [ <i>N</i> -[(1 <i>S</i> ,2 <i>S</i> )-2-(Amino-κ <i>N</i> )-1,2-Diphenylethyl]-4-methylbenzene-sulfonamidato-κ <i>N</i> ]chloro[(1,2,3,4,5,6-η)-1,3,5-trimethylbenzene]-ruthenium |
| Widmer's reagent                          | <i>N,N</i> -Dimethyl-formamide di- <i>tert</i> -butyl acetal                             | 1,1-Di- <i>tert</i> -butoxy-trimethylamine   |

---

## INTRODUCTION

---

The purpose of this introduction is to describe the state of the field of time-resolved structural biology generally and the rationale for this thesis project in the context of this wider field.

Inside the cells of our bodies, proteins, enzymes and other complex molecular machineries are constantly moving. X-ray crystallography, a mature and incredibly influential field, has allowed the determination, to near atomic precision, of static structures of hundreds of thousands[1] of biological macromolecules. However, only a few notable examples show structural changes developing along a reaction pathway, and crystallography is typically viewed as a static technique rather than one that yields dynamic information. With modern synchrotron radiation and X-ray free electron laser (XFEL) sources, it is now possible to collect time-resolved data and potentially observe changes along a reaction pathway. Modern synchrotron light-sources are capable of time resolution below one nanosecond.[2] XFELs push this to the sub-picosecond regime. This has resulted in a growing interest in time-resolved studies.[2] However, such experiments are challenging, and one crucial step that must be addressed is the defined activation or triggering of the system for the time-resolved experiment. Possible solutions include rapid mixing or light-triggering with pulsed lasers. Light can offer a faster response and thus higher time resolution than mixing and there has therefore been a great focus on naturally photoreactive proteins such as photoactive yellow protein, Photosystem I, and Photosystem II.[3–5] However, the vast majority of proteins are of course not naturally light activated. Therefore, there is also considerable interest in introducing synthetic photoreactive functionality, such as photoswitches or photocages.[6–8]

## 1.1 TRIGGERING METHODS

Reaction initiation, or triggering, is a key part of any time-resolved structural experiment. This is because the result of the experiment is the average electron density of all molecules within the crystal. In other words, the contents of every unit cell contribute equally to the final electron density map. Therefore, mobile parts of the structure that are in different conformations in different unit cells give rise to “motion blur” in the final electron density map. Similarly, any proteins in the crystal undergoing the reaction of interest will contribute to the overall average density at each time point, but only proportionally to their population in the crystal. If only a very small fraction of proteins are in intermediate state *X* while a diffraction picture is collected, the change to the average density will be minimal. Therefore, through a reaction triggering event that is as uniform as possible, synchronisation ensures that at any given time as many individual molecules within the crystals are in the same stage of the reaction as possible.

Another important but subtle point should also be noted. Even in the case of a single molecule experiment, triggering is necessary. Take the imagined case of a single enzyme molecule, being continuously observed in its native environment, with high time resolution. The enzyme may have an average turnover of three substrate molecules per second. However, this does not mean the reaction itself takes one third of a second. Rather, the vast majority of individual *frames* are empty of interesting data. Suppose one frame is 1  $\mu\text{s}$  and the enzyme substrate complex has three intermediate states with lifetimes of 5  $\mu\text{s}$ , 500  $\mu\text{s}$ , and 2 ms. To a reasonable approximation, the reaction is complete within 10 ms. The remaining 323 ms are wasted data. This particular case is not too extreme. Consider instead the situation when an interesting intermediate has a 100 ns lifetime and frames are 10 ns, while the average turnover (for a given substrate concentration) is one substrate molecule per 10 s.

The choice of triggering method limits the achievable time resolution, regardless of the analysis method. Rapid mixing techniques are limited by diffusion, but microsecond time resolution can be achieved in some situations. For example, when microcrystals are used in time-resolved X-ray crystallography (TRX) experiments in combination with rapid mixing, diffusion over the short distance from the outside to the centre of the crystal is relatively fast as complete diffusion of a substrate throughout the crystal is proportional to the dimensions of the crystal. However, as mixing methods are not the focus of this thesis mixing methods will not be discussed further.

The only choice for reaction initiation on fast ( $< \mu\text{s}$  timescales) is laser light excitation. Lasers are required because the achievable pulse durations can be very short, while the brightness remains high. This allows for very high time resolution. Depending on the laser used,

the pulse duration may be as low as 60 fs (e.g. Ti:sapphire mode-locked oscillators or chirped pulse amplifiers)[9, 10] or in the region of 4 – 6 ns (e.g. Q-switched neodymium-doped yttrium aluminium garnet (Nd:YAG)). The duration of the pulse is an important limiting factor in the time resolution of the experiment.

There are several ways in which a system can respond or be made responsive to light. For example, Photosystem II and photoactive yellow protein are naturally light-reactive proteins. Structures of their different states at time points shortly before and after laser activation have been obtained by XFEL experiments.[5, 11] These proteins are exceptional cases, however. The majority of proteins or enzymes and their associated dynamics are not light-activatable.

Proteins that are not otherwise light-activatable can be made amenable to laser excitation using a synthetic photoswitch or photocage. This can be done by site-specific incorporation of unnatural amino acids into the protein.[12–14] Bioorthogonal chemical modification of a fully expressed protein can also be used, but this may also require incorporation of an unnatural amino acid as a prerequisite step. Alternatively, a photocaged small molecule substrate or ligand may be used.

#### 1.1.1 Photoswitches

Photoswitches are chromophores which contain, typically, an isomerisable group. Azobenzenes, for example, contain two aromatic rings joined by an isomerisable azo group. There are also examples of photoswitches that undergo other types of reversible photoreaction, e.g. spiropyran  $\leftrightarrow$  merocyanine.

Photoswitches are defined by their reversibility. Typically, irradiation with a certain wavelength of light induces a double bond isomerisation. Often, this is *trans* to *cis*, but there are some examples of photoswitches that are *cis* in their resting state. Reversal can be achieved with a different wavelength of light (fast) or by thermal relaxation (slow). Azobenzene photoswitches have been used to investigate conformational changes in proteins.[15]

#### 1.1.2 Photocages

Photocages are photo-reactive species that, after absorption of light, undergo a photoreaction leading to release of a leaving group. This leaving group is bound covalently to the photocage. In this sense, the photocage is, by itself, not the entire compound. Often, the combination is referred to as a photocaged compound or caged compound. The use of caged compounds is not restricted to reaction triggering for TRX. There are several examples of photocages being used in cellular studies, to trigger certain biological processes or initiate photoinduced

gene expression (optogenetics). Photocages can be used as a reaction trigger when the protected functionality is itself reactive. Alternatively, the bulk of a photocage can be used to sterically prevent a substrate from entering a binding site until released.[16] In this case, diffusion is still a limiting factor, albeit a minor one if the caged substrate is present in solvent channels within the crystal. One of the earliest examples of TRX using photocages was reported by Schlichting et al. in 1990.[17] Laue crystallography data were collected for caged adenosine triphosphate (ATP) bound to the Ha-Ras p21 protein before photolysis, and 4 and 14 min after photolysis. The photocage was  $\alpha$ -methyl-2-nitrobenzyl (MNB). The light source was a Xenon flash lamp.

The crucial photoreaction of photocages is photolysis (often referred to as photocleavage). Photolysis is defined by IUPAC as “the cleavage of one or more covalent bonds in a molecular entity resulting from absorption of light, or a photochemical process in which such cleavage is an essential part”.[18] There are three distinct categories of photolysis reaction. In direct photolysis, the transition that is excited is from the bonding to the anti-bonding orbital of the bond that is broken. Lysis is effectively instantaneous, upon photon absorption. This typically requires high energy X-ray or extreme ultraviolet (XUV) photons. However, ligand-metal bonds in transition metal complexes may be weak enough to directly photolyse with ultraviolet (UV) light. Barends et al., for example, triggered the dissociation of CO from a haem group in myoglobin.[19, 20] Following direct photolysis of the Fe-CO bond, the protein undergoes structural changes within 500 fs. A 532 nm laser pulse with 150 fs duration was used to excite the sample. Each sample was probed once with an XFEL at a certain time interval after laser excitation. The time frame investigated was 0.6 ps in 0.1 ps intervals. Unexcited or ‘dark’ diffraction images were also collected.

The second category is bond lysis occurring via a single photochemical step. This can occur in a number of ways. Essentially, an excited state caged molecule relaxes to form two separate ground state molecules: one a no longer caged compound, the other a by-product of the photocage itself. Examples of photocages of this type include coumarinyl (Cm) and 4-hydroxyphenacyls (4-HP). Reactions of excited molecules, or relaxation from an excited state to the ground state, tends to occur on the order of ps, unless triplet pathways are involved. Triplet excited states may have lifetimes of  $\mu$ s or even seconds. However, 4-HP cages undergo rapid ( $\tau \approx 60$  ps) bond cleavage from the  $T_1$  excited state.[21] 4-HP caged guanosine-5'-triphosphate (GTP) was used by Kötting et al. in a kinetic study of the enzyme Ras GTPase, where time-resolved fourier transform infrared (FTIR) was used to analyse the enzyme dynamics after triggering the release of caged GTP.[22]

In the third category, the initial photochemical reaction step results in a metastable photoproduct. This initial photoproduct undergoes

further thermal reaction steps, eventually arriving at a bond-cleaving step. The endpoint of this process is release of the caged moiety. Depending on the thermal steps involved, this type of photocage will have much slower overall photolysis kinetics. 2-nitrobenzyl (NB) photocages are of this type. As well as photolysis rates, other properties of individual photocages will vary. These include quantum yield, absorption properties (possible excitation wavelengths), as well as other physical and chemical properties such as solubility and stability. Many of these properties (including rate) may depend on the nature of the leaving group.

Photocages are occasionally used in organic chemistry as any other protecting group: they can be removed under a particular set of conditions (irradiation by light), while other protecting groups in the same molecule remain stable. This is the principle of orthogonal protection. Some authors have exploited photocages that require different wavelengths of light for photolysis for orthogonal deprotection. However, the unique properties of photocages are much better suited to their use as triggers, rather than traditional protecting groups. One reason for this is that photochemistry, in general, is not very well suited to synthetic applications. The procedures are difficult to scale up as it can be difficult to efficiently deliver photons to an entire reaction volume. In some cases, the photo-by-products of photocage removal act as an internal filter, reducing reaction efficiency. Advances in synthetic flow chemistry have been beneficial to the field of synthetic photochemistry.[23]

However, photocages offer a method of reaction triggering, or release of a certain molecule with high spatial and temporal control. It is this that makes them particularly well suited to triggering applications.

### 1.1.3 Reaction initiation using a photocage: practical considerations

When using laser excitation in combination with a photocage to trigger a reaction, several parameters are important to consider. The wavelength and energy of the pulse, as well as the properties of the sample, determine the extent of excitation.

Let us consider an example using an excitation wavelength of 355 nm and let it be assumed that the photocage chromophore has an extinction coefficient  $\epsilon_{355} = 4000 \text{ M}^{-1} \text{ cm}^{-1}$ . It is assumed, additionally, that only the crystal itself is hit by the laser, no excess aqueous buffer is involved and the depth of the crystal is 50  $\mu\text{m}$ . Finally, to calculate the amount of sample that is likely to be excited we also need to know the concentration of the photocage in the crystal.

Here there are two possibilities. If the crystal was soaked by mixing with photocaged substrate solution, some photocaged substrate may have bound in the active site of the protein. However, if the crystals were not back-soaked in a buffer solution free of photocaged

substrate, there is likely to be photocaged substrate also within the solvent channels of the protein crystal. In this case, the concentration of the photocage is approximately equal to the concentration of photocaged substrate buffer solution, adjusted for dilution by the crystal mother liquor. If the crystals are subsequently back-soaked in caged compound-free crystallisation buffer, the concentration is instead approximately equal to the concentration of protein active sites per unit volume in the crystal structure, although this will depend to some extent on the caged compound binding affinity. Let it be assumed that the former case is true and that, in this example, a concentration of 30 mM caged compound was used, diluted to 20 mM when mixed with crystal mother liquor.

In this example, using the Beer-Lambert Law, the absorbance of the sample is thus  $4000 \text{ M}^{-1} \text{ cm}^{-1} \times 0.02 \text{ M} \times 0.005 \text{ cm} = 0.4$ . This means approximately 40 % of incident light is transmitted through the crystal. In other words, the intensity of the laser pulse at the back of the crystal is 40% of the intensity at the front. This does not guarantee totally uniform excitation, but does demonstrate that the sample is fully penetrated by the laser in this case. The spatial extent of the pulse is also important when considering how to achieve a uniform illumination. If it is not possible to illuminate the entire crystal, the  $x$  and  $y$  spread of the laser spot should at least be larger than the X-ray probe beam. This is assumed to be the case for this example.

This simple Beer-Lambert treatment may be inappropriate, however, depending on the intensity distribution of the laser pulse. At high intensities, maximum excitation is achieved within a small volume and the reduction in intensity is not proportional to the total intensity. Depending on the timescales involved, this maximum excitation may be 50 % as stimulated emission will occur in a two-level system at this point. However, longer pulse durations will allow some excited chromophores to relax. If they relax back to the initial ground state, they can be excited again, raising the effective fraction excited above 50 %.

The amount of sample which is excited does not alone determine the amount of sample where a reaction is effectively triggered. The photochemical quantum yield determines the fraction of excited chromophores which undergo photoreaction. If the photo-decaging reaction occurs by bond breaking during relaxation from the excited to the ground state (e.g. coumarinyl (Cm), 4-hydroxyphenacyls (4-HP)), the fraction excited multiplied by the quantum yield gives the amount of released substrate. If, however, the decaging reaction is more complex (nitrobenzyl photocages), the effective quantum yield of caged compound release may be lower. It is this effective quantum yield,  $Q_{\text{eff}}$ , and not necessarily the photochemical quantum yield  $\phi$ , which needs to be known.

Note again two cases. In one case, photocaged substrate molecules are bound to the active site and not necessarily present elsewhere. In another case, photocaged substrate molecules are present in the crystal but not directly interacting with the protein. This situation may be useful if the effective quantum yield is not very high, as the concentration of photocaged substrate could be much higher than the concentration of protein active sites. Therefore, the fraction of successful reaction initiation events may be higher than the fraction determined by excitation yield and effective quantum yield of photocaged substrates.

Another possibility exists, which may increase the overall activated fraction. Rather than a single laser pulse, a train of pulses could be delivered. This would be effective if the pulses are separated for sufficient time for activation to occur, allowing multiple activation events in short succession. Overall time resolution would be reduced (limited by the overall duration of the entire pulse train), but higher signal for the activated fraction would be obtained.

#### 1.1.4 *Sample response*

The purpose of laser pulse activation and photocaged substrate is to provide an unprotected functional moiety (i.e. active site or substrate). However, not every protein molecule in the crystal will be activated, and those that are may not all be activated simultaneously. Also, intermediates may react backwards as well as forwards. These issues will limit data quality and achievable time resolution.

Chemical and photochemical reactions can occur on a broad range of timescales. Photochemical events, in particular, may occur on pico- to nanosecond timescales, although triplet excited states can have much longer lifetimes. Timescales of chemical transformations can range from nanoseconds to seconds or longer. Reactions involving large macromolecules like proteins often occur on these longer timescales. However, some steps may be faster than others. Even if one turnover of an enzyme may take seconds, there may still be interesting events happening on nano to microsecond timescales. In addition, it may not be known *a priori* what timescales are most important for a given protein or enzymatic reaction. Thus, the ideal experiment should have extremely high time resolution (down to nano or even picoseconds) and a broad dynamic range of post-excitation delay times.

Due to the demands of TRX experiments, fast cleavage rate and high quantum yield are highly desirable qualities. Good aqueous solubility and stability under 'dark' conditions are also important. The possibility to initiate a reaction with near-UV light is also ideal – shorter wavelength UV (e.g. 280 nm) may cause unwanted damage to proteins.

The requirement of high quantum yield is especially important, due to the inherent difficulties in extracting difference density from diffrac-

tion data, when only a fraction of the proteins within a crystal have undergone an interesting reaction. Changes in difference density must be extracted from small modulations in the intensity of diffraction spots, and errors (both systematic and random) may be larger than the intensity modulation, unless a large proportion of proteins within the crystal have reacted.

## 1.2 TOPICS DISCUSSED IN THIS THESIS

The focus of this thesis is experimental organic synthesis. It is assumed that the reader understands basic workup methods and nuclear magnetic resonance (NMR) spectroscopy – mainly  $^1\text{H}$  NMR results will be presented. Mechanisms of synthetic reactions will be discussed, where they are well-known. Otherwise some plausible mechanism(s) will be presented if possible.

Due to the author's interest in reaction mechanism in general, there is a detailed examination of one particular reaction which is key to this thesis. That is the photocleavage of nitrobenzyl photocages. This will be examined in great detail with reference both to the author's work, and extensive literature. The literature on nitrobenzyl photocages and their reaction mechanisms is quite extensive. A fully comprehensive review is outside the scope of this PhD thesis. Nevertheless, a reasonably thorough treatment is given.

In addition to literature review and experimental work, an attempt was made to understand some of these results with density functional theory (DFT).

The focus of Chapter 2 is the synthesis of photocaged L-aspartates using a subset of NB cages:  $\alpha$ -carboxynitrobenzyl (CNB). This is also the topic of the published work.[24] Characterisation of stability and quantum yield as well as a qualitative investigation of radiolability are presented in this chapter. Chapter 3 details investigations towards an asymmetric synthetic route for CNB photocages.

More detailed studies on mechanism and reaction kinetics of CNB photocleavage reactions are the focus of Chapter 4; this includes some computational work with DFT.

Chapter 5, Conclusions, presents a summary of the work presented in this thesis.

Experimental organic synthesis procedures are listed in Chapter 6, Bibliography contains the list of references.



## $\alpha$ -CARBOXYNITROBENZYL PHOTOCAGES: SYNTHESIS AND CHARACTERISATION

### 2.1 INTRODUCTION

CNB photocages are a subclass of the NB photocages. They have two major advantages over typical NB photocages. Firstly, their photocleavage times can be shorter (on the order of  $\mu\text{s}$  in some cases)[24–26]. The parent (unsubstituted) nitrobenzyl photocage cleavage time constant is more often on the order of ms.[27] Secondly, they tend to have greater aqueous solubility. These properties are both beneficial to the goal of macromolecular TRX. Faster photocleavage rates allow better time-resolution. Enhanced aqueous solubility improves their applicability to TRX as proteins are normally in aqueous environments (protein crystals contain a lot of water).

A caged amino acid, 1-( $\alpha$ -carboxy-2-nitrobenzyl)-L-aspartate (**1-CNB-L-Asp**), was chosen as a synthetic target, along with a piperonyl analogue: 1-( $\alpha$ -carboxy-6-nitropiperonyl)-L-aspartate (**1-CNP-L-Asp**). This modification is known to enhance absorption at longer wavelengths (typically an additional band presents with  $\lambda_{\text{max}} \sim 350 \text{ nm}$ ).[28] A brominated derivative was also chosen as a target: 1-(4-bromo- $\alpha$ -carboxynitrobenzyl)-L-aspartate (**1-(4-Br-CNB)-L-Asp**). It has previously been reported that this substituent improved the rate of photocleavage.[29]

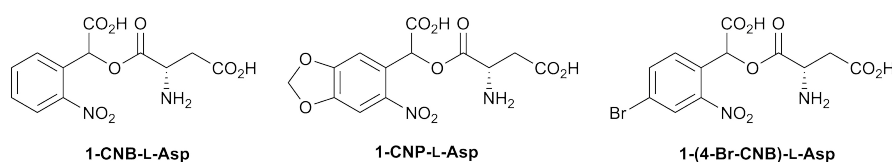


Figure 2.1: Photocaged L-aspartates synthesised and characterised as part of this thesis work.

The improved aqueous solubility of CNB cages is easily explained. The carboxylic acid group is polar and ionises at above ca. pH 5. The reason for the effect on photocleavage rate is much less clear.

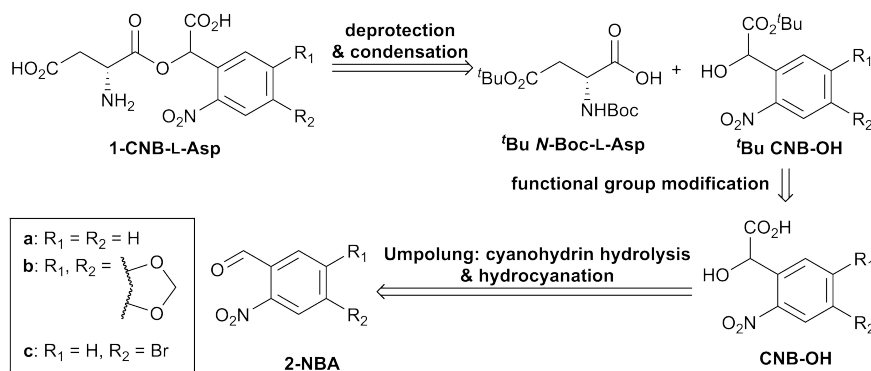
The primary effect of the 3,4-methylenedioxy substitution pattern has a clear cause. The oxygen lone-pairs interact with the aromatic system, reducing the gap between the highest occupied molecular orbital (HOMO) and the lowest unoccupied molecular orbital (LUMO). Thus, a lower energy  $n \rightarrow \pi^*$  transition gives rise to the additional absorption band at 360 nm, allowing these photocages to be excited more efficiently at longer wavelengths. Unfortunately, as is discussed

in sections [2.3.2](#) and [4.3.1](#), this also results in a lowered photocleavage rate and quantum yield.<sup>[24]</sup>

The effect of the 4-bromo substituent was expected to be an increase in rate, as mentioned above. We found this not to be the case.<sup>[24]</sup> Instead, the quantum yield was somewhat higher – these data are presented in [Section 2.3.2](#).

## 2.2 SYNTHESIS

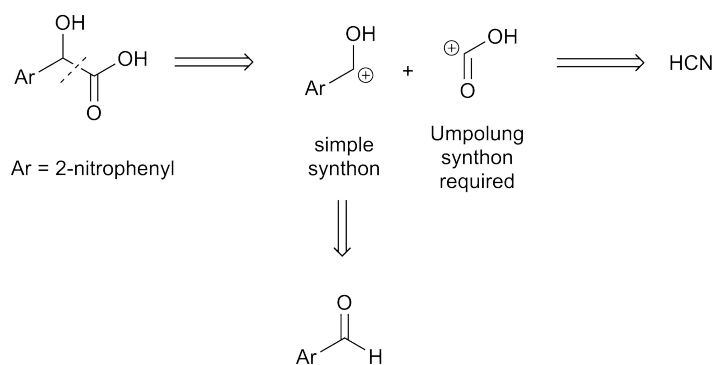
The retrosynthetic analysis of **CNB** caged L-aspartates is shown in [Scheme 2.1](#). The first step is protection of amine and carboxyl protecting groups, and disconnection at the ester bond. This results in 4-*tert*-butyl *N*-Boc L-aspartate and the alcohol precursors (***t*Bu CNB-OH**). Functional group modification presents 2-nitromandelic acids (**CNB-OH**) as potential precursors for ***t*Bu CNB-OH**. Umpolung via the cyanohydrins formed from the commercially available aldehydes (**2-NBA**) completes the retrosynthesis. The entire synthesis is discussed herein, beginning with the Umpolung synthesis of hydroxyacids (**CNB-OH**). In this text, the abbreviation **CNB** refers both specifically to the parent  $\alpha$ -carboxy-2-nitrobenzyl moiety and its derivatives ( $\alpha$ -carboxy-6-nitropiperonyl, **CNP**;  $\alpha$ -carboxy-4-bromo-2-nitropiperonyl, **4-Br-CNB**). Likewise, **2-NBA** may refer to 2-nitrobenzaldehyde or the class of substituted 2-nitrobenzaldehydes including 6-nitropiperonal (**6-NPA**) and 4-bromo-2-nitrobenzaldehyde (**4-Br-NBA**).

Scheme 2.1: Retrosynthesis of 1-**CNB** caged L-aspartates.2.2.1 Synthesis of  $\alpha$ -hydroxyacids: Umpolung via cyanide addition to carbonyl

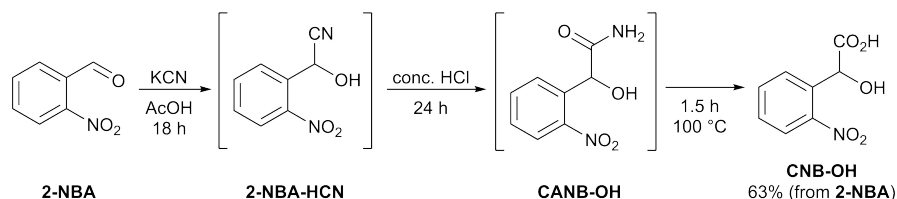
Disconnection at the carbon-carbon bond between the hydroxyl and the carboxyl groups yields two electrophilic centres ([Figure 2.2](#)).

$\alpha$ -Hydroxyacids are thus a classic example of a synthetic product that requires Umpolung techniques. Using cyanide as a nucleophile is one way to achieve this. Nucleophilic attack of an aldehyde by cyanide forms a cyanohydrin. Hydrolysis of the cyanide group reverses the Umpolung to afford the  $\alpha$ -hydroxyacid.

Initially, a published procedure ([Scheme 2.3](#))[25] was reproduced, which starts from 2-nitrobenzaldehyde (**2-NB**). According to the protocol, the aldehyde is treated with KCN in acetic acid at room temperature for 1.5 h, conc. HCl is then added and the mixture is stirred for 6 h at r.t. and 8 h at 80 °C. 1.5 h is, in fact, insufficient for complete

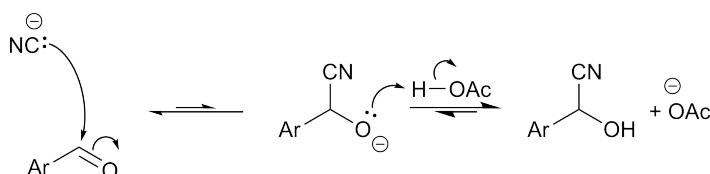
Scheme 2.2: Retrosynthetic analysis – disconnection of  $\alpha$ -hydroxyacid.

conversion to the cyanohydrin (**2-NBA-HCN**). Overnight (18 h) reaction is adequate. Conversely, for the final stage, 1 – 1.5 h at reflux is enough to hydrolyse the  $\alpha$ -carboxamido-2-nitrobenzyl alcohol (**CANB-OH**). 24 h reaction time is sufficient for the intermediate stage. Note that in this work, the minimum reaction time for complete conversion was not found for the first two stages. Thus, the following interpretation consistent with this discrepancy is presented. Grewer and colleagues carried out their reaction at 8 h, r.t.; then 6 h at r.t. after addition of conc. HCl and finally 1.5 h at 80 °C. They mistakenly swapped the times for stages one and three in the published article.

Scheme 2.3: Synthesis of 2-nitromandelic acid (**CNB-OH**), based on Grewer's protocol,<sup>[25]</sup> with some modifications to reaction times and temperatures. Yield shown is after recrystallisation from hot EtOAc/hexanes.

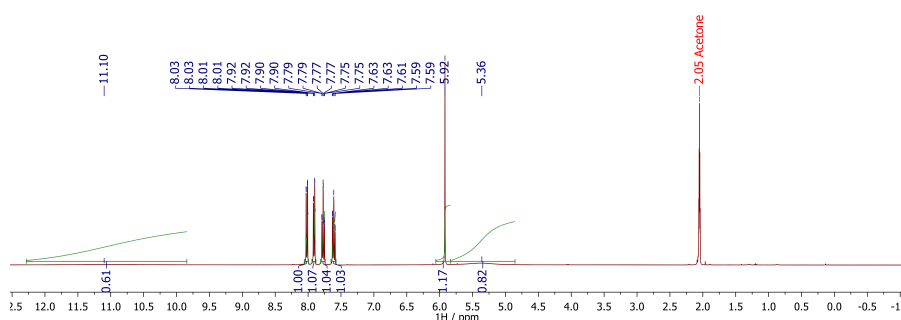
KCN in acetic acid creates an equilibrium between HCN and  $\text{CN}^-$ . The  $\text{p}K_{\text{a}}$  difference is about 4, so only 0.01 % of cyanide is deprotonated, though the anion is more nucleophilic. This is based on the aqueous  $\text{p}K_{\text{a}}$  of each compound in water, so will be somewhat different in glacial acetic acid. Nevertheless, it illustrates the point. It is the anionic cyanide species that attacks the aldehyde (Scheme 2.4). The initially formed alkoxide is unstable, and the equilibrium would normally favour aldehyde and  $\text{CN}^-$ . Under acidic conditions, however, this intermediate is protonated to form the cyanohydrin. The hydrolysis of cyanide to carboxyl is presented in Scheme 2.8.

The identity of the product as 2-nitromandelic acid (**CNB-OH**) was confirmed by  $^1\text{H}$  NMR analysis (see Figure 2.2). There is no aldehyde hydrogen signal present (typically seen at ca. 10 ppm), instead the



Scheme 2.4: Cyanation of an aromatic aldehyde.

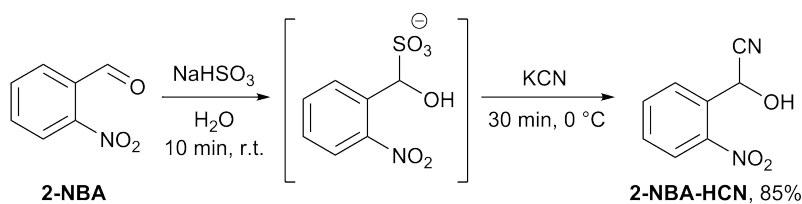
benzylic CH resonates at 5.92 ppm. A very broad signal due to the carboxyl group stretches from 12.5 to 10.0 ppm. A broad OH peak is seen at 5.36 ppm and all signals are consistent with the data published by Grever.[25] The only exception is that they did not report any carboxylic acid hydrogen signal. This is not surprising as these signals can vary and are often not present.

Figure 2.2:  $^1\text{H}$  NMR (400 MHz, acetone- $d_6$ ) spectrum of 2-nitromandelic acid (CNB-OH).

This reaction has the advantage of producing the hydroxyacid (CNB-OH) in a one-pot reaction with multiple stages. However, one major disadvantage of the procedure is a safety concern. The cyanohydrin formation stage relies on *in situ* generated HCN (best done in a closed reaction flask). This is eventually boiled off at the reflux stage of the reaction. This could be very dangerous in the case of a ventilation failure. This was a strong motivation to search for an alternative.

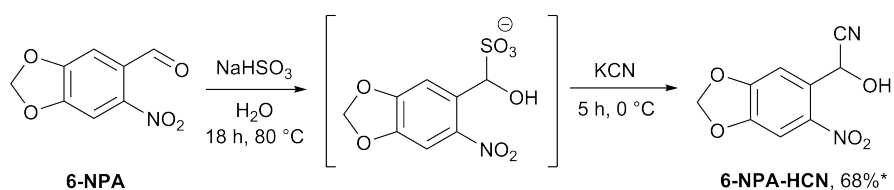
Another procedure reported in the literature uses sodium bisulfite and KCN in water.[30] In this reaction, bisulfite attacks the aldehyde via a lone-pair on the sulfur atom. This, combined with a proton transfer, gives the bisulfite addition intermediate shown in Scheme 2.5. The next step is an  $\text{S}_{\text{N}}2$  reaction displacing  $\text{SO}_3^{2-}$  with  $\text{CN}^-$ . This reaction is effective and high-yielding when 2-nitrobenzaldehyde (2-NBA) is the starting material.[30]

However, when this was attempted with a different starting aldehyde, 6-nitropiperonal (6-NPA), the reaction did not result in high yields. The procedure was attempted three times, with yields ranging from trace to 41 to 68%. Yields were based on  $^1\text{H}$  NMR integration, as the product contained some recovered starting material. The best result employed an inert atmosphere and  $80^\circ\text{C}$  for 18 h for the first stage, followed by  $0 - 4^\circ\text{C}$  for 18 h for the second stage. Perhaps



Scheme 2.5: Synthesis of the cyanohydrin (**2-NBA-HCN**) via bisulfite addition intermediate, as reported by Rossi.[30]

the electron-donating methylenedioxy substituent impairs bisulfite addition or the subsequent  $S_N2$ . Also, sodium bisulfite in solution is sensitive to oxidation, a fact which was not considered during the first two attempts. Further optimisation of this protocol may indeed have produced superior results.



Scheme 2.6: Synthesis of 6-nitropiperonal cyanohydrin (**6-NPA-HCN**). The product was not purified. \*yield based on  $^1\text{H}$  NMR integration, remainder was starting material (**6-NPA**).

The  $^1\text{H}$  NMR spectrum of the mixture is shown in Figure 2.3, with assignments. The signal at 10.21 ppm corresponds to the aldehyde hydrogen resonance. The consistency of the integrals helps distinguish the two components of the mixture. The sum of integrals is 1.81 for the aldehyde and 5.18 for the cyanohydrin (excluding the OH peak). The molar ratio is therefore approximately 9:26, aldehyde to cyanohydrin. The total molar amount of the mixture was  $0.50\text{ g}/215.21\text{ g mol}^{-1}$  (composite formula mass for the mixture) = 2.3 mmol. The reaction was carried out with 2.6 mmol of **6-NPA**. Thus, the total yield of the mixture was 88%. Approximately 1.7 mmol was **6-NPA-HCN**, or a yield of 65% based on  $^1\text{H}$  NMR integration. Note that this is a rather crude approximation that does not account for any compounds present that are not **6-NPA** or **6-NPA-HCN**.

The more downfield pair of aromatic signals belong to the aromatic hydrogens *ortho* to the nitro group of each compound. The signal assigned to the cyanohydrin OH has a lower integral than all the other signals of the compound. This was probably because exchange between acetone- $d_6$  and water was occurring. Signals for both  $\text{H}_2\text{O}$  and HDO are clearly present in the spectrum.[31] This means the HDO could also have undergone exchange with the cyanohydrin OH, reducing the signal intensity as some was replaced by OD. The aldehyde  $\text{CH}_2$  signal is a singlet, in the cyanohydrin these two hydrogens have

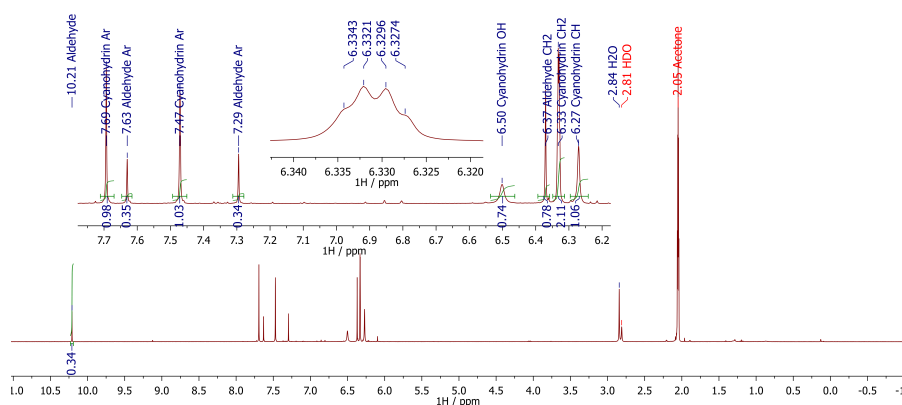
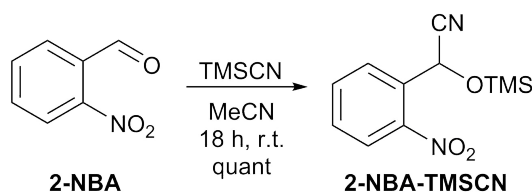


Figure 2.3:  $^1\text{H}$  NMR (400 MHz, acetone- $d_6$ ) spectrum of the crude product mixture obtained using the conditions described in Scheme 2.6.

become diastereotopic, thus appearing as two very close doublets,  $^2J_{\text{HH}} = 0.9\text{ Hz}$ . This is very small for a geminal coupling constant but consistent with a methylenedioxy fragment (electron donating groups tend to give small geminal hydrogen coupling constants). The signal at 6.27 ppm is consistent with a benzylic cyanohydrin CH; Rossi, Margulis et al. reported 6.19 ppm for the corresponding signal for **2-NBA-HCN**.<sup>[32]</sup> A more rigorous assignment could have been performed for the cyanohydrin. However, a simpler and easier approach was discovered: the uncatalysed addition of trimethylsilyl cyanide (**TMSCN**) to aldehydes.<sup>[33]</sup>

In this reaction, a slight excess of **TMSCN** (1.05 eq.) is used and the reaction is carried out for typically 10 – 12 h, at r.t. or 85 °C in acetonitrile under dry conditions. 2-Nitrobenzaldehyde (**2-NBA**) reacts efficiently, giving 95% yield after 12 h at 20 °C (see also Scheme 2.7, overleaf).<sup>[33]</sup> Electron-donating groups impede the reaction, e.g. 4-methoxybenzaldehyde requires 18 h at 85 °C for 33% yield.<sup>[33]</sup> Fortunately, the reaction was effective when a mixture of electron-donating and withdrawing groups were present, as with 6-nitropiperonal (**6-NPA**).<sup>[24]</sup> This reaction proved to be sufficiently general, and obviated the need for stoichiometric *in situ* generated HCN (though it must be noted that, improperly handled, **TMSCN** will also degrade to release HCN). Furthermore, the reaction is operationally very simple: no more workup is needed than the evaporation of acetonitrile under reduced pressure.

The  $^1\text{H}$  NMR spectrum of **6-NPA-TMSCN** is shown in Figure 2.4. In this particular example, not a trace of aldehyde can be seen. The peak assignments can be found in the supporting information of the published work.<sup>[24]</sup> Interestingly, in this case the methylene shift is not resolved as a pair of diastereotopic signals, but appears as a singlet. The shift at 0.28 ppm is consistent with a trimethylsilyl (**TMS**) group. In the case of **6-NPA-TMSCN**, an accurate mass was also obtained, but not for **2-NB-TMSCN** or **4-Br-2-NB-TMSCN**.



Scheme 2.7: The addition of **TMSCN** to 2-nitrobenzaldehydes (**2-NBA**), based on the protocol of Manju & Trehan.[33] The yield of “quant.” is based on our own work.

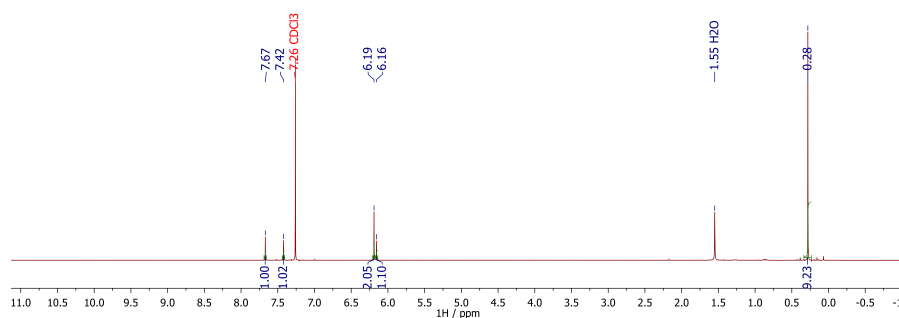


Figure 2.4:  $^1\text{H}$  NMR (400 MHz,  $\text{CDCl}_3$ ) spectrum of the **TMS**-protected cyanohydrin (**6-NPA-TMSCN**).

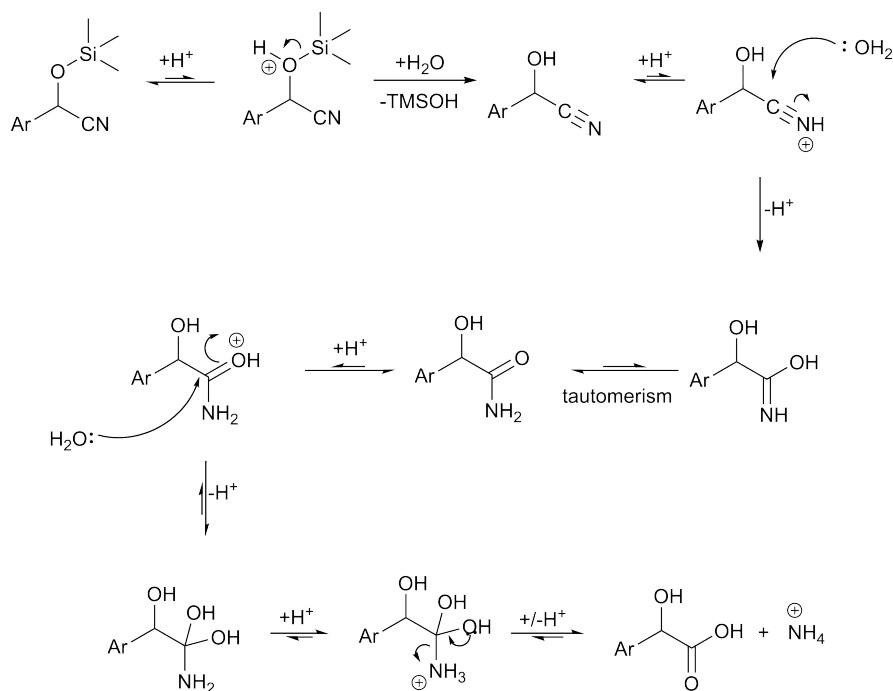
The conversion of **TMS** protected cyanohydrins (**2-NBA-TMSCN**) is essentially the same as that above for the conversion of cyanohydrins to the hydroxyacids (**CNB-OH**). The mechanism of (**TMS**) cyanohydrin hydrolysis is shown in [Scheme 2.8](#).

### 2.2.2 Attempted selective protection of the carboxyl group

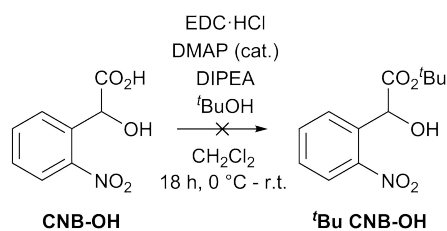
The alcohol precursors (***t*Bu CNB-OH**) for ester condensation can be synthesised in a single step from 2-nitromandelic acids (**CNB-OH**). However, attempts at doing so provided either no desired product or impure product in low yields.

In the first attempt, 1-ethyl-3-(3-dimethylaminopropyl)carbodiimide hydrochloride (**EDC-HCl**) and *tert*-butanol with 4-(dimethylamino)pyridine (**DMAP**) ([Scheme 2.9](#)) produced a product mixture with a very complex  $^1\text{H}$  NMR spectrum. None of the desired product was detected by thin-layer chromatography (**TLC**) analysis. In this case, the failure is likely due to *tert*-butanol being a rather sterically hindered nucleophile. Most likely attack by the hydroxyl group of **CNB-OH** is favoured, leading to polymeric products.

Isobutene and sulfuric acid in dichloromethane at low temperature was poorly selective for the desired alkylation and produced a significant amount of di-*tert*-butyl 2-nitromandelate (***t*Bu CNB-O<sup>t</sup>Bu**). The literature protocol states that 0.2 ml  $\text{H}_2\text{SO}_4$  at  $-50^\circ\text{C}$  was added to a suspension of **CNB-OH** in  $\text{CH}_2\text{Cl}_2$  and isobutene, and simply “stirred for 8 h while warming to room temperature” to give a final

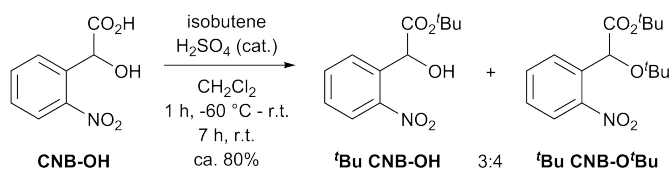


Scheme 2.8: Mechanism of (TMS) cyanohydrin hydrolysis to afford hydroxyacids.



Scheme 2.9: A failed attempt at condensation of the hydroxyacid (CNB-OH) with *tert*-butanol, using the carbodiimide coupling reagent EDC-HCl.

isolated yield of 60%.<sup>[25]</sup> Several attempts to reproduce this failed. Leaving the reaction overnight produced too much doubly alkylated product (*t*Bu CNB-*O**t*Bu). Warming very slowly to r.t. over the entire 8 h gave 83% recovered starting material and 9% CNB-OH. The best result was that shown in Scheme 2.10, where the combined yield of *t*Bu CNB-OH and *t*Bu CNB-*O**t*Bu was approximately 80%. The ratio of singly to doubly alkylated products was 3:4. This was determined by the integrals of the benzylic CH peaks in the <sup>1</sup>H NMR spectrum of the mixture (Figure 2.5). The identity of the peaks belonging to *t*Bu CNB-OH can be confirmed based on literature values.<sup>[25]</sup> The CH shift (5.79 ppm) and additional *tert*-butyl shift (1.26 ppm) can also be seen in the <sup>1</sup>H NMR spectrum of a sample containing primarily *t*Bu CNB-*O**t*Bu (Figure 2.6).



Scheme 2.10: Alkylation of 2-nitromandelic acid (**CNB-OH**) with *in situ* generated *tert*-butyl carbocation.

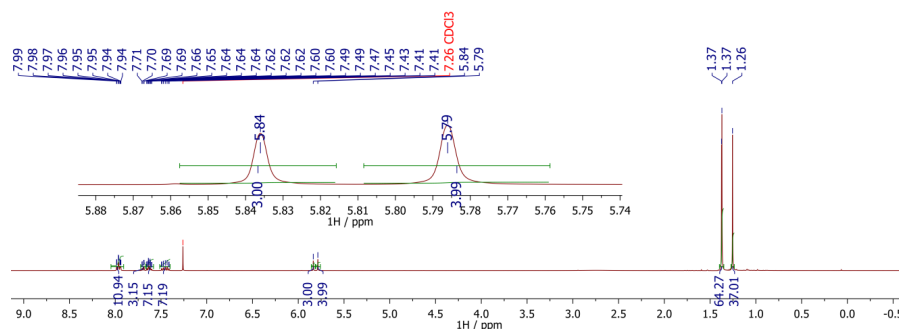


Figure 2.5:  $^1\text{H}$  NMR (400 MHz,  $\text{CDCl}_3$ ) spectrum of a mixture of compounds **tBu CNB-OH** and **tBu CNB-O<sup>t</sup>Bu**. The latter has an additional *tert*-butyl peak at 1.26 ppm, while its benzylic CH resonates at 5.79 ppm.

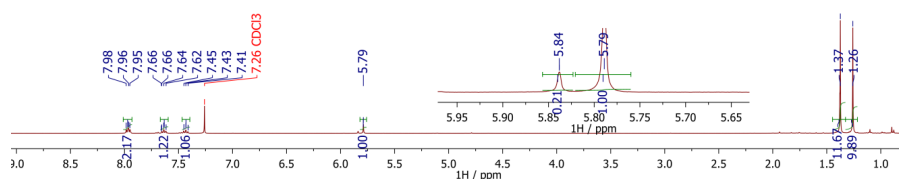
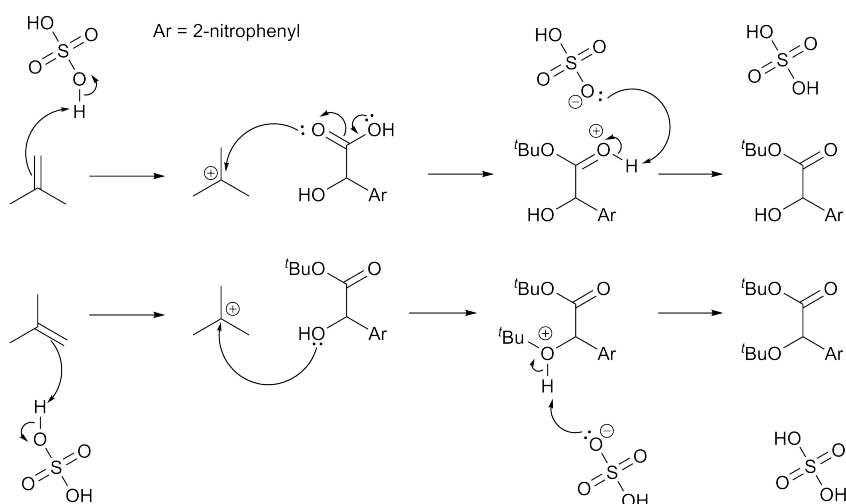


Figure 2.6:  $^1\text{H}$  NMR (400 MHz,  $\text{CDCl}_3$ ) spectrum of **tBu CNB-O<sup>t</sup>Bu**, this sample was not purified, but very little alcohol can be seen. This was the result when the reaction warmed to r.t. overnight. The ratio of **tBu CNB-OH** to **tBu CNB-O<sup>t</sup>Bu** is approximately 1:5.

The mechanism of this reaction is straightforward. Sulfuric acid protonates isobutene to form the *tert*-butyl carbocation and this strong electrophile can attack either the carboxylic acid or the hydroxyl group (Scheme 2.11).

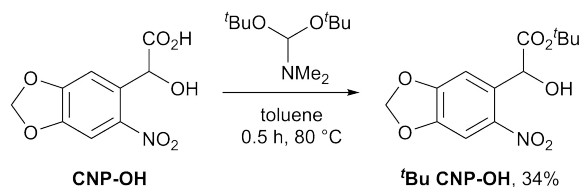
The product of addition to only the hydroxyl was not detected, which suggests that the carboxylic acid group is alkylated first (as is shown in Scheme 2.11). Therefore, careful tweaking of reaction conditions may have eventually yielded superior results. However, it was decided to search for an alternative.

An attempt was also made using Widmer's reagent[34] (*N,N*-dimethylformamide di-*tert*-butyl acetal), shown in Scheme 2.12. Widmer's publication does not discuss the mechanism of its use as an alkylating agent. However, a reference therein is useful. Abdulla and Brinkmeyer discuss formamide acetal chemistry in great detail.[35] One mechanism is given for dimethylformamide di-*sec*-butyl acetal (Scheme 2.13,



Scheme 2.11: Mechanism of *tert*-butyl carbocation formation and addition to carboxylic acid and hydroxyl.

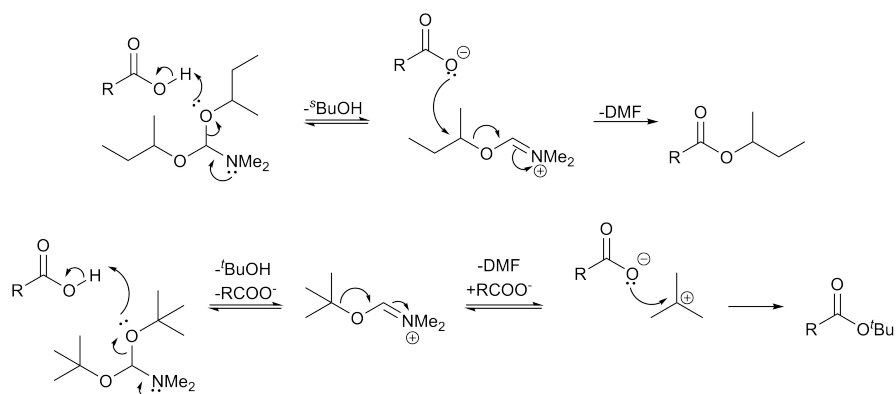
top). The  $S_N2$  displacement of dimethylformamide by the carboxylate may not be effective for the more sterically hindered dimethylformamide di-*tert*-butyl acetal. The reaction probably proceeds by the same first step (formation of the charged *O*-alkyl imidate), followed by a more favourable  $S_N1$  step to give a *tert*-butyl carbocation (Scheme 2.13, bottom). This works but the reaction produces a number of side-products (several spots were observed by TLC analysis) leading to a poor yield after purification.



Scheme 2.12: Selective alkylation of the hydroxyacid (**CNP-OH**).

Just as an aside, one method which might work (though was not tested), would be to rely on  $pK_a$  differences, e.g. treat **CNB-OH** with a weak base like  $K_2CO_3$  to form the carboxylate. Then add *tert*-butyl iodide, or another source of the tertiary carbocation (not more than one equivalent). The anionic carboxylate would most likely be more nucleophilic than the alcohol.

Good results were finally obtained following a lengthier three-step procedure found in the literature.[32] Here, the hydroxyl group is selectively acetylated with acetic anhydride, giving compound **CNB-OAc** (Scheme 2.14). Some mixed anhydride is also formed (**Ac CNB-OAc**), but this is readily cleaved during workup. THF and water are added after acetylation is complete, and the reaction is stirred for 2 h at 45 °C to hydrolyse any mixed anhydride as well as the excess acetic



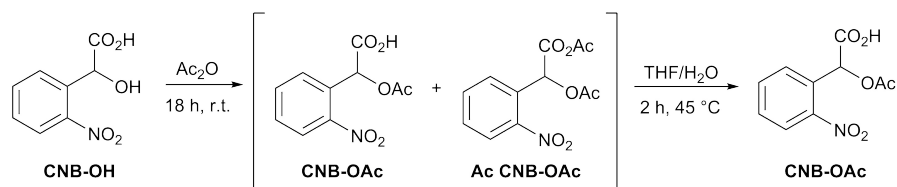
Scheme 2.13: Alkylation mechanisms using dimethylformamide acetals as alkylating agents.

(top) with the di-*sec*-butyl acetal.[35]

(bottom) my proposed mechanism with the di-*tert*-butyl acetal.

anhydride. Then, an extractive workup is performed, using toluene to help phase separation. However, the reaction is very simple and there are no ionic reagents or by-products to remove. Extractive aqueous workup is unnecessary, and azeotropic removal of water and acetic acid with toluene can be performed directly. Complete removal of acetic acid is difficult and the crude 'yield' often over 100%. Further purification is possible (detailed in [Chapter 4](#)), but the crude material is adequate for the next step. [Figure 2.7](#) shows the  $^1\text{H}$  NMR spectrum of the acetate (CNB-OAc), the peak at 2.17 ppm is due to the -OAc group.

The mechanism of reaction is  $\text{S}_{\text{N}}\text{Ac}$  (nucleophilic acyl substitution, [Scheme 2.15](#)). The alcohol lone-pair attacks the carbonyl carbon to form a tetrahedral intermediate. This collapses, expelling  $\text{AcO}^-$ , which then acquires a proton from the initial oxonium (not shown). The mechanistic steps are equilibria. However, the excess of acetic anhydride, and the greater thermodynamic stability of ester vs. anhydride, drives the reaction to completion. The same mechanism can occur with attack from the carboxylic acid. However, as mentioned previously, the resulting mixed anhydride is not stable to workup conditions.



Scheme 2.14: Acetylation of 2-nitromandelic acid (CNB-OH).

*tert*-Butyl trichloroacetimidate (TBTA) is then used to alkylate the carboxylic acid group to afford the fully protected precursor ( $^t\text{Bu}$

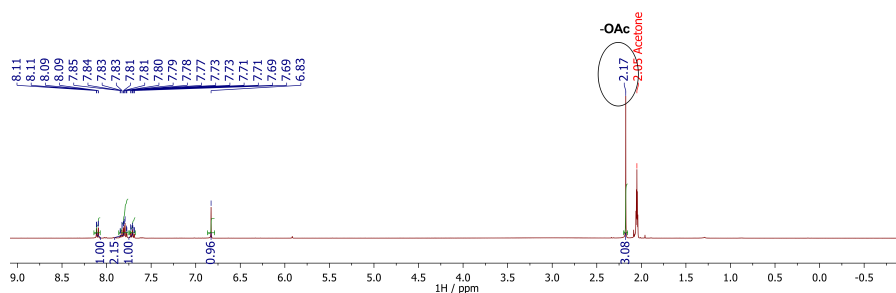
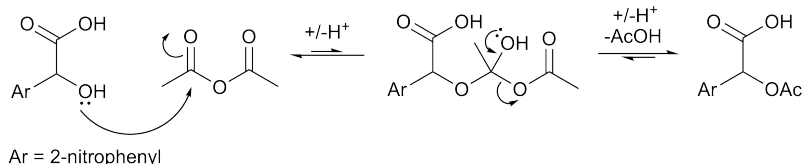
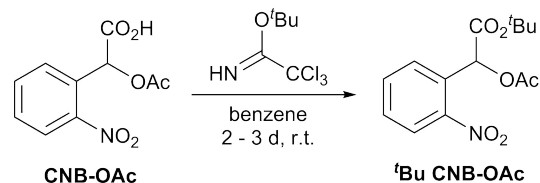


Figure 2.7:  $^1\text{H}$  NMR (400 MHz, acetone- $d_6$ ) spectrum of **CNB-OAc**.



Scheme 2.15: Acetylation reaction mechanism by  $\text{S}_{\text{N}}\text{Ac}$ .

**CNB-OAc**, Scheme 2.16). The reaction time is lengthy and TLC analysis has never showed complete consumption of starting material, even after 2 – 3 days. However, this is sufficient for yields of 70% or more. Figure 2.9 shows the new *tert*-butyl peak at 1.40 ppm. The by-product of the reaction is trichloroacetamide, much of which can be removed by filtration. The rest is removed by column chromatography; as can be expected, the product has a much higher  $R_f$  than the starting material (**CNB-OAc**). With 10% EtOAc-hexanes, **CNB-OAc** remains on the baseline. The yield given is usually that obtained over several steps, as compounds **CNB-OH** and **CNB-OAc** are difficult to purify on silica gel. This is due to their acidic functionality and high polarity. There are also typically little to no major impurities detectable by  $^1\text{H}$  NMR in unpurified **CNB-OH** and **CNB-OAc** samples (see Figure 2.8 for an example with **CNP-OH**). Thus delaying purification until *t*Bu **CNB-OAc** improves ease of synthesis and maximises yield (inevitably some product is lost during most purification procedures). However, more thorough purification of these compounds can be performed for samples to be used for high-performance liquid chromatography (HPLC) or spectroscopic analysis. These details are presented in Section 2.3.2.



Scheme 2.16: The alkylation of carboxylic acid **CNB-OAc** with *tert*-butyl 2,2,2-trichloroacetimidate (TBTA).

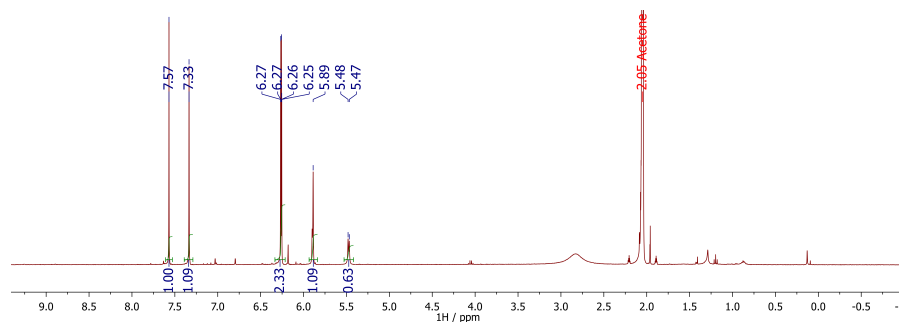


Figure 2.8:  $^1\text{H}$  NMR (400 MHz, acetone- $d_6$ ) spectrum of an unpurified sample of CNP-OH.

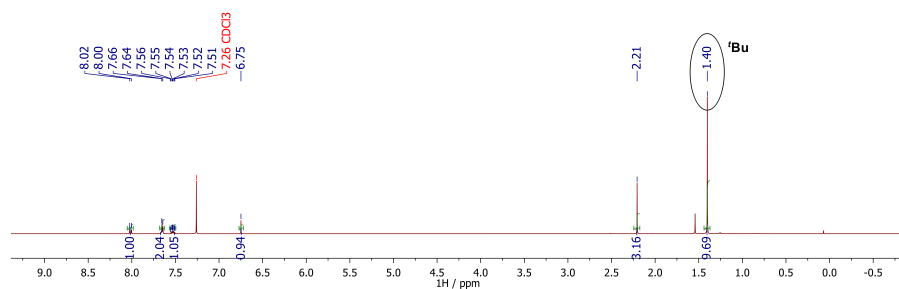
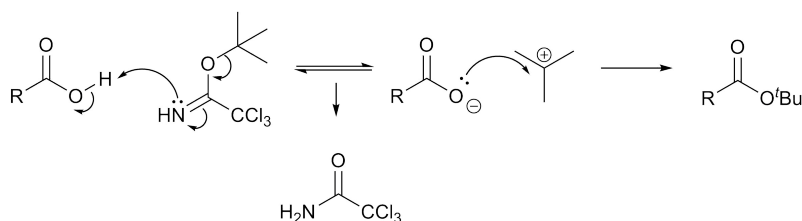


Figure 2.9:  $^1\text{H}$  NMR (400 MHz,  $\text{CDCl}_3$ ) spectrum of fully protected hydroxyacid ( $t\text{Bu}$  CNB-OAc) after purification.

The mechanism of reaction is likely similar to that of the Widmer reagent discussed previously. In this case, protonation of the acetimidate nitrogen encourages  $\text{S}_{\text{N}}1$  cleavage to give *tert*-butyl carbocation and trichloroacetamide (Scheme 2.17). The carbocation then alkylates the carboxylate to afford the product.

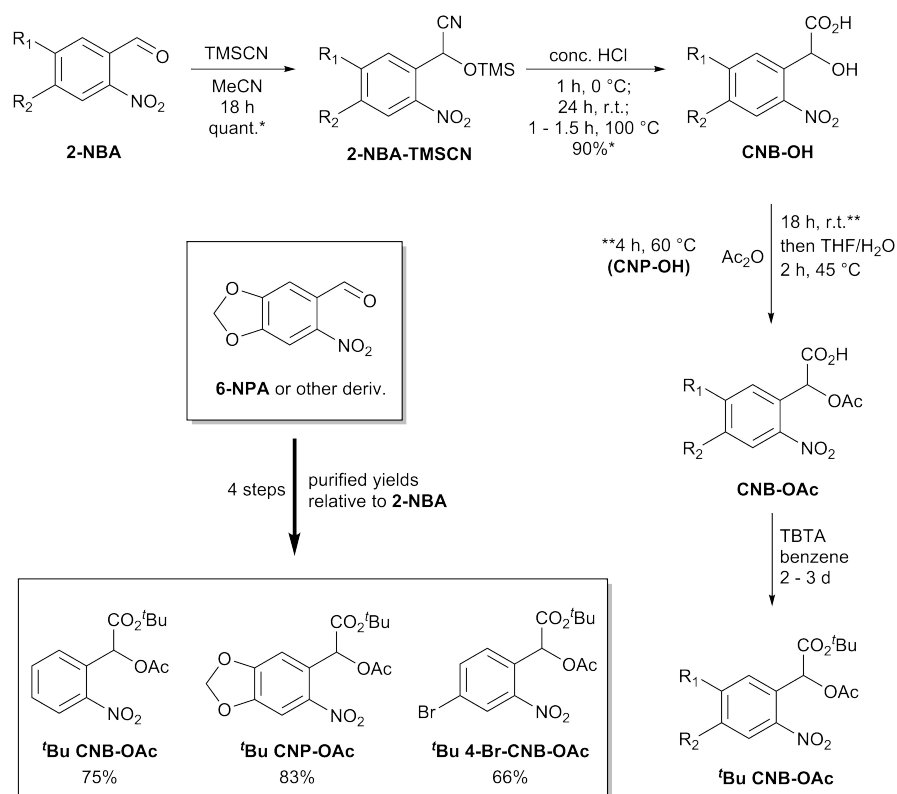


Scheme 2.17: Proposed mechanism of alkylation with *tert*-butyl 2,2,2-trichloroacetimidate.

Caesium carbonate (5 mol %) in methanol cleaves the acetate to produce  $t\text{Bu}$  CNB-OH (Scheme 2.18). This proceeds cleanly. The  $^1\text{H}$  NMR spectrum of the crude product (Figure 2.10) shows clearly the absence of the OAc signal at 2.21 ppm, and a new OH peak at 3.83 ppm.

The mechanism of this reaction is  $\text{S}_{\text{N}}\text{Ac}$  displacement with methanol. Caesium carbonate acts as a basic catalyst. A proposed mechanism is shown in Scheme 2.19, where  $\text{Cs}^+$  also enhances the reaction, acting as a Lewis acid catalyst by coordinating to the carbonyl oxygen. The





Scheme 2.20: Synthesis of *tert*-butyl 2-acetyloxy-2-nitromandelates (***t*Bu CNB-OH**) in four steps from commercially available 2-nitrobenzaldehydes (**2-NBA**). Synthesis details and yields are as published in our paper.[24] \* yield of crude.

Next, we look at the synthesis of caged aspartates (**1-CNB-L-Asp**) from the protected intermediates ***t*Bu CNB-OAc** (via ***t*Bu CNB-OH**) and 4-*tert*-butyl *N*-Boc-L-aspartate (**di-*t*Bu N-Boc-1-CNB-L-Asp**).

#### 2.2.4 Carbodiimide ester condensation

The next step is deacetylation to the alcohol (discussed above), followed by condensation with the amino acid building block (**4-*t*Bu N-Boc-L-Asp**). The coupling reagent 1-ethyl-3-(3-dimethylamino-propyl)carbodiimide hydrochloride (**EDC-HCl**) (see [Figure 2.11](#)) was employed, along with **DMAP**. *N,N'*-dicyclohexylcarbodiimide (**DCC**) is also often used. However, **EDC-HCl** and its urea by-product are water-soluble, making workup of the reaction much easier. Conversely dicyclohexylurea (**DCU**) is insoluble in water, and insoluble or sparingly soluble in most solvents. It is usually removed by filtration. However, depending on the solvent used, some **DCU** remains unless repeated crystallisations and filtrations are performed.

Addition of H<sub>2</sub>O to a carbodiimide produces a stable urea product. This is a major driving force in carbodiimide condensations. The

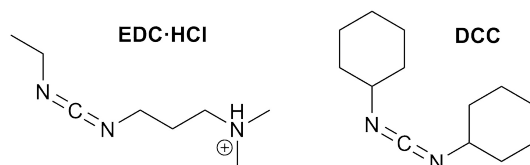
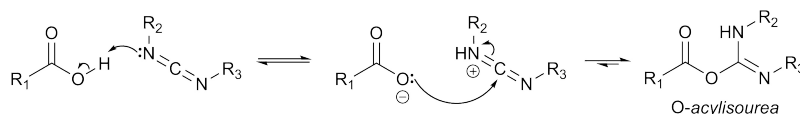


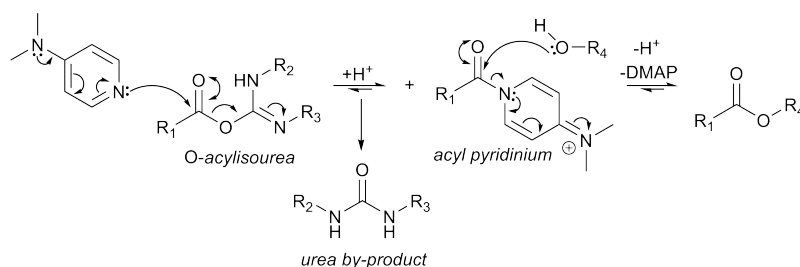
Figure 2.11: Carbodiimide esterification reagents **EDC·HCl** and **DCC**.

mechanism itself is a little more complicated. Carbodiimide is able to deprotonate the carboxylic acid (Scheme 2.21). The carboxylate then attacks the electrophilic carbon centre to form an *O*-acylisourea. This is a type of activated ester.



Scheme 2.21: The mechanism forming the *O*-acylisourea intermediate.

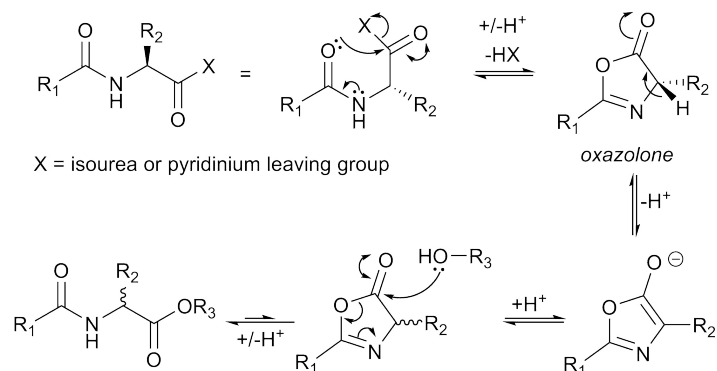
These intermediates are unstable and can form side-products, depending on the reaction conditions. A rearrangement can produce an *N*-acylurea, which is more stable and does not react further. The use of **DMAP** inhibits this rearrangement by reacting to form another activated ester – the acyl pyridinium intermediate (Scheme 2.22).[36] This is of particular importance in ester couplings (vs. amide couplings) as alcohols are poorer nucleophiles than amines.  $S_NAc$  displacement of pyridinium by the alcohol gives the ester product.



Scheme 2.22: The mechanism of ester formation from the *O*-acylisourea intermediate, **DMAP** and alcohol.

There is another problem, unfortunately, with carbodiimide coupling reactions. This is even more important in Chapter 3, where asymmetric synthesis of the  $\alpha$ -carboxy-2-nitrobenzyl alcohol (**CNB-OH**) is discussed. However, the synthesis from the racemic alcohol (**CNB-OH**) is also affected. When coupling to an *N*-acyl amino acid, cyclisation of the activated ester (*O*-acylurea or acyl pyridinium intermediate) can occur, as shown in Scheme 2.23.[36] The oxazolone species is acidic due to the aromatic stabilisation of the 6  $\pi$ -electron system of the anion. It is possible that the base effecting deprotonation in these reactions is **DMAP**, when **DMAP** is present. This is also

consistent with the observation that higher **DMAP** loadings promote epimerisation in these coupling reactions.[36]

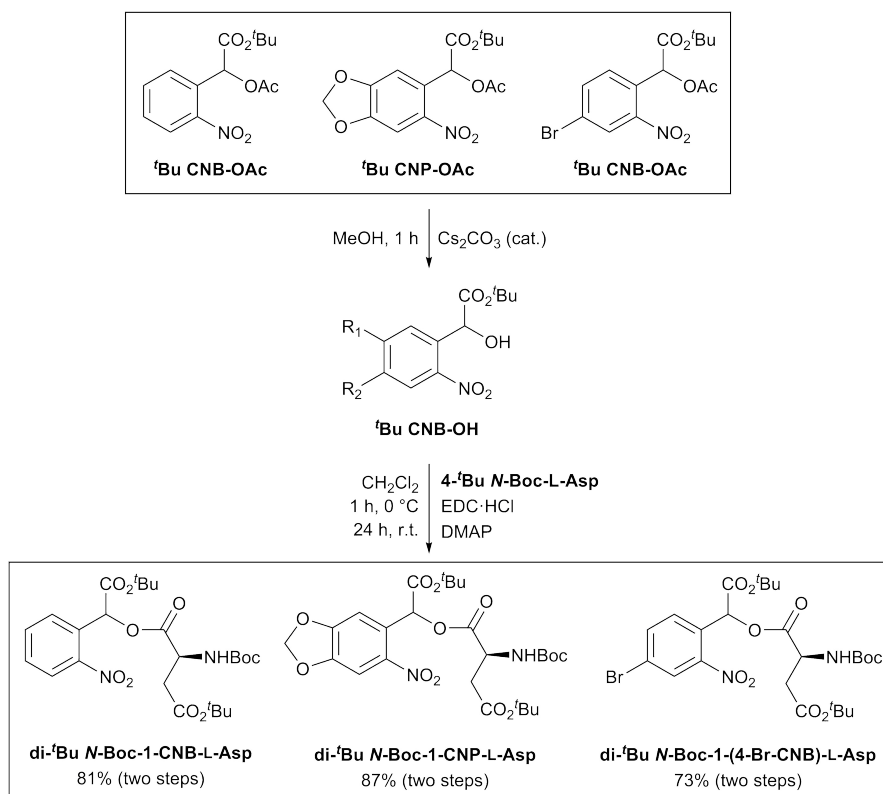


Scheme 2.23: Mechanism of formation of the oxazolone intermediate and resulting epimerisation.

The conditions used to carry out the coupling of *tert*-butyl 2-nitromandelates (*t*Bu CNB-OH) to 4-*t*Bu *N*-Boc-L-Asp were taken from a literature procedure.[37] 4-*t*Bu *N*-Boc-L-Asp was used in 10% excess, 0.9 eq. of **DMAP** was used, and 1.5 eq. of **EDC·HCl**. The yields from *tert*-butyl *O*-acetyl 2-nitromandelates (*t*Bu CNB-OAc) were 81% (**di-*t*Bu *N*-Boc-1-CNB-L-Asp**), 87% (**di-*t*Bu *N*-Boc-1-CNP-L-Asp**) and 73% (**di-*t*Bu *N*-Boc-1-(4-Br-CNB)-L-Asp**), in two steps and without purification of the alcohol (Scheme 2.24). The esters (substituted **di-*t*Bu *N*-Boc-1-CNB-L-Asp**) were purified by column chromatography after aqueous workup and obtained as 1:1 diastereomeric mixtures (possibly also containing enantiomers).

The products were identified by  $^1\text{H}$  and  $^{13}\text{C}$  NMR, and high-resolution mass spectrometry (**HRMS**). The  $^1\text{H}$  and  $^{13}\text{C}$  NMR spectra clearly show a double set of peaks, with an approximately 1:1 ratio of the two diastereomers. This is most easily seen in the closely spaced benzylic CH signals at 6.81 and 6.80 ppm (Figure 2.12, inset a). The nitrobenzyl aromatic signals appear as three multiplets in the region 8 – 7.5 ppm. The NH signal appears as a triplet at 5.54 ppm. The signal is not a true triplet. Rather, each diastereomer gives rise to a doublet and together they overlap to give a triplet. The CH adjacent to NH gives a multiplet in the region 4.72 – 4.70 ppm. Both the NH and the CH have satellites at 5.15 and 4.56 ppm, respectively. This is due to restricted rotation about the amide bond of the Boc group. Two diastereotopic protons give rise to multiplets at 2.96 – 2.91 and 2.85 – 2.74 ppm (Figure 2.12, inset b). While the former is poorly resolved, the latter multiplet is, in fact, two double doublets – one for each diastereomer. They overlap slightly but are still resolvable and can be assigned the coupling constants  $^2J_{\text{HH}} = 24\text{ Hz}$  and  $^3J_{\text{HH}} = 4\text{ Hz}$ . Full assignments are given in the supporting information of the published article.[24]

This does not reveal whether or not, or to what extent, epimerisation of the L-aspartate derived chiral centre occurs under these conditions.



Scheme 2.24: Synthesis of protected photocaged L-aspartates (substituted **di-<sup>t</sup>Bu N-Boc-1-CNB-L-Asp**) from *tert*-butyl *O*-acetyl 2-nitro-mandelates (**<sup>t</sup>Bu CNB-OAc**) by caesium carbonate catalysed methanolysis, followed by ester condensation with **EDC-HCl/DMAP**.

The literature protocol this was based on used 0.74 eq. of **DMAP**.<sup>[37]</sup> However, **DMAP** loadings above 0.5 eq. are liable to promote epimerisation.<sup>[36]</sup> This was perhaps not a problem for Herzon et al.,<sup>[37]</sup> as the acid used in their work is not a peptide or *N*-acyl amino acid. In the case of the synthesis presented here (Scheme 2.24), epimerisation is a real risk. The product (**di-<sup>t</sup>Bu N-Boc-1-CNB-L-Asp**) has not been tested for the presence of enantiomers. The use of such a high catalytic loading of **DMAP** was, in hindsight, probably a mistake.

### 2.2.5 Global deprotection of *N*-Boc and *tert*-butyl groups

The combination of Boc and *tert*-butyl groups was chosen as both can be removed by trifluoroacetic acid (**TFA**) in dichloromethane. There was, however, a potential pitfall with this method, as well as potential problems with the chemical properties of the end product itself. The photocaged aspartates (**1-CNB-L-Asp**) contain a hydrolytically unstable ester group.

It was hypothesised that any water present in the reaction mixture during deprotection would also hydrolyse the ester, promoted by

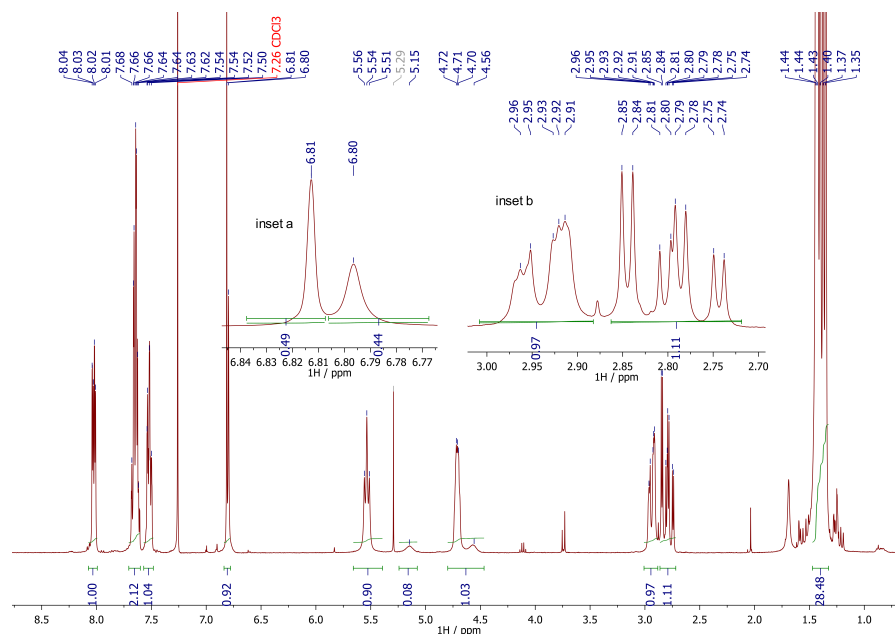
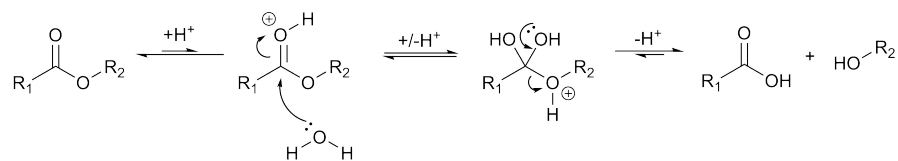


Figure 2.12:  $^1\text{H}$  NMR (400 MHz,  $\text{CDCl}_3$ ) spectrum of **di-*t*Bu N-Boc-1-CNB-L-Asp**.

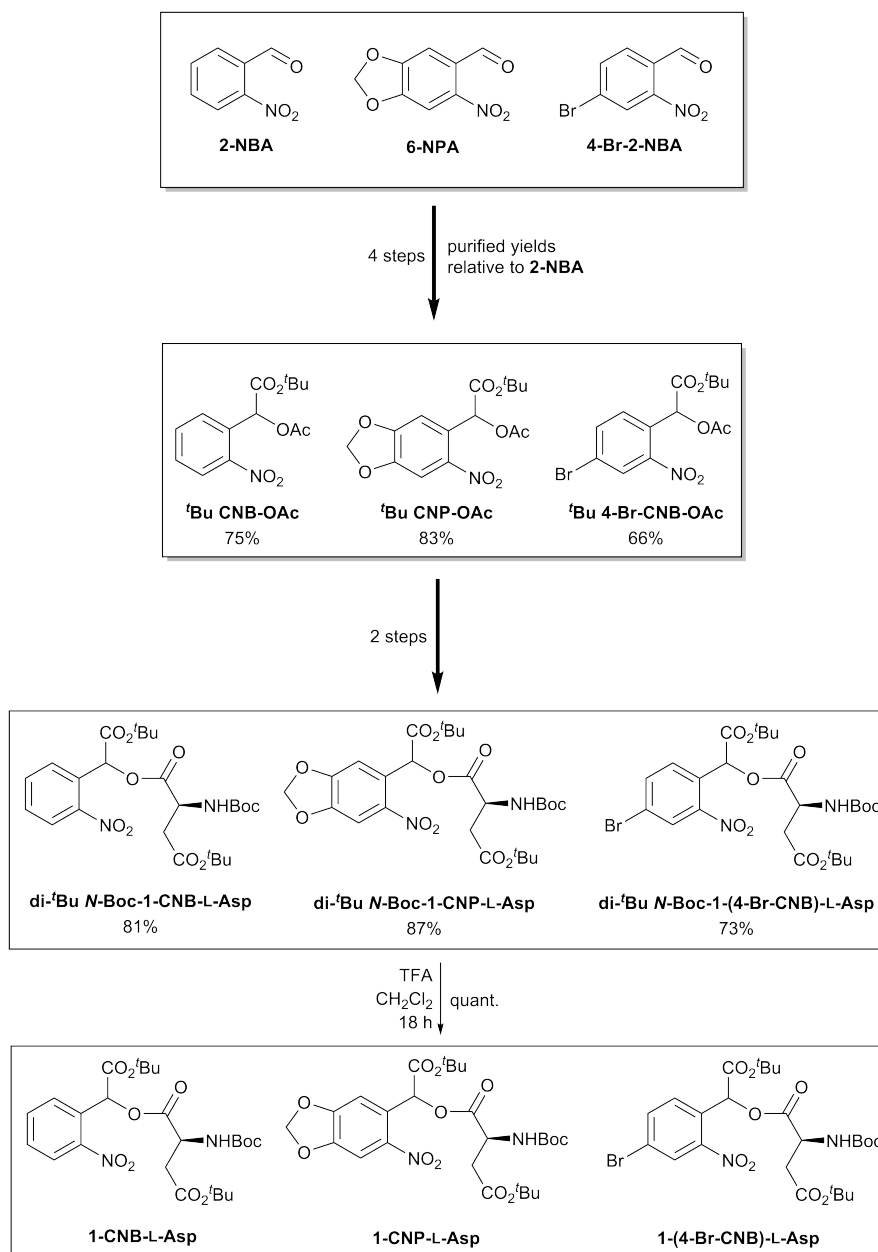
acidic catalysis by **TFA** (Scheme 2.25). Therefore as a rule, **TFA** was distilled using oven-dried glassware (including a Vigreux column) directly before use. Reaction mixtures were also protected from atmospheric moisture with a calcium chloride drying tube. It must be noted that, given the ester hydrolysis is an equilibrium reaction, small amounts of water may not be sufficient to result in a noticeable degree of unwanted hydrolysis. Quantification of hydrolysis in samples where thoroughly dried **TFA** was used vs. ‘typical’ **TFA** was not carried out. It was observed that the photocaged L-aspartates (**1-CNB-L-Asp**) dried to a more solid consistency when these precautions were used. In other cases, the product remained somewhat sticky and residual **TFA** was more difficult to remove. This is likely due to both the hygroscopicity of the products and the water–**TFA** azeotrope.



Scheme 2.25: Acid catalysed ester hydrolysis. **TFA** would be the proton source and trifluoroacetate the proton scavenger.

### 2.2.6 Synthetic summary

The synthesis of **CNB** caged aspartates, which has been published,<sup>[24]</sup> is summarised in Scheme 2.26. The synthesis proceeds with good



Scheme 2.26: Summary of the synthesis of CNB caged aspartates.

yields and may be more general than exemplified by the three end products shown here. Having developed a successful synthesis, the next step was to characterise the products.

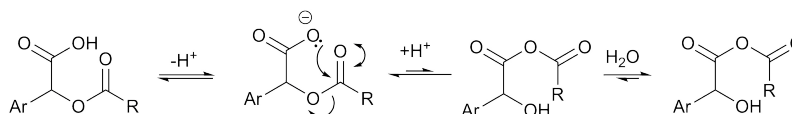
## 2.3 CHARACTERISATION

## 2.3.1 Aqueous stability

The half-lives of **CNB** caged aspartates in aqueous solution range from approximately 10 – 29 h, depending on photocage analogue and pH.[24] Buffer concentration also presumably plays a role, but this was not explored. Details regarding how this was measured are found in the supporting information of the published work.[24]

The diastereomers were found to have different hydrolysis rates. The diastereomer with a more downfield benzylic hydrogen shift was hydrolysed approximately twice as fast as the other diastereomer. This effect was seen at every pH and with every analogue.

It was noted that the hydrolysis rate is slowed at low pH, in line with a neighbouring-group mechanism (Scheme 2.27), as proposed by Rossi et al.,[30] who observed a similar effect. The pH at which this change of mechanism occurred was different for each cage analogue. It occurred between pH 4.2 and 5.8 for the **CNB** analogue (**1-CNB-L-Asp**), whereas for the  $\alpha$ -carboxynitropiperonyl (**CNP**) analogue (**1-CNP-L-Asp**) the rate was slower at pH 5.8 compared to pH 7. This suggests a  $pK_a$  in the range 4.2 – 5.8 for the benzylic carboxyl of **1-CNB-L-Asp**, and between 5.8 and 7 for **1-CNP-L-Asp**.



Scheme 2.27: Neighbouring-group participation mechanism, as proposed by Rossi et al.,[30] enabling more rapid hydrolysis at higher pH.

Interestingly, for **1-(4-Br-CNB)-L-Asp**, no reduction of rate was observed with decreasing pH, possibly indicating the  $pK_a$  of the benzylic carboxyl is lower than 4.2. However, at pH 9 the rate was also decreased. It was proposed that this is the result of a low  $pK_{aH}$  of the amine group and that the neighbouring ester is less electrophilic when the amine is not protonated.

Regarding aqueous solubility, systematic studies to find the saturation concentration were not conducted. However, a **1-CNB-L-Asp** concentration of 500 mM in water has been achieved, the brominated derivative had a similar solubility. The **CNP** analogue was found to be slightly less soluble, but concentrations between 30 and 100 mM have been achieved in aqueous solutions.

The following table and figures were reproduced from our published work.[24]

Table 2.1: Hydrolysis half-lives of photocaged L-aspartates.  $^1\text{H}$  NMR integrals of the benzylic CH signals of each diastereoisomer were measured once per hour for 24 h at r.t. in aqueous buffers with a water suppression pulse sequence. The uncertainties quoted are derived from the  $\sigma$  confidence intervals of the fitted parameters (vide infra, Figures 2.13, 2.14, 2.15).

<sup>a</sup>50 mM sodium citrate, 400 mM ammonium sulfate, 12.5% DMSO- $d_6$ .

<sup>b</sup>50 mM sodium phosphate, 12.5% DMSO- $d_6$ .

| pH               | half-life / h                        |            |                                      |        |   |            |
|------------------|--------------------------------------|------------|--------------------------------------|--------|---|------------|
|                  | <b>1-CNB-L-Asp</b><br>(A / B isomer) |            | <b>1-CNP-L-Asp</b><br>(A / B isomer) |        | <b>1-(4-Br-CNB)-L-Asp</b><br>(A / B isomer) |            |
| 4.2 <sup>a</sup> | 16.9 ± 0.4                           | 29 ± 2     | 15 ± 2                               | 24 ± 4 | 11.2 ± 0.2                                  | 19.3 ± 0.6 |
| 5.8 <sup>b</sup> | 13 ± 1                               | 23 ± 2     | 16 ± 1                               | 26 ± 2 | 10.3 ± 0.4                                  | 18 ± 1     |
| 7.0 <sup>b</sup> | 13.9 ± 0.2                           | 25.7 ± 0.6 | 13 ± 1                               | 22 ± 2 | 10.2 ± 0.1                                  | 18.5 ± 0.2 |
| 9.0 <sup>b</sup> | 14.6 ± 0.2                           | 26.2 ± 0.4 | 13 ± 1                               | 21 ± 4 | 17.2 ± 0.6                                  | 28 ± 2     |

### 2.3.2 Quantum yields

Effective quantum yields of L-aspartate were measured using HPLC and phenylglyoxylic acid actinometry. L-Aspartate itself is difficult to quantify by HPLC methods with UV detection. Monitoring the absorption at 200 or 210 nm is possible. However, underivatized amino acids such as L-aspartate tend to have very short retention times on reversed-phase columns. Derivatization with *o*-phthalaldehyde was investigated as this increases retention time and allows detection at longer UV wavelengths (shorter wavelengths like 210 nm tend to have poorer signal to noise).[40] Unfortunately, this proved to be impractical as long elution times were necessary (gradient elution). Furthermore, samples had to be derivatised and eluted as soon as possible after an irradiation experiment, to limit error due to thermal hydrolysis of the photocaged aspartate. This hydrolysis problem was instead turned into an advantage. Standard calibration experiments were performed for the hydrolysis products **CNB-OH**, **CNP-OH**, and **4-Br-CNB-OH**. These analytes required no derivitisation and short, isocratic HPLC elutions were possible. It is acknowledged that Anke Puchert assembled the small optical table with holders for the cuvette, light-emitting diode (LED) and lens, and assisted with some of the irradiation experiments. Otherwise, all work was carried out by the author. The effective quantum yields of release,  $Q_{\text{eff}}$ , were found to be  $0.105 \pm 0.006$ ,  $0.048 \pm 0.002$  and  $0.14 \pm 0.01$ , respectively for the **CNB**, **CNP** and 4-bromo- $\alpha$ -carboxynitrobenzyl (**4-Br-CNB**) analogues.[24] The following sections (2.3.2.1, 2.3.2.3 and 2.3.3) are copied from our published work,[24] with minor editing of the compound naming and figure numbering schemes.

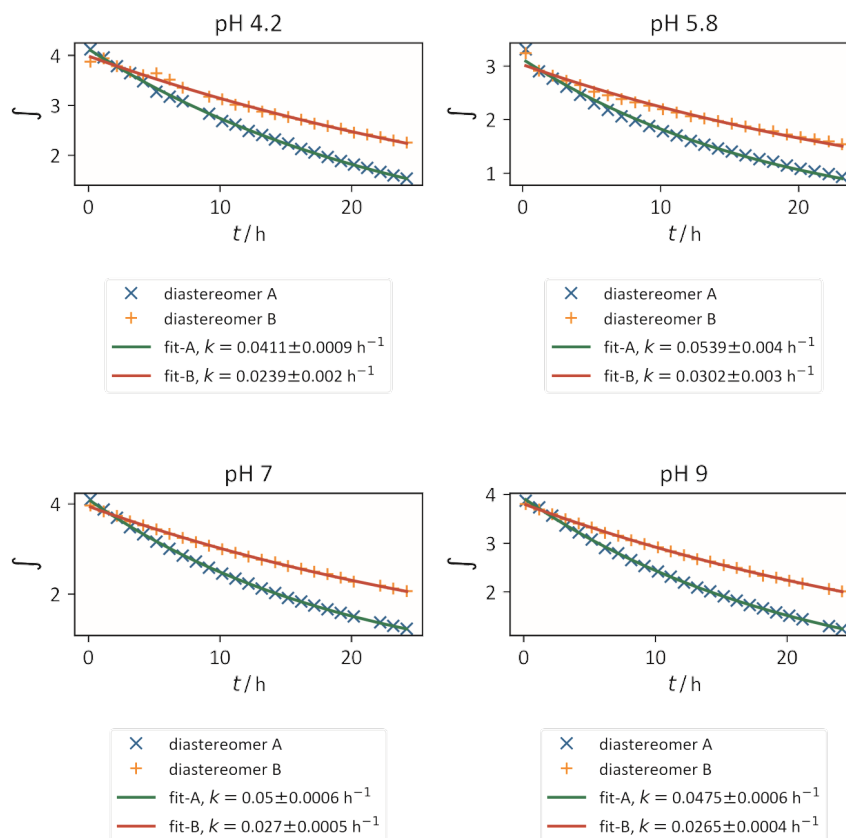


Figure 2.13: Plots of  $^1\text{H}$  NMR integrals (benzylic CH signals) over time at various pHs, showing the hydrolysis of **1-CNB-L-Asp** under these conditions.  $\times$  and  $+$  denote the experimental data and the exponential fits are plotted as lines. The decays obeyed the first-order exponential decay function  $f(t) = Ae^{-kt}$ . Least-squares curve fitting was carried out using the SciPy[38] python library, the data were plotted using Matplotlib[39] and the quoted errors are the  $1\sigma$  confidence interval of  $k$  estimated by the fitting algorithm `scipy.optimize.curve_fit()`. Note that the pH 4.2 sample was dissolved in 50 mM citrate buffer with 400 mM ammonium sulfate, the other samples were dissolved in 50 mM phosphate buffer. Therefore, the pH 4.2 data are not directly comparable with the others. DMSO- $d_6$  was added to each sample (12.5% of total volume), and the integral of the residual dimethyl sulfoxide (DMSO) signal was set to 10 in each spectrum. In this case the rate is fastest at pH 5.8, slowest at pH 4.2 and decreases with increasing pH in the range measured. We propose two effects to explain this – one, that at lower pH, the  $\alpha$ -carboxyl group is protonated and cannot participate in a neighbouring-group mechanism,[32] whereas at higher pH the primary amine is not protonated and therefore the neighbouring carbonyl is less electrophilic.

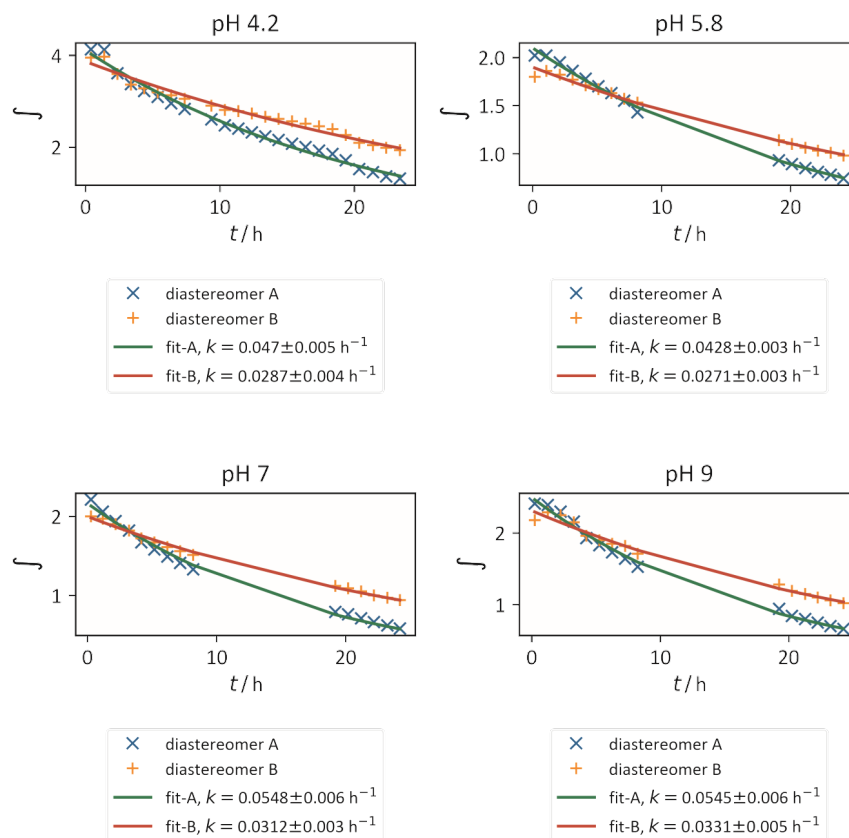


Figure 2.14: Plots of  $^1\text{H}$  NMR integrals (benzylic CH signals) over time at various pHs, showing the hydrolysis of **1-CNP-L-Asp** under these conditions. x and + denote the experimental data and the exponential fits are plotted as lines. The decays obeyed the first-order exponential decay function  $f(t) = Ae^{-kt}$ . Least-squares curve fitting was carried out using the SciPy[38] python library, the data were plotted using Matplotlib[39] and the quoted errors are the  $1\sigma$  confidence interval of  $k$  estimated by the fitting algorithm `scipy.optimize.curve_fit()`. Note that the pH 4.2 sample was dissolved in 50 mM citrate buffer with 400 mM ammonium sulfate, the other samples were dissolved in 50 mM phosphate buffer. Therefore, the pH 4.2 data are not directly comparable with the others. DMSO- $d_6$  was added to each sample (12.5% of total volume), and the integral of the residual DMSO signal was set to 10 in each spectrum. In some samples, several data points are missing due to an error that occurred with the automatic sample changer during the night, which was not remedied until morning. In the case of compound **1-CNP-L-Asp**, the maximum rate is at pH 7 (isomer A) or pH 9 (isomer B), whereas the lowest rates are at pH 5.8.

### 2.3.2.1 LED Characterisation

Irradiation was carried out using a M365LP1-C1 collimated LED from Thorlabs with a variable power supply (set to 200 mA at one

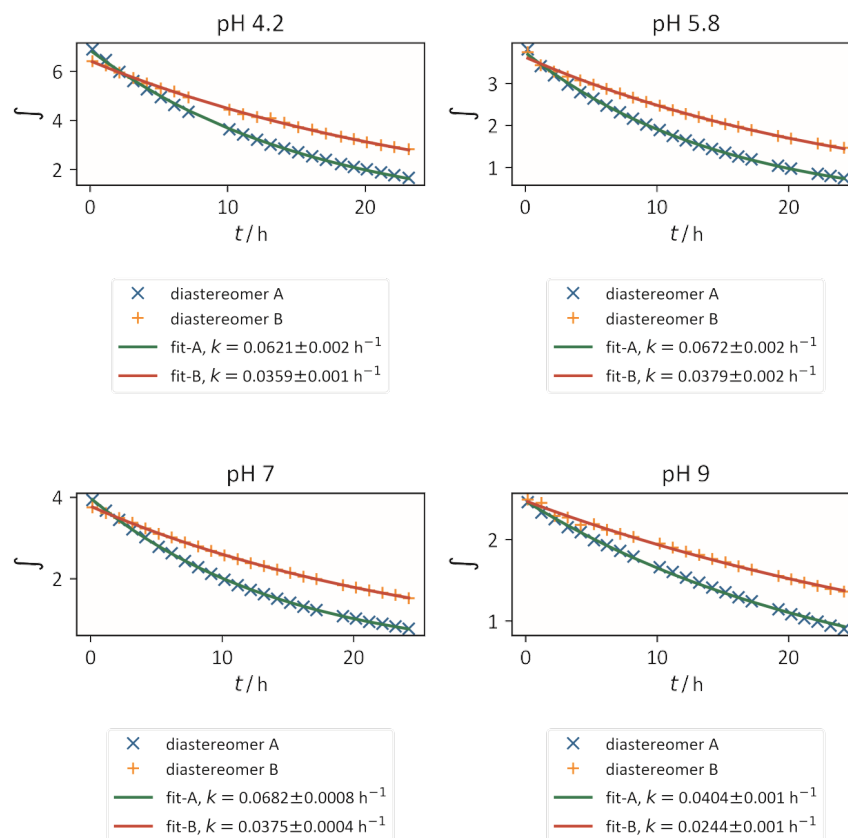


Figure 2.15: Plots of  $^1\text{H}$  NMR integrals (benzylic CH signals) over time at various pHs, showing the hydrolysis of **1-(4-Br-CNB)-L-Asp** under these conditions. x and + denote the experimental data and the exponential fits are plotted as lines. The decays obeyed the first-order exponential decay function  $f(t) = Ae^{-kt}$ . Least-squares curve fitting was carried out using the SciPy[38] python library, the data were plotted using Matplotlib[39] and the quoted errors are the  $1\sigma$  confidence interval of  $k$  estimated by the fitting algorithm `scipy.optimize.curve_fit()`. Note that the pH 4.2 sample was dissolved in 50 mM citrate buffer with 400 mM ammonium sulfate, the other samples were dissolved in 50 mM phosphate buffer. Therefore, the pH 4.2 data are not directly comparable with the others. DMSO- $d_6$  was added to each sample (12.5% of total volume), and the integral of the residual DMSO signal was set to 10 in each spectrum. In the case of compound **1-(4-Br-CNB)-L-Asp**, hydrolysis rates were highest at pH 5.8 and 7, with the lowest rate at pH 9. We propose that the rate is fastest when both the  $\sigma$ -carboxyl and the amine are ionised.

controller and division 3 out of 7 on an upper dial),  $\lambda_{\text{max}} = 365$  nm. The beam diameter was 50 mm, which was focused with an additional lens (fused silica UV anti-reflective coating, 100 mm focal length) onto a cuvette placed in a holder. Cuvettes were 1 cm  $\times$  1 cm (with two frosted sides), Quartzglass Suprasil<sup>®</sup> from Hellma Analytics, with a small

stir bar in the base. According to a literature protocol,<sup>[41]</sup> phenylglyoxylic acid (50 mM in 25 % H<sub>2</sub>O-MeCN) was used as a chemical actinometer to determine the irradiant power in terms of einsteins (moles of photons) incident on the cuvette per minute. The LED was allowed to warm up for 30 min before each experiment. Two identical cuvettes were prepared with 3.0 ml of actinometer solution, and one was kept in the dark, so that  $\Delta A = A_{\text{dark}} - A_{\text{light}}$ . Absorbance changes were monitored at 380 nm ( $\Phi_{\text{app}} = 0.735$ ) and 390 nm ( $\Phi_{\text{app}} = 0.728$ ), and converted to  $\Delta c$  by  $\Delta c = \delta A \div \Delta \epsilon$  (where  $\Delta \epsilon = 29$  and  $16 \text{ M}^{-1} \text{ cm}^{-1}$  at 380 and 390 nm, respectively).  $\Delta n/\text{einstein}$  was then given by  $\Delta n = \Delta c \times V \div \Phi_{\text{app}}$ .  $\Delta n/\text{min}$  was then obtained for both series together by linear least-squares regression to the equation  $\delta n = \Delta n/\text{min} \times t$ , and the uncertainty in  $\Delta n/\text{min}$  was given by the  $2\sigma$  error in the fitted parameter. These were also corrected for the absorption spectrum of the actinometer solution and the LED spectrum (see below for details, Figure 2.16). The procedure was repeated twice measuring once per minute for 25 min (total irradiation time), and twice every 5 min for 25 min. The mean result was  $0.59 \pm 0.01 \mu\text{einstein}$  ( $n = 4$ ) per minute. In order to determine the incident light on the cuvette from the amount absorbed, spectra were recorded of the light source (intensity spectrum, recorded with an OceanOptics USB2000+ series spectrometer) and of each actinometer solution (absorbance spectra, measured with a Cary 50 Bio UV-Visible spectrophotometer), each with a spectral resolution of 1 nm in the range 315 – 415 nm. The LED spectrum was normalised to a sum of 1. Then, the overall absorption (as a fraction,  $F_A$ ) of LED light by the solution was given by:

$$F_A = \sum_{\lambda=315 \text{ nm}}^{\lambda=415 \text{ nm}} I_{\lambda}(1 - 10^{-A_{\lambda}})$$

where  $I_{\lambda}$  is the normalised intensity at wavelength  $\lambda$ , and  $A_{\lambda}$  is the absorbance of the actinometer solution at that wavelength. Incident photon amount per minute,  $\Delta n_I$ , is then given by  $\Delta n_A \div F_A$ .

### 2.3.2.2 HPLC Standards

Standards of pure hydroxyacid (CNB-OH derivatives) were prepared volumetrically by dissolving 0.1 mmol in 100 ml of sodium phosphate buffer (12.5 mM, pH 7), and dilutions were carried out with a burette (see Section 6.7 for synthesis and purification of hydroxyacids). Standards were then analysed by HPLC (Waters Nova-Pak<sup>®</sup> C18 column,  $3.9 \times 150$  mm, 4  $\mu\text{m}$  particle size), with isocratic elution (9 % MeOH-12.5 mM sodium phosphate, pH 7). The analysing wavelength was 280 nm, and 0.3 mM L-Tyrosine was used as an internal standard (ISTD). The HPLC instrument was an Agilent Technologies 1260 Infinity, with a G1311B Quaternary Pump, G1329B Sample Holder with

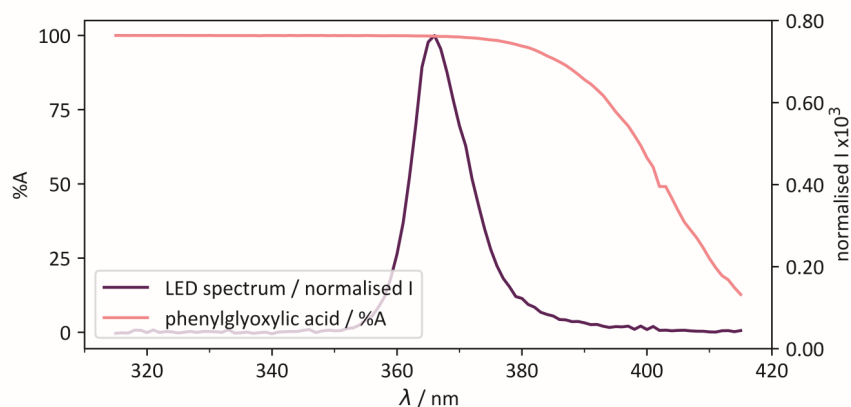


Figure 2.16: %A ( $100 - \%T$ ) of a cuvette containing 50 mM phenylglyoxylic acid in 25%  $H_2O - MeCN$ , and a spectrum of the LED light source with the intensity normalised to sum to 1. The sum of intensities at each point multiplied by %A gives a total spectral absorption of 98% (including a correction for approximately 4% of unabsorbed light reflecting back into the cuvette).

programmable injection robot and a G1365C multiple wavelength detector for UV/Vis analysis.

### 2.3.2.3 Photocage Irradiation and HPLC Analysis

For each experiment, a 10 ml, 1 mM solution of **1-CNB-L-Asp** derivative in sodium phosphate buffer (50 mM, pH 7) was prepared volumetrically. Then, 3.0 ml of photocage (**1-CNB-L-Asp** derivative) was transferred to the cuvette and irradiated by the UV LED for a fixed time,  $t$ . Next, aliquots were taken from both the irradiated and non-irradiated samples, which were filtered through a 0.22  $\mu m$  polyvinylidene fluoride (PVDF) syringe filter. The aliquots were allowed to stand for ca. 3 days to allow complete hydrolysis of the remaining starting material (**1-CNB-L-Asp** derivative), in order to simplify HPLC analysis (hydroxyacids<sup>[4]</sup> were used as a proxy for remaining **1-CNB-L-Asp** derivative, due to the hydrolysis of **1-CNB-L-Asp** derivative over time and the ease of preparation of pure standards of CNB-OH derivatives). The hydrolysis products (CNB-OH derivatives) were analysed by HPLC with reference to the standard calibration described above, and using the same method and equipment. Conversion in the below graphs was obtained by the difference in concentration between irradiated and non-irradiated aliquots of the same sample, multiplied by the volume. In each of the below figures (Figure 2.17, Figure 2.18 and Figure 2.19), maximum possible conversion is 3  $\mu mol$ , the  $x$ -axis is given in terms of total photons absorbed in  $\mu einstein$  ( $\mu mol$  of photons), after correcting for the absorption of incident photons per minute (determined by phenylglyoxylic acid actinometry). This was necessary due to slight differences in the absorbance of each solution

and allows the determination of  $\Phi_{\text{app}}$  (the apparent quantum yield) by orthogonal diagonal regression (ODR) linear fit of the graph of amount conversion vs. photons absorbed, taking into account errors in both the independent and dependent variables.

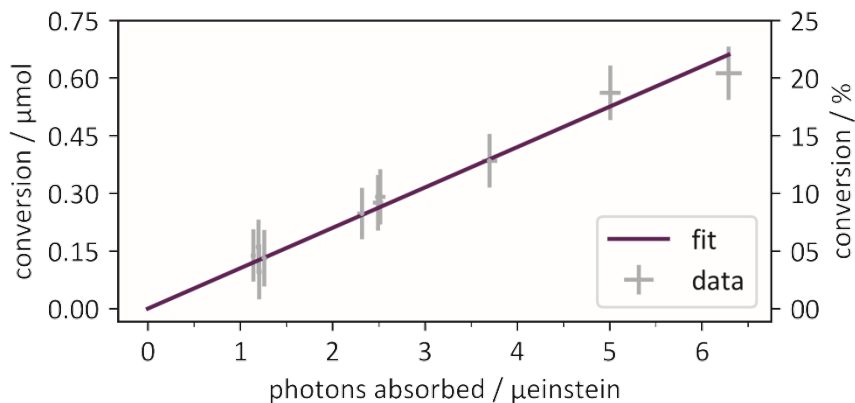


Figure 2.17: Amount conversion of **1-CNB-L-Asp** vs. photons absorbed.  $\Phi_{\text{app}} = 0.105 \pm 0.006$ . Error bars and error in  $\phi$  are  $2\sigma$ . ODR – implemented by the Python package `scipy.odr` – was used as a fitting algorithm. A linear function was used for fitting, with an explicit intercept at  $(0,0)$  and a gradient of  $\Phi_{\text{app}}$ .

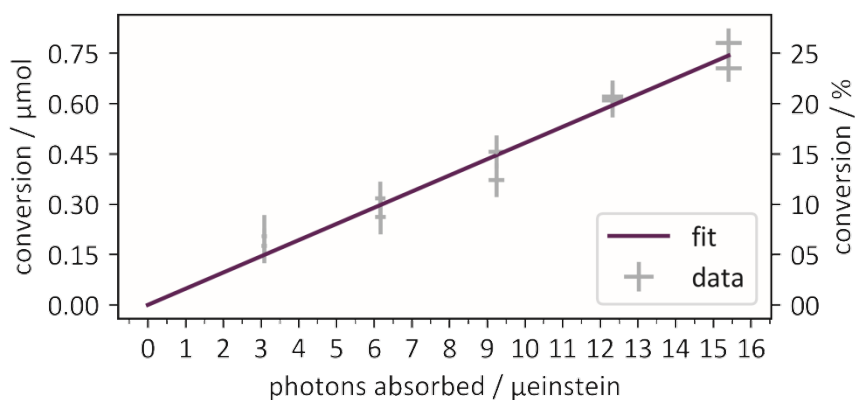


Figure 2.18: Amount conversion of **1-CNP-L-Asp** vs. photons absorbed.  $\Phi_{\text{app}} = 0.048 \pm 0.002$ . Error bars and error in  $\phi$  are  $2\sigma$ . ODR was used as a fitting algorithm. A linear function was used for fitting, with an explicit intercept at  $(0,0)$  and a gradient of  $\Phi_{\text{app}}$ .

### 2.3.3 Absorption properties

As expected, the CNP analogue had an additional absorption band at  $\lambda_{\text{max}} = 360 \text{ nm}$  ( $\epsilon \sim 4000 \text{ M}^{-1} \text{ cm}^{-1}$ ), while the CNB cage and **4-Br-CNB** derivatives absorbed most strongly at 280 nm, although the

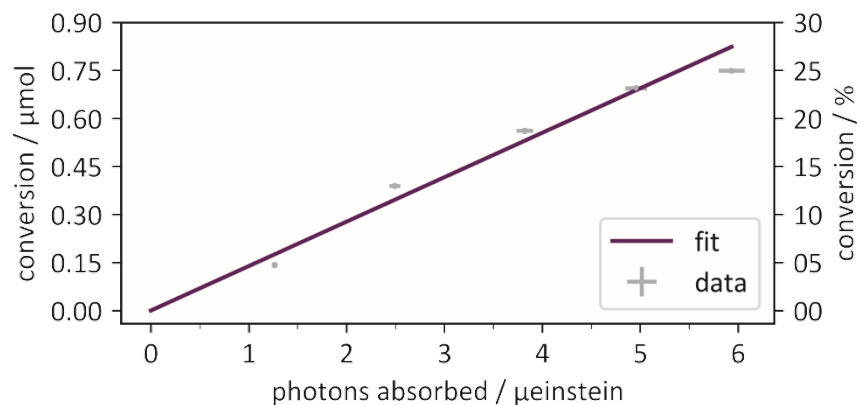


Figure 2.19: Amount conversion of **1-(4-Br-CNB)-L-Asp** vs. photons absorbed.  $\Phi_{\text{app}} = 0.14 \pm 0.01$ . Error bars and error in  $\phi$  are  $2\sigma$ . ODR was used as a fitting algorithm. A linear function was used for fitting, with an explicit intercept at (0,0) and a gradient of  $\Phi_{\text{app}}$ . NB: these results appear to show some non-linearity. A more accurate  $\Phi_{\text{app}}$  may be obtained if a larger number of 5 and 10 min determinations are taken, and the longer experiments discarded.

bromo derivative exhibited a shoulder at 310 nm. UV spectra of the compounds are found in the supporting information of the published work, reproduced below (Figure 2.20, Figure 2.21 and Figure 2.22).[24]

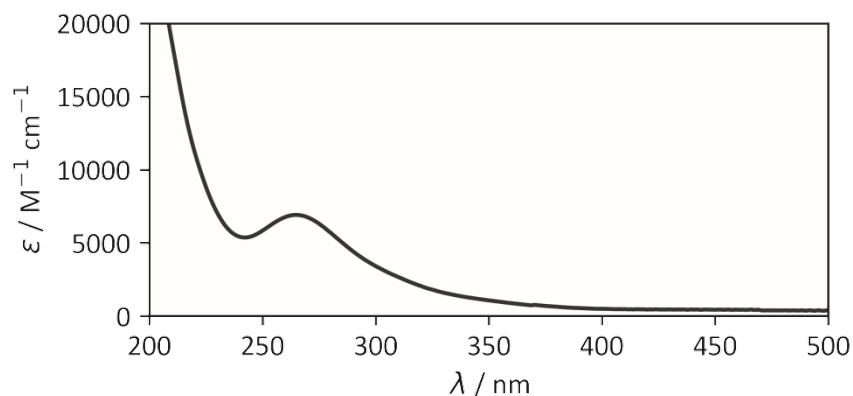


Figure 2.20: UV absorption spectrum of **1-CNB-L-Asp**, 0.1 mM in 50 mM sodium phosphate, pH 7.

#### 2.3.4 Photocleavage times

The mechanism and rates are discussed much more thoroughly in Chapter 4 (Section 4.3.1). However, the results were in line with those previously reported,[25, 26] with  $\mu\text{s}$  cleavage times for the observed

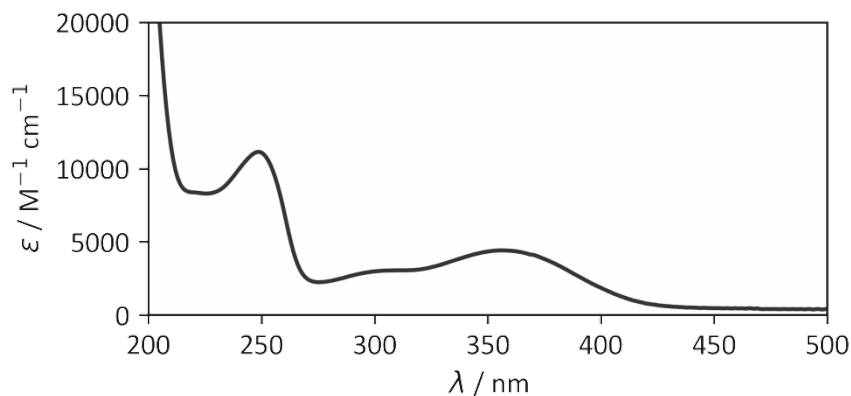


Figure 2.21: UV absorption spectrum of **1-CNP-L-Asp**, 0.1 mM in 50 mM sodium phosphate, pH 7.

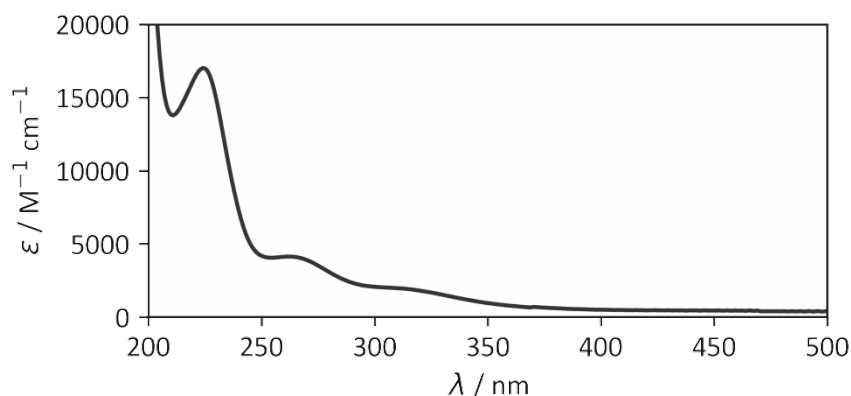


Figure 2.22: UV absorption spectrum of **1-(4-Br-CNB)-L-Asp**, 0.1 mM in 50 mM sodium phosphate, pH 7.

*aci*-nitro intermediates generated by irradiation of **1-CNB-L-Asp** and **1-(4-Br-CNB)-L-Asp**.

The exception was the **CNP** derivative, which generated an *aci*-nitro species with a lifetime of almost 1 ms.[24]

### 2.3.5 Radiation damage

Due to the intention of using these photocages for **TRX** experiments, experiments were proposed to monitor their behaviour under exposure to X-ray radiation. Solutions of caged aspartate were applied to mylar loops mounted in the experimental hutch at ID30 at the European Synchrotron Radiation Facility (**ESRF**). The X-ray flux was  $4.97 \times 10^9$  phs<sup>-1</sup>, with a photon energy of 12.765 37 keV. However, these results are only qualitative, as exact dose absorbed by photocage films per unit time could not be determined under these conditions. Some

examples are shown in [Figure 2.23](#), [Figure 2.24](#) and [Figure 2.25](#). It is clear that the photocages are reacting due to X-ray exposure. The precise mechanism and radiolysis products are unknown at this time. The absorbance changes are superficially similar to those seen due to photolysis, but this does not necessarily mean the same product is generated.

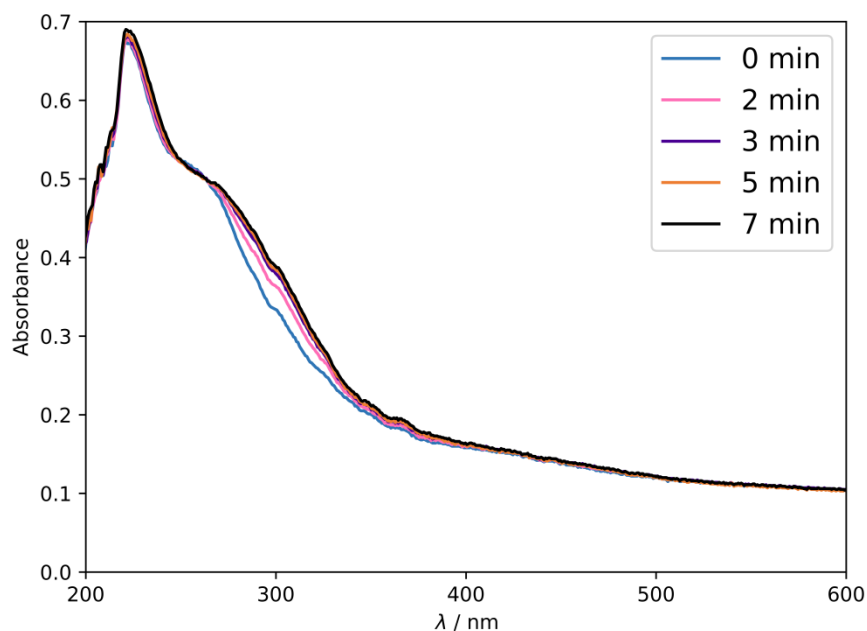


Figure 2.23: **1-CNB-L-Asp**, online [UV](#) spectroscopic measurement during X-ray irradiation.

A number of different processes may be occurring. One is reduction of the photocages by solvated electrons, generated by ionisation of the solvent (water). Core-shell electrons may also be ejected from the photocages themselves. Finally, X-ray excited optical luminescence ([XEOL](#)) may generate [UV](#) photons capable of initiating the normal decaying reaction of the photocages. Regardless of precise mechanism and dose limits, the results suggest that X-ray experiments using photocages should be carried out carefully, with a low-dose strategy.

Fortunately, [TRX](#) normally requires serial crystallography methods, which enable low-dose data collection as each crystal is normally exposed to X-ray radiation only once.

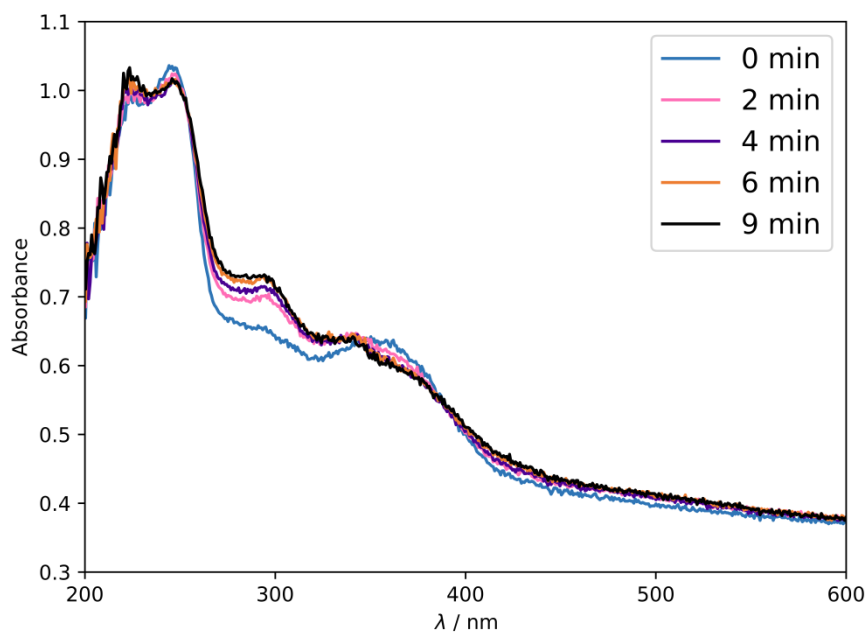


Figure 2.24: **1-CNP-L-Asp**, online UV spectroscopic measurement during X-ray irradiation.

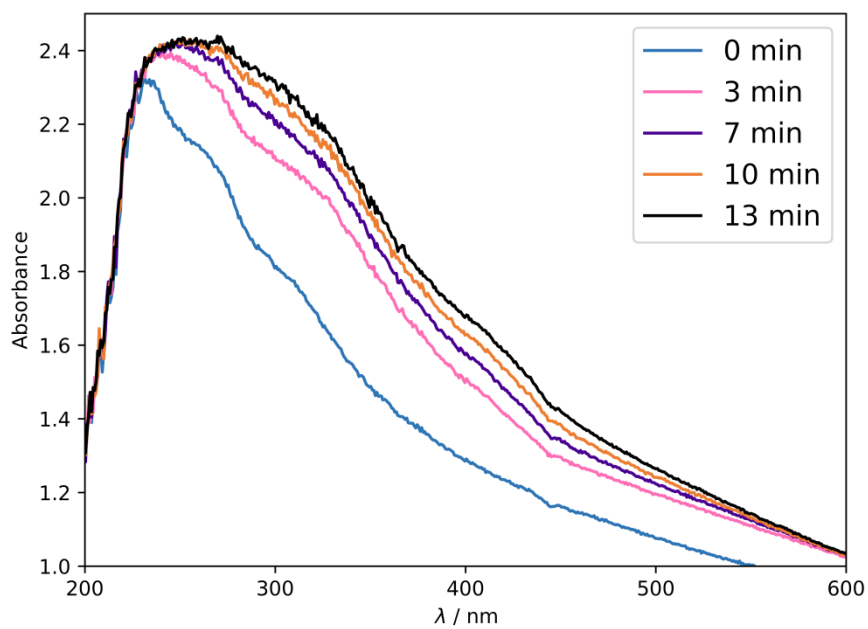


Figure 2.25: **1-(4-Br-CNB)-L-Asp**, online UV spectroscopic measurement during X-ray irradiation.

## 2.4 CONCLUSIONS AND FUTURE WORK

A robust and reproducible synthesis was developed for CNB caged L-aspartates, with good yields. This route may be extendable to other aromatic systems (via the starting nitrobenzaldehyde) or other amino acids/leaving groups (depending on the coupling step). These represent possible avenues for future work.

One drawback of the current synthesis is that the caged aspartates are produced as a mixture of diastereoisomers. Furthermore, it is possible that the reaction conditions promote epimerisation of the chiral centre derived from the L-aspartate fragment. Addressing the enantioselective synthesis of the CNB fragment is the topic of the next chapter.

# 3

## ASYMMETRIC SYNTHESIS OF $\alpha$ -CARBOXYNITROPIPERONYL PHOTOCAGES

---

The work presented in this chapter was carried out in collaboration with Owen Tuck, who worked as a summer student with the author in 2018.

Owen's work is credited where appropriate.

### 3.1 INTRODUCTION

The published synthesis of  $\alpha$ -carboxy-2-nitrobenzyl (CNB) photocages is presented in Chapter 2 (Section 2.2).[24] A racemic alcohol is produced, which when coupled to L-aspartate results in two diastereomers and possibly also their enantiomers (if epimerisation of the aspartate chiral centre has occurred).

The chiral centre resulting in the  $\alpha$ -carboxy substituent of CNB cages may complicate synthesis, characterisation and application. As mentioned above, coupling of the racemic cage precursor to a chiral amino acid results in a mixture of diastereoisomers. In the case of the CNB caged aspartates, the two diastereomers were not separable by column chromatography, thus NMR and other analyses were performed with the mixture.

Even if the leaving group is not chiral, any application involving proteins or other biomolecules will mean the interaction of a racemic photocage with another chiral entity. Therefore, the response to each enantiomer will differ.

In some cases, the presence of both enantiomers/epimers may not be a problem. In a TRX experiment, for example, one isomer may bind preferentially to the active site of the target enzyme. In this case, the system self-selects and the results are almost identical to the case where a single isomer was provided.

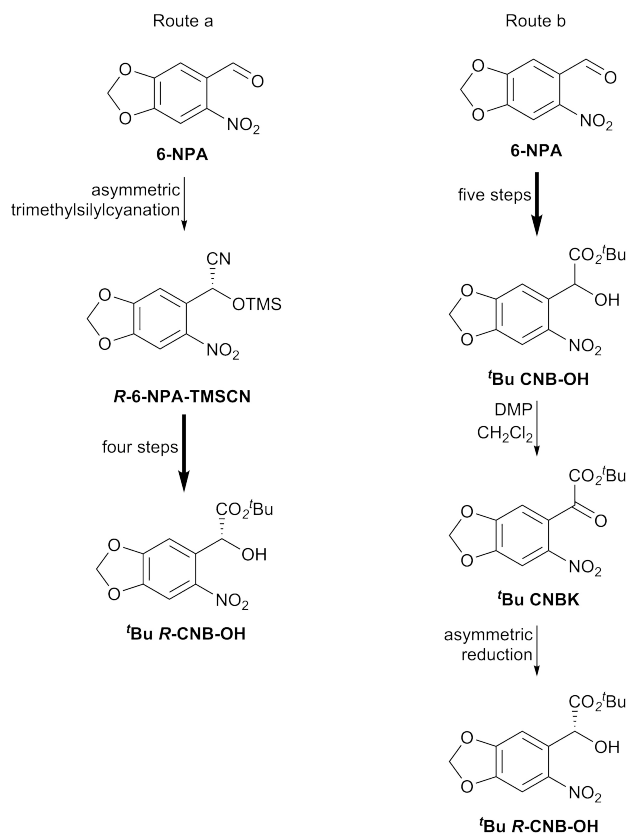
On the other hand, if both isomers bind equally well, or the difference in binding affinity ( $K_i$ ) is small, a mixture of both will be present. This may complicate data processing, as the electron density maps obtained by processing diffraction data are the average electron density of every protein in the volume of the crystal exposed to X-ray.

Due to the issues associated with racemic CNB cages, outlined above, the search for an enantioselective route was proposed as a worthwhile project.

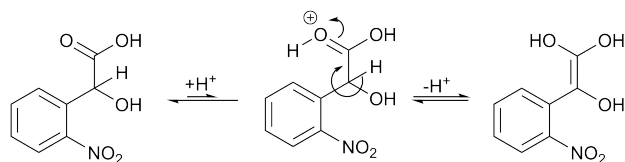
In this chapter, asymmetric synthesis of CNP type cages is the focus. However, once a successful method is found, it should be tested for generality with CNB or 4-Br-CNB type cages.

To form the chiral center present in CNB, two routes were initially proposed (Scheme 3.1). In route a, The chiral centre is formed in the first step of the synthesis and then the remainder of the synthetic route is followed in the same way as the published work.[24] Route b starts with the published synthesis,[24] then the racemic <sup>t</sup>Bu CNB-OH is oxidized to a ketone. This would then be reduced asymmetrically to give <sup>t</sup>Bu R- or S-CNB-OH.

Early asymmetric induction offers a simpler and shorter synthesis. However, it is possible that some of the succeeding reaction steps could racemise the chiral centre via enolate or enol chemistry (Scheme 3.2). Introducing the chiral centre as late as possible would mitigate these risks. Therefore, this is what was attempted initially.



Scheme 3.1: Possible routes to enantiopure <sup>t</sup>Bu CNB-OH, early (right) vs. late (left) asymmetric induction.



Scheme 3.2: Acid-catalysed racemisation of 2-nitromandelic acid via an enol-type mechanism.

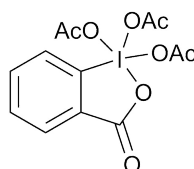
### 3.1.1 Aims

The aim of this chapter is to outline the investigations made into the enantioselective synthesis of **CNP-OH** or **Me/<sup>t</sup>Bu CNP-OH** using chiral control via chiral catalysts. A comparison of the relative merits of chiral resolution vs. chiral control is presented. Finally, some potential routes are proposed as avenues for future work.

## 3.2 LATE INSTALLATION OF CHIRAL CENTRE BY ASYMMETRIC REDUCTION

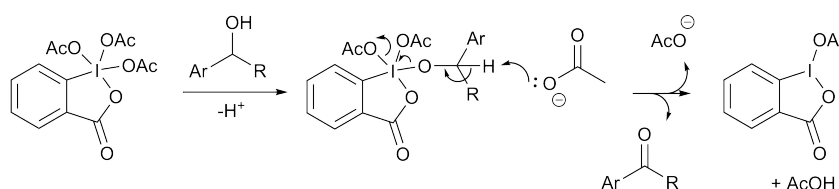
3.2.1 Dess-Martin oxidation of tert-butyl  $\alpha$ -carboxy-6-nitropiperonyl alcohol (*t*Bu CNP-OH)

The asymmetric reduction route requires an asymmetric ketone (e.g. *t*Bu CNPK), which could be reduced with preference for one prochiral face over the other. The Dess-Martin oxidation proved effective and operationally simple to carry out. The reaction uses the hypervalent iodine complex Dess-Martin periodinane (DMP) in CH<sub>2</sub>Cl<sub>2</sub>. The structure of the hypervalent iodine complex is shown in Figure 3.1. The oxidation mechanism for secondary alcohols is shown in Scheme 3.3. The alcohol exchanges with an acetate. From this intermediate, a cascade of electron-pair movements starts with deprotonating the alcoholic C-H, while the O-I bond is broken and a new carbonyl  $\pi$ -bond is formed. An acetate group also leaves the iodine centre, which has been reduced from I(V) to I(III).



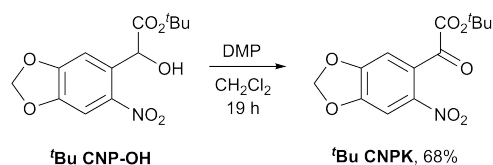
Dess-Martin Periodinane (DMP)

Figure 3.1: Structure of hypervalent iodine complex DMP.



Scheme 3.3: Mechanism of DMP oxidation of secondary alcohols.

Using DMP, synthesis of the  $\alpha$ -ketoester from racemic *t*Bu CNP-OH was successful (Scheme 3.4). In some cases a small amount of starting material remains which co-elutes with the product. This material is of course racemic and will diminish any enantiomeric excess in an asymmetric reduction. Highly pure *t*Bu CNPK can be obtained by vapour diffusion recrystallisation of the product after chromatography (see <sup>1</sup>H NMR spectrum in Figure 3.2). It is clear that the benzyl hydrogen and the OH signals of *t*Bu CNP-OH are not present, therefore corroborating the sole presence of *t*Bu CNPK.



Scheme 3.4: DMP oxidation of *t*Bu CNP-OH to afford *t*Bu CNPK. Shown here is the isolated yield after column chromatography and recrystallisation (vapour diffusion, EtOAc/hexanes).

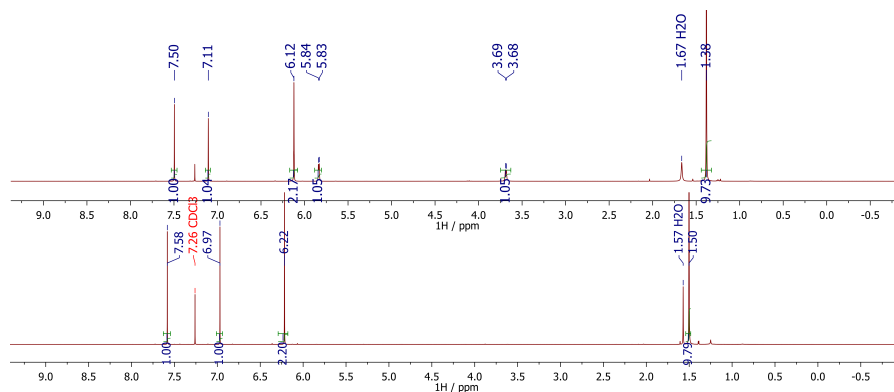
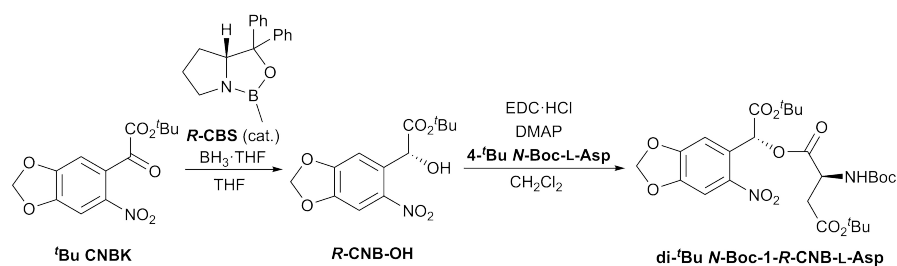


Figure 3.2: (top)  $^1\text{H}$  NMR (400 MHz,  $\text{CDCl}_3$ ) spectrum of *t*Bu CNP-OH. (bottom)  $^1\text{H}$  NMR (600 MHz,  $\text{CDCl}_3$ ) spectrum of *t*Bu CNPK. Sample was purified by column chromatography followed by recrystallisation (vapour diffusion, EtOAc/hexanes).

### 3.2.2 Corey-Bakshi-Shibata reduction

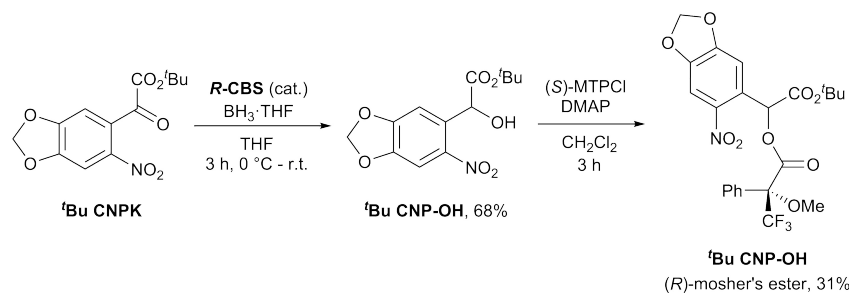
It was proposed that Corey-Bakshi-Shibata (CBS)[42] reduction of the 2-nitrophenyl  $\alpha$ -ketoester (e.g. *t*Bu CNPK) to the chiral alcohol (*t*Bu CNP-OH) could offer a route where the chiral centre is introduced directly before coupling to an amino acid building block (or similar, see Scheme 3.5). As discussed in Chapter 2 (Section 2.2.4), the conditions used in the published coupling to 4-*tert*-butyl *N*-Boc-L-aspartate may lead to epimerisation of the amino acid chiral centre in di-*t*Bu *N*-Boc-1-CNB-L-Asp.[24, 36] Therefore, determination of both enantiomeric and diastereomeric excess will be necessary in order to properly optimise the coupling reaction. However, the first problem to be addressed is the enantioselective synthesis of *R*- or *S*-CNP-OH.

Attempted reduction of *t*Bu CNPK with (*R*)-2-methyl-CBS[42] oxazaborolidine (*R*-CBS) and  $\text{BH}_3\cdot\text{THF}$  was sluggish, and required multiple equivalents (2.66 eq.) of  $\text{BH}_3\cdot\text{THF}$  and reaction at room temperature to reach completion (Scheme 3.6). The chirality of the synthesised alcohol is usually confirmed by reaction with both *R*- and *S*-Mosher's acid chlorides to give the Mosher's esters.[43] The Mosher's ester of *t*Bu CNP-OH was synthesised and  $^1\text{H}$  NMR showed the presence of two diastereomers (Figure 3.3). The inset clearly shows two sets of peaks for the piperonyl moiety. There are four aromatic sig-



Scheme 3.5: Proposed enantio- and diastereoselective route to **di-*t*Bu N-Boc-1-*R*-CNB-L-Asp**.

nals between 7.01 and 6.85 ppm. Also seen are two methylene shifts (6.31 and 6.29 ppm), two *tert*-butyl peaks (1.45 and 1.41 ppm) and two methoxy peaks (3.72 and 3.54 ppm). The integrals are all present in a 1:1 ratio (within error). Therefore no enantioselectivity was achieved in the reduction. One possible explanation could be that the bulky *tert*-butyl group impeded catalysis and higher temperature and excess  $\text{BH}_3\cdot\text{THF}$  promoted the uncatalysed reaction.



Scheme 3.6: CBS reduction of ***t*Bu CNPK** and Mosher's ester derivatisation of the alcohol (***t*Bu CNP-OH**). Work of Owen Tuck.

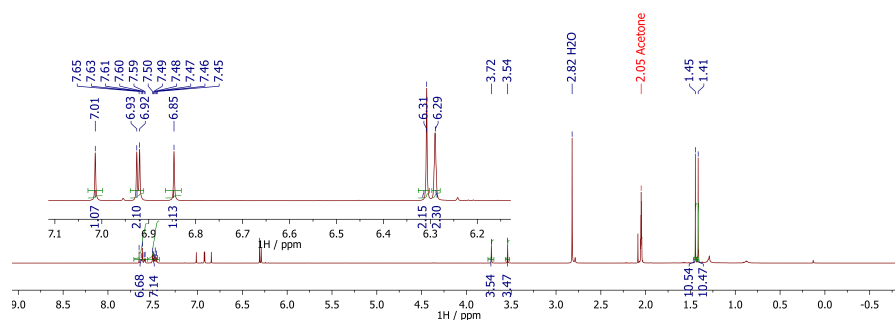
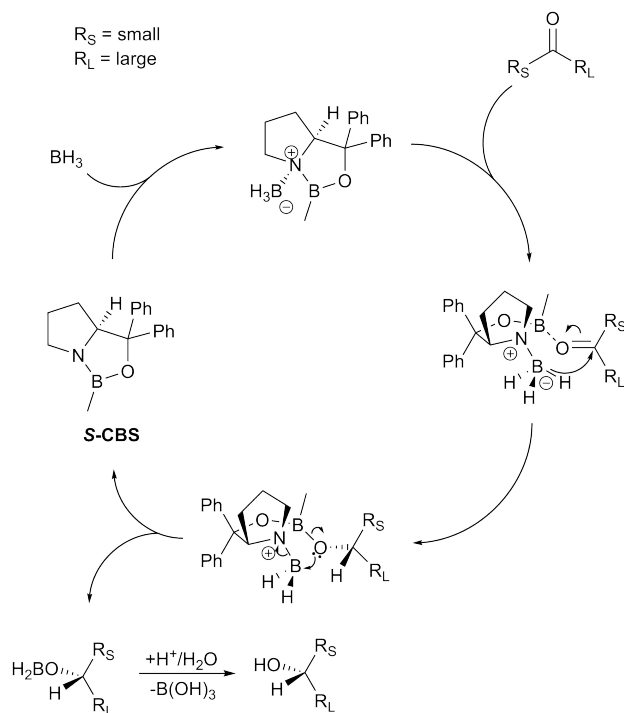


Figure 3.3:  $^1\text{H}$  NMR (600 MHz, acetone- $d_6$ ) spectrum of the (*R*)-mosher's ester derived from ***t*Bu CNP-OH**. Work of Owen Tuck.

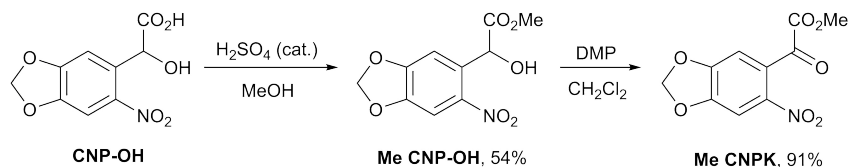
The catalytic cycle proposed by Corey et al. is shown in [Scheme 3.7](#).<sup>[44]</sup>  $\text{BH}_3$  coordinates to the nitrogen centre and the carbonyl lone-pair coordinates to boron, templating the reaction geometry. Sterics constrain the reaction; both the phenyl groups and restricted ring system prevent the carbonyl carbon being attacked underneath the crowded ring sys-

tem. Therefore, the reacting partners project out equatorially. Further steric interactions due to the axial methyl and propylene fragments favour the geometric depicted. Hydride attack then occurs from the coordinated  $\text{BH}_3$ . In fact, in our case, both groups are somewhat bulky. It was hypothesised that this was the cause of reactivity and selectivity problems; thus it was proposed to change the starting material and use a **Me CNP-OH** instead of a *t*-Bu CNP-OH, which could potentially have reduced the steric problems.



Scheme 3.7: Mechanism of asymmetric reduction with methyl (*S*)-oxazaborolidine. This mechanism was proposed by Corey et al.[44, 45]

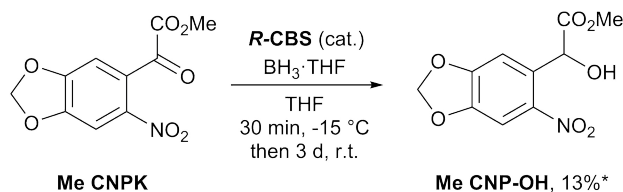
The methyl ester (**Me CNP-OH**) was synthesised from the hydroxyacid (**CNP-OH**) and oxidised to the  $\alpha$ -ketoester (**Me CNPK**) as shown in Scheme 3.8.



Scheme 3.8: Methylation of 6-nitropiperonyl hydroxyacid (**CNP-OH**) followed by **DMP** oxidation to the methyl ketoester (**Me CNPK**).

Unfortunately, attempted **CBS** reduction of **Me CNPK** proceeded similarly to the reaction with the *tert*-butyl ketoester. Extra care was taken to use dry, degassed THF and  $\text{BH}_3 \cdot \text{THF}$  (0.6 eq.) was added

slowly at 0 °C. However, only partial conversion to **Me CNP-OH** was achieved even after allowing the mixture to warm to r.t., and no further conversion was observed after extended reaction time. Additional equivalents of  $\text{BH}_3\cdot\text{THF}$  were not added this time, as this would likely only produce racemic **Me CNP-OH** as with the *tert*-butyl ketoester.



Scheme 3.9: Attempted asymmetric reduction of **Me CNPK**. \*yield determined by  $^1\text{H}$  NMR with 1,3,5-trimethoxybenzene as **ISTD**.

It could be argued that substoichiometric loading of  $\text{BH}_3$  is not sufficient in this case. However, the yield of approximately 13% ( $^1\text{H}$  NMR with internal standard, see Figure 3.4) suggests this is not the problem. Perhaps the steric demands of the **CBS** catalyst are too strict – that any ester group is too large and that the small group should be a methyl, i.e. as substrate a methyl ketone, not a methyl keto-ester. Indeed, in the original publication by Corey et al.,<sup>[44]</sup> no larger ‘small’ group was trialed than ethyl or chloromethyl.

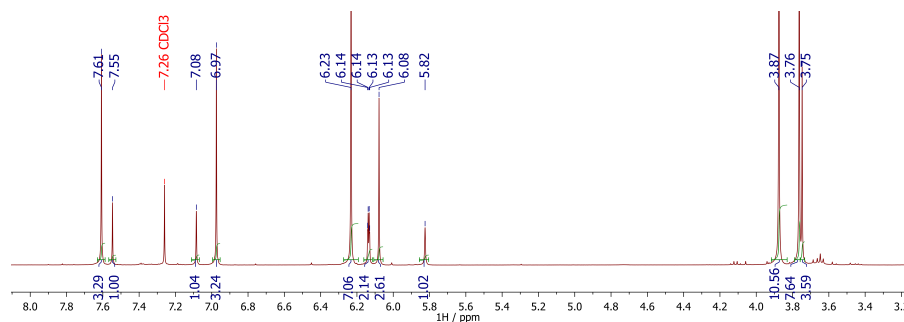


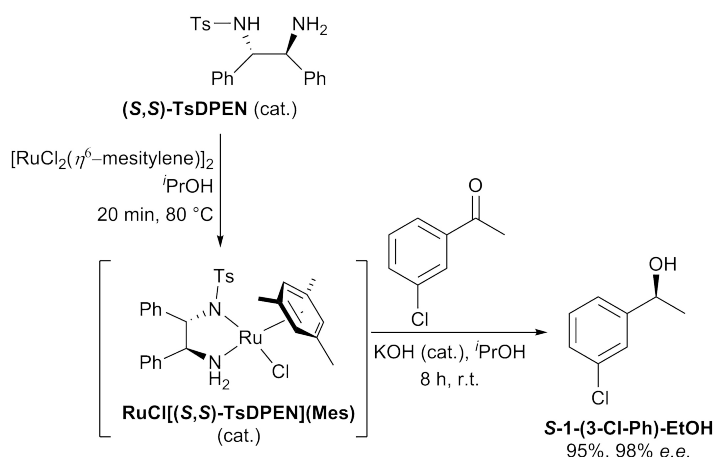
Figure 3.4:  $^1\text{H}$  NMR (400 MHz,  $\text{CDCl}_3$ ) spectrum of a mixture of **Me CNPK** and **Me CNP-OH** (15.8 mg), and **ISTD** (1.9 mg). Trimethoxybenzene aromatic shift at 6.08 ppm and benzylic CH of **Me CNP-OH** at 5.82 ppm were used to quantify the yield of 13%.

### 3.2.3 Ruthenium catalysed asymmetric transfer hydrogenation

The synthetic route was then changed, and another catalyst was used to attempt the reduction of the ketone precursor (***t*Bu CNPK**). The chiral Ruthenium(I) catalyst was reported by Hashiguchi et al. to provide high enantioselectivity ( $\geq 96\%$  *e.e.* in most cases tested) in transfer hydrogenation reactions of the exemplary aryl ketones.<sup>[46]</sup> The catalyst is  **$\text{RuCl}[(S,S)\text{-TsDPEN}](\text{Mes})$** . In the publication by

Hashiguchi, the catalytic species is formed *in situ* from the pre-catalyst  $[\text{RuCl}_2(\eta^6\text{-mesitylene})]_2$  and (1*S*,2*S*)-*N*-(4-toluenesulfonyl)-1,2-diphenylethylenediamine (**S,S-TsDPEN**) by heating at 80 °C for 20 min in isopropanol (*i*PrOH) under argon atmosphere.[46] The transfer hydrogenation is then initiated with the addition of aryl ketone and KOH (both in *i*PrOH) and carried out for typically up to 24 h at r.t. An example transformation is shown in [Scheme 3.10](#). It should be noted that in their publication, where the aryl group is the 'large' group, no 'small' group larger than ethyl was trialled. However, as asymmetric reduction protocols for ketones are somewhat limited, it was decided to attempt this anyway.

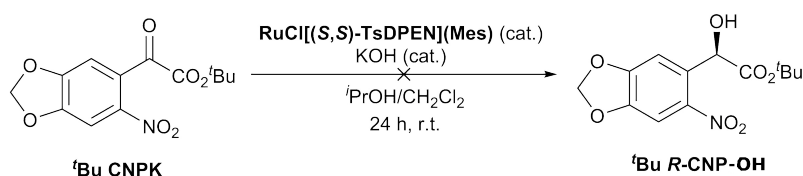
It is also possible to purchase an alternative pre-catalyst from Sigma-Aldrich, potentially obviating the need to generate the complex *in situ*.[47] This complex is Ruthenium(I) chloride[(1*S*,2*S*)-*N*-(4-toluenesulfonyl)-1,2-diphenylethylenediamine]( $\eta^6$ -mesitylene) (**RuCl[(S,S)-TsDPEN](Mes)**).



Scheme 3.10: An example asymmetric transfer hydrogenation from the publication of Hashiguchi et al.[46] The authors determined *e.e.* by comparison of the optical rotation with a previously reported literature value.

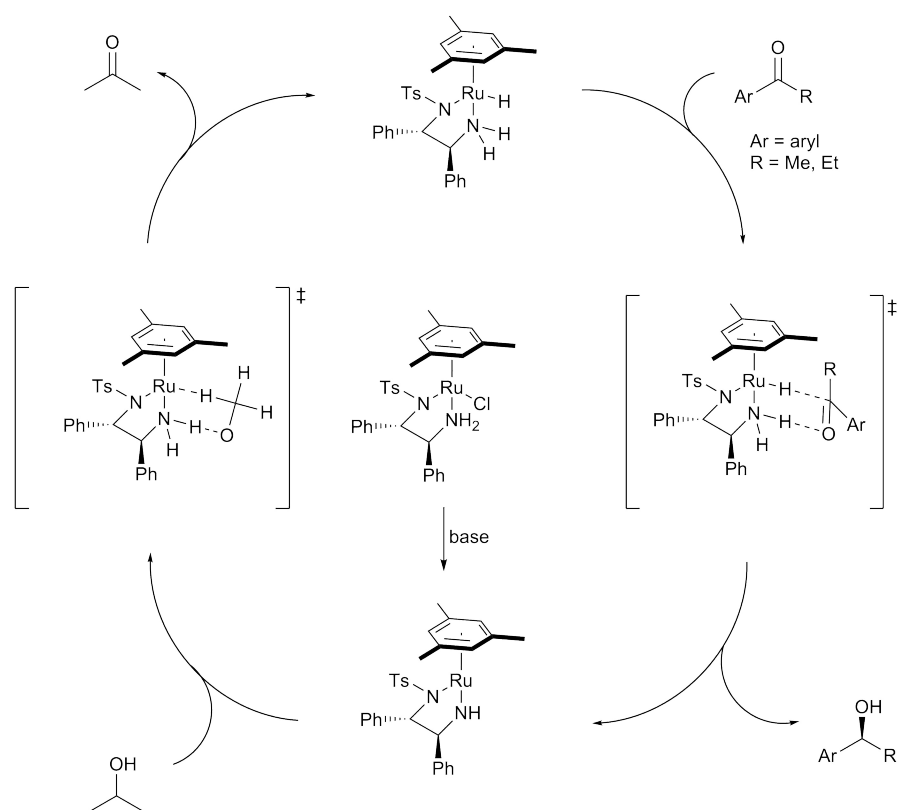
Unfortunately, the reaction was not successful. In the first attempt, ***t*Bu CNPK** did not dissolve well in *i*PrOH, and TLC analysis indicated no successful conversion after 24 h. Some faint spots were observed on the TLC plate, but did not match an authentic sample of ***t*Bu CNP-OH**. The second attempt ([Scheme 3.11](#)) employed a mixed solvent system (*i*PrOH/ $\text{CH}_2\text{Cl}_2$ ) which solved the solubility problem but no successful reaction was achieved. No doubt there is a possibility that further troubleshooting may lead to a positive result.

As noted previously, and by analogy to the [CBS](#) reduction, the published protocol only trialled acetophenones and ethyl aryl ketones. In our case, the steric demands of a bulky substituent may be a problem for catalysis. It is important, then to discuss the mechanism of this reaction, shown in [Scheme 3.12](#). Deprotonation of the pre-catalyst



Scheme 3.11: Attempted asymmetric transfer hydrogenation of  $t\text{-Bu CNPK}$  based on the work of Hashiguchi et al.[46]

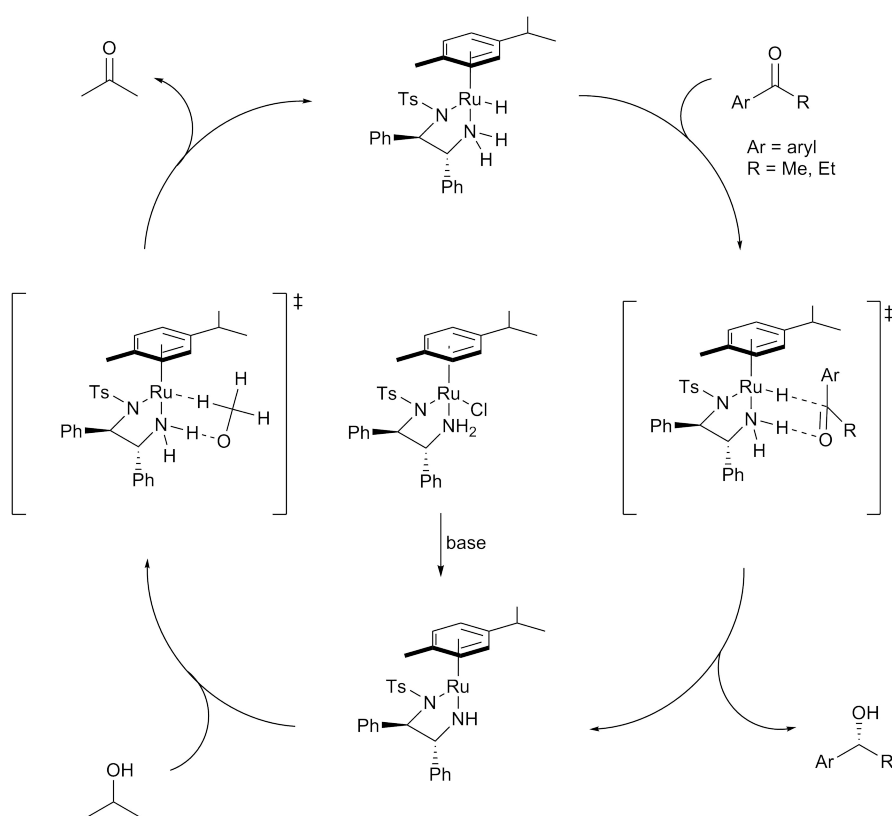
$(\text{RuCl}[(S,S)\text{-TsDPEN}](\text{Mes}))$  and dissociation of the chloride ligand generates the catalytically active species with a vacant coordination site. Isopropanol can coordinate to this species, becoming oxidised to acetone and producing a Ruthenium(I) hydride. The aryl ketone can then coordinate in a similar fashion, with the carbonyl oxygen hydrogen bonded to H-N and the carbonyl carbon positioned for nucleophilic attack by the metal hydride.



Scheme 3.12: Catalytic cycle for asymmetric transfer hydrogenation catalysed by  $\text{RuCl}[(S,S)\text{-TsDPEN}](\text{Mes})$ . The proposed cycle is based on a similar catalytic cycle proposed by Wu et al. for the same reaction using  $(R,R)\text{-TsDPEN}$  instead of the  $S,S$ -enantiomer and 4-isopropyltoluene instead of mesitylene as the  $\eta^6$   $\pi$ -donor ligand.[48]

Wu et al. suggest that the hydrogen transfer occurs through a mono-hydride transfer mechanism, involving two separate hydride transfer

steps and an outer sphere mechanism.[48] That is, the substrate does not bind to the catalyst and each hydride transfer occurs in a concerted fashion, as is shown. Enantioselectivity is achieved largely through steric interactions. The favoured transition transition state is that with the larger (aryl) group furthest away from the various aromatic groups surrounding the ruthenium centre. Interestingly, in Scheme 3.12, it appears as if the dominant factor is the steric clash with the mesitylene ligand. However, Wu et al. showed that changing the enantiomer of **TsDPEN** reverses the selectivity and gives the other enantiomer, albeit with reduced yield and *e.e.*[48] With 4-isopropyltoluene as the  $\pi$ -donor ligand and (*R,R*)-**TsDPEN**, (*R*)-1-phenylethanol was produced with 100% conversion and 98% *e.e.* The same conditions with (*S,S*)-**TsDPEN** resulted in 32% conversion and 70% *e.e.* In this case, the aromatic group appears to clash with the 4-isopropyltoluene ligand. This highlights a complex interplay between all coordinated ligands and the substrate.



Scheme 3.13: Catalytic cycle proposed by Wu et al.[48]

Digression aside, a key concern here is that the steric demands of the catalytic system may be too strict for our bulky substrate (*<sup>t</sup>Bu CNPK*), or perhaps even for **Me CNPK** (though this has not been attempted). It was decided that asymmetric reduction of a ketoester precursor may not be feasible as these steric issues may be present with any enantioselective reduction method.



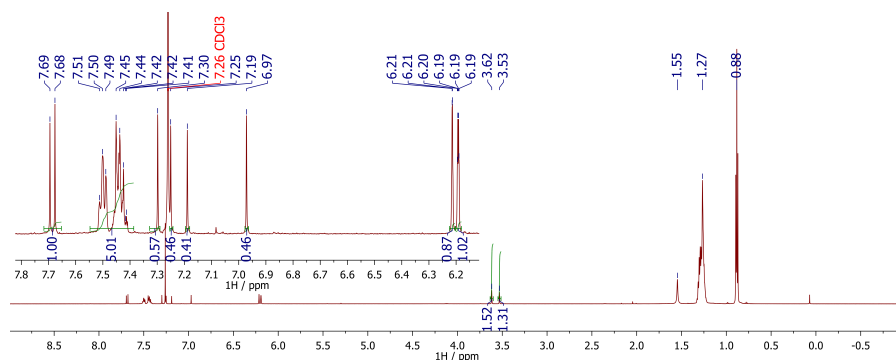


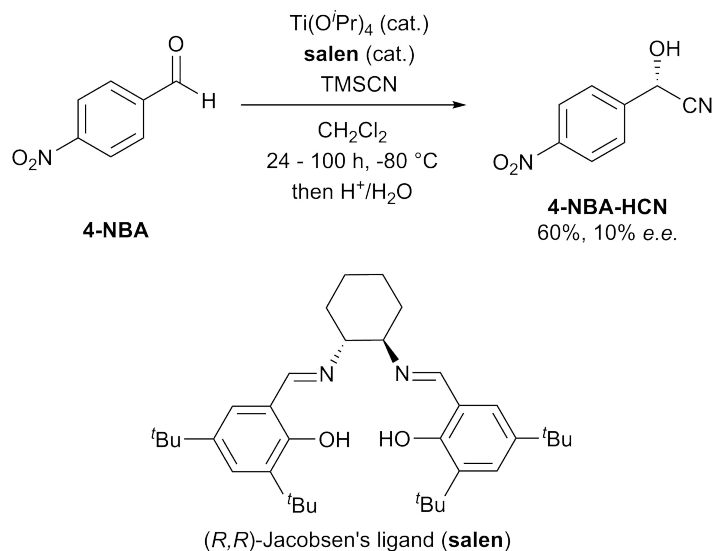
Figure 3.5:  $^1\text{H}$  NMR (600 MHz,  $\text{CDCl}_3$ ) spectrum of the *R*-Mosher's ester derivative of **6-NPA-HCN**. Two sets of peaks are present, one set for each diastereomer, in a 1:1 ratio. The contamination of this sample by heptane or hexane (1.27 and 0.88 ppm) has no bearing on the result.

7.55 – 7.40 ppm. The 3-H nuclei of the 6-nitropiperonyl moiety resonate at 7.30 and 7.25 ppm. The benzylic (or 6-nitropiperonylic) C-H nuclei resonate at 7.19 and 6.97 ppm. The large separation  $\Delta\delta$  is likely due to their proximity to the Mosher chiral centre. An even larger separation is possible if the assignments of the peaks at 7.19 and 7.25 ppm are swapped. The peaks in the range 6.21 – 6.19 ppm correspond to the methylenedioxy units of the 6-nitropiperonyl moieties, though only one is properly resolved as a double doublet. Finally, the two methoxy signals are at 3.62 and 3.53 ppm.

In the publication by Oguni, it was found that a particular form of the catalyst gave high activity and very high enantioselectivity.[49] Instead of the *in situ* combination of **L-DIPT** and  $\text{Ti}(\text{O}^i\text{Pr})_4$  with TMS-CN and aldehyde, **L-DIPT** and  $\text{Ti}(\text{O}^i\text{Pr})_4$  are mixed at  $0^\circ\text{C}$  in  $\text{CH}_2\text{Cl}_2$  then stirred for 30 min at r.t. Benzene is added, the mixture is lyophilised to give a residue. This residue and 2 eq.  $i\text{PrOH}$  gives the optimum catalyst system. This alternative catalyst system has not been tested in this thesis due to the lack of time.

The next catalyst system to be investigated was one published by Belokon et al.[51] A review found that the catalyst system comprised of titanium(IV) and (*R,R*)-Jacobsen's ligand (**salen**) provided the highest consistent enantioselectivities.[52] It is important to note, however, that electron-withdrawing groups were not well tolerated. Trimethylsilylcyanation of 4-nitrobenzaldehyde (**4-NBA**) with  $\text{Ti}(\text{O}^i\text{Pr})_4$  and **salen** afforded 60% yield and 10% *e.e.* (see Scheme 3.16). Experiments with benzaldehyde or rings with electron-donating groups gave better results.

It seems to be a general problem that electron-withdrawing ring substituents (such as our required nitro group) are detrimental to this strategy. It is possible however, that the mixed electron-donating and electron-withdrawing system of **6-NPA** would offer some balance.



Scheme 3.16: Literature example of asymmetric TSMCN addition to **4-NBA**.<sup>[52]</sup>

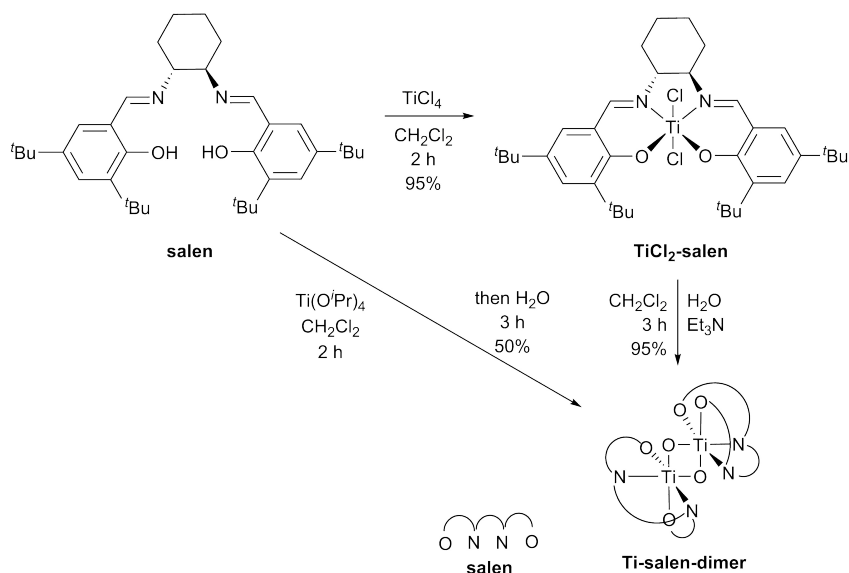
Thus the titanium(IV)/Jacobsen's ligand system was trialled for the asymmetric trimethylsilylation of **6-NPA**.

However, instead of the *in situ* catalyst, synthesis of the catalytically active dimer was attempted, as described by Belokon et al.<sup>[51]</sup> The **Ti-salen-dimer** was found to be much more active than the *in situ* generated catalyst or the **TiCl<sub>2</sub>-salen** complex. Reactions using the monomeric complex used 0.1 mol % catalyst and 24 h at r.t.; the dimer required only 1 h at r.t. with the same loading. Therefore, it was decided to attempt to use this more active catalyst.

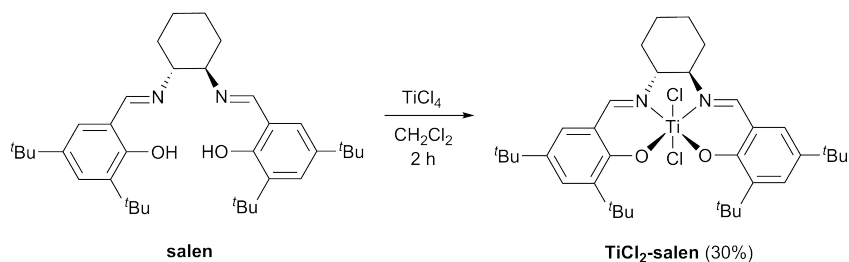
**Ti-salen-dimer** can be synthesised either following route a ( $\text{Ti(O}^i\text{Pr)}_4$  and **salen** in one step) or route b ( $\text{TiCl}_4$  and **salen** in two steps) (Scheme 3.17).

The synthesis of **Ti-salen-dimer** was repeated (Scheme 3.18), starting with the ligand (**salen**) and  $\text{TiCl}_4$ . The formation of the red **TiCl<sub>2</sub>-salen** complex was successful, albeit only in 30 % yield. The  $^1\text{H}$  NMR spectrum is shown in Figure 3.6. The signals are consistent with those reported by Belokon et al.<sup>[51]</sup> The signal at 8.30 ppm corresponds to the imine hydrogen. The aromatic signals at 7.60 and 7.34 ppm appear as doublets due to the asymmetry of the molecule. The same is true of the cyclohexane signals at 4.06, 2.60, and 2.09 ppm (likely the three hydrogen nuclei nearest to the nitrogen atom). The remaining two cyclohexane signals appear as a multiplet in the range 1.4 – 1.65 ppm. The integral appears to be only one because part of the region is obscured by one of the *tert*-butyl peaks. The signals at 1.52 and 1.33 ppm correspond to *tert*-butyl groups, due to the two positions. These peaks are not split due to the molecular asymmetry.

The next step afforded the yellow dimer complex in 74 % yield (Scheme 3.19). The  $^1\text{H}$  NMR spectrum is shown in Figure 3.7. The



Scheme 3.17: Synthesis of **Ti-salen-dimer** catalyst complex according to Belokon et al.[51]



Scheme 3.18: Synthesis of **TiCl<sub>2</sub>-salen** complex, based on the protocol of Belokon et al.[51]

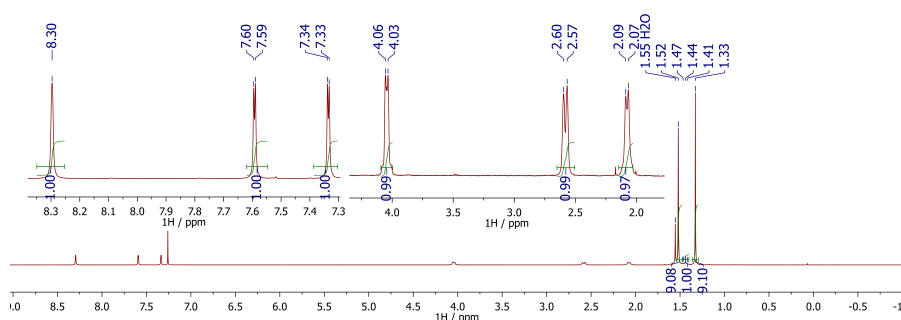
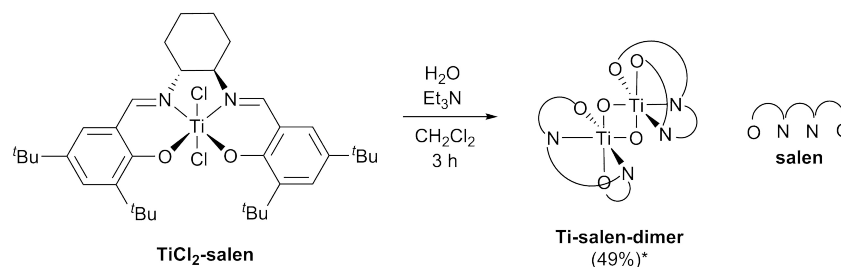


Figure 3.6:  $^1\text{H}$  NMR (400 MHz,  $\text{CDCl}_3$ ) spectrum of **TiCl<sub>2</sub>-salen**.

spectrum is very complex and does not match the spectrum reported in the literature.[51] Examining just the aromatic region (inset of Figure 3.7), twice as many signals are observed as reported by Belokon et al. for the desired **Ti-salen-dimer**. Upon closer inspection, it can be seen that the signals with the larger integrals (at 8.18, 7.82, 7.48, 7.32, 7.14, and 7.04 ppm) are consistent with the

spectrum reported by Belokon et al.[51] Thus, there appear to be two species present, in a 2:1 ratio of **Ti-salen-dimer** to the unknown product. The  $^1\text{H}$  NMR signals of the unknown component do not match **TiCl<sub>2</sub>-salen**.



Scheme 3.19: Synthesis of **Ti-salen-dimer** from **TiCl<sub>2</sub>-salen**, based on the protocol by Belokon et al.[51] \*yield estimated by  $^1\text{H}$  NMR.

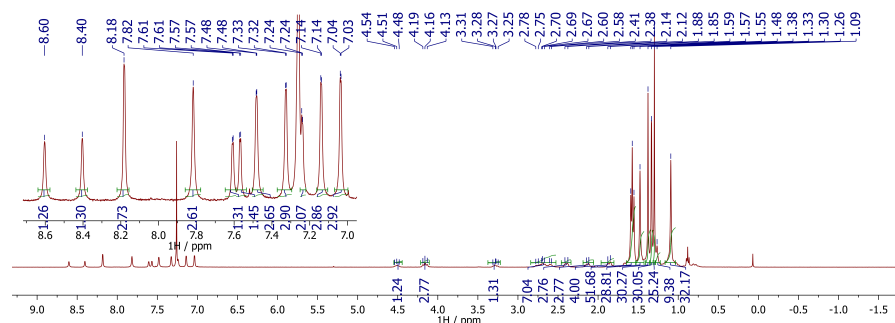
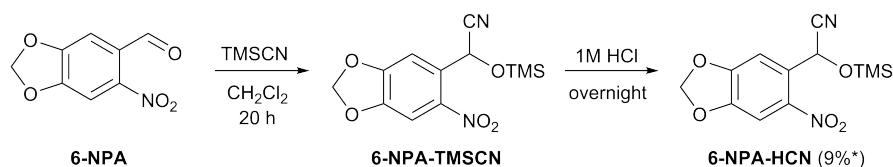


Figure 3.7:  $^1\text{H}$  NMR (400 MHz,  $\text{CDCl}_3$ ) spectrum of product mixture from the reaction of **TiCl<sub>2</sub>-salen** with  $\text{H}_2\text{O}$  and  $\text{Et}_3\text{N}$ , following the procedure of Belokon et al.[51]

Purification of this mixture has not yet been attempted. Only a crude trial of the catalytic activity has been carried out, due to time constraints. **6-NPA** (1 mmol) and the crude **Ti-salen-dimer** (1.8 mg, ca. 1  $\mu\text{mol}$  actual dimer based on the  $^1\text{H}$  NMR data in Figure 3.7) were dissolved in  $\text{CH}_2\text{Cl}_2$  (10 ml). TMSCN (0.15 ml, 1.2 mmol) was added. TLC analysis after 24 h at r.t. showed poor conversion, perhaps not more than the background, uncatalysed reaction.

A control experiment for the uncatalysed reaction had been performed previously (Scheme 3.20). The yield of cyanohydrin was 9% (determined by  $^1\text{H}$  NMR integration of the crude mixture of **6-NPA** and **6-NP-HCN**, with 1,3,5-trimethoxybenzene as an internal standard). It had been observed in another experiment that TMSCN and **6-NPA**, if present in a product mixture, will react in the absence of solvent, eventually completing the conversion to **6-NPA-TMSCN** after a number of days at 4  $^\circ\text{C}$ .

Therefore, in this control experiment, **6-NPA-TMSCN** was immediately deprotected to give the cyanohydrin (**6-NPA-HCN**).



Scheme 3.20: Control reaction for background uncatalysed TMSCN addition to **6-NPA** in  $\text{CH}_2\text{Cl}_2$  at r.t. The yield of recovered starting material was 69%\*. \*yields based on  $^1\text{H}$  NMR analysis with an internal standard.

Though it may still be worth further investigation, the electronic properties of nitrobenzaldehydes are a problem for this type of titanium catalysed asymmetric trimethylsilyl cyanation, as previously noted. Another point may also be reiterated: if the chiral centre is installed in the first step (even at 99% *e.e.*), every subsequent reaction step is a racemisation risk and must be treated as such. Therefore, the *e.e.* of every synthetic intermediate must be assayed and reaction conditions optimised where necessary. The route may also be non-viable if any of the steps result significant racemisation.

The ability to choose and synthesise one particular enantiomer by chemical (reagent or catalyst) control is an attractive goal. At face value, the synthesis of an exact compound with a particular stereochemical configuration seems direct, and efficient. Further investigations may yet discover a means of preparing the desired **R-CNP-OH** in high enantiomeric excess using chiral control.

A more practical approach may however be a more simple one: relying on the chiral pool, or simply separating the enantiomers (chiral resolution).

### 3.3.2 Use of the chiral pool

Mandelic acid can be purchased as a single enantiomer and nitrated with nitric acid (Scheme 3.21), which would give **R-CNB-OH**. This may be a viable route but has the problem addressed previously that successive steps (or indeed the nitration) may racemise the compound. Enantiopure 3,4-methylenedioxy mandelic acid needed to produce **R-CNP-OH** is not available, however (to the author's knowledge). This proposed solution therefore lacks generality.



Scheme 3.21: Proposed route to enantiopure **<sup>t</sup>Bu R-CNB-OH** using enantiopure starting material.

### 3.3.3 Chiral resolution

Instead of attempting to produce the required precursor (**R-CNP-OH** or **<sup>t</sup>Bu R-CNB-OH**) in an enantioselective manner, the simplest solution would be to produce racemic mixtures and separate the enantiomers. Chiral chromatography is one possibility. However, this is very expensive to do on any reasonable (> 100 mg) scale.

It was proposed that the carboxyl group of **CNP-OH** or **CNP-OAc** would allow the formation of a diastereomeric salt when treated with an enantiopure, chiral amine. A racemic sample of **CNP-OH** was mixed in a 1:1 ratio with (*R*)-2-aminopropan-1-ol in <sup>i</sup>PrOH at 60 °C. The mixture was layered with diethyl ether and placed in the freezer to produce the first crop of crystals. The yield (71 %) was too high to be a single diastereomer. The salt was digested with <sup>i</sup>PrOH and recrystallised again from EtOH/H<sub>2</sub>O to give 30 % yield. However, enantiomeric excess of the free acid still needs to be determined.

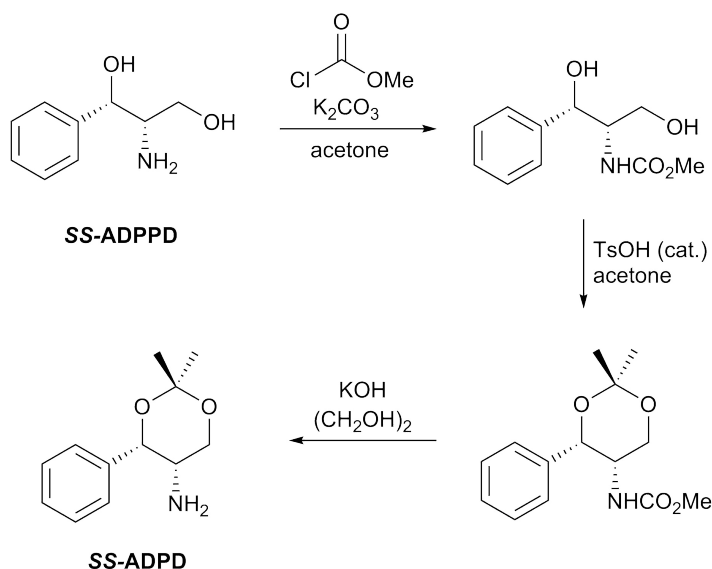
Initial attempts at separating **CNP-OH** into its enantiomers using an analytical chiral column (CHIRACEL OZ-3, 50 mm × 1.9 mm, 3 μm particle size) were unsuccessful. Methanol/ethanol mixtures from 0 to 100% methanol with 0.1 % TFA as additive did not separate the enantiomers and retention times were consistently too short (about as fast as eluent retention).

It was proposed that a chiral shift reagent for <sup>1</sup>H NMR may offer a solution. It has been shown that (*S,S*)-5-amino-2,2-dimethyl-4-phenyl-1,3-dioxan (**ADPD**) and (*R,R*)-5-amino-4-(4-biphenyl)-2,2-dimethyl-1,3-dioxan (**ABDD**) can be used as chiral shift reagents for <sup>1</sup>H NMR.[53] These reagents are effective for chiral carboxylic acids due to the formation of diastereomeric salts. **ABDD** produces a larger shift ( $\Delta\delta$ ) between two enantiomeric hydrogen nuclei. These reagents are not commercially available, but can be prepared by condensation of the appropriate diol with acetone. Protection of the amine group may also be necessary. A possible route is presented in [Scheme 3.22](#).

### 3.3.4 Conclusions and future work

This project remains largely unsolved. Several attempts at catalyst controlled asymmetric induction appear to have failed, but require further investigation before they can be said to be futile. Oguni's alternative catalyst system using pre-complexed [Ti(<sup>i</sup>Pr)<sub>2</sub>(**L-DIPT**)] and 1.5 eq. <sup>i</sup>PrOH should be investigated.[49] The **Ti-salen-dimer** should also be trialled in the TMSCN addition to nitrobenzaldehydes.[51] Several controls could be carried out, e.g. testing the catalysts with benzaldehyde.

The crude simplicity of chiral resolution may ultimately offer the most practical and successful solution, compared to the perceived elegance and academic rigour of controlled and selective synthesis.



Scheme 3.22: Proposed synthesis of **SS-ADPD** from (*S,S*)-2-amino-1-phenylpropane-1,3-diol (**ADPPD**). The same sequence starting with (*R,R*)-2-amino-1-(4-biphenyl)propane-1,3-diol would give **ABDD**.

However, this remains to be seen. An effective means of determining *e.e.* would allow for optimisation of recrystallisation protocols. It should also be investigated whether **CNP-OAc** is more effective for diastereomeric salt formation and recrystallisation than **CNP-OH**. If this is effective and provides high *e.e.*, the recrystallisation of diastereomeric salts would be repeated on a scale of  $\geq 2$  g.

It will then be necessary to continue the synthesis to **<sup>t</sup>Bu R-CNP-OH**, checking *e.e.* at every step. The ester coupling reaction will also need to be carefully re-optimised, probably using lower temperature and lower **DMAP** loading.[36] The *e.e.* and *d.r.* of the ester will need to be analysed for the optimisation.



# 4

## NITROBENZYL PHOTOCLEAVAGE REACTION MECHANISMS

---

The work presented in this chapter was carried out in collaboration with Anke Puchert, Owen Tuck, and Yannik Pfeifer.

Their contributions are credited where appropriate.

## 4.1 INTRODUCTION

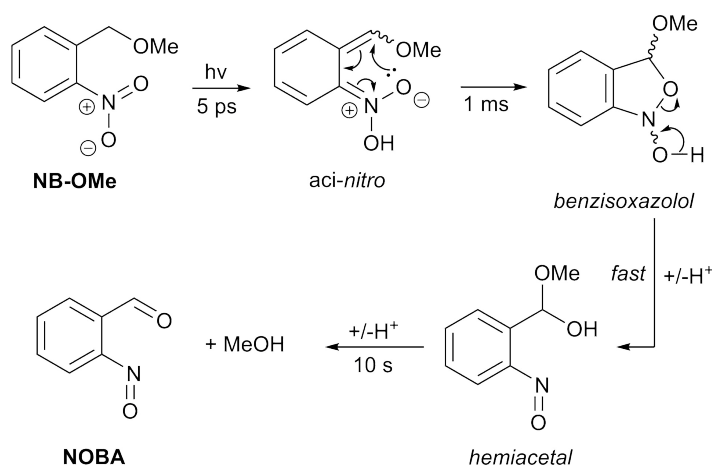
In order for a photocaged molecule to be useful as a reaction trigger, for example for time-resolved X-ray crystallography (TRX), the photocleavage reaction must be faster than the subsequent process of interest (e.g. an enzyme reaction). Therefore the photocleavage reaction mechanism is discussed here. The mechanism informs experiments carried out to gain information about cleavage kinetics of the photocaged L-aspartates, the synthesis of which is presented in Chapter 2. In this chapter, experimental results are presented from both nanosecond laser flash photolysis (ns-LFP) and femtosecond transient absorption spectroscopy (fs-TAS). These two complementary techniques probe very different aspects of the reaction.

The photocleavage reaction mechanism observed in nitrobenzyl photocages is complex. Release of caged substrate occurs only after the series of thermal reactions that follow the photochemical initiation. As a result, overall photocleavage timescales can be rather long (ms – s), which is a clear disadvantage of nitrobenzyl photocages when rapid initiation is desired. However, these photocages can be modified to have other advantageous properties, for example aqueous solubility (carboxyl substitution of CNB cages) and longer wavelength absorption (CNP cages). With the exception of the CNP cages, the carboxyl substitution reduces the cleavage times to the  $\mu$ s range.

### 4.1.1 Nitrobenzyl methyl ethers and caged ATP

The generally accepted mechanism, which can be found in a review by Klán et al.[6] and other sources,[27] is shown in Scheme 4.1. For the sake of simplicity, several details have been omitted. For example, the *aci*-nitro species has four geometric isomers and the benzisoxazolol has two. Two of the isomers of the *aci*-nitro intermediates are protomers which interconvert very rapidly (on the order of ns or perhaps faster – proton transfer via solvent-caged hydronium offers a low barrier of ca. 10 kcal mol<sup>-1</sup>)[54]. Therefore they may not be resolvable spectroscopically with ns-LFP experiments. Furthermore, the nitronate form dominates in aqueous solution at neutral pH, because the *aci*-nitro is acidic. Sometimes it is referred to as a nitronic acid.

The study of Il'ichev and co-workers was extremely thorough.[27] They carried out picosecond pump-probe experiments with 2-nitrobenzyl methyl ester (NB-OMe) in acetonitrile. They observed a broad transient absorption feature ( $\lambda_{\text{max}} = 413$  nm), growing within 5 ps of excitation with a subpicosecond 248 nm pulse. This persisted up to the maximum time-delay allowed by their instruments: 1.8 ns. They assigned this transient to an *aci*-nitro intermediate formed directly from the singlet excited state of NB-OMe. The same intermediate was



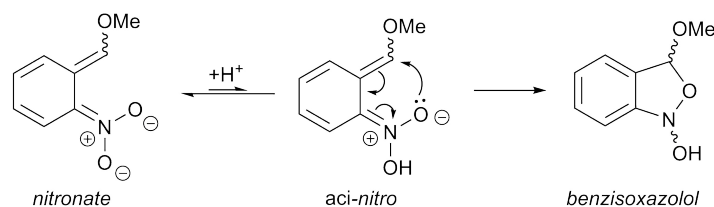
Scheme 4.1: Mechanism proposed by Il'ichev et al.[27] Photoinduced hydrogen atom transfer (HAT) results in an *aci*-nitro intermediate. This species cyclises to give the benzisoxazolol, which ring opens to give a hemiacetal. The time constants shown are those which were measured at pH 7 (extrapolated to zero buffer concentration).

observed in their *ns-LFP* experiments and in those experiments they could measure its decay rate.

Time-resolved **UV** spectroscopy experiments can detect *aci*-nitro intermediates quite easily because they absorb at longer wavelengths than the starting nitrobenzyls. This is not the case for benzisoxazolol and hemiacetal intermediates. In the literature, most authors report only the lifetimes of *aci*-nitro species observed with UV/Vis flash photolysis. Il'ichev et al. do observe kinetic features corresponding to other species in their flash photolysis data.[27] However, this is only made possible because of complementary studies with step-scan infrared (**IR**). Peak assignments for this were aided by density functional theory (**DFT**) calculations. These intermediates are not easily observed by UV/Vis experiments, such as *ns-LFP* (or indeed femto- or picosecond transient absorption spectroscopy).

Their work is important as a demonstration of the techniques needed to probe each of these intermediates.[27] Furthermore they made some key findings. pH-rate profiles showed that the *aci*-nitro cyclisation step is acid-catalysed, whereas the decay of the benzisoxazolol intermediates exhibited both general acid and base catalysis, dependent on pH. They also found that the benzisoxazolols are not observed in aqueous solutions above pH 6, indicating their decay rate exceeds the rate of formation. In a computational study,[54] the same author reported a barrier of  $18.4 \text{ kcal mol}^{-1}$  for cyclisation of an *aci*-nitro derived from 2-nitrotoluene. Conversely, the barrier to cyclisation was  $31.3 \text{ kcal mol}^{-1}$  for the nitronate. This is consistent with their experimental findings suggesting acid catalysis. The nitronate species dominates at higher pH due to the acidity of the *aci*-nitro ( $pK_a = 3.6$

for the *aci*-nitro generated by 2-nitrotoluene, ca. 4.3 for that generated from **NB-OMe**). Thus, at above pH 4, nitronate intermediates dominate and a proton source is required for cyclisation (Scheme 4.2). Interestingly, it was found that the rate continues to increase with decreasing pH, well below pH 4, suggesting an additional pathway via a protonated, positively charged *aci*-nitro derivative. This additional pathway is beyond the scope of this discussion.



Scheme 4.2: Acid-catalysed mechanism of *aci*-nitro cyclisation.

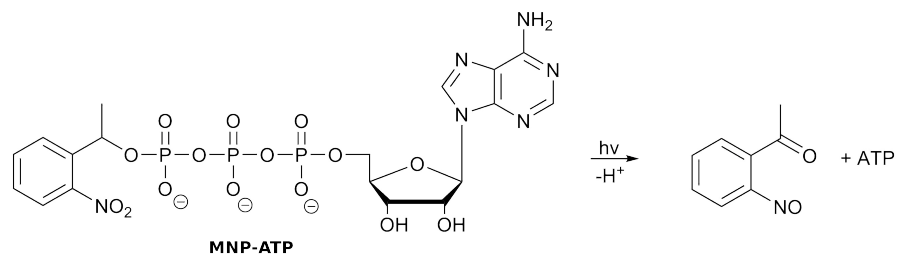
The *aci*-nitro decay rates ranged from  $108\text{ s}^{-1}$  at pH 2 to less than  $1\text{ s}^{-1}$  above pH 9 – time constants ( $\tau$ ) of 10 ns to 1 s.[53] The benzisoxazolol decay rates lay within the range  $10^2 - 10^4\text{ s}^{-1}$  (or  $\tau \sim 0.1 - 10\text{ ms}$ ), with a minimum rate at about pH 3. The hemiacetal species had a very long lifetime,  $\tau \sim 1 - 100\text{ s}$ .

They also investigated

$P^3$ -1-(2-nitro)phenylethyladenosine-5'-triphosphate, or caged ATP

(**MNP-ATP**, Scheme 4.3).[27] Similar trends were observed:

rate-determining cyclisation of the *aci*-nitro species at pH 6 or above. Below this, both the *aci*-nitro and benzisoxazolol decay rates increased with decreasing pH. However, the *aci*-nitro decay rate was faster. No long-lived hemiacetal-type intermediate was detected – this would really be a phosphorylated hemioorthoester, with ATP as an excellent leaving group. It is not surprising that such an intermediate was not detected. Extreme variability of rate with pH was also observed for the *aci*-nitro generated by **MNP-ATP**, from  $108\text{ s}^{-1}$  at pH 2 to  $1\text{ s}^{-1}$  at pH 10 or higher. The rate was  $100\text{ s}^{-1}$  at pH 7.



Scheme 4.3: Photolysis of caged ATP (**MNP-ATP**).

This work was also hugely important in showing the real role played by the benzisoxazolol intermediates, which few other researchers had been able to observe.[27] Several publications have reported on the kinetics of various nitrobenzyl photocages using only *ns-LFP* results,

which often only give information about the *aci*-nitro intermediates. McCray et al.,[55] for example reported the kinetics of the same caged ATP (**MNP-ATP**) based only on *ns-LFP* experiments. In retrospect, however, the pH range they investigated would not have generated detectable benzisoxazolol.

#### 4.1.2 Photochemistry of 2-nitrotoluene

The photophysics and photochemistry of 2-nitrotoluene (**2-NT**) have been investigated by Schmierer et al.[56] This work is a useful reference for understanding the photochemical reactivity of nitrobenzyl compounds in general. It is also useful to compare the results of *fs-TAS* experiments with **CNP-OAc** that are presented here.

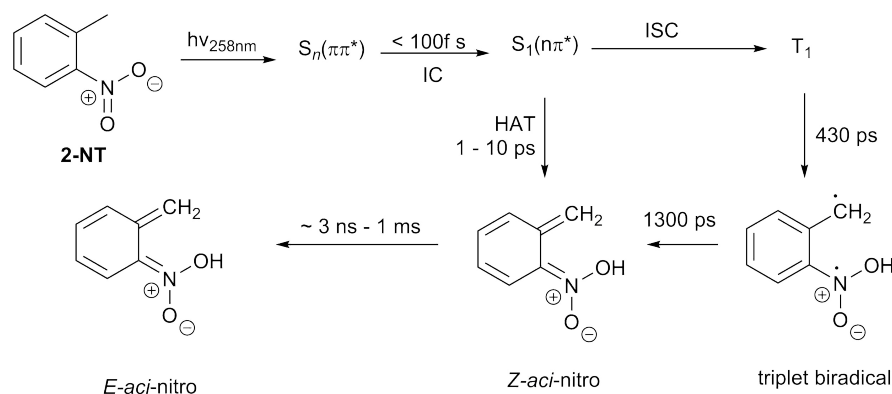
Additionally, it is of note that very few studies of this kind have been published investigating the sub-nanosecond photophysical and photochemical behaviour of nitrobenzyl photocages. To this author's knowledge, the work of Il'ichev et al.[27] and the report by Schmierer and co-workers are the only examples.[56] Only the former investigated photocages with leaving groups, whereas Schmierer's investigation was limited to nitrobenzyl compounds without any leaving group. The sparsity of these examples highlight the novelty of the experiments presented here.

Schmierer et al. used a combination of *fs-TAS*, femtosecond stimulated Raman (*fs-SR*) and (TD-)DFT computations to study **2-NT**. They used THF for *fs-TAS* experiments and deuterated MeCN for *fs-SR* measurements. The wavelength used for laser excitation was 258 nm. A summary of their findings follows.

An absorption feature centred at 400 nm rises bi-modally with time constants of 1 – 10 ps and 1500 ps. The authors attributed these to a singlet and triplet channel, respectively, and assigned the 400 nm absorption to the *Z-aci*-nitro tautomer of **2-NT**. They also noted that after 1 ms, this peak has shifted to 390 nm. They assigned this to the *E-aci*-nitro tautomer. The authors also proposed an initial excitation into a higher  $\pi\pi^*$  state, which decays into the  $S_1$  state ( $n\pi^*$ ). This can undergo hydrogen atom transfer (**HAT**) to form the *Z-aci*-nitro, fluorescence to the ground state, or intersystem crossing (**ISC**) to the triplet manifold. There, they assigned the 430 ps time constant to formation of a triplet biradical, which then forms *Z-aci*-nitro by recombination of the radical pair ( $\tau = 1300$  ps). Their kinetic model is summarised in [Scheme 4.4](#).

#### 4.1.3 Carboxynitrobenzyl photocages

Most publications reporting the kinetics of  $\alpha$ -carboxy-2-nitrobenzyl photocages also rely solely on *ns-LFP* data.[25, 30, 32, 57–59] There is one exception to this, a publication by Cheng et al.[26] The au-

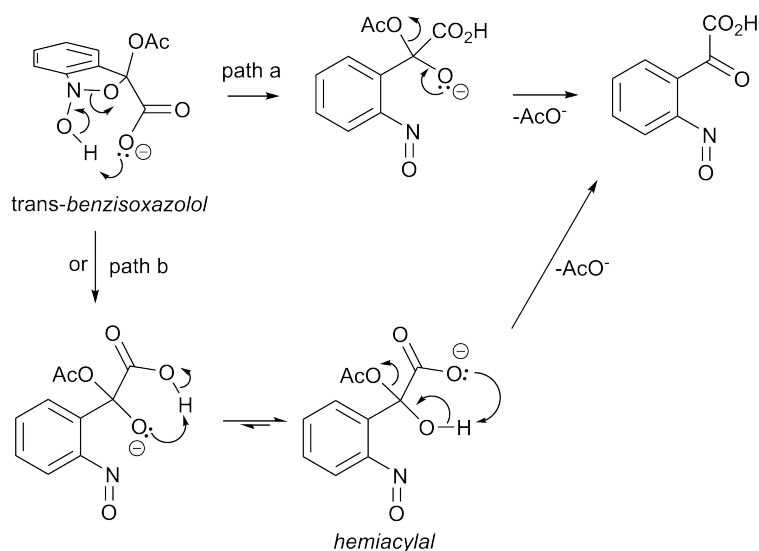


Scheme 4.4: The kinetic model proposed by Schmierer et al. for the photochemistry of 2-nitrotoluene (2-NT).

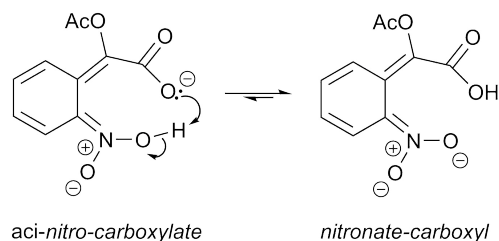
thors used a combination of *ns-LFP* and step-scan *IR*. They found that the decay of *aci*-nitro species produced by irradiation of  $\alpha$ -carboxy-2-nitrobenzyl-L-glutamate coincided with the release of L-glutamate observed by the step-scan *IR* experiment. Their experiment was carried out at pH 7.4 in 25 mM phosphate buffer. The decay constant measured was 23  $\mu\text{s}$ , typical for an  $\alpha$ -carboxy-2-nitrobenzyl photocage. No pH-rate studies were reported, so it is unknown how general this finding is, or under what conditions the benzisoxazolol decay may become rate-determining.

There is a feature of the  $\alpha$ -carboxy-2-nitrobenzyl type photocage that may enhance the rate of benzisoxazolol decay – at least for the *trans* isomer. Intramolecular deprotonation by carboxylate may offer an autocatalytic mechanism, promoting the formation of the nitroso, and expelling an alkoxide. The breaking N-O bond does not overlap with the acetate  $\sigma^*$ . However, the alkoxide may rotate or another of the oxygen lone-pairs may attack this  $\sigma^*$  to form carbonyl and expel acetate in a barrierless transition – path a in [Scheme 4.5](#). An alternative pathway (b) may go via a short-lived hemiacylal species, formed via proton transfer from the carboxyl in a 5-membered transition state. Although 5-membered transition states are quite favourable, solvent mediated proton transfers likely play a role in aqueous solution.

Another consequence of the  $\alpha$ -carboxyl group is to do with the tautomers available to the *aci*-nitro species. Typically, as discussed in [Section 4.1.1](#), the acidic *aci*-nitro deprotonates to form the nitronate species. However, in aqueous solution above pH 5, the carboxyl function is likely deprotonated. Removing a second proton from an *aci*-nitro-carboxylate may not be very favourable, except at high pH. Instead, the *aci*-nitro-carboxylate intermediates may form an equilibrium with a nitronate-carboxyl tautomer ([Scheme 4.6](#)). The equilibrium arrow is biased to the nitronate-carboxyl form based on density functional theory (DFT) calculations (see [Section 4.3.3](#)).



Scheme 4.5: Autocatalysis of *trans*-benzisoxazolol intermediate derived from  $\alpha$ -carboxy-2-nitrobenzylacetate.



Scheme 4.6: Equilibrium of two *aci*-nitro tautomers.

This raises the question of whether cyclisation proceeds preferentially through the *aci*-nitro species, via the nitronate-carboxyl tautomer or protonation to a neutral species. In the first case, pre-equilibration between the tautomers may be important to the rate. It is certainly possible that protonation to the neutral species may play a role, or even formation of a positively charged species at ca. pH 2 or below. However, for the sake of simplicity, it is assumed throughout this chapter that neutral pH conditions are used and, therefore, only structures with a single negative charge are considered.

Why are these points discussed? It must be stressed that the release of the leaving group (methanol, ATP or L-aspartate) is the determining factor for applications. Whether the study involves TRX or irradiation of whole cells followed by monitoring of response, the achievable time resolution is determined by the overall rate of release of the uncaged, active species. When the uncaging reaction is very complex, this requires an understanding of the individual steps. Crucially, which step is rate-determining, and what is its rate?

It has been established that the mechanism of nitrobenzyl photocleavage, or uncaging, is complex. It has been established that the

decay of photogenerated *aci*-nitro intermediates is rate-determining only in a subset of cases. Such detailed studies have not previously been performed for the CNB subset of nitrobenzyl photocages. The study by Cheng et al. is an exception,[26] but does not provide sufficient information. In fact, their results are in line with Il'ichev's findings for NB-OMe and MNB-ATP.[26] High pH conditions should be employed in order to look for benzisoxazolol intermediates of CNB cages.

Careful consideration of structure and reactivity may help in making predictions, especially if aided by computational methods. However, such predictions about the likely differences between CNB and NB reaction intermediates are, at best, well-informed conjecture. Only well-designed experiments can truly answer questions such as, why are the rates typically faster for CNB cages vs. NB cages, is the decay of the *aci*-nitro species still rate-determining at neutral pH, do benzisoxazolol intermediates become important at higher pH conditions.

#### 4.1.4 Aims

In this chapter, the photoreactions of  $\alpha$ -carboxynitrobenzyl (CNB) photocages are investigated using a variety of approaches – computational (DFT) and experimental (ns-LFP and fs-TAS). The intention is to understand as much as possible about the mechanism of photocleavage – both photochemical and subsequent thermal steps – and the kinetics of the processes involved. Methods (Section 4.2) describes the computational and experimental methods that were used, with some detail about the relevant theory. Some of the relevant work in the literature is covered in the Introduction to this chapter. Results & Discussion (Section 4.3) details the results of experimental and computational work carried out with the aforementioned goal in mind. A summary of these, and a proposed kinetic model of these reactions is presented in the Conclusions (Section 4.4). Experiments that would be useful, but have not been performed, are discussed under Future Work (Section 4.5).

## 4.2 METHODS

### 4.2.1 Computational methods

Various methods exist for calculating the molecular energy of a given chemical structure. Force-field methods require a model of atom positions including connectivity. These methods rely heavily on standard values for bond lengths, bond angles and torsion angles, and various empirical parameters.

Wave-function *ab initio* and DFT[60] based methods require only atomic coordinates and the number of electrons. Bonding information is derived by the method, as the modelled interactions between atoms and electrons determine this. Orbitals that can be occupied by electrons are approximated as linear combinations of basis sets, centred on each atom. The accuracy of a computation increases with the number of basis sets used – as does the computation time. The calculations presented in this thesis used the def2-TZVPD basis set. Structures were pre-optimised using the smaller def2-SVPD. This information is included here for the record, but a detailed discussion of basis sets is beyond the scope of this thesis. Unless otherwise stated, all optimised structures and all calculated energies used the def2-TZVPD basis set. All calculations were performed using Turbomole 7.3.

It is necessary to discuss the abbreviation ‘DFT’. Density functional theory is a fully *ab initio* theory in the sense that no empirical parameters are required. However, density functional theory, in the true sense, cannot be solved analytically. Therefore, density functional approximations (DFAs) are the methods that are actually used. Despite this important distinction, the convention is to refer to all such methods simply as ‘DFT’. In this case, whether or not DFT is truly *ab initio* depends on the functionals used – Becke’s three-parameter exchange with Lee, Yang & Parr’s correlation functional (B3LYP)[61] is an extremely popular DFT functional that employs empirical parameters. Conversely, the PBEo hybrid functional, based on the exchange and correlation functionals developed by Perdew, Burke and Ernzerhof[62, 63] may be derived in a parameter-free manner, in which case it can be said to be *ab initio*. [64] All of the calculations presented in this thesis used the PBEo hybrid functional.

Often, the pathway from reactant to product via some transition state is depicted in an extremely simplistic two-dimensional graph (e.g. Figure 4.1). The independent variable is referred to only as “reaction coordinate”, which has a rather vague definition in these contexts. The dependent variable is the energy of the molecule in a given state (reaction coordinate). These diagrams show that in order for a system to progress from reactants to products, some energy ( $E_a$ ) is required to overcome a barrier represented by the transition state, even if the net result reduces the total energy of the system ( $\Delta H$  is negative).

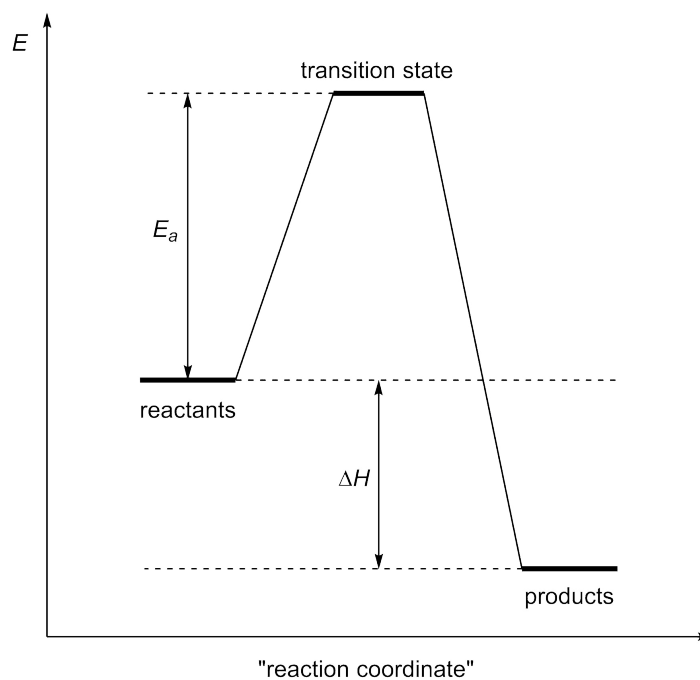


Figure 4.1: An example of a reaction coordinate diagram.  $E$  represents the energy of the reactants, products or transition state.  $E_a$  is the activation energy (only shown for the forward direction) and  $\Delta H$  is the enthalpy change.

The true potential energy surface (PES), however, is a multidimensional hypersurface. The independent variable has as many dimensions as the molecule has vibrational degrees of freedom ( $3N - 6$  for a non-linear molecule without any symmetries). The energy of the molecule depends on its coordinates within this search space. The 2D "reaction coordinate" picture is, at best, a poor approximation of a slice through one of these dimensions. Nevertheless, it is a useful simplification, given that multidimensional hypersurfaces are difficult to render in a 2D image, let alone for the reader to understand. Typically, accurate absolute energies cannot be given. However, errors are highly systematic – a large portion of this comes from basis set error. Thus, when comparing the relative energies of two species or conformers, accurate results can be obtained.

Computational methods such as DFT provide the means to calculate estimates for the relative energies of ground state conformations and transition states on the multidimensional PES. It is important to note that these are estimates and that many assumptions and simplifications must be made in order to treat a problem with DFT. Solvent molecules, for example, are rarely modelled explicitly and are modelled instead by a polarisable continuum field. When solvent molecules are explicitly modelled this is usually done in small numbers of solvent molecules. All of the calculations presented in this thesis used a conductor-like screening model (COSMO),<sup>[65]</sup> as implemented by Turbomole.<sup>[66]</sup>

Use of so-called “implicit” solvent models, such as COSMO,[65] reduces the overall accuracy of DFT calculations. However, explicitly modelling solvent molecules is often simply too expensive. Furthermore, the vast majority of chemical reactions that are studied experimentally or find application in the real world involve solution-phase, not gas-phase chemistry. Therefore, gas-phase DFT calculations are completely neglected in this thesis.

Geometry optimisation is the process of finding the coordinates with the minimum energy, nearest to a given set of starting coordinates. When a minimum energy structure is found, its vibrational spectrum and zero-point vibrational energy can also be computed. This additional term is included in comparisons of the relative energy. All vibrational frequency calculations and zero-point energy calculations used COSMO[65] as a solvent model, and employed an empirical scaling factor (0.958 for PBE0/def2-TZVPD).[67]

Transition states (TSs) can also be found by this method. However, instead of a minimum on the PES, a first-order saddle point is the target. This means the structure is a maximum in only one dimension and a minimum energy structure in all others. This requires an initial guess very close to the TS structure in order to converge. The initial guess is found by scanning an interatomic distance, relevant to the reaction of interest. This distance is set to a series of values in discrete steps, and normal geometry optimisations are performed at each step with this distance frozen – this is referred to as a relaxed scan. The structure found to have the highest energy is used as an initial guess for the TS search, with the constraint removed. This was the method used to locate the transition state geometries presented here and compute their energies. When a transition state was found, calculation of the vibrational frequencies (using the NumForce module of Turbomole) confirmed a correct TS (first-order saddle point) if only one mode was found with an imaginary frequency.

A few additional technical details should be noted about the computational methods used. Resolution of identity (ri)[68] was used in every case, as this speeds up calculations significantly. Grimme’s D3 dispersion correction was also used.[69] DFT methods use an iterative process to converge on a self-consistent field (SCF) with an associated energy term and a density matrix. A convergence threshold had to be set; for the SCF energy the convergence threshold used was  $1.0 \times 10^{-8}$ ; for the density matrix this was set to  $1.0 \times 10^{-7}$ . If further iterations result in changes smaller than these thresholds, the single-point calculation has converged. The convergence criterion for geometry optimisations is based on the gradient of the energy with respect to Cartesian coordinates. The threshold for this was set to  $1.0 \times 10^{-4}$ . DFT calculations also used weighted derivatives, and NumForce calculations used central differences, as these parameters provide superior results.

Calculations involving excited states can also be performed to investigate the PES of various excited states. Excited state calculations are also required to provide computed UV or visible spectra. Time-dependent DFT (TDDFT) can do this, albeit poorly.[70] Reliable results require high level wave function methods such as complete active space self-consistent field (CASSCF),[71] restricted active space self-consistent field (RASSCF), CC2[72], or second-order algebraic diagrammatic construction (ADC(2)).[73] A detailed discussion of these methods is outside the scope of this thesis. Instead, the focus is on ground-state PES and transition states accessible by cheaper DFT methods.

#### 4.2.2 Experimental methods

Strictly speaking, laser flash photolysis (LFP) and femtosecond pump-probe techniques are both transient absorption spectroscopy methods. However, the term “laser flash photolysis” or “LFP” has become the common nomenclature when experiments looking at longer timescales are concerned, whereas ultrafast pump-probe experiments tend to be referred to as transient absorption spectroscopy (TAS). Thus they are referred to here as ns-LFP and fs-TAS.

A subtle but interesting difference in the excitation modes of these two methods is worth mentioning. Due to the very short duration of a laser pulse used to excite a sample in an fs-TAS experiment, a single excitation event can be said to occur, to a very good approximation. There is the possibility of two- or multiphoton excitation, but after the excited state species has had time to relax to the ground state, or generate a photoproduct, the pump pulse is gone.

Conversely, in ns-LFP the pulse duration is typically several nanoseconds in duration. This is sufficient time for relaxation to the ground state in order to be re-excited. This is not likely to impact the data in any significant way. However, it is also sufficient time for photoproducts to be generated, which may then also be exposed to a part of the pump pulse. This mechanism, by which secondary photoproducts may potentially be generated, could have consequences for the data that are ultimately recorded.

ns-LFP and fs-TAS are both powerful tools to study photophysical processes, and photochemical reactions and kinetics. However, some limitations must be acknowledged, due to the nature of UV-visible spectroscopy. Transient absorbance features measured in such a way are typically broad. If several transient species are present, their spectral features may overlap, making kinetic analysis and spectral assignment challenging.

Time-resolved infrared measurements, such as step-scan or transient vibrational spectroscopy (TVS), offer richer data content and discriminatory power. These may also be used as complements to ns-LFP/fs-TAS experiments. In addition, computational methods such as DFT are bet-

ter suited for the computation of vibrational spectra. This is useful in assisting in the assignment of transient vibrational features observed in experiments. UV-visible spectra can also be calculated, but typically require more expensive wave function based methods – though this is also required for the computation of excited state vibrational spectra.

All graphs were plotted using Python scripts written by the author (see [Appendix IV](#)), some parts of which were modifications of code written by Dr. David von Stetten. The matplotlib,[\[39\]](#) NumPy,[\[74\]](#) and SciPy[\[38\]](#) libraries were used extensively.

#### 4.2.2.1 Nanosecond laser flash photolysis

[ns-LFP](#) provides information about ground-state intermediates generated following excited state photochemistry. The majority of these experiments were carried out by the author, some of which have been published.[\[24\]](#)

The first of these measurements were performed using an Applied Photophysics LKS80 Laser Flash Photolysis Spectrometer. This instrument belongs to Professor Julia Rehbein, who was at that time an Emmy-Nöther grant holder, appointed at the Chemistry Department of the University of Hamburg. Professor Rehbein was kind enough to allow the author to use her equipment on a number of occasions. Solutions of caged L-aspartate were excited by a Surelite SL I-10 [Nd:YAG](#) laser. Professor Rehbein configured the laser in order to employ the 355 nm third harmonic. The rationale for this was that 355 nm laser light is less likely to damage proteins or biological samples. This wavelength would also be likely used during application of the photocages in time-resolved structural biology experiments. Therefore, it is important to investigate their reactivity under these conditions.

Every [ns-LFP](#) experiment detailed here was recorded with the Applied Photophysics LKS80 device with excitation (laser ‘pump’) provided by a Surelite SL I-10 [Nd:YAG](#), unless otherwise stated.  $\lambda = 355$  nm, repetition rate = 10 Hz, pulse width 4 – 6 ns, beam diameter (full width half maximum ([FWHM](#))) = 6 mm,  $E = 26$  mJ.

Understanding how this instrument works is key to obtaining useful kinetic data. A sample solution was placed in a quartz cuvette with four clear sides. The laser excitation path was perpendicular to the path from the probe lamp (pulsed Xenon arc lamp, cross-beam configuration). The sample was exposed to the full broad-band light pulse from the arc lamp. A monochromator grating selected a single wavelength to forward to the detector, a photomultiplier tube ([PMT](#)). Due to the spectral characteristics of the arc lamp and [PMT](#), the effective wavelength range for detection was 200 – 600 nm, with extremely low sensitivity at the extremes of this range. Sensitivity was highest at 400 and 500 nm, with a small local minimum at 450 nm. A simplified schematic of the device is shown in [Figure 4.2](#).

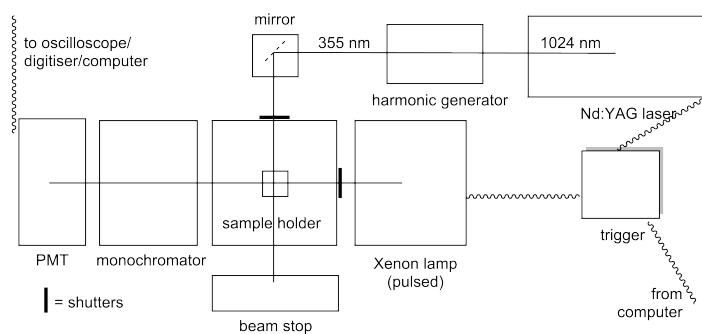


Figure 4.2: An overview of the layout of the LKS80 ns-LFP spectrometer.

Time resolution was also limited by the pulsed arc lamp. The pulsed mode increases sensitivity of detection by high light intensity. However, a measurement of the change of absorbance of a sample over time requires a stable light source. The intensity of light from a single arc lamp pulse varies over time. Within the pulse, there is a plateau region. Only during this short time-window is the light source stable enough to collect useful kinetic measurements. According to the LKS80 manual, the window is 400  $\mu\text{s}$  long. In practice, due to experimental limitations with the instrument, the longest measurements resulting in good data were 18  $\mu\text{s}$  in duration.

As mentioned previously, for a typical measurement, the sample was placed in a cuvette suitable for a cross-beam experiment. The arc lamp was pulsed to record a background measurement of intensity over time, for the chosen time-window ( $I_0/t$ ). The kinetic measurement was recorded in the same way, but the Nd:YAG excitation laser was also triggered, giving the vector quantity  $I_{\text{ex}}/t$ . The default procedure was to record the background intensity measurement once, followed by a series of measurements with laser excitation. The average of all traces with laser excitation gives the vector quantity  $I_{\text{ex}}/t$ .  $\Delta A/t$ , then, equals  $\log(I_0/t \div I_{\text{ex}}/t)$ . This can be done automatically by the LKS80 software and is suitable for reversible photoreactions.

The nitrobenzyl decaying reaction, however, is irreversible. When exciting the sample at 355 nm, the nitroso photoproducts absorb the excitation (or pump) laser light more strongly than the nitrobenzyl photocages themselves. Replacement of sample, therefore, is important for obtaining useful data.

Unfortunately, a flow cell was not available for this instrument. The very first experiments were performed with laser excitation at 266 nm. Sample was not replaced between exposures to laser light. One problem resulting from this mistake was that averaging measurements using different background light levels resulted in a non-zero baseline absorbance in the pre-trigger region of the measurement.

In order to obtain good results, the software was configured for no automatic averaging. Several measurements were recorded, each with one background measurement and one with the laser shutter

open. The cuvette was refilled manually with fresh sample for each measurement. This was somewhat expensive in terms of sample consumption, as the cuvette volume is approximately 3 ml. The cuvette was also rinsed with fresh sample between measurements in order to minimise cross-contamination. Unless stated otherwise, samples were always refreshed in this way after each exposure to a laser pulse.

In some cases, data were also measured recording emission vs. time. In order to do this, the shutter for the probe lamp is closed when the sample is exposed to the laser pulse. These emission features were present in some of the data that was collected. The decay of the emission peak contains information about the excited state lifetime,  $\tau$ . However, this was often neglected, for two reasons. Firstly, this lifetime is likely below the pulse width of the pump laser. Secondly, the emission vs. time data were saved by the software in units of Volts, whereas the kinetic data were pre-processed for background. That is, they were saved as unitless absorbance, measured as a function of time. Correction for the fluorescence features would require the intensity over time data (both background and pumped). These are sometimes seen as a negative absorbance feature immediately following laser excitation.

Time resolution is limited by the laser pulse width and the PMT detector. Typically, the device is configured to oversample, leading to very noisy data. Reduction of oversampled data was achieved by averaging consecutive data points in chunks of a certain size. A data reduction of factor 50 was used in some cases – that is, every 50 data points were averaged to a single data point, to give a final time resolution of  $0.1 \mu\text{s}$  in a dataset oversampled at a rate of 500 MHz. In those case, a  $5 \text{ k}\Omega$  resistor ( $R$ ) was used. Assuming a  $50 \text{ pF}$  capacitance ( $C$ ) for the detector, signal rise time from 10 – 90% is approximately  $5RC = 5 \times 5 \text{ k}\Omega \times 50 \text{ pF} = 0.12 \mu\text{s}$ , which is the effective time resolution of these experiments. In experiments with higher time resolution, a  $50 \Omega$  resistor was used, resulting in a time resolution of approximately 12 ns. In these cases, the original datasets were oversampled at a rate of 2.5 GHz – oversampling by a factor of 30. This oversampling caused a lot of high-frequency noise in the data, which was rectified by data reduction, taking the mean of several consecutive data values.

Due to the limited time range that can be investigated with the LKS80 instrument of Professor Rehbein, some measurements were performed by collaborators. Professor Henrike M. Müller-Werkmeister and Yannik Pfeifer were responsible for these (e.g. Figure 4.7). They used an Edinburgh Instruments LP920 LFP spectrometer with Spectra Physics Quanta Ray Nd:YAG Lab170 pump laser.  $\lambda = 355 \text{ nm}$ , repetition rate = 10 Hz, pulse  $\sim 2 - 3 \text{ ns}$ , beam width (FWHM)  $< 8 \text{ mm}$ ,  $E = 30 \text{ mJ}$ . The experiments were carried out by Yannik Pfeifer at the University of Potsdam under the supervision of Professor Müller-

Werkmeister. Figure 4.7 was produced using data they recorded (also credited in figure caption). The LP920 device was also equipped with an Andor technology DH720 intensified charge-coupled device (ICCD) detector for spectral acquisition mode.

#### 4.2.2.2 A brief digression into photophysical and photochemical theory

When exposed to light, the excited state that is first populated depends on the molecular geometry and the energy of the photon absorbed. This state will be denoted  $S_n^{v=m}$ , where  $n$  and  $m$  are non-zero. Vibrational relaxation (VR) typically occurs within 10 fs to 1 ps to populate  $S_n$  from  $S_n^{v=m}$ . Higher excited states ( $n > 1$ ) may undergo internal conversion (IC) from  $S_n^{v=m}$  to an isoenergetic state  $S_{n'}^{v=m'}$ , where  $n' < n$  and  $m' > m$ . This process is also very fast and the rate is inversely proportional to the energy difference between two states, with typical time constants of 1 – 100 ps ( $\log(k_{IC}/s^{-1}) = 12 - 2\Delta\tilde{\nu}/\mu\text{m}^{-1}$ ).<sup>[75]</sup> IC and VR steps typically out-compete other processes until  $S_1$  is populated, as these radiationless transitions are extremely fast. The result is Kasha's rule: emission – or photochemical transformation – occurs only from the lowest excited state of a given multiplicity. Naturally, we are dissatisfied by rules, and great efforts have been made to provide examples that do not satisfy this rule, so called anti-Kasha photochemistry.<sup>[76]</sup> Nevertheless the rule holds in most cases, and  $S_1$  is usually the most important state. Radiationless IC from  $S_1$  to the ground state is favourable only in rare cases, so  $S_1$  decays by fluorescence. Typical lifetimes are on the order of picoseconds. Some of these processes are depicted in the Jabłoński diagram (Figure 4.3).

Other pathways are also possible, such as ISC to the triplet manifold; this process is slower than IC, and the resulting triplet states typically have very long lifetimes – from  $\mu\text{s}$  to seconds, due to slow phosphorescence.

The above are photophysical processes. Photochemistry is chemical transformation that occurs via one of these excited states (often  $S_1$  or  $T_1$ , due to Kasha's rule). This can happen in a number of ways. One is via a conical intersection (CI), joining the excited state PES to the ground state PES of a species chemically distinct from the original ground state. There can also be an energetic barrier connecting the excited states of the two species, resulting in population of the new species in its excited state, followed by relaxation to the ground state. Another possibility is that the excited state relaxes to a vibrationally hot ground state of the original species, which is energetic enough to overcome an energy barrier that is typically inaccessible.

fs-TAS is able to probe these ultrafast photophysical and photochemical events.

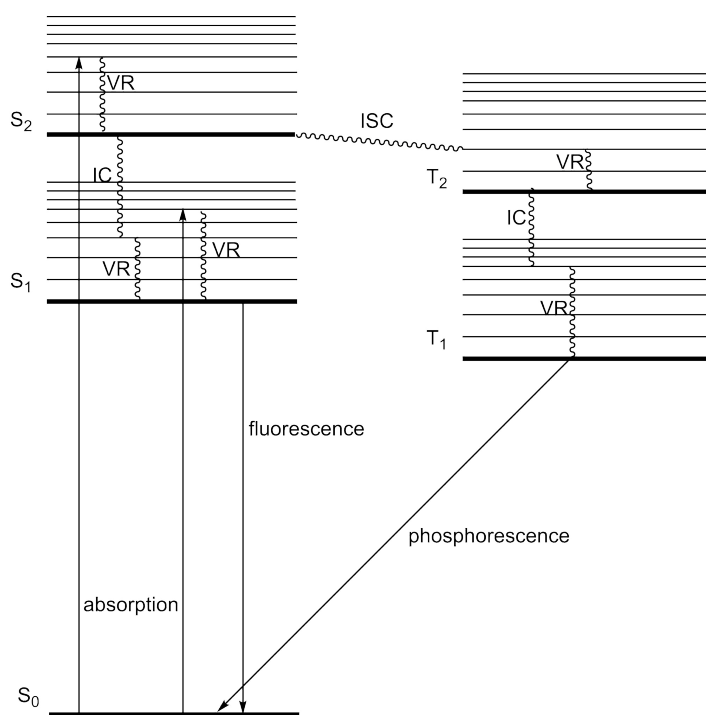


Figure 4.3: Jabłoński diagram depicting radiative transitions (fluorescence and phosphorescence), and nonradiative transitions (IC; VR; ISC).

#### 4.2.2.3 Synthesis of caged acetates

Caged acetates (**CNB-OAc** and **CNP-OAc**) were chosen for use in *fs-TAS* experiments, due to their relative ease of synthesis. These compounds are intermediates in the synthesis of **1-CNB-L-Asp** or **1-CNP-L-Asp**. The acetates are easier to produce in large quantities (e.g. 1 – 2 g scale) and easier to purify than the aspartates. The acetates (**CNB-OAc**) are not normally purified when used as a synthetic intermediate. Indeed, neither are the precursors (**CNB-OH**). The impure samples of **CNB-OH** and **CNB-OAc** typically contain some dark coloured impurities. However, for spectroscopic studies, high purity is ideal. Especially if there are impurities that absorb UV or visible light, or impurities with fluorescent properties that may interfere with the results collected.

Carboxylic acids are difficult to purify by flash chromatography on silica gel. Partial ionisation results in a tail of carboxylates interacting strongly with silanol groups on the silica surface. The addition of formic acid (**FA**) to the eluent helps by suppressing ionisation of the carboxylic acid. Mixtures of CH<sub>2</sub>Cl<sub>2</sub>, MeOH and **FA** were effective, but nevertheless further purification was performed. After chromatography, the caged acetates (**CNB-OAc**) were recrystallised by vapour diffusion (EtOAc/*n*-pentane). **CNP-OAc** for use in *fs-TAS* experiments was synthesised as described in Section 6.8,[24] and purified by flash

chromatography (CH<sub>2</sub>Cl<sub>2</sub>-FA-MeOH, 975:20:5) followed by vapour diffusion recrystallisation (EtOAc/*n*-hexane).

#### 4.2.2.4 Femtosecond transient absorption spectroscopy

This technique uses a laser that can generate extremely short light pulses – typically on the order of 10 – 100 fs – and typically of infrared light. Each pulse is split into multiple parts. One part, the largest fraction of the pulse, is used to generate a suitable wavelength for sample excitation (pump). A small part of the pulse is used as a probe beam. The probe beam is split into a continuum using, for example, a CaF crystal. The pump beam is frequency doubled, tripled, or doubled twice to produce a harmonic frequency in the visible or UV. The choice of frequency depends on the sample of interest, or other experimental considerations. A tunable pump wavelength can be achieved with an optical parametric amplifier (OPA).

The detectors used for these experiments typically have sampling rates of 1 to 3 kHz. This is far too slow for a technique that can probe excited states with picosecond lifetimes. However, the time-resolution is not directly related to the detector sampling rate, which only limits the data collection rate.

The pump and probe pulses in these experiments follow two different paths from the laser source to the sample and then the detector. One beam travels along a delay stage with a pair of mirrors, which move to different positions in order to collect different time points. Each time point is then determined by the speed of light and the difference in the distance that the two beams travelled. Light of different wavelengths do not travel at the same speed in air; thus, there is a slight shift in the time of reaction initiation in fs-TAS data across the spectrum.

A small part of the probe light is diverted by a partially transmissive mirror prior to interaction with the sample. This is used as a reference for the spectrum of the probe pulse recorded by the detector after the interaction. Measurements alternate between pumped and unpumped for each mirror position of the delay stage. This gives the most accurate calculation of the spectral  $\Delta A$  at every time point.

Background spectra are also recorded for calibration and to measure the cross-phase modulation (CPM). A detailed discussion of this is outside the scope of this thesis, but the CPM results in an important artefact in the spectral data over time. This artefact is centred at  $t_0$  and is shifted slightly to later times as the wavelength of the probe increases. This is of course important to consider in the data analysis.

The probe and pump pulse paths, and the sample itself, must be carefully aligned to coincide in one point in space. A full measurement may take several hours, and this alignment should be kept stable throughout the experiment. In practice, this is difficult to achieve.

Data are typically recorded at a rate of 3 kHz, as allowed by the detector response time. Thus, the sample is exposed to a probe pulse every 333  $\mu\text{s}$  and a pump pulse every 666  $\mu\text{s}$ . The pump pulse may have a low energy (1 mJ or less), but its short duration results in a high peak power. This can lead to sample heating or two-photon excitation events, especially if the power is too high.

Due to these effects and the short time between probes, it is important for the interaction volume to be refreshed with new sample continuously. This applies even if the sample undergoes a fully reversible photoreaction. Sample solution is typically replaced using a flow cell, an optical cell with inlets and outlets connected to a pump. Alternatively, a liquid jet may be used.

In order to investigate the initial photochemical reaction step and the excited state of **CNB-OAc**, *fs-TAS* experiments were carried out by Anke Puchert. The results may also be published in her PhD thesis with a more complete treatment (e.g. singular value decomposition and global analysis/global fitting of decay associated spectra). An excellent example of the thorough investigation of *fs-TAS* data was published by Schmierer et al., on the photophysics of 2-nitrotoluene.[56]

Presented here instead is a small sample of the data with a rather crude and simplistic analysis. These are shown here as they were performed using samples prepared by the author (assisted by Owen Tuck). The results are also relevant to the investigation of **CNB** photocage reaction mechanisms presented within this chapter.

The synthesis and sample preparation were carried out by Owen Tuck and the author. The pump-probe measurements were carried out by Anke Puchert. Data averaging, background subtraction and conversion of raw pixel data to wavelength was performed by Anke Puchert. The crude data processing and fitting results shown here were carried out by the author, as was the production of the figures.

Experiments were carried out with **CNP-OAc** (10 mM) dissolved in sodium phosphate buffer (125 mM, pH 7), with a total volume of 30 ml used for the flow-cell reservoir. A circular flow system was used; therefore a small concentration of photoproduct may have built up in the reservoir over the course of the experiment. This is hoped to be negligible compared to the 10 mM concentration of **CNP-OAc**; however, this cannot be said with certainty at this time.

The excitation wavelength was 400 nm. The pulse energy was 0.73  $\mu\text{J}$ . The optical path length of the sample was 250  $\mu\text{m}$ . The pump beam dimensions (*FWHM*) were 50  $\mu\text{m}$   $\times$  50  $\mu\text{m}$ ; the probe beam 35  $\mu\text{m}$   $\times$  35  $\mu\text{m}$ . The average data were taken from 8 sets of measurements with sample and 15 background sets with only buffer. Each set of measurements used 3000 (background) or 6000 (sample) laser shots.

### 4.3 RESULTS & DISCUSSION

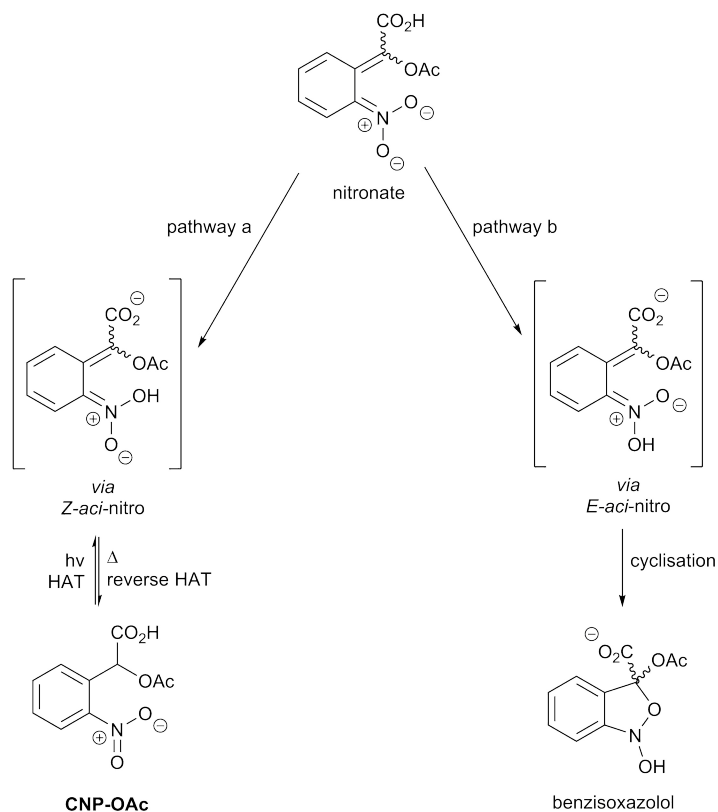
#### 4.3.1 Observing *aci*-nitro intermediates: nanosecond laser flash photolysis

As discussed previously, nitrobenzyl photocages generate metastable *aci*-nitro intermediates as their immediate photoproducts. Typically, these species exhibit a transient absorption band in the near UV (typically  $\lambda_{\max} \sim 400$  nm).[5, 25, 27, 55] The decay of these species is likely due to at least two reaction pathways; a) reverse HAT to the ground state nitrobenzyl and b) cyclisation to the benzisoxazolol species (Scheme 4.7). Each of these steps occurs via protonation in the Il'ichev mechanism.[27] Direct protonation of the carbon centre, forming the original nitrobenzyl directly from the nitronate, may also be possible. However, this is likely to be a less favourable pathway, as the delocalised negative charge will tend to have a higher density at the nitro group. On the other hand, as discussed in Section 4.1.3, the behaviour of nitrobenzyls bearing a benzylic carboxyl group may be somewhat different. All measurements were performed under neutral pH conditions in phosphate buffer. Thus, the initial species in solution will have been significantly ionised. The *aci*-nitro intermediates, once formed, may have undergone a proton transfer to the carboxylate, resulting in a tautomer bearing a nitronate conjugated with a carboxyl group. A small fraction of the population may react via protonation to the neutral species, or deprotonation to the dianion. However, all the key mechanistic steps required for nitrobenzyl photocleavage are possible while maintaining the charge of the molecule as a monoanion. Therefore, this is likely to be the most favourable route at neutral pH conditions. Henceforth, references to the *aci*-nitro intermediate will imply a carboxylate, and those to the nitronate intermediates a carboxyl group.

*aci*-Nitro intermediates are acidic and all experiments were performed at neutral pH. Therefore, it is likely that the species observed in the following kinetic traces are the nitronates formed by deprotonation. Indeed, this is likely also the case for the literature reports by Grewer,[25] Cheng,[26] or McCray.[55] Il'ichev et al.[27] noted a kinetic component with a rate of  $4.5 \times 10^6 \text{ s}^{-1}$ , observed at 420 nm in one of their measurements. This  $1 - e^{-kt}$  rising component was attributed to population of the nitronate species by deprotonation of *aci*-nitro intermediates. A similar feature was observed in some of the experiments presented here (*vide infra*).

##### 4.3.1.1 1-CNB-L-Asp

The decaying signal shown in Figure 4.4 is assigned to the nitronate intermediates generated as a result of exciting a solution of 1-CNB-L-Asp with 355 nm laser light. The absorbance signal, observed at 430 nm, decays biexponentially. This is consistent with the formation



Scheme 4.7: reaction pathways available from the nitronate intermediate. Pathway a = proton transfer to *Z-aci-nitro* and reverse HAT. Pathway b = proton transfer to *E-aci-nitro* followed by cyclisation to the benzisoxazolol intermediate. It is assumed that at neutral pH, most species are singly ionised, but reaction paths are controlled by particular tautomers.

of two nitronate species, an *E*- and a *Z*-isomer. The lifetimes of the two components are 1.5  $\mu\text{s}$  and 10  $\mu\text{s}$ . The rise time of the signal is roughly on the order of the detector response time (ca. 0.1  $\mu\text{s}$ ).

The signal observed at 310 nm (Figure 4.5) shows an instantaneous rise, followed by a decaying signal with a lifetime of  $0.13 \pm 0.01 \mu\text{s}$ . This is similar to the rise time observed in Figure 4.4, and consistent with the rate reported by Il'ichev et al. for the deprotonation of *aci-nitro* intermediates. After this initial decay, the signal grows with two  $(1 - e^{-t/\tau})$  components, with time constants of  $0.38 \pm 0.05 \mu\text{s}$  and  $6.2 \pm 0.5 \mu\text{s}$ . Although they deviate somewhat from those obtained by fitting the signal shown in Figure 4.4, they are of the same order. This growth at 310 nm may be tentatively assigned to the nitroso end product of the decaying reaction, based on its similarity to the nitroso growth at 330 nm reported by Il'ichev et al.[27] This is by no means conclusive, but lends support to the hypothesis that, under neutral pH conditions, decay of nitronate signal (ca. 430 nm) coincides with product release (as reported by Cheng et al. in the case of 5-CNB-L-Glu).[26]

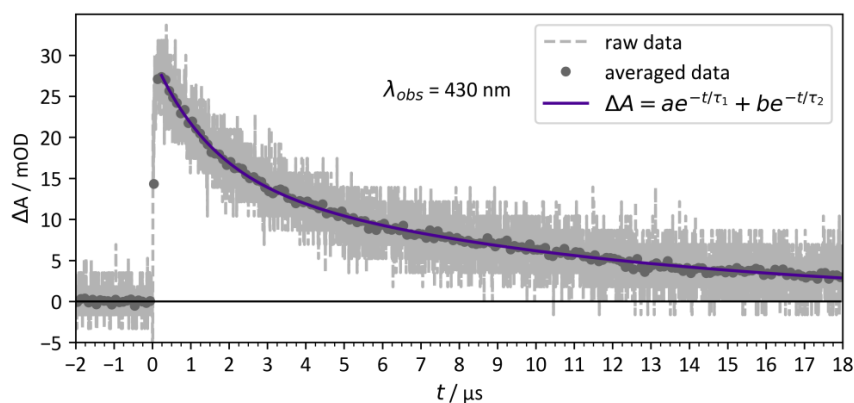


Figure 4.4: **1-CNB-L-Asp**, nitronate species observed by LFP experiment.  $\lambda_{\text{pump}} = 355 \text{ nm}$ ,  $c = 0.4 \text{ mM}$  (in sodium phosphate, 50 mM, pH 7), average of four measurements, resistor = 5 k $\Omega$ . Data were recorded at 500 MHz (oversampled). Data were reduced by a factor of 50.  $\tau_1 = 1.5 \pm 0.1 \mu\text{s}$ ,  $\tau_2 = 10.4 \pm 0.4 \mu\text{s}$ ,  $a = 46 \pm 2 \%$ ,  $b = 54 \pm 2 \%$ . Published figure.[24]

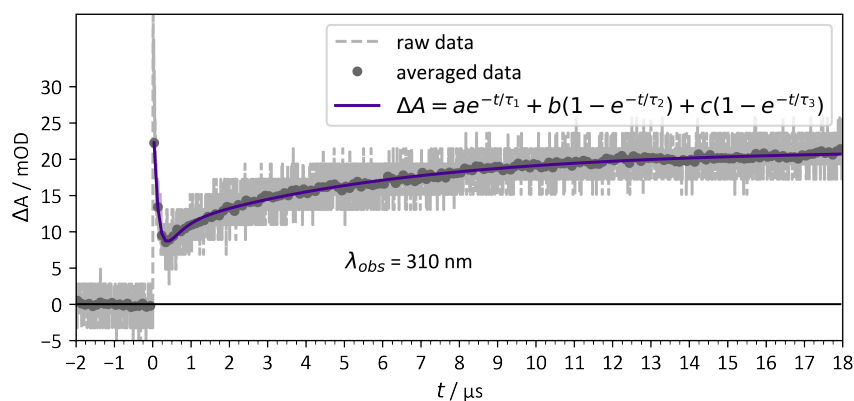


Figure 4.5: **1-CNB-L-Asp**, *aci*-nitro (decay) and possible nitroso (biexponential rise) species observed by LFP experiment.  $\lambda_{\text{pump}} = 355 \text{ nm}$ ,  $c = 0.4 \text{ mM}$  (in sodium phosphate, 50 mM, pH 7), average of three measurements (note – in this case, the sample was not refreshed between measurements, but a new background was recorded each time), resistor = 5 k $\Omega$ . Data were recorded at 500 MHz (oversampled). Data were reduced (averaged) by a factor of 50.  $\tau_1 = 0.13 \pm 0.01 \mu\text{s}$ ,  $\tau_2 = 0.38 \pm 0.05 \mu\text{s}$ ,  $\tau_3 = 6.2 \pm 0.5 \mu\text{s}$ ,  $a$  is independent of  $b$  and  $c$ ,  $b = 49 \pm 4 \%$ ,  $c = 52 \pm 3 \%$ .

#### 4.3.1.2 **1-CNP-L-Asp**

When first investigating the photocleavage kinetics of **1-CNP-L-Asp**, only a short lived species was observed at 460 nm. Professor Rehbein's equipment could not be used for measurements over longer timescales than about 18  $\mu\text{s}$ . The species observed with this instrument had a

lifetime of  $224 \pm 4$  ns. This was initially assumed to be the nitronate decay, albeit much faster than any previously reported in the literature. However, this lifetime is also consistent with the deprotonation of *aci*-nitro intermediates observed by Il'ichev et al., with a lifetime of  $370 \pm 40$  ns (Figure 4.6). This may suggest that the *aci*-nitro species generated by **1-CNP-L-Asp** is more acidic than that of **NB-OMe**, but a direct comparison cannot be made as buffer conditions differ. It does also suggest that **1-CNB-L-Asp** generates a more acidic *aci*-nitro species (lifetime ca.  $0.1 \mu\text{s}$ ) than **1-CNP-L-Asp**. The pathway from nitronate to benzisoxazolol (pathway b, Scheme 4.7) is acid-catalysed, which would suggest that the more basic nitronate (**CNP**) should cyclise faster.

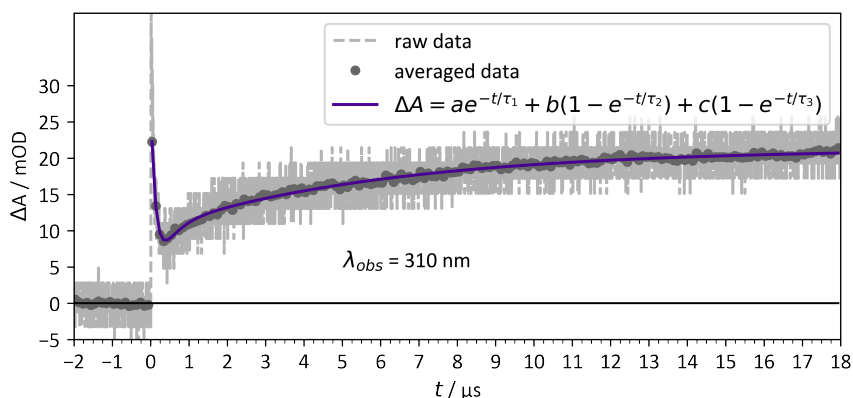


Figure 4.6: **1-CNP-L-Asp** *aci*-nitro deprotonation.  $\lambda_{\text{pump}} = 355$  nm,  $c = 0.4$  mM (in sodium phosphate, 50 mM, pH 7), average of four measurements, Data were recorded at 1 GHz (oversampled). Data were reduced by a factor of 10.  $\tau_1 = 199 \pm 4$  ns,  $\tau_2 = 9 \pm 1 \mu\text{s}$ ,  $a = 86 \pm 1\%$ ,  $b = 14.6 \pm 0.5\%$ . Peak occurs at 30 ns,  $1/e$  rise time ca. 20 ns. Published figure.[24]

However, Figure 4.7 shows a kinetic trace recorded with an instrument that can measure up to 10 ms. This was therefore assigned to the nitronate intermediate, which is much more long lived ( $\tau = 0.87 \pm 0.04$  ms) than those generated by **CNB** or **4-Br-CNB** photocages.

A crude partial spectrum of the *aci*-nitro species generated by excitation of **1-CNP-L-Asp** was recorded using the LKS80 instrument. Kinetic traces were recorded at several wavelengths. These were 460, 600, 580, 560, 540, 520, 500, and 480 nm, recorded sequentially in that order. The sample solution was not replenished for every shot in this case, due to limited sample volume. As a result of this, the yield of transient *aci*-nitro was slightly reduced in each successive measurement and the shape of the spectrum was affected. Data were reduced by adjacent averaging (factor 10) as in other measurements presented here. To construct the partial spectrum, the index of the maximum absorbance value of the first spectrum (460 nm) was noted.

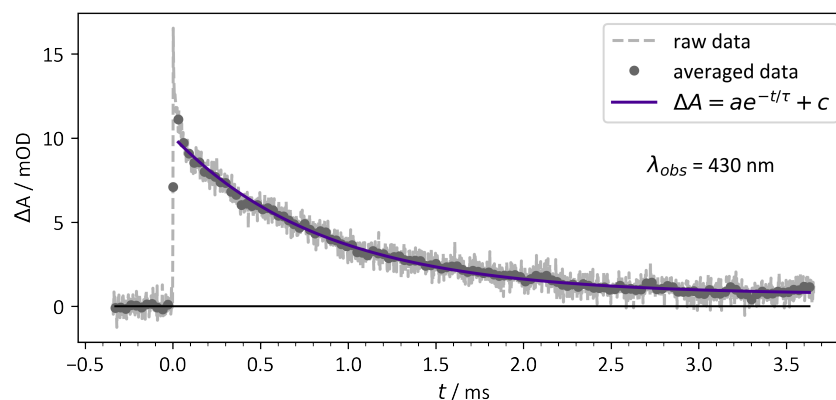


Figure 4.7: **1-CNP-L-Asp** nitronate decay. Figure was reproduced from paper, measurement performed by Yannik Pfeifer. Published figure.[24]  
 $\tau = 0.87 \pm 0.04$  ms.

Then the absorbance values at this index were taken from each kinetic trace. Thus, a partial spectrum of the *aci*-nitro is shown in Figure 4.8,  $t = 30$  ns after excitation – the peak is at  $\lambda = 460$  nm, but only half of the spectrum was recorded.

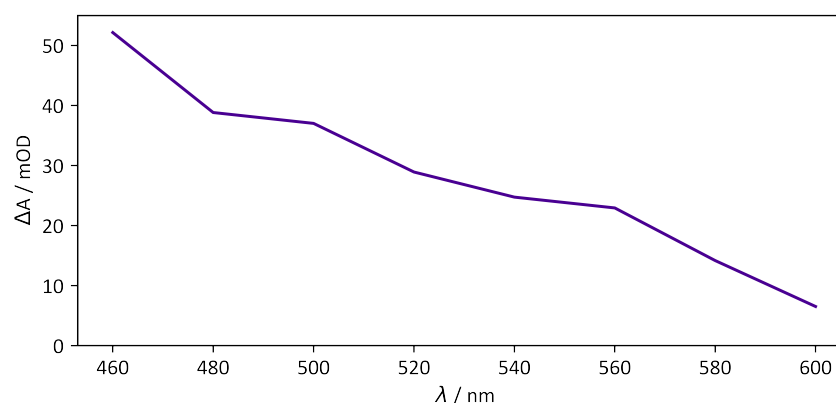


Figure 4.8: Partial spectrum of the proposed *aci*-nitro species generated by excitation of **1-CNP-L-Asp** (0.45 mM) in sodium phosphate buffer (50 mM, pH 7).  $t = 30$  ns after laser excitation.

A similar spectrum would be expected in the data collected for the excitation of **CNP-OAc** with a femtosecond laser pump and probe. In a femtosecond pump probe (or *fs-TAS*) experiment, the expected feature would appear after initial fast kinetics, and would appear constant until the end of the time range investigated (e.g. 1 – 2 ns).

4.3.1.3 *1-(4-Br-CNB)-L-Asp*

This compound behaved similarly to **1-CNB-L-Asp**. The published kinetic trace is reproduced in Figure 4.9.

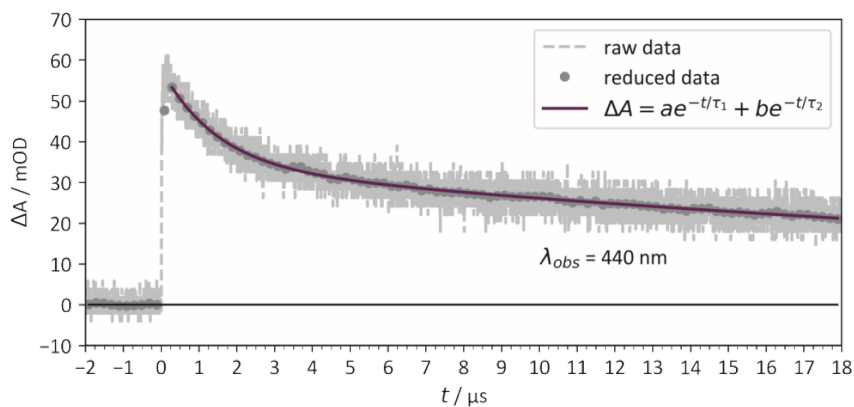


Figure 4.9: Decay of nitronate intermediates generated by a pulse of a Surelite™ SL I-10 Nd:YAG laser frequency tripled to 355 nm. Pump occurs at  $t = 0 \mu\text{s}$ . 10 000 data points over  $20 \mu\text{s}$  (oversampled), the data were then averaged (adjacent averaging, bin size = 50). A  $5 \text{ k}\Omega$  resistor was used. The photocaged aspartate (**1-(4-Br-CNB)-L-Asp**) was supplied as a  $0.5 \text{ mM}$  solution in sodium phosphate,  $50 \text{ mM}$ , pH 7. The decay constants obtained from non-linear least-squares fitting were  $\tau_1 = 1.48 \pm 0.08 \mu\text{s}$  ( $41 \pm 1\%$  of the signal) and  $\tau_2 = 38 \pm 1 \mu\text{s}$  ( $58.7 \pm 0.7\%$  of the signal). Average of three measurements.

## 4.3.2 Femtosecond transient absorption spectroscopy

**CNP-OAc** was investigated by fs-TAS. The sample was excited with a  $400 \text{ nm}$  pump pulse and probed with a continuum pulse at certain intervals  $\Delta t$  after excitation. Spectral data at certain time points are shown in Figure 4.10. The strongest feature is a short-lived transient absorbance at  $\lambda_{\text{max}} = 425 \text{ nm}$ . This decays to a steady-state positive  $\Delta A$ , consistent with a long-lived photoproduct (such as the *aci*-nitro). Furthermore, the peak of this long-lived species appears to slowly shift towards longer wavelengths – though this does not quite reach  $460 \text{ nm}$  within the time-frame of  $1 \text{ ns}$ , it may be that this shift would continue.

The species initially formed by photoinduced HAT from the  $S_1$  state would be the *Z-aci*-nitro tautomer. This can interconvert very rapidly with the *E-aci*-nitro form, but it is possible that fs-TAS is fast enough to capture that transition, from the *Z*- to the more stable *E*- form, prior to the ionisation observed to occur in the ns-LFP measurements. A similar shift of peak position was observed by Schmierer et al. in their fs-TAS experiments with 2-nitrotoluene, which they also assigned to

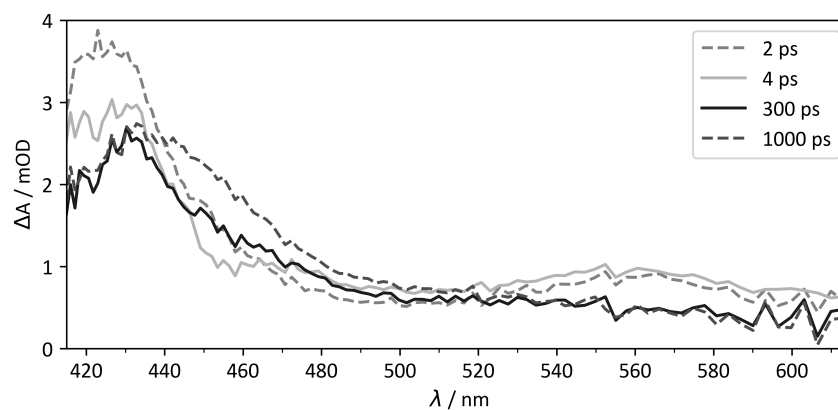


Figure 4.10: Spectral data extracted at different time points, from pump-probe measurements performed by Anke Puchert. **CNP-OAc** (10 mM) in sodium phosphate buffer (125 mM, pH 7). Times are uncorrected for drift due to slower moving long-wavelength light.

isomerisation from the *Z*- to the *E-aci*-nitro.[56] However, their shift was from 400 to 390 nm and occurred from 2 ns to 1 ms. THF was used as the solvent in their experiment; it follows that in an aqueous environment (or any protic solvent) this may be much faster.

Figure 4.11 shows two transient absorption features observed at 415 and 590 nm in a fs-TAS experiment investigating the photochemistry of **CNP-OAc**. The CPM artefacts in each of the below traces were aligned to  $t_0$  by ad-hoc correction ( $-0.4$  ps for 423 nm and  $-0.9$  ps for 565 nm). With these corrections in place, it can be seen that the rise of the transient at 423 nm is delayed slightly and coincides with the decay of the 565 nm transient. This occurs with a time constant of 0.45 ps and is consistent with vibrational relaxation from the excited state initially generated at the Frank-Condon point.

A more rigorous analysis would involve correction of  $t_0$  of all traces by aligning the CPM artefacts. Also, here data to be fitted were cut from the maximum of the rise signal found after the CPM. A more complex fitting algorithm that accounts for the rising as well as decaying signal may give more concrete support to the hypothesis that the 565 nm species decays by populating the 423 nm species.

It may be proposed that excitation with 400 nm light populates a vibrationally excited  $S_1$  state, or  $S_1^{v=m}$ . This species undergoes rapid ( $\tau = 0.45$  ps) vibrational relaxation to the vibrational ground state of  $S_1$ . The decay of  $S_1$  ( $\tau = 1.2$  ps) then occurs via a combination of fluorescence and photochemically induced hydrogen atom transfer (HAT) to form the *Z-aci*-nitro species.

The ns-LFP data collected for **1-CNP-L-Asp** suggest that the *aci*-nitro intermediate absorbs at 460 nm. Once formed, this would appear as a constant positive offset in fs-TAS data, as the deprotonation of *aci*-nitro

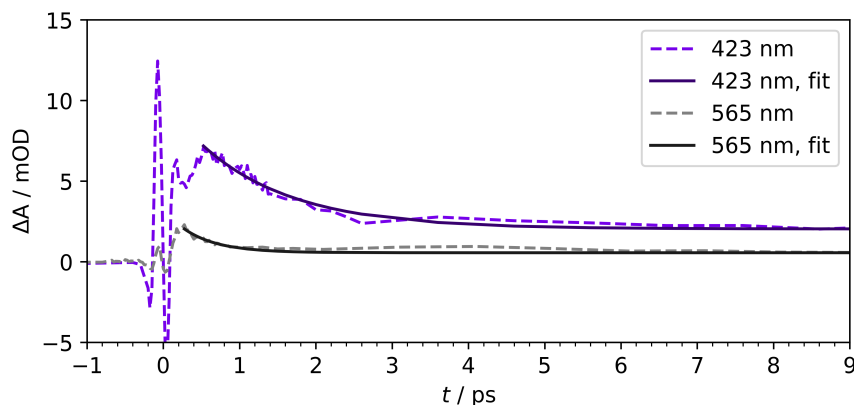


Figure 4.11: *fs-TAS* experimental data recorded by Anke Puchert. **CNP-OAc** (10 mM) in sodium phosphate buffer (pH 7, 125 mM) was excited with a 50 fs, 400 nm laser pulse. The data to be fitted were cut to the maximum signal after the *CPM*. The cropped data were fitted to the function  $\Delta A = ae^{-t/\tau} + c$ . The parameters obtained from fitting the 423 nm trace were  $a = 8.0 \pm 0.6$  mOD,  $\tau = 1.2 \pm 0.1$  ps and  $c = 2.0 \pm 0.1$  mOD. The fit parameters at 565 nm were  $a = 8 \pm 3$  mOD,  $\tau = 0.45 \pm 0.09$  ps and  $c = 0.56 \pm 0.06$  mOD.

transients is too slow to be observed within a nanosecond. Indeed, this was observed in Figure 4.10, along with a shift in  $\lambda_{\max}$  up to the longest observed  $\Delta t$  (1 ns). A kinetic trace at 460 nm was fitted as a model for the population of *E-aci-nitro* species from the initially formed *Z-aci-nitro*. However, the obtained fit was essentially a straight line, with an incredibly large error in the value for  $\tau$ . The “fit” is shown in Figure 4.12. This result makes sense if the time constant is significantly larger than 1 ns. The maximum value for  $\Delta A$  was reached 30 ns after excitation in the *ns-LFP* experiments for **1-CNP-L-Asp**, with a  $1/e$  rise time of approximately 20 ns. This is close to the resolution of the *ns-LFP* experiment, but a kinetic component of this order is consistent with the observed 0 order growth kinetics at 460 nm in the *fs-TAS* measurement. In fact, the fitting algorithm returned  $\tau = 3$  ns, albeit with an uncertainty of 467%.

The *fs-TAS* experiment was too fast, and the *ns-LFP* experiment too slow. Just like Goldilocks and the three bears, an experiment “in the middle” would have been just right.

#### 4.3.3 Density functional theory calculations

*DFT* was used to compute the relative energies of ground-state intermediates and transition states in the photocleavage reaction of  $\alpha$ -carboxy-2-nitrobenzyl photocages. In order to simplify the problem,  $\alpha$ -carboxy-2-nitrobenzyl acetate (**CNB-OAc**) and  $\alpha$ -carboxy-6-nitropiperonyl acetate (**CNP-OAc**) were used as model systems

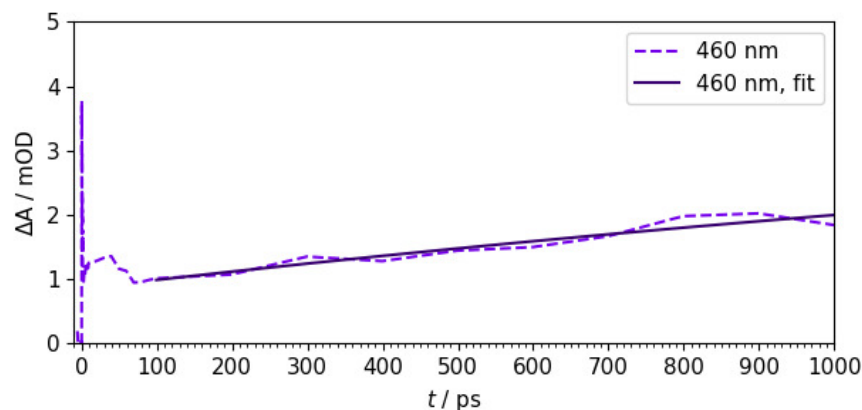


Figure 4.12: Kinetic trace at 460 nm, from pump-probe measurements performed by Anke Puchert. **CNP-OAc** (10 mM) in sodium phosphate buffer (125 mM, pH 7). The data to be fitted were cut to start from 100 ps.

(Figure 4.13). Treating caged aspartates computationally is not only more expensive due to the number of atoms (DFT scales as approximately  $O(n^3)$ ) but also due to increased complexity in terms of conformational space, possible tautomers, and protonation states. This is, admittedly, a limitation of this work. However, the approximation of the caged aspartate with acetate is a reasonable one, as both have carboxylate leaving groups. Also, the more complex features of the aspartate leaving group will, most likely, be little involved in the mechanism of cleavage. At most, energy barriers may be shifted somewhat up or down, or certain functional groups may participate as general acid ( $-\text{NH}_3^+ / -\text{CO}_2\text{H}$ ) or base ( $-\text{NH}_2 / -\text{CO}_2^-$ ) catalysts. Key trends are expected to be generalisable to some extent.

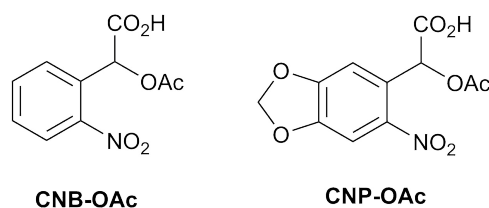


Figure 4.13: **CNB-** and **CNP-**caged acetate (**CNB-OAc** and **CNP-OAc**, respectively); model systems for **1-CNB-** and **1-CNP-L-Asp**.

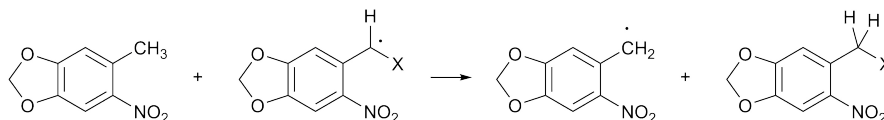
A note on nomenclature: especially where *aci*-nitro intermediates are concerned, there are four geometric isomers. Where both are specified (e.g. *EE-aci*-nitro), the second *E/Z* specifies the geometry of the nitronic acid, while the first specifies the C=C double bond geometry. Where only one is specified, this typically refers to the nitronic acid geometry, and implies that both *E-* and *Z-* isomers are possible at the C=C double bond.

One of the key findings of the computational studies is that thermal reverse **HAT** has a rather low activation barrier, both for **CNB-** and **CNP-OAc** ( $< 10 \text{ kJ mol}^{-1}$  from the *EZ-aci*-nitro intermediates). In fact, this appears to be more favourable than the cyclisation pathways leading to benzisoxazolol intermediates. This is somewhat unsurprising, given the low effective quantum yields determined for photocleavage of **1-CNB-**, **1-CNP-** and **1-(4-Br-CNB)-L-Asp** ( $Q_{\text{eff}} = 0.10, 0.05, \text{ and } 0.14$ , respectively).[24] The photochemical yield of the initial *aci*-nitro formation may be significantly higher than this.

It should also be noted, however, that the barrier to reverse **HAT** is higher from the *ZZ-aci*-nitro intermediates (close to  $50 \text{ kJ mol}^{-1}$  for both **CNB-** and **CNP-OAc**). Therefore, the ratio of C=C double bond isomers formed in the photochemical step will also have a significant impact on the overall effective quantum yield of photocleavage. Determining this ratio computationally is outside the scope of this thesis, but would be possible using molecular dynamics, for example with **TDDFT**; a similar question was modelled in this way by Dsouza and co-workers in an investigation of spironaphthopyran photochromism.[77] However, as mentioned previously, deficiencies in **TDDFT** limit the accuracy of this method. Wave-function methods would be more appropriate, albeit very computationally expensive.

There is an important limitation to note in the computed barriers to thermal reverse **HAT** presented here. All species have been treated with closed-shell **DFT** methods.

Conversely, in an investigation on the effect of the leaving group on quantum yield of nitrobenzyl decaging, Šolomek et al. computed radical stabilisation energies (**RSEs**) using unrestricted **B3LYP** (**UB3LYP**) using an isodesmic reaction model (depicted in **Scheme 4.8**).[78] They found that substituents that stabilise benzyl radicals also stabilise the *aci*-nitro species and increase the barrier to reverse **HAT** to the starting nitrobenzyl. Note, this treatment also does not compute the actual barrier to thermal reverse **HAT**. Nevertheless, it highlights a crucial limitation of restricted **DFT** in modelling certain types of reactions where radical intermediates or biradical transition states may be involved.



**Scheme 4.8:** The isodesmic reaction scheme used by Šolomek et al. to compute **RSEs** of various nitrobenzyls. The value for **RSE** is the energy difference between the left and right hand sides of the equation. X = leaving group.

In the case of **CNB-OAc**, the *EE-aci*-nitro is  $12 \text{ kJ mol}^{-1}$  lower in energy than the *EZ-aci* tautomer, whereas the *ZE-aci*-nitro is  $8 \text{ kJ mol}^{-1}$

lower in energy. This is consistent with the findings of Il'ichev et al., and the experiments reported by Schmierer and co-workers.[54, 56] The results for **CNP-OAc** also show this trend. It is also known that the *E-aci*-nitro species are formed from the *Z-aci*-nitro species after photochemical HAT. However, this proton transfer step was not modelled computationally, as this would require explicit treatment of solvent (water) molecules.

The computational results also support the assumption that the *aci*-nitro functional group is more acidic than the carboxyl, thus that nitronate-carboxyl tautomers are important for reactivity. The stabilisation compared to *E-aci* tautomers bearing a carboxylate was typically about  $50 \text{ kJ mol}^{-1}$ . However, similarly to the computational results of Il'ichev et al.,[54] the lowest barrier heights to cyclisation were from *E-aci*-nitro tautomers – typically  $50 - 60 \text{ kJ mol}^{-1}$ , as opposed to  $110 - 140 \text{ kJ mol}^{-1}$  for cyclisation from nitronate-carboxyl tautomers. The key difference here, is that a proton transfer, rather than a protonation, may be the key event that enables the cyclisation. Structures depicting the cyclisation of the *EE-aci*-nitro derivative of **CNB-OAc** to form the *cis*-benzisoxazolol are shown in Figure 4.14.

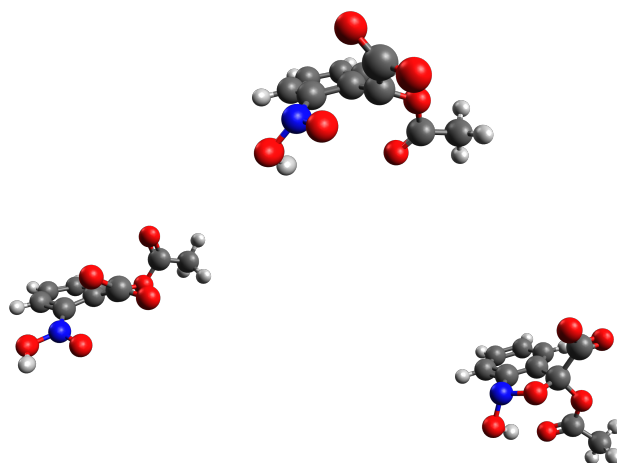


Figure 4.14: **CNB-OAc** (left) *EE-aci*-nitro; (middle) *EE-cyc*-TS; (right) *cis*-benzisoxazolol.

Once cyclisation has occurred, the benzisoxazolol intermediates are much lower in energy than the *aci*-nitro species (by ca.  $100 \text{ kJ mol}^{-1}$ ) or nitronate-carboxyl tautomers (by ca.  $50 \text{ kJ mol}^{-1}$ ). Also, the reverse activation barrier to revert to *aci*-nitro is typically ca.  $150 \text{ kJ mol}^{-1}$  or more.

Attempts to model the remainder of the reaction from the benzisoxazolol intermediates were also made, with limited success. Some converged benzisoxazolol structures were modified by removing a proton from the N-OH functionality and adding a proton to the carboxylate. Geometry optimisations using these modified structures

as an initial guess converged either on a nitroso-keto-acid and an ejected acetate (Figure 4.15; i.e. optimising the initial guess afforded the products as a ground state structure), or a tetrahedral tetrahedral oxyanion intermediate (a hemiacylal where the OH has been deprotonated), with a  $3 \text{ kJ mol}^{-1}$  barrier to further collapse to the final product (Figure 4.16; though the SVPD structures are shown here, the calculated barrier height used the TZVPD optimised optimised structures). Presumably, the hemiacylal would be a little more stable, but it is also unlikely to be a stable intermediate under these reaction conditions.

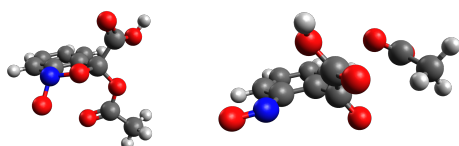


Figure 4.15: **CNB-OAc** (left) *cis*-benziate-carboxy tautomer guess structure; (right) nitroso-keto-acid with ejected acetate. The right-hand structure was the result of geometry optimisation of the left-hand structure at the PBEo/def2-SVPD level.

This is consistent with Il'ichev's findings showing that the collapse of the benzisoxazolol intermediates is base-catalysed. However, it would be necessary to locate a transition state for this process involving proton transfers with solvent molecules or some other base that may be present in solution. This kind of treatment is more difficult and has not been done here. Thus, the question of the rate determining step and the importance of the benzisoxazolol intermediates remains a challenge.

A summary of the barrier heights for various reactions is given in Table 4.1 and Table 4.2.

The barrier to elimination from the hemiacylal (deprotonated at OH) was only found for **CNB-OAc**, due to limited time. It is likely to be a similarly small barrier for the **CNP-OAc** derivative.

It was also hoped that these computations would shed some light on the differences in reaction kinetics observed in **CNB** vs. **CNP** cages. On the contrary, the overall picture shows the same trends in barrier heights and relative energies of various tautomers. Where there are differences, they are rather subtle, and may not be sufficient to explain

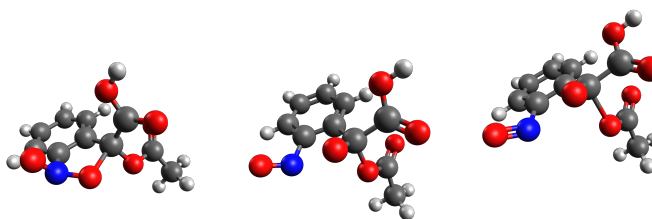


Figure 4.16: **CNB-OAc** (left) *trans*-benziate-carboxy tautomer guess structure; (middle) alkoxide bearing tetrahedral intermediate; (right) transition state for elimination of acetate from the tetrahedral intermediate. The middle structure was found by geometry optimisation of the left structure at the PBE0/def2-SVPD level. The middle structure was used as the starting point for the TS search that found the right structure, also at the PBE0/def2-SVPD level.

Table 4.1: Barrier heights computed for several reactions of **CNB-OAc**.

| STARTING STRUCTURE          | REACTION    | $E_a / \text{kJ mol}^{-1}$ |
|-----------------------------|-------------|----------------------------|
| <i>EZ-aci</i> -nitro        | reverse-HAT | 9.7                        |
| <i>ZZ-aci</i> -nitro        | reverse-HAT | 49.4                       |
| <i>EE-aci</i> -nitro        | cyclisation | 47.7                       |
| <i>ZE-aci</i> -nitro        | cyclisation | 64.6                       |
| <i>E</i> -nitronate-carboxy | cyclisation | 110.6                      |
| <i>Z</i> -nitronate-carboxy | cyclisation | 122.7                      |
| <i>trans</i> -hemiacylal    | elimination | 2.9                        |

Table 4.2: Barrier heights computed for several reactions of **CNP-OAc**.

| STARTING STRUCTURE          | REACTION    | $E_a / \text{kJ mol}^{-1}$ |
|-----------------------------|-------------|----------------------------|
| <i>EZ-aci</i> -nitro        | reverse-HAT | 7.8                        |
| <i>ZZ-aci</i> -nitro        | reverse-HAT | 47.0                       |
| <i>EE-aci</i> -nitro        | cyclisation | 46.6                       |
| <i>ZE-aci</i> -nitro        | cyclisation | 61.9                       |
| <i>E</i> -nitronate-carboxy | cyclisation | 134.7                      |
| <i>Z</i> -nitronate-carboxy | cyclisation | 128.6                      |

the observed differences in nitronate decay rate. The summaries of reaction pathways and transition states are almost identical. They are depicted in [Figure 4.17](#) and [Figure 4.18](#) (overleaf). The results of the

energy calculations are shown in more detail in Table 4.3 and Table 4.4 (both overleaf).

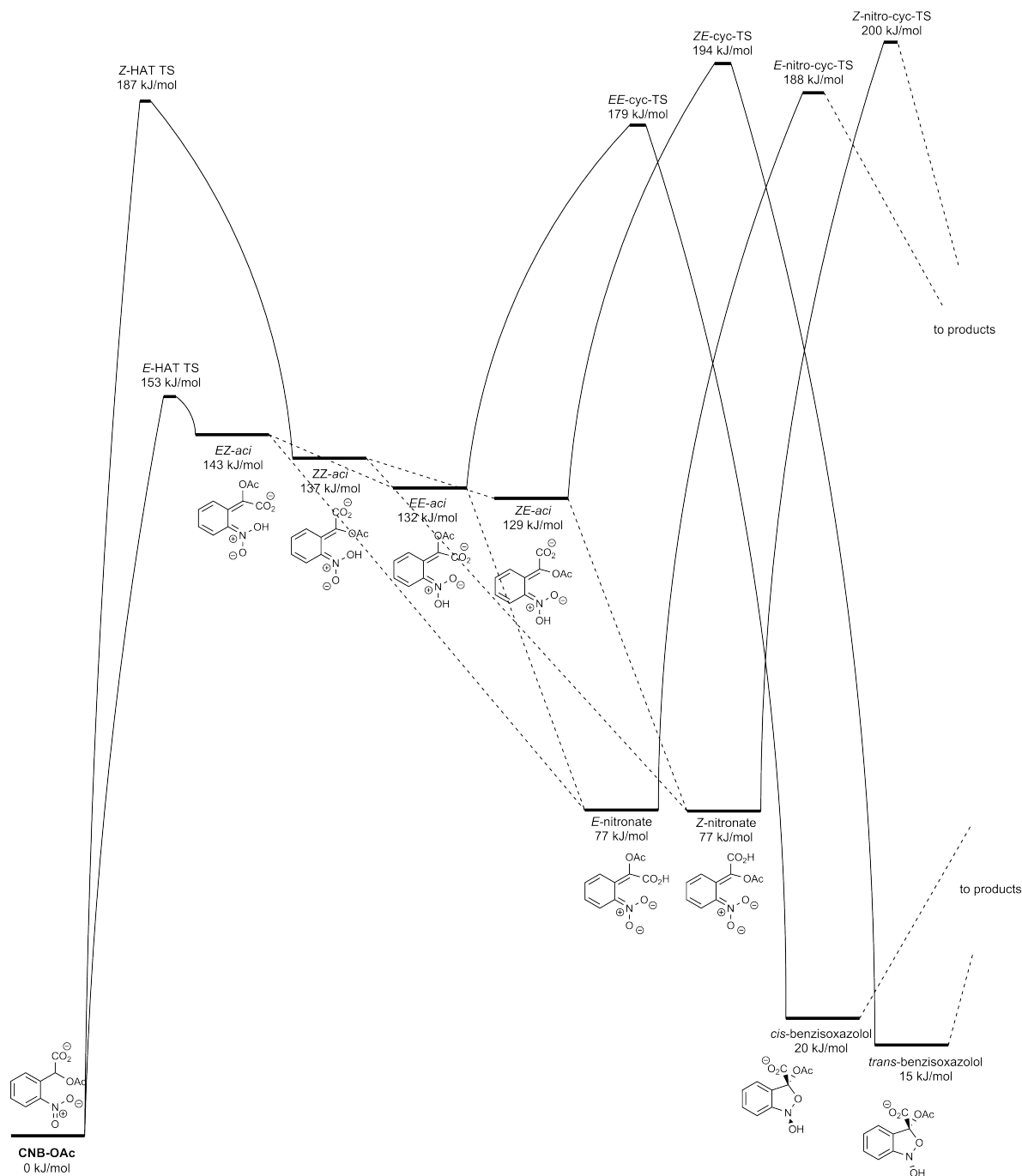


Figure 4.17: CNB-OAc – relative energies of intermediates and transition states.

Additionally, the experimental results seemed to suggest that the *aci*-nitro species generated by CNB photoexcitation is more acidic than that generated from a CNP cage. This is particularly counterintuitive, given that the cyclisation from the nitronate species is acid-catalysed,

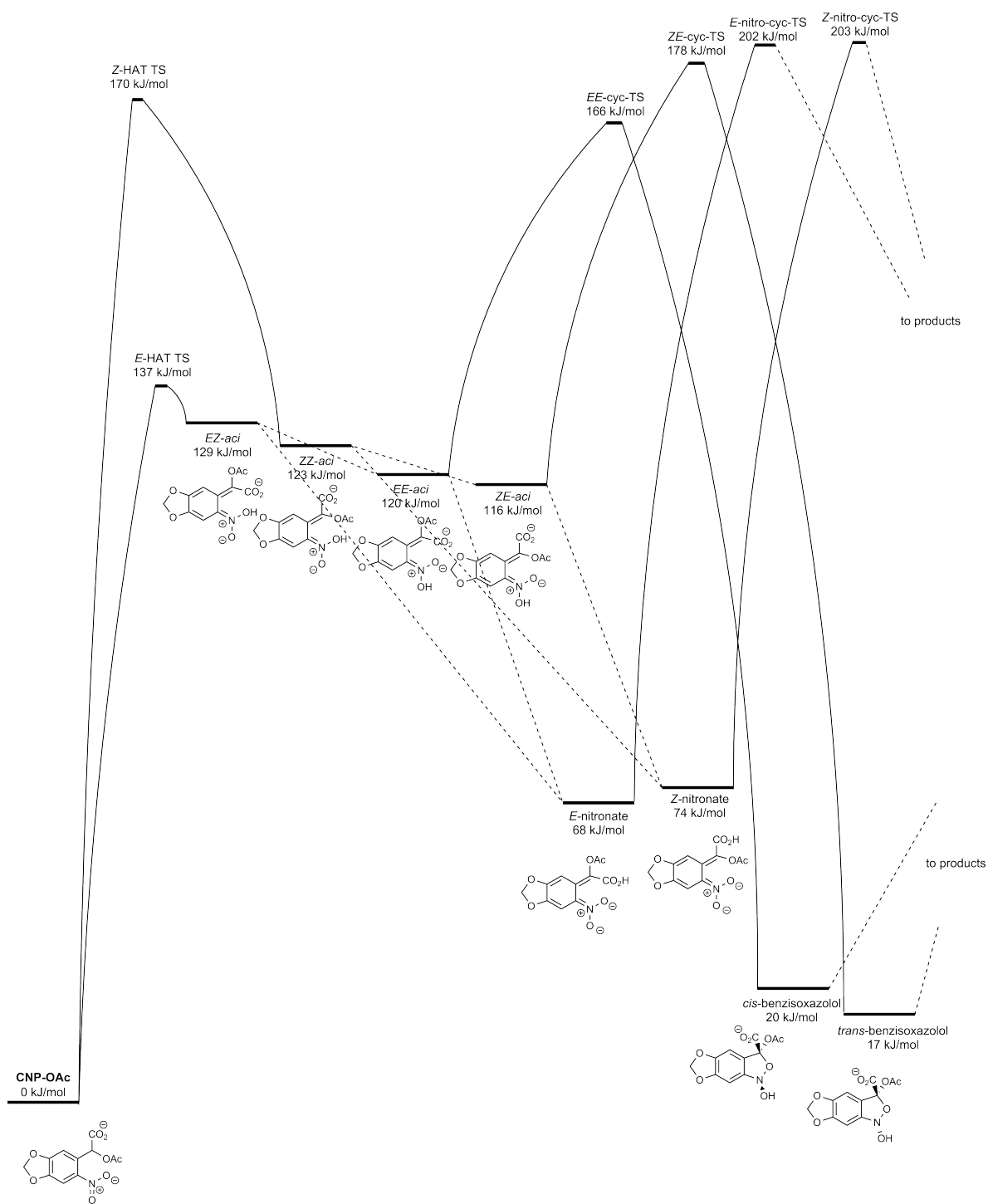


Figure 4.18: CNP-OAc – relative energies of intermediates and transition states.

therefore a less acidic *aci*-nitro should have a greater propensity to cyclise. Evidently, the results shown here are not the full picture.

Table 4.3: Energies of ground state structures and transition states found for the photoreaction of **CNB-OAc**.

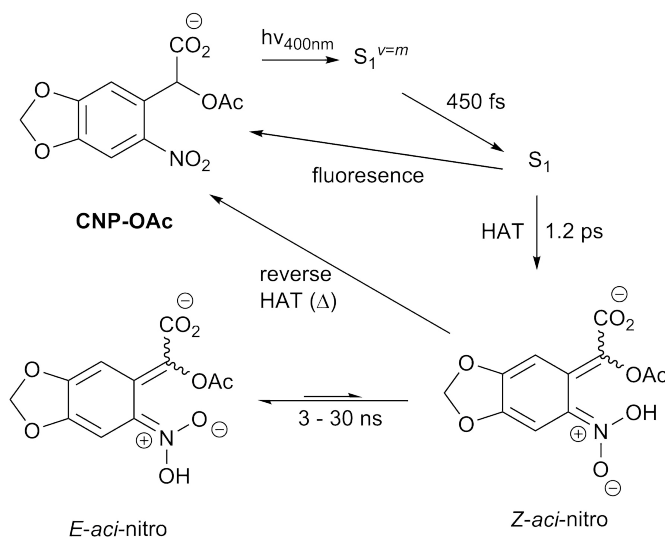
| STRUCTURE                         | $E/\text{Hartree}$ | $E/\text{kJ mol}^{-1}$ | ZPVE/ $\text{kJ mol}^{-1}$ | $E_{\text{tot}}/\text{kJ mol}^{-1}$ | $\Delta E/\text{kJ mol}^{-1}$ |
|-----------------------------------|--------------------|------------------------|----------------------------|-------------------------------------|-------------------------------|
| <b>CNP-OAc</b>                    | -891.470 47        | -2 340 555.7           | 445.5                      | -2 340 110.2                        | 0.0                           |
| <i>EE-aci-nitro</i>               | -891.418 57        | -2 340 419.5           | 440.9                      | -2 339 978.6                        | 131.7                         |
| <i>EZ-aci-nitro</i>               | -891.413 92        | -2 340 407.2           | 440.4                      | -2 339 966.8                        | 143.4                         |
| <i>ZE-aci-nitro</i>               | -891.419 67        | -2 340 422.3           | 441.5                      | -2 339 980.8                        | 129.4                         |
| <i>ZZ-aci-nitro</i>               | -891.416 44        | -2 340 413.9           | 441.2                      | -2 339 972.7                        | 137.6                         |
| <i>cis-benzisoxazolol</i>         | -891.462 26        | -2 340 534.2           | 444.3                      | -2 340 089.9                        | 20.4                          |
| <i>trans-benzisoxazolol</i>       | -891.463 98        | -2 340 538.7           | 444.2                      | -2 340 094.5                        | 15.8                          |
| <i>E-nitronate-carboxy</i>        | -891.439 72        | -2 340 475.0           | 442.3                      | -2 340 032.7                        | 77.5                          |
| <i>Z-nitronate-carboxy</i>        | -891.440 42        | -2 340 476.8           | 443.8                      | -2 340 033.0                        | 77.2                          |
| <i>E-HAT-TS</i>                   | -891.406 32        | -2 340 387.3           | 430.2                      | -2 339 957.1                        | 153.1                         |
| <i>Z-HAT-TS</i>                   | -891.393 85        | -2 340 354.5           | 431.3                      | -2 339 923.2                        | 187.0                         |
| <i>EE-cyc-TS</i>                  | -891.399 09        | -2 340 368.3           | 437.5                      | -2 339 930.8                        | 179.4                         |
| <i>ZE-cyc-TS</i>                  | -891.393 78        | -2 340 354.4           | 438.1                      | -2 339 916.3                        | 193.9                         |
| <i>E-nitronate-carboxy-cyc-TS</i> | -891.395 83        | -2 340 359.8           | 437.7                      | -2 339 922.1                        | 188.2                         |
| <i>Z-nitronate-carboxy-cyc-TS</i> | -891.391 35        | -2 340 348.0           | 437.7                      | -2 339 910.3                        | 199.9                         |
| <i>trans-hemiacylal-carboxy</i>   | -891.451 60        | -2 340 506.2           | 437.7                      | -2 340 068.5                        | 41.7                          |
| tetrahedral-TS                    | -891.449 50        | -2 340 500.7           | 435.1                      | -2 340 065.6                        | 44.7                          |

Table 4.4: Energies of ground state structures and transition states found for the photoreaction of **CNP-OAc**.

| STRUCTURE                         | $E/\text{Hartree}$ | $E/\text{kJ mol}^{-1}$ | ZPVE/ $\text{kJ mol}^{-1}$ | $E_{\text{tot}}/\text{kJ mol}^{-1}$ | $\Delta E/\text{kJ mol}^{-1}$ |
|-----------------------------------|--------------------|------------------------|----------------------------|-------------------------------------|-------------------------------|
| <b>CNP-OAc</b>                    | -1079.893 41       | -2 835 260.1           | 485.2                      | -2 834 774.9                        | 0.0                           |
| <i>EE-aci-nitro</i>               | -1079.846 48       | -2 835 136.9           | 481.6                      | -2 834 655.3                        | 119.6                         |
| <i>EZ-aci-nitro</i>               | -1079.842 49       | -2 835 126.5           | 480.9                      | -2 834 645.6                        | 129.4                         |
| <i>ZE-aci-nitro</i>               | -1079.848 16       | -2 835 141.3           | 482.3                      | -2 834 659.0                        | 115.9                         |
| <i>ZZ-aci-nitro</i>               | -1079.845 41       | -2 835 134.1           | 481.9                      | -2 834 652.2                        | 122.7                         |
| <i>cis-benzisoxazolol</i>         | -1079.885 36       | -2 835 239.0           | 484.1                      | -2 834 754.9                        | 20.0                          |
| <i>trans-benzisoxazolol</i>       | -1079.886 67       | -2 835 242.4           | 484.2                      | -2 834 758.2                        | 16.7                          |
| <i>E-nitronate-carboxy</i>        | -1079.866 14       | -2 835 188.6           | 481.2                      | -2 834 707.4                        | 67.6                          |
| <i>Z-nitronate-carboxy</i>        | -1079.864 09       | -2 835 183.2           | 482.4                      | -2 834 700.8                        | 74.2                          |
| <i>E-HAT-TS</i>                   | -1079.835 56       | -2 835 108.3           | 470.5                      | -2 834 637.8                        | 137.2                         |
| <i>Z-HAT-TS</i>                   | -1079.823 54       | -2 835 076.7           | 471.5                      | -2 834 605.2                        | 169.7                         |
| <i>EE-cyc-TS</i>                  | -1079.827 33       | -2 835 086.7           | 477.9                      | -2 834 608.8                        | 166.2                         |
| <i>ZE-cyc-TS</i>                  | -1079.823 22       | -2 835 075.9           | 478.7                      | -2 834 597.2                        | 177.8                         |
| <i>E-nitronate-carboxy-cyc-TS</i> | -1079.813 38       | -2 835 050.0           | 477.4                      | -2 834 572.6                        | 202.3                         |
| <i>Z-nitronate-carboxy-cyc-TS</i> | -1079.813 08       | -2 835 049.2           | 477.1                      | -2 834 572.1                        | 202.8                         |
| nitroso-carboxyl/acetate          | -1079.891 03       | -2 835 253.9           | 475.0                      | -2 834 778.9                        | -4.0                          |
| <i>trans-hemiacylal-carboxy</i>   | -1079.873 82       | -2 835 208.7           | 476.3                      | -2 834 732.4                        | 42.5                          |

## 4.4 CONCLUSIONS

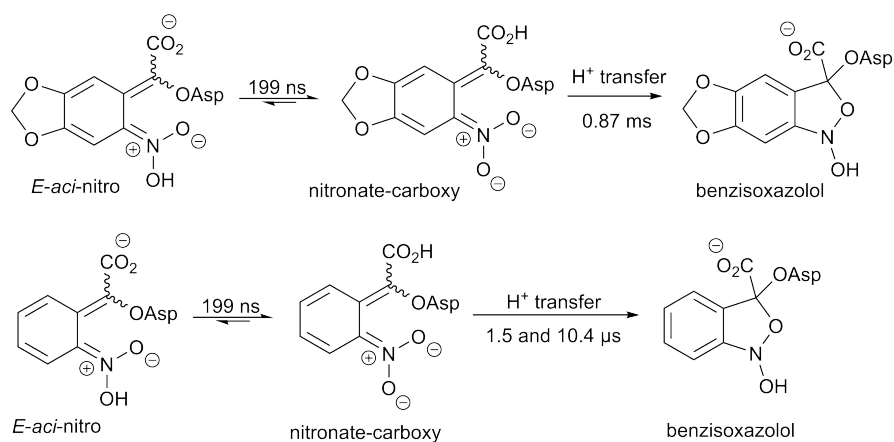
The photoreactions of **CNB** and **CNP** photocaged acetates and aspartates were investigated using *ns-LFP* and *fs-TAS*. The experimental data were compared to existing work in the literature and computed ground state energies and transition states using DFT. With this information, a kinetic model for the photoreactions of **CNB** cages is proposed. The kinetic model for **CNP-OAc** is shown in [Scheme 4.9](#), showing the steps up to and including the *E-aci-nitro*, the rate of formation of which is still uncertain, but is likely to be in the range  $(3 - 33) \times 10^7 \text{ s}^{-1}$ .



Scheme 4.9: Kinetic model for the photophysical and photochemical events associate with the excitation of **CNP-OAc**, investigated by *fs-TAS*. Note that the lifetime of  $S_1$  is  $1/(k_f + k_{\text{HAT}})$  – assuming there are no other important processes occurring from  $S_1$  that we have neglected (e.g. ISC to  $T_1$ ).

The slower steps, investigated by *ns-LFP* with **CNB** and **CNP** caged aspartates, are shown in [Scheme 4.10](#). These are only the steps up to the benisoxazolol intermediate. The collapse of this may be faster than its formation. However, there is still insufficient evidence to say this with certainty. Furthermore, these processes are highly pH-dependent, and benisoxazolol species may be more significant at acidic pH.

Vexingly, no satisfactory explanation has been found for the fact that the nitronate species generated by photoexcitation of **1-CNP-L-Asp** is so long-lived compared to those generated by the **CNB**- or **4-Br-CNB**-derivatives.



Scheme 4.10: Slower steps investigated in the photocleavage of **CNB-** and **CNP-** caged L-aspartate. The rate of benzisoxazolol collapse is uncertain. However, there is evidence to suggest that the release of L-aspartate coincides with the bimodal decay of the nitronate in the case of **1-CNB-L-Asp**.

#### 4.5 FUTURE WORK

Further *fs-TAS* experiments may be carried out with these photocages (**CNB-**, **CNP-**, and **4-Br-CNB-OAc**), along with thorough global analysis of spectral data over time. This may also be done with the photocaged aspartates, though it is unlikely that the early (< 1 ns) events will be largely affected by the leaving group. The hydroxyacids (**CNB-**, **CNP-**, and **4-Br-CNB-OH**) may also be investigated in this way, to investigate whether or not the early events occur in the same way in the absence of a good leaving group. In this case, the leaving group would be water. A true leaving group-free example would be a derivative of 2-nitrobenzylacetic acid – the  $\alpha$ -carboxy analogue to the femtosecond spectroscopy experiments of Schmierer et al.[56]

The above would also benefit from theoretical treatment suitable for computing the *PES* and vibrational spectra of excited states. One possible method is *ADC(2)*. This could be used to find optimised geometries of excited states as well as possible crossing-points (conical intersections or avoided crossings) joining states. In this way, the likely pathway from initial excited state to photoproducts may be modelled.

Time-resolved vibrational spectroscopy (*TRVS*) would complement the *fs-TAS* and *ns-LFP* experiments that probe electronic transitions. It would be ideal to investigate both sub-nanosecond events with pump-probe, and the longer timescales covered by step-scan or rapid-scan instruments. This, along with computed vibrational spectra, would either support or refute the assignments of transients presented here.

Furthermore, *TRVS* could solve questions that have not been fully answered here; for example, whether or not the benzisoxazolol species is kinetically important under the conditions used. In addition, pH-rate profiles and buffer dilution plots with both *TRVS* and *ns-LFP* experiments would enable the true microscopic rate constants for the individual steps to be extracted from the data. This is what was done by Il'ichev et al. for **NB-OMe** and **MNP-ATP**. [54]

## CONCLUSIONS

---

5.1  $\alpha$ -CARBOXYNITROBENZYL PHOTOCAGES

CNB photocages were synthesised and investigated for their potential as reaction initiation tools for time-resolved X-ray crystallography (TRX). They were shown to have both advantages and disadvantages for use in this context.

The aqueous solubility and  $\mu$ s cleavage times of the photocages synthesised in this thesis (with the exception of the CNP derivative) are advantageous. In the case of the CNP cage, the longer-wavelength absorption is still useful for biological applications. 400 nm light was shown to be effective for CNP's excitation, while at 360 nm its extinction coefficient is 10-fold that of CNB. On the other hand, the quantum yield for release of CNP caged aspartate was only 0.05 (vs. 0.10 for CNB), and the lifetime of the key nitronate transient was almost 1 ms. Naturally, tradeoffs in properties must be weighed against the desired application – if high time-resolution is not required and excitation by visible light is desired or even necessary, CNP may find its use. However, low quantum yield is a major problem for TRX and none of the CNB photocages performed well in this regard.

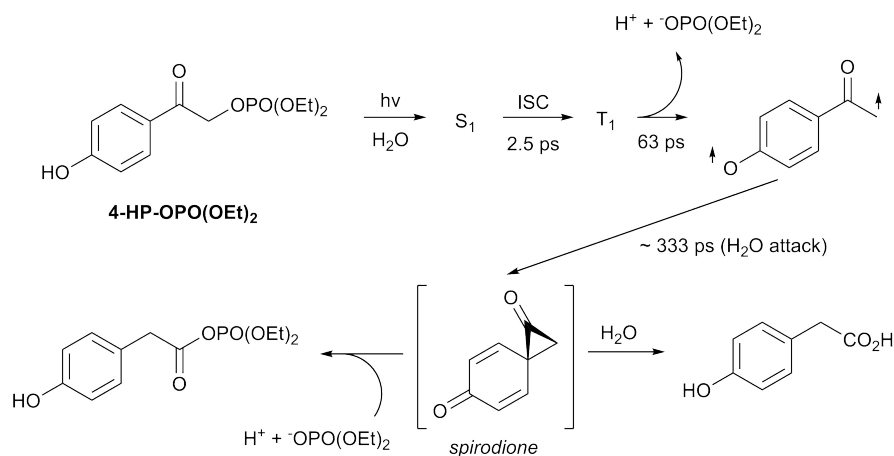
The hydrolytic instability of the CNB cages limits their applications somewhat, but is not necessarily a problem for TRX. Particularly for experiments involving microcrystal slurries suspended in buffer containing dissolved photocage, the time between preparation and measurement is sufficiently short (< 1 h) compared to the hydrolytic half-lives measured here for the CNB caged aspartates. It should also be noted, however, that these hydrolytic half-lives will be extremely dependent on the nature of the leaving group. Experiments requiring co-crystallisation of caged substrate and enzyme, or incorporation of a caged amino acid during protein expression, would require a leaving group that is not so readily hydrolysed.

CNB cages were also found to react during X-ray exposure, generating products detectable by UV-visible spectroscopy. This may occur via a number of mechanisms. One is the reduction of the photocage chromophore by solvated photoelectrons generated by radiolysis of the water in the aqueous buffer surrounding and pervading the crystal. A portion of the damage may also be caused by photoemission of core electrons within the photocage. Furthermore, XEOL may generate UV photons capable of triggering the photocleavage reaction itself. However, the sensitivity of photocages to X-ray exposure is likely a general problem, not restricted to the cages studied here. Usefully, as serial crystallography is fast becoming the method of choice for TRX, the low X-ray dose per crystal minimises the exposure of the photocage to X-ray radiation during data collection.

## 5.2 4-HYDROXYPHENACYL PHOTOCAGES

4-HP cages are a more promising class of cages for TRX, and future work should focus on this area. The phenolic group means they are usually soluble in water, though this does depend on the leaving group. However, the leaving group for a macromolecular TRX experiment is not likely to be something poorly water soluble. The biggest advantage of 4-HP cages is that very high quantum yields are achievable, although this is again highly dependent on the leaving group. Put simply, a good leaving group results in a high quantum yield. Quantum yields over 0.90 have been recorded for excellent leaving groups such as mesylate or tosylate.[21] Cleavage times are typically under 10 ns.[6] Quantum yields of 0.37 – 0.38 have been recorded for inorganic phosphate or ATP.[79]

Quantum yield and photolysis rate appear to correlate with leaving group ability. This is meant in the sense typically encountered in organic chemistry: a good leaving group is the conjugate base of a strong acid. In other words, quantum yield of release, as well as photolysis rate, will inversely correlate with the  $pK_a$  of the leaving group's conjugate acid. This is no surprise, given the mechanism of photocleavage for 4-HP cages proposed by Givens et al. and summarised in Scheme 5.1.[21]



Scheme 5.1: Kinetic model and mechanism of 4-HP cage photolysis, with diethyl phosphate as an example leaving group.

Water also plays an important role – the  $T_1$  lifetime of 4-HP-OPO(OEt)<sub>2</sub> decreased from  $\mu$ s in dry, degassed MeCN to 0.4 ns in 50 % aqueous MeCN, or 63 ps in water. This beneficial role of water is useful in biological TRX applications. The above model is also consistent with the observation that a good leaving group results in a good quantum yield. It suggests that the bond lysis from the  $T_1$  state is driven strongly by solvation of the leaving group, enabled by water.

The model shown in [Scheme 5.1](#) also shows a side reaction pathway that competes with the attack by water on the triplet biradical via the proposed spirodione intermediate. A poorer leaving group may spend longer in a solvent cage with the triplet biradical, thus increasing the probability of recombination to form a rearrangement product. Thus, the effective quantum yield of release would be reduced.

This strong dependence on leaving group will limit the systems where [4-HP](#) cages can be usefully applied. However, the importance of quantum yield makes their use highly desirable, if the functionality to be caged is a good leaving group.

A potential drawback that should be noted is the presence of the ketone group, necessary for [4-HP](#)'s photoreactivity. This may undergo unwanted reactions with certain functional groups present in biomolecules, e.g. imine formation, which may interfere with the desired experiment. [4-HP](#) cages are also liable to have a degree of hydrolytic instability, which would also depend heavily on the leaving group. Carboxylate or phosphate type leaving groups caged as the respective esters or phosphoesters, would be susceptible to hydrolysis by typical mechanisms (e.g.  $S_NAc$ , or the  $P=O$  analogue thereof). However, an additional  $S_N2$  pathway is made more favourable by hyperconjugation of the carbonyl  $\pi^*$  with the leaving group  $\sigma^*$ . Finally, the typical  $\lambda_{max}$  for [4-HP](#) cages is 280 nm. Excitation at 280 nm is problematic for biological samples. However, excitation with longer wavelengths has been shown to be possible, e.g. 343 nm.[\[16\]](#)

### 5.3 SUMMARY

Although the  $\alpha$ -carboxy substitution has resulted in interesting and beneficial changes in some properties with respect to more typical nitrobenzyl photocages, their low quantum yields will be an important limiting factor in their potential for use as TRX triggers.

4-HP photocages may represent the best class currently available for use in TRX experiments, due to their high quantum yields and extremely rapid (100 ps – 10 ns) cleavage times. Any work attempting to apply them to TRX or investigation into their analogues and their properties would be highly worthwhile.



## SYNTHETIC PROCEDURES

---

Many of the procedures presented here are taken directly from our published work on this topic, with some minor modifications.<sup>[24]</sup> In such cases the citation is included in the subsection heading.

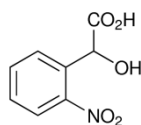
## 6.1 GENERAL METHODS[24]

Chemicals (reagent grade) were purchased from Sigma-Aldrich or TCI Europe, solvents (reagent or HPLC grade) were purchased from Thermo-Fisher, and all were used as received unless otherwise stated. Trifluoroacetic acid (reagent grade) was purchased from Thermo-Fisher and fractionally distilled immediately prior to use. Anhydrous acetonitrile (SureSeal™, with 3 Å molecular sieves) was purchased from Sigma-Aldrich and used as received. Where specified as 'anhydrous', dichloromethane was dried over 4 Å molecular sieves (10% w/v) for at least 48 h before use.[80] All reactions and purification procedures were conducted under red light, unless otherwise stated.

<sup>1</sup>H and <sup>13</sup>C NMR spectra were recorded on a Bruker AVANCE I/II/III 400, DRX 500 or AVANCE III HD 600 MHz instrument (<sup>1</sup>H frequencies). Chemical shifts (<sup>1</sup>H and <sup>13</sup>C respectively) are reported in ppm and were referenced to the residual solvent peaks at 7.26 and 77.16 ppm for CDCl<sub>3</sub>, 2.50 and 39.52 ppm for DMSO-*d*<sub>6</sub>, or 2.05 and 29.84 ppm for acetone-*d*<sub>6</sub>. [31] Coupling constants are given to the nearest 0.1 Hz and multiplicities are reported as: s (singlet), d (doublet), t (triplet), m (multiplet), app stands for apparent and br for broad. Where chemical shift assignments (numbered as in the name of each compound) were given these were determined by a combination of <sup>1</sup>H-<sup>1</sup>H correlation spectroscopy (COSY), <sup>1</sup>H-<sup>13</sup>C heteronuclear single quantum coherence spectroscopy (HSQC), and <sup>1</sup>H-<sup>13</sup>C heteronuclear multiple-bond coherence spectroscopy (HMBC) NMR experiments. UV/visible (Vis) measurements were performed with a Cary 50 Bio UV-Visible spectrophotometer and are reported with λ in units of nm and ε in units of M<sup>-1</sup> cm<sup>-1</sup>. HRMS experiments were carried out with an Agilent 6224 electrospray ionisation (ESI)-time of flight (ToF) spectrometer coupled to an Agilent HPLC 1200 series. Mass spectrometry (MS) measurements were performed using a Bruker UltrafleXtreme matrix-assisted laser desorption/ionisation (MALDI) ToF-ToF device equipped with a Smartbeam II laser (matrix: 2,5-dihydroxybenzoic acid) or an ESI-ToF LCT Premier (Waters/Micromass; used for the ionic compounds **1-CNB-L-Asp**, **1-CNP-L-Asp**, and **1-(4-Br-CNB)-L-Asp** as their ammonium trifluoroacetate forms, which were dissolved in water for sample delivery). Calculated is abbreviated as calcd. MALDI MS or ESI-ToF MS were used for some compounds where the accurate mass could not be detected by HRMS (ESI-ToF). Elemental analyses (Elem. Anal.) were performed with a EuroEA Elemental Analyser equipped with a HEKAtech HT Oxygen Analyser; bromine was determined using ion chromatography following digestion with a START-1500 T-280 microwave pressure digestion apparatus. Melting points were recorded on an LLG Labware MPM-H2 apparatus and are uncorrected. Thin-layer chromatography was performed with ALUGRAM® plates (silica gel 60 with fluorescent indicator UV254)

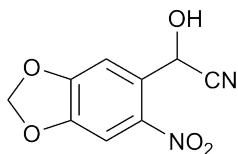
from Machery-Nagel and visualised using UV<sub>254</sub> illumination. Flash chromatography was carried out using ACROS Organics silica gel pore size 60 Å, particle size 0.030 – 0.200 mm.

## 6.2 2-NITROMANDELIC ACID (CNB-OH)

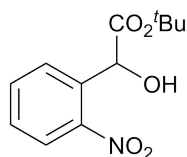


Potassium cyanide (3.00 g, 46.1 mmol) and water (2 ml) were added to a solution of 2-nitrobenzaldehyde (**2-NBA**, 4.00 g, 26.5 mmol) in AcOH (30 ml). The reaction vessel was closed and the mixture stirred for 17 h at r.t. Then, conc. HCl (50 ml) was added and the mixture was stirred for a further 24 h at r.t. Next, the reaction vessel was heated in an open flask for 1.5 h at 80 – 110 °C, boiling off the most volatile acids (including toxic HCN). The remaining solvents were removed *in vacuo* and the solid residue was extracted with EtOAc (10x 10 ml). The combined extracts were then washed with water (10 ml), dried (MgSO<sub>4</sub>), filtered, and concentrated *in vacuo* to afford the crude acid (4.79 g). The pure compound was obtained by recrystallisation (EtOAc/hexanes, 2:1); colourless crystals (3.32 g, 63%), mp 140.8 – 141.5 °C (EtOAc/hexane, lit.[25] 139 °C). <sup>1</sup>H NMR consistent with published spectra.[24, 25], UV (water) λ<sub>max</sub>, (ε): 265 (730).

## 6.3 6-NITROPIPERONAL CYANOHYDRIN (6-NPA-HCN)

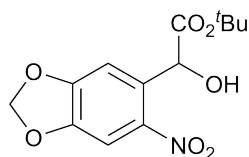


6-Nitropiperonal (**6-NPA**, 0.51 g, 2.61 mmol), followed by NaHSO<sub>3</sub>/Na<sub>2</sub>S<sub>2</sub>O<sub>5</sub> (0.31 g, 58.5% SO<sub>2</sub>, 2.83 mmol), were added to water (10 ml). The reaction mixture was stirred for 18 h at 80 °C under an inert atmosphere. Then, the mixture was cooled in an ice bath and KCN (0.20 g, 3.07 mmol) dissolved in water (1 ml) was added dropwise. The reaction mixture was then stirred at 0 °C for 5 h. The reaction mixture was warmed to r.t. and extracted with EtOAc (3x 10 ml). The combined extracts were washed with brine (5 ml); dried (MgSO<sub>4</sub>), filtered, and concentrated *in vacuo* to afford the crude product (0.50 g). Yield of **6-NPA-HCN** was 68% based on <sup>1</sup>H NMR integration (remainder was starting material – see [Figure 2.3](#)). <sup>1</sup>H NMR (400 MHz, CDCl<sub>3</sub>): δ 7.69 (1H, s, H<sub>5</sub>), 7.47 (1H, s, H<sub>2</sub>), 6.50 (1H, s, OH), 6.33 (2H, 2x d, *J* = 0.9 Hz, CH<sub>2</sub>), 6.27 (1H, s, CH), 0.28.

6.4 *tert*-BUTYL 2-NITROMANDELATE (***t*Bu CNB-OH**)

A solution of isobutene (8 wt. % in CH<sub>2</sub>Cl<sub>2</sub>, 12.5 ml, ca. 23 mmol) and conc. H<sub>2</sub>SO<sub>4</sub> (0.05 ml) were added to 2-nitromandelic acid (**CNB-OH**) (0.52 g, 2.6 mmol) at -60 °C in a liquid nitrogen/chloroform bath. The reaction mixture was stirred for 30 min before removing the bath and returned to r.t. within 0.5 h. The reaction mixture was stirred for a further 7 h. Then, the reaction mixture was diluted with diethyl ether (25 ml), quenched with sat. NaHCO<sub>3</sub> (10 ml), and stirred for a further 0.5 h. The biphasic mixture was then separated, and the organic phase washed again with sat. NaHCO<sub>3</sub> (10 ml), dried (MgSO<sub>4</sub>), filtered and concentrated *in vacuo* to afford a mixture of ***t*Bu CNB-OH** and ***t*Bu CNB-O*t*Bu** as a yellow oil (0.60 g). TLC analysis (20 % EtOAc-hexane), showed the products this time in approximately equal ratio. <sup>1</sup>H NMR (CDCl<sub>3</sub>) revealed a ratio of ca. 3:4 for ***t*Bu CNB-OH** to ***t*Bu CNB-O*t*Bu** (see [Figure 2.5](#)). ***t*Bu CNB-OH**, <sup>1</sup>H NMR (400 MHz, CDCl<sub>3</sub>): consistent with the published spectra.[24, 25] ***t*Bu CNB-O*t*Bu**, <sup>1</sup>H NMR (400 MHz, CDCl<sub>3</sub>): δ 7.98 – 7.95 (2H, m, Ar), 7.66 – 7.64 (1H, m, Ar), 7.45 – 7.41 (1H, m, Ar), 5.79 (1H, s, CH), 1.37 (9H, s, *t*Bu), 1.26 (9H, s, *t*Bu).

6.5 *tert*-BUTYL  $\alpha$ -CARBOXY-6-NITROPIPERONYL ALCOHOL  
(*t*Bu CNP-OH)

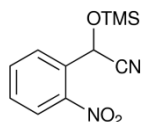


$\alpha$ -Carboxy-6-nitropiperonyl alcohol (**CNP-OH**, 0.25 g, 1.04 mmol) was suspended in dry toluene (1.5 ml) and treated with Widmer's reagent (0.99 ml, 4.1 mmol). The reaction mixture was heated at reflux for 0.5 h, then allowed to cool to r.t. EtOAc (5 ml) was added, and the organic solution was washed with water (2 ml), sat. NaHCO<sub>3</sub> (2x 2 ml), and brine (2 ml). Concentration of the organic solution afforded a residue (0.25 g), which was purified by flash chromatography (SiO<sub>2</sub> 27 g, 17.5% EtOAc-hexanes, *R<sub>f</sub>* 0.22) to give 0.15 g. Due to poor separation, this was purified again by flash chromatography (SiO<sub>2</sub> 15 g, gradient from 70% hexanes-CH<sub>2</sub>Cl<sub>2</sub> to CH<sub>2</sub>Cl<sub>2</sub>). Yield 0.10 g, 34%. <sup>1</sup>H NMR (400 MHz, CDCl<sub>3</sub>): consistent with the published spectrum.[24]

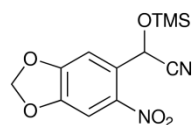
## 6.6 TMSCN ADDITION TO ALDEHYDES[24]

*General procedure*

Based on a literature procedure,[33] (substituted) 2-nitrobenzaldehyde (10 mmol) was dissolved in anhydrous acetonitrile (20 ml) under an inert atmosphere in oven-dried glassware. This was treated with trimethylsilyl cyanide (1.31 ml, 10.5 mmol) and stirred for 18 – 20 h at r.t. After this time, TLC analysis (20% EtOAc-hexanes) indicated complete consumption of the starting material. The solvents were removed under reduced pressure to afford the product which was used without purification in the next step.

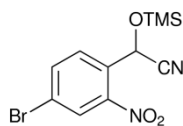
*2-Nitrobenzaldehyde cyanohydrin trimethylsilyl ether (2-NBA-TMSCN)*

2-Nitrobenzaldehyde (**2-NBA**, 10 mmol) was reacted for 20 h, and the title compound was obtained as an orange oil (2.45 g, quant.). <sup>1</sup>H NMR (500 MHz, CDCl<sub>3</sub>): δ 8.17 (1H, dd, *J* = 8.2, 1.0 Hz, H<sub>3</sub>), 8.02 (1H, app. d, *J* = 7.9 Hz, H<sub>6</sub>), 7.77 (1H, td, *J* = 7.7, 1.0 Hz, H<sub>5</sub>), 7.60 (1H, td, *J* = 7.8, 1.2 Hz, H<sub>4</sub>), 6.22 (1H, s, CH), 0.28 (9H, s, TMS). <sup>13</sup>C NMR (125 MHz, CDCl<sub>3</sub>): δ 146.5 (C<sub>2</sub>), 134.6 (C<sub>5</sub>), 132.2 (C<sub>1</sub>), 130.3 (C<sub>4</sub>), 128.6 (C<sub>6</sub>), 125.4 (C<sub>3</sub>), 118.0 (CN), 60.3 (CH), -0.4 (TMS).

*4,5-Methylenedioxy-2-nitrobenzaldehyde cyanohydrin trimethylsilyl ether (6-NPA-TMSCN)*

6-Nitropiperonal (**6-NPA**, 10 mmol) was reacted for 18 h, and the title compound was obtained as a yellow oil (2.96 g, quant.), which solidified on storage at 4 °C, mp 65.9 – 69.7 °C. <sup>1</sup>H NMR (400 MHz, CDCl<sub>3</sub>): δ 7.66 (1H, s, H<sub>3</sub>), 7.42 (1H, s, H<sub>6</sub>), 6.19 (2H, s, CH<sub>2</sub>), 6.15 (1H, s, CH), 0.28 (9H, s, TMS). <sup>13</sup>C NMR (100 MHz, CDCl<sub>3</sub>): δ 153.2 (C<sub>5</sub>), 148.7 (C<sub>4</sub>), 140.7 (C<sub>2</sub>), 130.0 (C<sub>1</sub>), 118.0 (CN), 107.4 (C<sub>6</sub>), 105.9 (C<sub>3</sub>), 103.7 (CH<sub>2</sub>), 60.2 (CH), -0.3 (TMS). HRMS (ESI-ToF) *m/z*: [M + Na]<sup>+</sup> calcd. for C<sub>12</sub>H<sub>14</sub>N<sub>2</sub>O<sub>5</sub>SiNa 317.0564; found 317.0513.

*4-Bromo-2-nitrobenzaldehyde cyanohydrin trimethylsilyl ether*  
(**4-Br-NBA-TMSCN**)

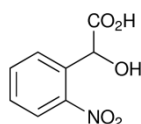


4-Bromo-2-nitrobenzaldehyde (**4-Br-NBA**, 10 mmol) was reacted for 18 h, and the title compound was obtained as a yellow oil (3.10 g, 94 %).  $^1\text{H}$  NMR (400 MHz,  $\text{CDCl}_3$ ):  $\delta$  8.32 – 8.30 (1H, m, H<sub>3</sub>), 7.91 – 7.88 (2H, m, H<sub>5</sub>/H<sub>6</sub>), 6.14 (1H, s, CH), 0.29 (9H, s, TMS).  $^{13}\text{C}$  NMR (125 MHz,  $\text{CDCl}_3$ ):  $\delta$  146.8 (C<sub>2</sub>), 137.5 (C<sub>5</sub>), 131.3 (C<sub>1</sub>), 130.2 (C<sub>6</sub>), 128.4 (C<sub>3</sub>), 123.9 (C<sub>4</sub>), 117.5 (CN), 60.0 (CH), –0.4 (TMS).

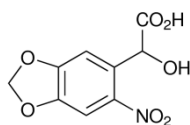
## 6.7 HYDROLYSIS OF TRIMETHYLSILYL CYANOHYDRINS[24]

*General Procedure*

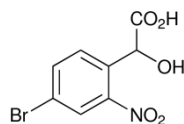
Based on a literature procedure,[25] (substituted) 2-nitrobenzaldehyde cyanohydrin trimethylsilyl ether (ca. 10 mmol) was cooled in an ice bath and suspended in conc. HCl (20 ml), then stirred for 1 h at 0 °C, 18 – 22 h at r.t., and 1 h at reflux (bath temp 100 h). Reaction progress was monitored by TLC. After cooling to r.t., the reaction mixture was diluted with a mixture of water (30 ml) and brine (30 ml), then extracted with EtOAc (3x 80 ml). The combined extracts were dried over MgSO<sub>4</sub>, filtered and concentrated *in vacuo* to afford the hydroxyacid, which was used without purification in the next step.

*2-Nitromandelic acid (CNB-OH)[25, 29]*

2-Nitrobenzaldehyde cyanohydrin trimethylsilyl ether (**2-NBA-TMSCN**, 2.45 g, 9.79 mmol) was treated according to the general procedure (the reaction mixture was stirred for 22 h at r.t. after the first stage). The title compound was obtained as a yellow solid (1.92 g, 97%). An analytical sample was obtained by flash chromatography (SiO<sub>2</sub>, CH<sub>2</sub>Cl<sub>2</sub>-MeOH-FA 97:2:1, *R<sub>f</sub>* 0.24); colourless crystals, mp 139.7 – 142.0 °C (AcOH/hexanes, lit.[25] 139 °C from EtOAc/hexanes). <sup>1</sup>H NMR (400 MHz, acetone-*d*<sub>6</sub>): δ 8.02 (1H, dd, *J* = 8.0, 1.2 Hz, H<sub>3</sub>), 7.91 (1H, dd, *J* = 7.6, 1.2 Hz, H<sub>6</sub>), 7.77 (td, *J* = 7.8, 1.2 Hz, H<sub>5</sub>), 7.61 (1H, td, *J* = 7.8, 1.6 Hz, H<sub>4</sub>), 5.92 (1H, s, CH), 5.72 – 5.00 (1H, br s, OH). <sup>13</sup>C NMR (100 MHz, acetone-*d*<sub>6</sub>): δ 172.6 (CO<sub>2</sub>H), 149.2 (C<sub>2</sub>), 135.3 (Ar), 134.1 (Ar), 130.0 (Ar), 129.9 (Ar), 125.4 (Ar), 70.2 (CH). MS (MALDI-ToF) *m/z*: [M + Na]<sup>+</sup> calcd. for C<sub>8</sub>H<sub>7</sub>NO<sub>5</sub>Na, 220.022; found, 220.190. Elem. Anal. calcd. for C<sub>8</sub>H<sub>7</sub>NO<sub>5</sub>: C, 48.74; H, 3.58; N, 7.10; O, 40.58; found: C, 48.83; H, 3.58; N, 7.03; O, 40.63.

*4,5-Methylenedioxy-2-nitromandelic acid (CNP-OH)*

6-Nitropiperonal cyanohydrin trimethylsilyl ether (**6-NPA-TMSCN**, 2.93 g, 9.95 mmol) was treated according to the general procedure (the reaction mixture was stirred for 20 h at r.t. after the first stage). The title compound was obtained as an ochre solid (2.23 g, 93%). An analytical sample was obtained by flash chromatography (SiO<sub>2</sub>, CH<sub>2</sub>Cl<sub>2</sub>-MeOH-FA 975:15:10, *R<sub>f</sub>* 0.28); yellow needles, 176.1 °C (dec., AcOH/hexanes). <sup>1</sup>H NMR (400 MHz, acetone-*d*<sub>6</sub>): δ 7.57 (1H, s, H<sub>3</sub>), 7.33 (1H, s, H<sub>6</sub>), 6.26 (1H, d, *J* = 0.9 Hz, CH<sub>2</sub>), 6.25 (1H, d, *J* = 0.9 Hz, CH<sub>2</sub>), 5.89 (1H, s, CH), 5.57 – 5.31 (1H, br s, CH-OH). <sup>13</sup>C NMR (150 MHz, acetone-*d*<sub>6</sub>): δ 172.3 (CO<sub>2</sub>H), 153.1 (C<sub>5</sub>), 148.5 (C<sub>4</sub>), 142.9 (C<sub>2</sub>), 133.0 (C<sub>1</sub>), 108.3 (C<sub>6</sub>), 105.9 (C<sub>3</sub>), 104.5 (CH<sub>2</sub>), 70.4 (CH). MS (MALDI-ToF) *m/z*: [M + Na]<sup>+</sup> calcd for C<sub>9</sub>H<sub>7</sub>NO<sub>7</sub>Na, 264.012; found, 264.160. Elem. Anal. calcd. for C<sub>9</sub>H<sub>7</sub>NO<sub>7</sub>: C, 44.83; H, 2.93; N, 5.81; O, 46.44; found: C, 44.95; H, 2.97; N, 5.74; O, 46.32.

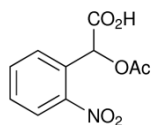
*4-Bromo-2-nitromandelic acid (4-Br-CNB-OH)*

4-Bromo-2-nitrobenzaldehyde cyanohydrin trimethylsilyl ether (**4-Br-NBA-TMSCN**, 3.10 g, 9.42 mmol) was treated according to the general procedure (the reaction mixture was stirred for 18 h at r.t. after the first stage). The title compound was obtained as a pale yellow solid (2.64 g, quant.). An analytical sample was obtained by flash chromatography (SiO<sub>2</sub>, CH<sub>2</sub>Cl<sub>2</sub>- MeOH-FA 975:15:10, *R<sub>f</sub>* 0.21); colourless crystals, mp 146.1 – 148.6 °C (AcOH/hexanes). <sup>1</sup>H NMR (400 MHz, acetone-*d*<sub>6</sub>): δ 8.19 (1H, d, *J* = 2.0 Hz, H<sub>3</sub>), 7.96 (1H, dd, *J* = 8.4, 2.0 Hz, H<sub>5</sub>), 7.87 (1H, d, *J* = 8.4 Hz, H<sub>6</sub>), 5.90 (1H, s, CH). <sup>13</sup>C NMR (100 MHz, acetone-*d*<sub>6</sub>): δ 172.1 (CO<sub>2</sub>H), 149.7 (C<sub>2</sub>), 137.0 (C<sub>5</sub>), 134.9 (C<sub>1</sub>), 131.7 (C<sub>6</sub>), 128.1 (C<sub>3</sub>), 122.1 (C<sub>4</sub>), 69.9 (CH). MS (MALDI-ToF) *m/z*: [M + Na]<sup>+</sup> calcd for C<sub>8</sub>H<sub>6</sub>BrNO<sub>6</sub>Na 297.933; found 298.075. Elem. Anal. calcd. for C<sub>8</sub>H<sub>6</sub>BrNO<sub>6</sub>: C, 34.81; H, 2.19; Br, 28.95; N, 5.07; O, 28.98; found: C, 34.46; H, 2.19; Br, 27.72; N, 4.84; O, 28.83.

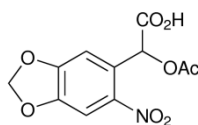
## 6.8 ACETYLATION OF HYDROXYACIDS[24]

*General procedure*

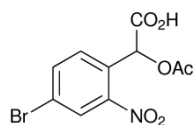
Based on a literature procedure,[32] (substituted) 2-nitromandelic acids (4 – 10 mmol) were suspended in neat Ac<sub>2</sub>O (1.8 ml/mmol) and stirred for 18 – 20 h at r.t., affording a clear solution. THF (1.5 ml/mmol) and water (1.5 ml/mmol) were added, producing a cloudy mixture which turned clear again while stirring for 2 h at 45 °C. The product mixture was cooled to r.t., toluene (3 ml/mmol) was added and the layers were separated. The aqueous phase was extracted again with 60 % EtOAc-toluene (2.5 ml/mmol) followed by EtOAc (2x 1 ml / mmol). The combined organic layers were washed with brine (1 ml/mmol), dried over MgSO<sub>4</sub>, filtered, and concentrated *in vacuo*. The residue was further concentrated azeotropically with toluene (3x 3 ml/mmol) and dried under high vacuum to afford the acetate. This procedure did not remove all traces of AcOH but provided sufficiently pure product to continue to the next step. An alternative workup is possible: extraction and washing steps can be skipped and the product mixture simply evaporated azeotropically with portions of toluene (e.g. 3x 3 ml/mmol).

*O-Ac-2-Nitromandelic acid (CNB-OAc)[32]*

2-Nitromandelic acid (**CNB-OH**, 1.91 g, 9.69 mmol) was treated according to the general procedure (the reaction time was 18 h) to afford the title compound as an oil (2.44 g, nominally 105%). <sup>1</sup>H NMR (400 MHz, acetone-*d*<sub>6</sub>): δ 8.53 – 8.15 (1H, br s, CO<sub>2</sub>H), 8.07 (1H, app d, *J* = 8.4, H<sub>3</sub>), 7.80 – 7.85 (1H, m, Ar), 7.70 – 7.64 (2H, m, Ar), 6.84 (1H, s, CH), 2.17 (3H, s, OAc). <sup>13</sup>C NMR (100 MHz, acetone-*d*<sub>6</sub>): δ 170.0 (C=O), 169.0 (CO<sub>2</sub>H), 149.3 (C<sub>2</sub>), 134.5 (Ar), 130.9 (Ar), 130.3 (C<sub>1</sub>), 130.2 (Ar), 125.7 (C<sub>3</sub>), 70.3 (CH), 20.4 (CH<sub>3</sub>). MS (MALDI-ToF) *m/z*: [M + Na]<sup>+</sup> calcd for C<sub>10</sub>H<sub>9</sub>NO<sub>6</sub>Na 262.033; found 262.187. Elem. Anal. calcd. for C<sub>10</sub>H<sub>9</sub>NO<sub>6</sub>: C, 50.22; H, 3.79; N, 5.86; O, 40.13; found: C, 51.01; H, 3.73; N, 4.42; O, 41.23.

*O*-Ac-4,5-Methylenedioxy-2-nitromandelic acid (**CNP-OAc**)

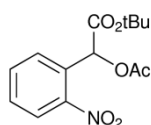
4,5-Methylenedioxy-2-nitromandelic acid (**CNP-OH**, 1.00 g, 4.15 mmol) was treated according to the general procedure, except the acetylation reaction was carried out for 4 h at 60 °C, then allowed to cool slightly before adding THF and water. Also, the second extraction failed to separate so the solvents were all combined before washing with brine. The title compound was obtained as a pale yellow solid (1.29 g, nominally 110 %), mp 144.3 – 145.5 °C. <sup>1</sup>H NMR (400 MHz, acetone-*d*<sub>6</sub>): δ 8.88 – 8.18 (1H, br s, CO<sub>2</sub>H), 7.59 (1H, s, H<sub>3</sub>), 7.13 (1H, s, H<sub>6</sub>), 6.82 (1H, s, CH), 6.27 (1H, s, CH<sub>2</sub>), 2.18 (3H, s, Ac). <sup>13</sup>C NMR (100 MHz, acetone-*d*<sub>6</sub>): δ 170.0 (COCH<sub>3</sub>), 168.9 (CO<sub>2</sub>H), 153.2 (C<sub>5</sub>), 149.3 (C<sub>4</sub>), 143.6 (C<sub>2</sub>), 127.2 (C<sub>1</sub>), 108.4 (C<sub>6</sub>), 106.2 (C<sub>3</sub>), 104.8 (CH<sub>2</sub>), 70.3 (CH), 20.5 (CH<sub>3</sub>). Elem. Anal. calcd. for C<sub>11</sub>H<sub>9</sub>NO<sub>8</sub>: C, 46.65; H, 3.20; N, 4.95; O, 45.20; found: C, 46.54; H, 3.19; N, 4.92; O, 44.33.

*O*-Ac-4-Bromo-2-nitromandelic acid (**4-Br-CNB-OAc**)

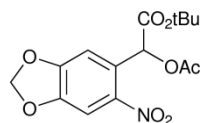
4-Bromo-2-nitromandelic acid (**4-Br-CNB-OH**, 2.64 g, 9.56 mmol) was treated according to the general procedure to afford title compound as a yellow oil (3.46 g, nominally 92 %). <sup>1</sup>H NMR (400 MHz, acetone-*d*<sub>6</sub>): δ 8.25 (1H, d, *J* = 2.0 Hz, H<sub>3</sub>), 7.98 (1H, dd, *J* = 8.4, 2.0 Hz, H<sub>5</sub>), 7.73 (1H, d, *J* = 8.4 Hz, H<sub>6</sub>), 6.80 (s, 1H, CH), 2.18 (3H, s, Ac), 1.96. <sup>13</sup>C NMR (100 MHz, acetone-*d*<sub>6</sub>): δ 169.8 (COCH<sub>3</sub>), 168.4 (CO<sub>2</sub>H), 149.8 (C<sub>2</sub>), 137.4 (C<sub>5</sub>), 132.0 (C<sub>6</sub>), 129.8 (C<sub>1</sub>), 128.6 (C<sub>3</sub>), 123.4 (C<sub>4</sub>), 69.9 (CH), 20.4 (CH<sub>3</sub>).

6.9 *tert*-BUTYL ESTER PROTECTION[24]*General procedure*

Based on a literature procedure,[32] (substituted) *O*-acetyl-2-nitromandelic acid (ca. 4 – 10 mmol) was dissolved in anhydrous benzene (1.8 ml/mmol) under an inert atmosphere, treated with TBTA (1.5 eq.), and stirred for 2 – 3 d at r.t. After this time, the product mixture was filtered, the filtrate concentrated *in vacuo*, and the crude product was purified by flash chromatography to give the *tert*-butyl ester.

*tert*-Butyl *O*-Ac-2-nitromandelate (***t*Bu CNB-OAc**)[32]

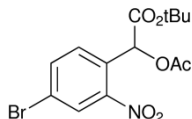
*O*-Ac-2-nitromandelic acid (**CNB-OAc**, 2.44 g, nominally 10.2 mmol) was reacted for 66 h according to the general procedure. Flash chromatography (150 g SiO<sub>2</sub>, 10 % EtOAc-hexanes, *R<sub>f</sub>* 0.19) afforded the title compound as a clear oil (2.19 g, 75 % over 4 steps). <sup>1</sup>H NMR (500 MHz, CDCl<sub>3</sub>): δ 7.98 (1H, app d, *J* = 8.1 Hz, H<sub>3</sub>), 7.63 (2H, app d, *J* = 4.0 Hz, H<sub>4</sub>/H<sub>5</sub>), 7.54 – 7.48 (1H, m, H<sub>6</sub>), 6.73 (1H, s, CH), 2.18 (3H, s, Ac), 1.37 (9H, s, *t*Bu). <sup>13</sup>C NMR (100 MHz, CDCl<sub>3</sub>): δ 169.5 (C=OCH<sub>3</sub>), 166.5 (C=O<sup>t</sup>Bu), 148.3 (C<sub>2</sub>), 133.5 (C<sub>4</sub>), 129.8 (C<sub>1</sub>), 129.7 (C<sub>6</sub>), 129.2 (C<sub>5</sub>), 125.1 (C<sub>3</sub>), 83.6 (C(CH<sub>3</sub>)<sub>3</sub>), 70.3 (CH), 27.8 (COC(CH<sub>3</sub>)<sub>3</sub>), 20.7 (COCH<sub>3</sub>). HRMS (ESI-ToF) *m/z*: [M + Na]<sup>+</sup> calcd. for C<sub>14</sub>H<sub>17</sub>NO<sub>6</sub>Na, 318.0948; found, 318.0905.

*tert*-Butyl *O*-Ac-4,5-methylenedioxy-2-nitromandelate (***t*Bu CNP-OAc**)

*O*-Ac-4,5-methylenedioxy-2-nitromandelic acid (**CNP-OAc**, 1.08 g, nominally 3.81 mmol) was reacted for 48 h according to the general procedure. Flash chromatography (100 g SiO<sub>2</sub>, 15 % EtOAc-hexanes, *R<sub>f</sub>* 0.22) afforded the title compound as a yellow oil (1.04 g, 83 % over 4 steps), which slowly crystallised, mp 72.2 – 74.2 °C. <sup>1</sup>H NMR (400 MHz, CDCl<sub>3</sub>): δ 7.53 (1H, s, H<sub>3</sub>), 7.02 (1H, s, H<sub>6</sub>), 6.73 (1H, s, CH), 6.14 (2H, s, CH<sub>2</sub>), 2.19 (3H, s, Ac), 1.41 (9H, s, *t*Bu). <sup>13</sup>C NMR (100 MHz, CDCl<sub>3</sub>): δ 169.5 (C=OCH<sub>3</sub>), 166.7 (C=O<sup>t</sup>Bu), 152.1 (C<sub>5</sub>), 148.2 (C<sub>4</sub>), 142.7 (C<sub>2</sub>), 126.8 (C<sub>1</sub>), 107.9 (C<sub>6</sub>), 106.1 (C<sub>3</sub>), 103.4 (CH<sub>2</sub>), 83.5

( $\underline{\text{C}}(\text{CH}_3)_3$ ), 70.6 (CH), 27.9 ( $\underline{\text{C}}(\text{CH}_3)_3$ ), 20.8 ( $\text{COCH}_3$ ). HRMS (ESI-ToF)  $m/z$ :  $[\text{M} + \text{Na}]^+$  calcd. for  $\text{C}_{15}\text{H}_{17}\text{NNaO}_8$ , 362.0852; found, 362.0884.

*tert*-Butyl *O*-Ac-4-bromo-2-nitromandelate (***t*Bu 4-Br-CNB-OAc**)

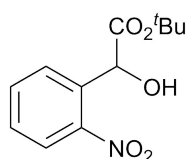


*O*-Ac-4-Bromo-2-nitromandelic acid (**4-Br-CNB-OAc**, 3.46 g, 9.25 mmol) was reacted for 44 h according to the general procedure, except the product mixture was not filtered before concentrating. Flash chromatography (150 g  $\text{SiO}_2$ , 6% EtOAc-hexanes,  $R_f$  0.26) afforded the title compound as a colourless oil (2.46 g, 71%, 66% over 4 steps).  $^1\text{H}$  NMR (500 MHz,  $\text{CDCl}_3$ ):  $\delta$  8.15 (1H, d,  $J = 2.0$  Hz, H<sub>3</sub>), 7.77 (1H, dd,  $J = 8.3, 1.9$  Hz, H<sub>5</sub>), 7.53 (1H, d,  $J = 8.4$  Hz, H<sub>6</sub>), 6.69 (1H, s, CH), 2.20 (3H, s, Ac), 1.40 (9H, s, *t*Bu).  $^{13}\text{C}$  NMR (125 MHz,  $\text{CDCl}_3$ ):  $\delta$  169.4 ( $\underline{\text{C}}\text{OCH}_3$ ), 166.1 ( $\underline{\text{C}}\text{O}_2^t\text{Bu}$ ), 148.7 (C<sub>2</sub>), 136.5 (C<sub>5</sub>), 130.6 (C<sub>6</sub>), 129.0 (C<sub>1</sub>), 128.2 (C<sub>3</sub>), 123.2 (C<sub>4</sub>), 84.0 ( $\underline{\text{C}}(\text{CH}_3)_3$ ), 70.0 (CH), 27.9 ( $\underline{\text{C}}(\text{CH}_3)_3$ ), 20.7 ( $\text{COCH}_3$ ). HRMS (ESI-ToF)  $m/z$ :  $[\text{M} + \text{Na}]^+$  calcd. for  $\text{C}_{14}\text{H}_{16}\text{BrNO}_6\text{Na}$ , 396.0053; found 396.0139.

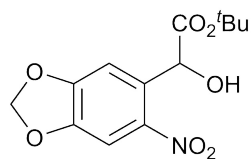
## 6.10 DEACETYLATION[24]

*General procedure*

$\text{Cs}_2\text{CO}_3$  (5 mol %) was added to a stirred solution of (substituted) *tert*-butyl *O*-acetyl-2-nitromandelate (0.20 M) in methanol. After stirring for 1 h at r.t., the reaction mixture was diluted to triple volume with EtOAc, filtered over a short silica plug, and concentrated *in vacuo* to afford the crude alcohol, which was used without purification in the next step.

*tert*-Butyl 2-nitromandelate (***t*Bu CNB-OH**)

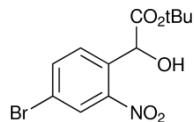
*tert*-Butyl *O*-Ac-2-nitromandelate (***t*Bu CNB-OAc**, 0.78 g, 2.64 mmol) was treated according to the general procedure to afford the title compound (0.67 g, quant.).  $^1\text{H}$  NMR (500 MHz,  $\text{CDCl}_3$ ):  $\delta$  7.91 (1H, dd,  $J = 8.1, 0.8$  Hz, H<sub>3</sub>), 7.67 (1H, app d,  $J = 7.6$  Hz, H<sub>6</sub>), 7.59 (1H, td,  $J = 7.6, 0.8$  Hz, H<sub>5</sub>), 7.44 (1H, td,  $J = 7.8, 1.2$  Hz, H<sub>4</sub>), 5.80 (1H, s, CH), 3.91 – 3.75 (1H, br s, OH), 1.34 (9H, s, *t*Bu).  $^{13}\text{C}$  NMR (125 MHz,  $\text{CDCl}_3$ ):  $\delta$  171.0 ( $\underline{\text{C}}\text{O}_2^t\text{Bu}$ ), 148.2 (C<sub>2</sub>), 133.6 (C<sub>1</sub>), 133.2 (C<sub>5</sub>), 129.1 (C<sub>6</sub>), 129.0 (C<sub>4</sub>), 125.0 (C<sub>3</sub>), 84.1 ( $\underline{\text{C}}(\text{CH}_3)_3$ ), 69.8 (CH), 27.7 ( $\text{C}(\underline{\text{C}}\text{H}_3)_3$ ). HRMS (ESI-ToF)  $m/z$ :  $[\text{M} + \text{Na}]^+$  calcd. for  $\text{C}_{12}\text{H}_{15}\text{NO}_5\text{Na}$ , 276.0848; found, 276.0808.

*tert*-Butyl 4,5-methylenedioxy-2-nitromandelate (***t*Bu CNP-OH**)

*tert*-Butyl *O*-Ac-4,5-methylenedioxy-2-nitromandelate (***t*Bu CNP-OAc**, 0.97 g, 2.86 mmol) was treated according to the general procedure to afford the crude alcohol as a yellow oil (0.81 g, 95 %).  $^1\text{H}$  NMR (400 MHz,  $\text{CDCl}_3$ ):  $\delta$  7.48 (1H, s, H<sub>3</sub>), 7.12 (1H, s, H<sub>6</sub>), 6.18 – 6.06 (2H, m, CH<sub>2</sub>), 5.81 (1H, s, CH), 4.06 – 3.86 (1H, br s, OH), 1.38 (9H, s, *t*Bu).  $^{13}\text{C}$  NMR (100 MHz,  $\text{CDCl}_3$ ):  $\delta$  170.8 ( $\underline{\text{C}}\text{O}_2^t\text{Bu}$ ), 151.9 (C<sub>5</sub>), 147.5 (C<sub>4</sub>), 142.1 (C<sub>2</sub>), 130.9 (C<sub>1</sub>), 107.7 (C<sub>6</sub>), 105.8 (C<sub>3</sub>), 103.2 (CH<sub>2</sub>),

83.7 ( $\underline{\text{C}}(\text{CH}_3)_3$ ), 69.9 (CH), 27.7 ( $\text{C}(\underline{\text{C}}\text{H}_3)_3$ ). HRMS (ESI-ToF)  $m/z$ :  $[\text{M} + \text{Na}]^+$  calcd. for  $\text{C}_{13}\text{H}_{15}\text{NNaO}_7$ , 320.0764; found, 320.0753.

*tert*-Butyl 4-bromo-2-nitromandelate (***t*Bu 4-Br-CNB-OH**)



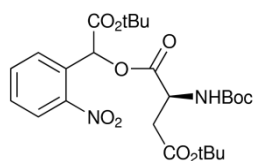
*tert*-Butyl *O*-Ac-4-bromo-2-nitromandelate (***t*Bu 4-Br-CNB-OAc**, 0.58 g, 1.55 mmol) was treated according to the general procedure to afford the crude alcohol as a yellow solid (0.47 g, 92 %).  $^1\text{H}$  NMR (400 MHz,  $\text{CDCl}_3$ ):  $\delta$  8.08 (1H, d,  $J = 2.0$  Hz, H<sub>3</sub>), 7.74 (1H, dd,  $J = 8.4, 2.0$  Hz, H<sub>5</sub>), 7.61 (1H, d,  $J = 8.4$  Hz, H<sub>6</sub>), 5.82 (1H, d,  $J = 2.6$  Hz, CH), 3.69 (1H, d,  $J = 2.0$  Hz, OH), 1.37 (9H, s, *t*Bu).  $^{13}\text{C}$  NMR (100 MHz,  $\text{CDCl}_3$ ):  $\delta$  170.7 ( $\text{CO}_2^t\text{Bu}$ ), 148.7 (C<sub>2</sub>), 136.2 (C<sub>5</sub>), 132.6 (C<sub>1</sub>), 130.4 (C<sub>6</sub>), 128.0 (C<sub>3</sub>), 122.3 (C<sub>4</sub>), 84.9 ( $\underline{\text{C}}(\text{CH}_3)_3$ ), 69.3 (CH), 27.8 ( $\text{C}(\underline{\text{C}}\text{H}_3)_3$ ). HRMS (ESI-ToF)  $m/z$ :  $[\text{M} + \text{Na}]^+$  calcd. for  $\text{C}_{12}\text{H}_{14}\text{BrNO}_5\text{Na}$ , 353.9948; found, 353.9959.

## 6.11 COUPLING TO L-ASPARTATE[24]

*General procedure*

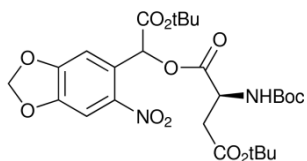
Based on a literature protocol,[37] (substituted) *tert*-butyl 2-nitromandelate (1 – 2 mmol) was dissolved in anhydrous CH<sub>2</sub>Cl<sub>2</sub> (10 ml/mmol) under an inert atmosphere, 4-*tert*-butyl *N*-Boc L-aspartate (1.1 eq.) was added, and the mixture was cooled in an ice bath for 15 min. Then, DMAP (0.9 eq.) and EDC·HCl (1.5 eq.) were added and the mixture was stirred for 1 h at 0 °C. The ice bath was removed, and stirring continued for 24 h at r.t. After this time, the reaction mixture was placed again in an ice bath for 15 min, quenched with brine (10 ml/mmol), allowed to warm to r.t., and extracted with CH<sub>2</sub>Cl<sub>2</sub> (10 ml/mmol). The combined extracts were washed sequentially with 0.5 M HCl (10 ml/mmol), water (10 ml/mmol), and NaHCO<sub>3</sub> (10 ml/mmol), dried over MgSO<sub>4</sub>, filtered, and concentrated *in vacuo* to afford the crude *ester*. The compounds were purified by flash chromatography.

*tert*-Butyl *N*-Boc-1-(*tert*-butyloxycarbonyl-(2-nitrophenyl)methyl)  
L-aspartate (*di*-<sup>*t*</sup>Bu *N*-Boc-1-CNB-L-Asp)



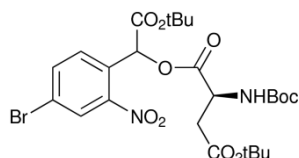
*tert*-Butyl 2-nitromandelate (<sup>*t*</sup>Bu CNB-OH, 0.67 g, 2.65 mmol) was treated according to the general procedure to afford the crude ester. Flash chromatography (SiO<sub>2</sub> 126 g, 18 % EtOAc-hexanes, *R<sub>f</sub>* 0.29) afforded the title compound as a clear, sticky oil (1.12 g, 81 %), ca. 1:1 mixture of diastereoisomers (based on ArCH NMR integrals). <sup>1</sup>H NMR (400 MHz, CDCl<sub>3</sub>): δ 8.05 – 7.98 (1H, m, H<sub>3</sub>'), 7.69 – 7.59 (2H, m, H<sub>5</sub>'/H<sub>6</sub>'), 7.55 – 7.48 (1H, m, H<sub>4</sub>'), 6.81, 6.79 (1H, 2 s, ArCH), 5.59 – 5.50 (1H, m, NH), 4.76 – 4.66 (1H, m, H<sub>2</sub>), 3.00 – 2.89 (1H, m, H<sub>3</sub>), 2.87 – 2.71 (1H, m, H<sub>3</sub>), 1.46 – 1.32 (27H, m, 3x <sup>*t*</sup>Bu). <sup>13</sup>C NMR (100 MHz, CDCl<sub>3</sub>): δ 170.2, 170.1, 170.0, 169.9 (4x C=O<sup>*t*</sup>Bu), 165.9, 165.7 (2x C<sub>1</sub>), 155.5, 155.4 (2x N-CO<sup>*t*</sup>Bu), 148.1 (C<sub>2</sub>'), 133.59, 133.57 (2x C<sub>5</sub>'/C<sub>6</sub>'), 129.75, 129.72 (2x C<sub>4</sub>'), 129.68, 129.66 (2x C<sub>1</sub>'), 129.4, 129.3 (2x C<sub>5</sub>'/C<sub>6</sub>'), 125.2 (C<sub>3</sub>'), 83.8, 83.7, 81.94, 81.92, 80.2 (5x C(CH<sub>3</sub>)<sub>3</sub>), 71.4, 71.3 (2x ArCH), 50.2 (C<sub>2</sub>), 37.9, 37.7 (2x C<sub>3</sub>), 28.4, 28.1, 28.0, 27.8 (4x C(CH<sub>3</sub>)<sub>3</sub>). HRMS (ESI-ToF) *m/z*: [M + Na]<sup>+</sup> calcd. for C<sub>25</sub>H<sub>36</sub>N<sub>2</sub>O<sub>10</sub>Na 547.2262; found 547.2209.

*tert*-Butyl N-Boc-1-(*tert*-butyloxycarbonyl-(4,5-methylenedioxy-2-nitrophenyl)methyl) L-aspartate (*di*-<sup>t</sup>Bu N-Boc-1-CNP-L-Asp)



*tert*-Butyl 4,5-methylenedioxy-2-nitromandelate (<sup>t</sup>Bu CNP-OH, 0.47 g, 1.39 mmol) was treated according to the general procedure. Flash chromatography (SiO<sub>2</sub> 89 g, 20% EtOAc-hexanes, *R<sub>f</sub>* 0.30) afforded the title compound as a colourless foam (0.70 g, 87% over two steps), ca. 1:1 mixture of diastereoisomers (estimated based on H6' (or H6', or H6') NMR integrals). <sup>1</sup>H NMR (400 MHz, CDCl<sub>3</sub>): δ 7.55, 7.54 (1H, 2 s, H<sub>3'</sub>), 7.06, 7.04 (1H, 2 s, H6'), 6.79, 6.77 (1H, 2 s, ArCH), 6.17 – 6.11 (2H, m, OCH<sub>2</sub>), 5.57 – 5.49 (1H, m, NH), 4.73 – 4.65 (1H, m, H<sub>2</sub>), 2.98 – 2.88 (1H, m, H<sub>3</sub>), 2.84 – 2.72 (1H, m, H<sub>3</sub>), 1.46 – 1.36 (27H, m, 3x <sup>t</sup>Bu). <sup>13</sup>C NMR (150 MHz, CDCl<sub>3</sub>): δ 170.2, 170.1, 170.0, 169.9 (4x CCO<sub>2</sub><sup>t</sup>Bu), 166.0, 165.8 (2x C<sub>1</sub>), 155.6, 155.4 (2x NCO<sub>2</sub><sup>t</sup>Bu), 152.2 (C<sub>5'</sub>), 148.2 (C<sub>4'</sub>), 142.5 (C<sub>2'</sub>), 126.8, 126.7 (2x C<sub>1'</sub>), 108.1, 108.0 (2x C<sub>6'</sub>), 106.1 (C<sub>3'</sub>), 103.4 (OCH<sub>2</sub>), 83.7, 83.6, 82.0, 80.3 (4x C(CH<sub>3</sub>)<sub>3</sub>), 71.8, 71.6 (2x ArCH), 50.3 (C<sub>2</sub>), 38.0, 37.7 (2x C<sub>3</sub>), 28.4, 28.2, 28.1, 27.9 (4x C(CH<sub>3</sub>)<sub>3</sub>). HRMS (ESI-ToF) *m/z*: [M + Na]<sup>+</sup> calcd. for C<sub>26</sub>H<sub>36</sub>N<sub>2</sub>NaO<sub>12</sub>, 591.2166; found 591.2213.

*tert*-Butyl N-Boc-1-(*tert*-butyloxycarbonyl-(4-bromo-2-nitrophenyl)methyl) L-aspartate (*di*-<sup>t</sup>Bu N-Boc-1-(4-Br-CNB)-L-Asp)

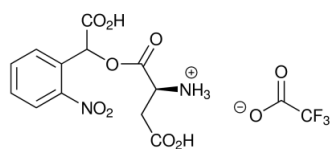


*tert*-Butyl 4-bromo-2-nitromandelate (<sup>t</sup>Bu 4-Br-CNB-OH, 0.47 g, 1.42 mmol) was treated according to the general procedure, except reagent loadings were relative to the amount of compound <sup>t</sup>Bu 4-Br-CNB-OAc used in the previous step (1 eq. = 1.55 mmol). Flash chromatography (SiO<sub>2</sub> 87 g, 14% EtOAc-hexanes, *R<sub>f</sub>* 0.28) afforded the title compound as a clear oil (0.68 g, 73% over two steps), ca. 1:1 mixture of diastereoisomers (estimated based on ArCH NMR integrals). <sup>1</sup>H NMR (400 MHz, CDCl<sub>3</sub>): δ 8.19 – 8.16 (1H, m, H<sub>3'</sub>), 7.78 – 7.73 (1H, m, H<sub>5'</sub>), 7.58 – 7.51 (1H, m, H<sub>6'</sub>), 6.75, 6.74 (1H, 2 s, ArCH), 5.58 – 5.48 (1H, m, NH), 4.75 – 4.65 (1H, m, H<sub>2</sub>), 2.98 – 2.89 (1H, m, H<sub>3</sub>), 2.85 – 2.72 (1H, m, H<sub>3</sub>), 1.48 – 1.35 (27H, 3x <sup>t</sup>Bu). cNMR (100 MHz, CDCl<sub>3</sub>): δ 170.2,

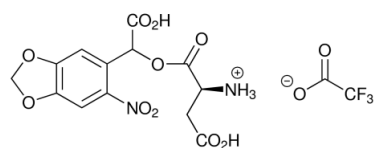
170.1, 170.04, 169.97 (4x  $\text{C}\text{C}\text{O}_2^t\text{Bu}$ ), 165.4, 165.3 (2x  $\text{C}_1$ ), 155.6, 155.4 (2x  $\text{N}\text{C}\text{O}_2^t\text{Bu}$ ), 148.4 ( $\text{C}_2'$ ), 136.6 ( $\text{C}_5'$ ), 130.7, 130.6 (2x  $\text{C}_6'$ ), 128.84, 128.79 (2x  $\text{C}_1'$ ), 128.2 ( $\text{C}_3'$ ), 123.2, 123.1 (2x  $\text{C}_4'$ ), 84.2, 84.1, 82.1, 80.3 (4x  $\text{C}(\text{CH}_3)_3$ ), 71.1, 71.0 (2x  $\text{ArCH}$ ), 50.2 ( $\text{C}_2$ ), 37.8, 37.6 (2x  $\text{C}_3$ ), 28.4, 28.2, 28.0, 27.8 (4x  $\text{C}(\text{CH}_3)_3$ ). HRMS (ESI-ToF)  $m/z$ :  $[\text{M} + \text{Na}]^+$  calcd. for  $\text{C}_{25}\text{H}_{35}\text{BrN}_2\text{NaO}_{10}$ , 627.1347; found 627.1353.

6.12 DEPROTECTION OF *N*-BOC AND *tert*-BUTYL ESTERS[24]*General procedure*

In an oven dried flask, protected photocage (**di-<sup>t</sup>Bu N-Boc-1-CNB-L-Asp** derivative) (0.2 – 0.3 mmol) was dissolved in anhydrous CH<sub>2</sub>Cl<sub>2</sub> (5 ml/mmol), to which was added freshly distilled TFA (5 ml/mmol). The reaction mixture was placed under a CaCl<sub>2</sub> drying tube and stirred for 24 h. The product mixture was concentrated *in vacuo* and then co-evaporated with dry CH<sub>2</sub>Cl<sub>2</sub> (3x 2 ml) to afford the photocaged L-aspartate trifluoroacetate salt (**1-CNB-L-Asp** derivative), which was sufficiently pure for further experiments.

*1-(carboxy-(2-nitrophenyl)methyl) L-aspartate trifluoroacetate salt (1-CNB-L-Asp)*

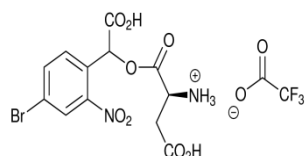
**di-<sup>t</sup>Bu N-Boc-1-CNB-L-Asp** (0.15 g, 0.29 mmol) was treated according to the general procedure to afford the title compound as a white solid (0.12 g, 97%). UV/Vis (50 mM phosphate buffer, pH 7)  $\lambda_{\max}$  ( $\epsilon$ ): 265 (5160). <sup>1</sup>H NMR (400 MHz, DMSO-*d*<sub>6</sub>):  $\delta$  9.10 – 8.22 (3H, br s, NH<sub>3</sub><sup>+</sup>), 8.15 – 8.06 (1H, m, H<sub>3</sub>'), 7.86 – 7.68 (3H, m, Ar), 6.78 (1H, s, ArCH), 4.57 – 4.48 (1H, m, H<sub>2</sub>), 3.07 – 2.82 (2H, m, H<sub>3</sub>). <sup>13</sup>C NMR (100 MHz, DMSO-*d*<sub>6</sub>):  $\delta$  170.64, 170.60 (2x C<sub>4</sub>), 167.8, 167.70, 167.66, 167.6 (4x C<sub>1</sub>/ $\alpha$ -carboxy), 158.5 (q, *J* = 35.0 Hz, TFA CO), 147.83, 147.79 (2x C<sub>2</sub>'), 134.11, 134.06, 130.64, 130.58, 129.8, 129.7 (6x Ar), 128.22, 128.18 (2x C<sub>1</sub>'), 125.1 (C<sub>3</sub>'), 118.2 (app t, *J* = 294.5 Hz, CF<sub>3</sub>), 70.8, 70.7 (2x ArCH), 48.6 (C<sub>2</sub>), 34.3, 34.1 (2x C<sub>3</sub>). MS (ESI-ToF) *m/z*: [M + H]<sup>+</sup> calcd. for C<sub>12</sub>H<sub>13</sub>N<sub>2</sub>O<sub>8</sub> 313.0666; found 313.21.

*1-(carboxy-(4,5-methylenedioxy-2-nitrophenyl)methyl) L-aspartate trifluoroacetate salt (1-CNP-L-Asp)*

**di-<sup>t</sup>Bu N-Boc-1-CNP-L-Asp** (0.26 g, 0.23 mmol) was treated according to the general procedure to afford the title compound as a yellow solid (0.21 g, 98%), ca. 1:1 mixture of diastereoisomers (estimated

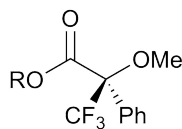
based on H6' NMR integrals). UV/Vis (50 mM phosphate buffer, pH 7)  $\lambda_{\max}$  ( $\epsilon$ ): 248 (10300), 312 (2680), 357 (4060).  $^1\text{H}$  NMR (600 MHz, DMSO- $d_6$ ):  $\delta$  8.96 – 8.25 (3H, br s,  $\text{NH}_3^+$ ), 7.73, 7.71 (1H, 2 s, H3'), 7.31, 7.24 (1H, 2 s, H6'), 6.76, 6.74 (1H, 2 s, ArCH), 6.30 – 6.26 (2H, m, OCH<sub>2</sub>), 4.54, 4.49 (1H, 2 t,  $J = 5.4, 4.9$  Hz, H<sub>2</sub>), 3.05 – 2.82 (2H, m, H<sub>3</sub>).  $^{13}\text{C}$  NMR (150 MHz, DMSO- $d_6$ ):  $\delta$  170.7, 170.6 (2x C<sub>4</sub>), 167.7, 167.62, 167.61, 167.5 (4x C<sub>1</sub>/ $\alpha$ -carboxy), 158.3 (q,  $J = 33.0$  Hz, TFA CO), 152.1, 151.9 (2x C<sub>5'</sub>), 148.2 (C<sub>4'</sub>), 142.1 (C<sub>2'</sub>), 125.04, 125.01 (2x C<sub>1'</sub>), 116.7 (app d,  $J = 295.5$  Hz, CF<sub>3</sub>), 108.2, 108.0 (2x C<sub>6'</sub>), 105.6 (C<sub>3'</sub>), 103.94, 103.93 (2x OCH<sub>2</sub>), 70.9, 70.8 (2x ArCH), 48.6 (C<sub>2</sub>), 34.3, 34.1 (2x C<sub>3</sub>). MS (ESI-ToF)  $m/z$ : [M + H]<sup>+</sup> calcd. for C<sub>13</sub>H<sub>13</sub>N<sub>2</sub>O<sub>10</sub> 357.06; found 357.16.

*1-(carboxy-(4-bromo-2-nitrophenyl)methyl) L-Aspartate trifluoroacetate salt*  
(**1-(4-Br-CNB)-L-Asp**)



**di-<sup>t</sup>Bu N-Boc-1-(4-Br-CNB)-L-Asp** (0.16 g, 0.27 mmol) was treated according to the general procedure to afford the title compound as a white crystalline solid (0.13 g, 96%), ca. 1:1 mixture of diastereoisomers (estimated based on H6' NMR integrals). UV/Vis (50 mM phosphate buffer, pH 7)  $\lambda_{\max}$  ( $\epsilon$ ): 224 (16000), 262 (3640), 307 (sh, 1600).  $^1\text{H}$  NMR (400 MHz, DMSO- $d_6$ ): 14.33 – 11.99 (2H, br s, 2x CO<sub>2</sub>H), 8.85 – 8.40 (3H, br s,  $\text{NH}_3^+$ ), 8.33, 8.31 (1H, 2 d,  $J = 1.8, 1.8$  Hz, H<sub>3'</sub>), 8.08 – 7.98 (1H, m, H<sub>5'</sub>), 7.77, 7.71 (1H, 2 d,  $J = 8.4, 8.4$  Hz, H<sub>6'</sub>), 6.72, 6.71 (1H, 2 s, ArCH), 4.55 – 4.46 (1H, m, H<sub>2</sub>), 3.06 – 2.79 (2H, m, H<sub>3</sub>).  $^{13}\text{C}$  NMR (100 MHz, DMSO- $d_6$ ): 170.62, 170.58 (2x C<sub>4</sub>), 167.64, 167.59, 167.3, 167.2 (4x C<sub>1</sub>/ $\alpha$ -carboxy), 158.4 (app d,  $J = 33.0$  Hz, TFA CO), 148.4, 148.3 (2x C<sub>2'</sub>), 136.72, 136.69 (2x C<sub>5'</sub>), 131.8, 131.5 (2x C<sub>6'</sub>), 127.8 (C<sub>1'</sub>), 127.6, 127.5 (2x C<sub>3'</sub>), 122.74, 122.72 (2x C<sub>4'</sub>), 70.5, 70.3 (2x ArCH), 48.6, 48.5 (2x C<sub>2</sub>), 34.3, 34.1 (2x C<sub>3</sub>). MS (ESI-ToF)  $m/z$ : [M + H]<sup>+</sup> calcd. for C<sub>12</sub>H<sub>12</sub>BrN<sub>2</sub>O<sub>8</sub> 390.98, 392.98; found 391.11, 393.11 (1:1 isotopic ratio).

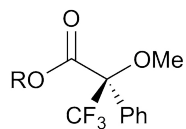
## 6.13 MOSHER'S ESTER PROTOCOL A



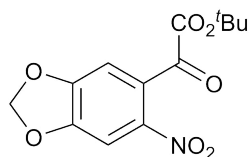
*Work of Owen Tuck.*

S-Mosher's acid chloride (0.22 ml, 1.2 mmol) was added to a stirred mixture of DMAP (24 mg, 0.2 mmol) and the requisite alcohol (0.1 mmol) in CH<sub>2</sub>Cl<sub>2</sub> (1 ml). The mixture was stirred for 3 h at r.t., then partitioned between H<sub>2</sub>O (3 ml) and Et<sub>2</sub>O (6 ml). The aqueous phase was extracted again with Et<sub>2</sub>O (2x 6 ml). The organic extracts were dried (MgSO<sub>4</sub>), filtered, and concentrated *in vacuo* to afford the crude *ester*. This was purified by flash chromatography (10% EtOAc-pentanes) to give the *R*-Mosher's ester derivative.

## 6.14 MOSHER'S ESTER PROTOCOL B

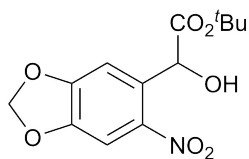


*R*-Mosher's acid (80 mg, 0.34 mmol) and the requisite alcohol (0.1 mmol) were dissolved in dry CH<sub>2</sub>Cl<sub>2</sub> (2 ml). DCC (0.15 ml, 0.9 mmol) and DMAP (33 mg, 0.3 mmol) were added and the mixture was stirred for 24 h at r.t. TLC analysis after this time indicated complete reaction. The mixture was filtered, concentrated, and purified by flash chromatography (10 g SiO<sub>2</sub>, 10 – 20% EtOAc/*n*-heptane) to afford the *R*-Mosher's ester.

6.15 *tert*-BUTYLOXYCARBONYL 6-NITROPIPERONYL KETONE (*<sup>t</sup>Bu* CNPK)*tert*-Butyl 4,5-methylenedioxy-2-nitromandelate

(*<sup>t</sup>Bu* CNP-OH, 0.39 g, 1.3 mmol) was dissolved in CH<sub>2</sub>Cl<sub>2</sub> (13 ml) and to this was added DMP (0.64 g, 1.5 mmol). The reaction mixture was stirred for 19 h at r.t., then CH<sub>2</sub>Cl<sub>2</sub> (30 ml) was added, and the mixture was filtered. The filtrate was concentrated *in vacuo* to afford a residue (0.57 g). This was purified by flash chromatography (57 g SiO<sub>2</sub>, 20 % EtOAc-hexanes) followed by vapour diffusion recrystallisation (EtOAc/hexanes) to afford the *ketone* as yellow rods (0.26 g, 68 %). <sup>1</sup>H NMR (600 MHz, CDCl<sub>3</sub>): δ 7.58 (1H, s, H<sub>5</sub>), 6.97 (1H, s, H<sub>2</sub>), 6.22 (2H, s, CH<sub>2</sub>), 1.50 (9H, s, *<sup>t</sup>Bu*). <sup>13</sup>C NMR (600 MHz, CDCl<sub>3</sub>): δ 184.2 (ArCO), 158.7 (CO<sub>2</sub>*<sup>t</sup>Bu*), 153.0 (C<sub>3</sub>), 150.4 (C<sub>4</sub>), 143.3 (C<sub>6</sub>), 130.1 (C<sub>1</sub>), 109.2 (C<sub>2</sub>), 104.7 (C<sub>5</sub>), 104.1 (CH<sub>2</sub>), 85.2 (C(CH<sub>3</sub>)<sub>3</sub>), 27.8 (C(CH<sub>3</sub>)<sub>3</sub>). HRMS (ESI-ToF) m/z: [M + Na]<sup>+</sup> calcd for C<sub>13</sub>H<sub>13</sub>NNaO<sub>7</sub>, 318.0584; found, 318.0583; [M - *<sup>t</sup>Bu* + Na + H]<sup>+</sup> calcd for C<sub>9</sub>H<sub>5</sub>NNaO<sub>7</sub>, 261.9958; found, 261.9956. MS (EI-DIP) m/z: 57.09 (100 %, *<sup>t</sup>Bu*<sup>+</sup>), 41.06 (29 %), 120.11 (17 %), 62.05 (14 %), 195.15 (11 %, MH<sup>+</sup> - CO<sub>2</sub>*<sup>t</sup>Bu*). Elem. Anal. calcd for C<sub>13</sub>H<sub>13</sub>NO<sub>7</sub>: C, 52.89; H, 4.44; N, 4.74; O, 37.93; found: C, 52.92; H, 4.44; N, 4.73; O, 37.89.

6.16 *tert*-BUTYL  $\alpha$ -CARBOXY-6-NITROPIPERONYL ALCOHOL  
(***t*Bu CNP-OH**) VIA COREY-BAKSHI-SHIBATA CATALYSIS



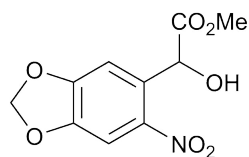
*Work of Owen Tuck.*

***t*Bu CNPK** (147 mg, 0.50 mmol) and *R*-CBS (28 mg, 0.10 mmol) were dissolved in dry THF (2.5 ml) under inert conditions at 0 °C. BH<sub>3</sub>·THF (1 M in THF) was added in portions of 0.17 ml, every 30 min (total: 1.36 ml 1 M BH<sub>3</sub>·THF). TLC analysis at this point indicated complete consumption of ***t*Bu CNPK**. The product mixture was concentrated *in vacuo*, and the residue partitioned between 0.5 M HCl (5 ml) and EtOAc (5 ml). The aqueous phase was extracted again with EtOAc (2x 5 ml). The combined extracts were dried (MgSO<sub>4</sub>), filtered, and concentrated *in vacuo* to afford the crude *alcohol* (106 mg). The pure product was obtained by flash chromatography (12 g SiO<sub>2</sub>, CH<sub>2</sub>Cl<sub>2</sub>, *R<sub>f</sub>* 0.18); yellow powder (101 mg, 68%). <sup>1</sup>H NMR spectrum consistent with that reported previously. The *R*-Mosher's ester was synthesised using 30 mg of ***t*Bu CNP-OH**, according to Mosher's ester protocol A. The yield of *R*-Mosher's ester was 31%. This was analysed by <sup>1</sup>H and <sup>19</sup>F NMR spectroscopy, which indicated 0% *e.e.*

## 6.17 ATTEMPTED ASYMMETRIC REDUCTION WITH RUTHENIUM CATALYST

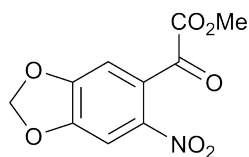
*Work of Owen Tuck.*

**<sup>t</sup>Bu CNPK** (59 mg, 0.2 mmol) was dissolved in a mixture of dry *i*PrOH (2 ml) and dry CH<sub>2</sub>Cl<sub>2</sub> (2 ml). This solution was added to RuCl[(*S,S*)-TsDPEN](Mes) (0.15 mg, 1 μmol) under an inert atmosphere. Dry KOH (0.02 ml, 0.1 M in *i*PrOH) was then added. The reaction mixture was stirred for 12 h at r.t. TLC analysis indicated no formation of the desired product. Another portion of KOH (0.02 ml, 0.1 M in *i*PrOH) was added, and the reaction was allowed to proceed over five days, but no alcohol product was detected by TLC analysis after this time.

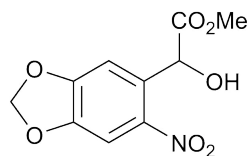
6.18 METHYL  $\alpha$ -CARBOXY-6-NITROPIPERONYL ALCOHOL (**Me CNP-OH**)

4,5-Methylenedioxy-2-nitromandelic acid (**CNP-OH**, 1.00 g, 4.15 mmol) was dissolved in anhydrous MeOH (80 ml) containing H<sub>2</sub>SO<sub>4</sub> (0.01 ml). The reaction mixture was heated at reflux for 3 h, then quenched with solid NaHCO<sub>3</sub>. The solvent was removed under vacuum and the residue partitioned between water and EtOAc (40 ml each). The aqueous phase was extracted again with EtOAc (2x 10 ml). The organic extracts were dried (MgSO<sub>4</sub>), filtered, and concentrated *in vacuo* to afford the crude *methyl ester* (0.72 g). Recrystallisation of the crude material from EtOAc (10 ml) with an *n*-pentane vapour bath (40 ml) afforded **Me CNP-OH** as yellow plates (0.57 g, 54%). <sup>1</sup>H NMR (400 MHz, CDCl<sub>3</sub>):  $\delta$  7.54 (1H, s, H<sub>5</sub>), 7.08 (1H, s, H<sub>2</sub>), 6.14 (1H, d,  $J = 1.2$  Hz, CH<sub>2</sub>), 6.13 (1H, d,  $J = 1.2$  Hz, CH<sub>2</sub>), 3.74 (3H, s, Me), 3.70 (1H, br s, OH). <sup>13</sup>C NMR (100 MHz, CDCl<sub>3</sub>):  $\delta$  172.3 (CO<sub>2</sub>Me), 152.3 (C<sub>3</sub>), 148.0 (C<sub>4</sub>), 142.1 (C<sub>6</sub>), 130.4 (C<sub>1</sub>), 108.7 (C<sub>2</sub>), 106.2 (C<sub>5</sub>), 103.4 (CH<sub>2</sub>), 70.3 (ArCH), 53.4 (Me).

## 6.19 METHYLOXYCARBONYL 6-NITROPIPERONYL KETONE (Me CNPK)

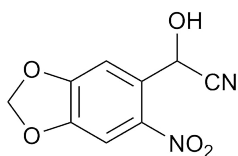


**Me CNP-OH** (0.49 g, 1.9 mmol) was dissolved in  $\text{CH}_2\text{Cl}_2$  (20 ml). DMP (1.22 g, 2.88 mmol) was added, and the reaction mixture was stirred for 23 h at r.t. The mixture was diluted with  $\text{CH}_2\text{Cl}_2$  (15 ml) then filtered over Celite<sup>®</sup>. The cake was washed with  $\text{CH}_2\text{Cl}_2$  (3x 10 ml). The filtrate was concentrated *in vacuo* to afford the crude *ketone* (0.60 g). Flash chromatography (60 g  $\text{SiO}_2$ , 40% EtOAc/*n*-heptane,  $R_f$  0.39) afforded the pure product as a yellow solid (0.44 g, 91%).  $^1\text{H}$  NMR (400 MHz,  $\text{CDCl}_3$ ):  $\delta$  7.59 (1H, s, H<sub>5</sub>), 6.96 (1H, s, H<sub>2</sub>), 6.23 (2H, s, CH<sub>2</sub>), 3.86 (3H, s, Me).  $^{13}\text{C}$  NMR (100 MHz,  $\text{CDCl}_3$ ):  $\delta$  182.8 (ArCO), 160.3 (CO<sub>2</sub>Me), 153.2 (C<sub>3</sub>), 150.7 (C<sub>4</sub>), 142.9 (C<sub>1</sub>), 129.5 (C<sub>6</sub>), 109.0 (C<sub>2</sub>), 104.8 (C<sub>5</sub>), 104.2 (CH<sub>2</sub>), 53.6 (Me).

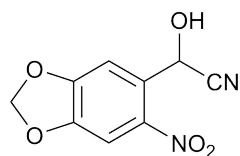
6.20 METHYL  $\alpha$ -CARBOXY-6-NITROPIPERONYL ALCOHOL (**Me CNP-OH**)  
VIA COREY-BAKSHI-SHIBATA CATALYSIS

All THF used in this reaction was anhydrous and was degassed with three freeze-pump-thaw cycles prior to the experiment. *R*-CBS (29 mg, 0.10 mmol) were dissolved in THF (10 ml) under inert atmosphere and cooled to  $-15^{\circ}\text{C}$  in an ice/acetone bath. Dropwise addition of **Me CNPK** (0.25 g, 1.0 mmol) in THF (3 ml) and  $\text{BH}_3 \cdot \text{THF}$  (1 M in THF, 0.6 ml) begun at  $-13^{\circ}\text{C}$ . The addition took 20 min, and the reaction mixture was maintained below  $-10^{\circ}\text{C}$  for a further 30 min. TLC analysis indicated partial conversion of **Me CNPK** to **Me CNP-OH**. No further reaction was observed after allowing the reaction mixture to warm to r.t. and to stir for three days. The product mixture was treated with 1 M HCl (10 ml) and extracted with EtOAc (3x 10 ml). The combined organic extracts were washed with brine (10 ml), dried ( $\text{MgSO}_4$ ), filtered, and concentrated *in vacuo* to afford a thick oil (0.16 g). A portion (15.8 mg) was analysed by  $^1\text{H}$  NMR with 1,3,5-trimethoxybenzene (1.9 mg, 11  $\mu\text{mol}$ ) as an internal standard. Yield of **Me CNP-OH**: 13%, based on CH integral ( $\delta$  5.82 ppm) of 1 compared to 2.6 for the aromatic shift of the ISTD at 6.08 ppm. Indicates ca. 13  $\mu\text{mol}$  or 3.2 mg of **Me CNP-OH** present in 15.8 mg sample, or 32 mg, 0.13 mol in total mass.  $^1\text{H}$  NMR shifts were consistent with those previously reported.

6.21 UNCATALYSED TMSCN ADDITION TO 6-NITROPIPERONAL (**6-NPA**)  
IN CH<sub>2</sub>CL<sub>2</sub>: CONTROL

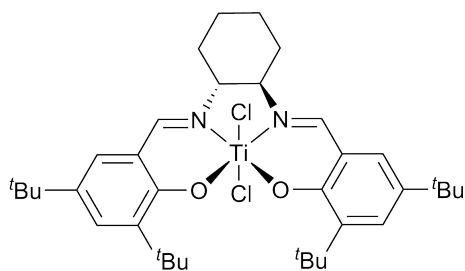


6-Nitropiperonal (**6-NPA**, 0.20 g, 1.0 mmol) was dissolved in anhydrous CH<sub>2</sub>Cl<sub>2</sub> (5 ml). TMSCN (0.13 ml, 1.0 mmol) was added. The reaction mixture was stirred for 20 h at r.t. Then, 1 M HCl (10 ml) was added and the reaction was stirred at r.t. while monitoring by TLC analysis. This was left overnight and the CH<sub>2</sub>Cl<sub>2</sub> evaporated. TLC analysis then indicated complete removal of the TMS protecting group. The product mixture was extracted with EtOAc (3x 10 ml). The organic extracts were washed with water (10 ml) and brine (10 ml), dried (MgSO<sub>4</sub>), and concentrated *in vacuo* to provide a mixture of **6-NPA** and **6-NPA-HCN** as a yellow solid (0.16 g). The crude product (27.0 mg) and 1,3,5-trimethoxybenzene (3.1 mg) were dissolved in DMSO-*d*<sub>6</sub> and analysed by <sup>1</sup>H NMR. The yields determined in this way were 9% **6-NPA-HCN** and 69% recovered **6-NPA**.

6.22 TMSCN ADDITION TO 6-NITROPIPERONAL (**6-NPA**) CATALYSED BY L-DIPT AND Ti(O<sup>i</sup>Pr)<sub>4</sub>

**L-DIPT** (0.07 ml, 0.33 mmol), Ti(OiPr)<sub>4</sub> (0.08 ml, 0.33 mmol) and TMSCN (0.19 ml, 1.5 mmol) were added to a stirred solution of anhydrous CH<sub>2</sub>Cl<sub>2</sub> (3 ml) at 0 °C. 6-Nitropiperonal (**6-NPA**, 0.21 g, 1.1 mmol) was added dropwise as a solution in anhydrous CH<sub>2</sub>Cl<sub>2</sub> (2 ml). The reaction mixture was allowed to slowly warm to r.t. while stirring for 27 h. TLC analysis indicated incomplete reaction. An additional portion of TMSCN (0.06 ml, 0.5 mmol) was added, and the reaction was stirred for an additional 19 h at r.t. Then, 1 M HCl (10 ml) was added, and the reaction mixture was stirred overnight; the CH<sub>2</sub>Cl<sub>2</sub> evaporated during this time. The product mixture was extracted with EtOAc (3x 10 ml), and the organic extracts were washed with water (10 ml) and brine (10 ml). This was dried (MgSO<sub>4</sub>), filtered, and concentrated *in vacuo* to afford the crude *cyanohydrin* (0.24 g). This was purified by flash chromatography to afford the product as a slightly yellow solid (0.13 g, 54%). A sample (23 mg) was converted to the *R*-Mosher's ester (see Mosher's ester protocol B), in 23% yield. <sup>1</sup>H NMR analysis indicated a 1:1 mixture of diastereomers (0% *e.e.* for the cyanohydrin formation).

6.23 TITANIUM DICHLORIDE COMPLEX WITH (*R,R*)-JACOBSEN'S LIGAND  
(**TiCl<sub>2</sub>-salen**)

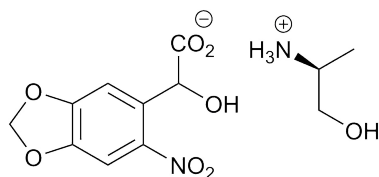


(*R,R*)-Jacobsen's ligand (**salen**, 0.50 g, 0.91 mmol) was dissolved in anhydrous CH<sub>2</sub>Cl<sub>2</sub> (10 ml). TiCl<sub>4</sub> (1 M in CH<sub>2</sub>Cl<sub>2</sub>, 0.91 ml, 0.91 mmol) was added dropwise, and the reaction mixture was stirred for 2 h at r.t. The product mixture was concentrated *in vacuo*, and the residue was washed with 50% Et<sub>2</sub>O/*n*-pentane followed by *n*-pentane. The red solid was then recrystallised from hot CHCl<sub>3</sub> to afford the complex (**TiCl<sub>2</sub>-salen**) as red crystals (0.18 g, 30%). <sup>1</sup>H NMR (400 MHz, CDCl<sub>3</sub>): δ 8.30 (2H, s, HC=N), 7.59 (2H, d, *J* = 2.3 Hz, Ar), 7.34 (2H, d, *J* = 2.3 Hz, Ar), 4.11 – 3.98 (2H, m, Cy), 2.65 – 2.50 (2H, m, Cy), 2.15 – 2.00 (2H, m, Cy), 1.55 – 1.39 (4H, m, Cy), 1.52 (18H, s, <sup>t</sup>Bu), 1.33 (18H, s, <sup>t</sup>Bu).

6.24 DIMER COMPLEX OF TITANIUM AND (*R,R*)-JACOBSEN'S LIGAND  
(**Ti-salen-dimer**)

**TiCl<sub>2</sub>-salen** (0.13 g, 0.20 mmol) was dissolved in anhydrous CH<sub>2</sub>Cl<sub>2</sub> (2 ml). Water (3.5  $\mu$ l, 0.2 mmol) and Et<sub>3</sub>N (0.06 ml, 0.4 mmol) were added, and the reaction mixture was stirred for 3 h at r.t. The product mixture was washed with water, dried (MgSO<sub>4</sub>), filtered, and concentrated *in vacuo* to give the crude dimer complex (0.12 g). <sup>1</sup>H NMR analysis (Figure 3.7) showed the desired product was present in an approximately 2:1 molar ratio with an unknown species.

## 6.25 CRYSTALLISATION OF DIASTEREOMERIC SALTS



4,5-Methylenedioxy-2-nitromandelic acid (**CNP-OH**, 0.60 g, 2.5 mmol) was dissolved in *i*PrOH (40 ml) at 60 °C and treated with (*R*)-2-aminopropan-1-ol (0.2 ml, 2.5 mmol). This was allowed to cool, layered with Et<sub>2</sub>O (100 ml), and placed in the freezer (-20 °C) for 24 h.

The crystallised product was removed by filtration and washed with cold *i*PrOH/Et<sub>2</sub>O (1:2) followed by Et<sub>2</sub>O to afford a yellow solid (0.56 g, 142% of theory for single-diastereoisomer). This was digested in warm *i*PrOH (50 ml), cooled, filtered, and washed with *i*PrOH to give 0.45 g (114%), which was recrystallised again from EtOH/H<sub>2</sub>O. Yield 0.24 g, 61%. Enantiomeric excess remains to be determined.



## BIBLIOGRAPHY

---

- [1] RSCB PDB. *The Protein Data Bank*. URL: <https://www.rcsb.org/>.
- [2] Matteo Levantino, Briony A Yorke, Diana CF Monteiro, Marco Cammarata and Arwen R Pearson. In: *Current Opinion in Structural Biology* 35 (2015), pp. 41–48. DOI: <https://doi.org/10.1016/j.sbi.2015.07.017>.
- [3] Friedrich Schotte et al. In: *Proceedings of the National Academy of Sciences* 109 (2012), pp. 19256–19261. DOI: [10.1073/pnas.1210938109](https://doi.org/10.1073/pnas.1210938109).
- [4] Andrew Aquila et al. In: *Optical Express* 20 (2012), pp. 2706–2716. DOI: <https://doi.org/10.1364/OE.20.002706>.
- [5] Christopher Kupitz et al. In: *Nature* 513 (2014), pp. 261–265. DOI: [10.1038/nature13453](https://doi.org/10.1038/nature13453).
- [6] Petr Klán et al. In: *Chemical Reviews* 113 (2013), pp. 119–191. DOI: [10.1021/cr300177k](https://doi.org/10.1021/cr300177k).
- [7] Günter Mayer and Alexander Heckel. In: *Angewandte Chemie International Edition* 45 (2006), pp. 4900–4921. DOI: <https://doi.org/10.1002/anie.200600387>.
- [8] Hsien-Ming Lee, Daniel R. Larson and David S. Lawrence. In: *ACS Chemical Biology* 4 (2009), pp. 409–427. DOI: [10.1021/cb900036s](https://doi.org/10.1021/cb900036s).
- [9] D. E. Spence, P. N. Kean and W. Sibbett. In: *Opt. Lett.* 16 (1991), pp. 42–44. DOI: [10.1364/OL.16.000042](https://doi.org/10.1364/OL.16.000042).
- [10] Donna Strickland and Gerard Mourou. In: *Optics Communications* 55 (1985), pp. 447–449. DOI: [https://doi.org/10.1016/0030-4018\(85\)90151-8](https://doi.org/10.1016/0030-4018(85)90151-8).
- [11] Kanupriya Pande et al. In: *Science* 352 (2016), pp. 725–729. DOI: [10.1126/science.aad5081](https://doi.org/10.1126/science.aad5081).
- [12] Alexander Deiters, Dan Groff, Youngha Ryu, Jianming Xie and Peter G. Schultz. In: *Angewandte Chemie International Edition* 45 (2006), pp. 2728–2731. DOI: <https://doi.org/10.1002/anie.200600264>.
- [13] Chungjung Chou, Douglas D. Young and Alexander Deiters. In: *ChemBioChem* 11 (2010), pp. 972–977. DOI: <https://doi.org/10.1002/cbic.201000041>.

- [14] Stephanie Kesgin-Schaefer, Johannes Heidemann, Anke Puchert, Knut Koelbel, Briony A. Yorke, Nils Huse, Arwen R. Pearson, Charlotte Uetrecht and Henning Tidow. In: *The FEBS Journal* 286 (2019), pp. 2329–2340. DOI: <https://doi.org/10.1111/febs.14797>.
- [15] Christian Renner and Luis Moroder. In: *ChemBioChem* 7 (2006), pp. 868–878. DOI: <https://doi.org/10.1002/cbic.200500531>.
- [16] Eike C. Schulz et al. In: *Nature Methods* 15 (2018), pp. 901–904. DOI: [10.1038/s41592-018-0180-2](https://doi.org/10.1038/s41592-018-0180-2).
- [17] Ilme Schlichting et al. In: *Nature* 345 (1990), pp. 309–315. DOI: [10.1038/345309a0](https://doi.org/10.1038/345309a0).
- [18] M. Nič, J. Jiráť, B. Košata, A. Jenkins and A. McNaught. *IUPAC Compendium of Chemical Terminology*. IUPAC, Research Triangle Park, NC: IUPAC, 2009.
- [19] Thomas R. M. Barends et al. In: *Science* 350 (2015), pp. 445–450. DOI: [10.1126/science.aac5492](https://doi.org/10.1126/science.aac5492).
- [20] Friedrich Schotte, Manho Lim, Timothy A. Jackson, Aleksandr V. Smirnov, Jayashree Soman, John S. Olson, George N. Phillips, Michael Wulff and Philip A. Anfinrud. In: *Science* 300 (2003), pp. 1944–1947. DOI: [10.1126/science.1078797](https://doi.org/10.1126/science.1078797).
- [21] Richard S. Givens et al. In: *Journal of the American Chemical Society* 130 (2008), pp. 3307–3309. DOI: [10.1021/ja7109579](https://doi.org/10.1021/ja7109579).
- [22] Carsten Kötting, Jörn Güldenhaupt and Klaus Gerwert. In: *Chemical Physics* 396 (2012), pp. 72–83. DOI: <https://doi.org/10.1016/j.chemphys.2011.08.007>.
- [23] Dario Cambié, Cecilia Bottecchia, Natan J. W. Straathof, Volker Hessel and Timothy Noël. In: *Chemical Reviews* 116 (2016), pp. 10276–10341. DOI: [10.1021/acs.chemrev.5b00707](https://doi.org/10.1021/acs.chemrev.5b00707).
- [24] Joanna I. Zaitseva-Kinneberg et al. In: *RSC Adv.* 9 (15 2019), pp. 8695–8699. DOI: [10.1039/C9RA00968J](https://doi.org/10.1039/C9RA00968J).
- [25] Christof Grewer, Jürgen Jäger, Barry K. Carpenter and George P. Hess. In: *Biochemistry* 39 (2000), pp. 2063–2070. DOI: [10.1021/bi9919652](https://doi.org/10.1021/bi9919652).
- [26] Qing Cheng, Mark G. Steinmetz and Vasanthi Jayaraman. In: *Journal of the American Chemical Society* 124 (2002), pp. 7676–7677. DOI: [10.1021/ja0259988](https://doi.org/10.1021/ja0259988).
- [27] Yuri V. Il'ichev, Markus A. Schwörer and Jakob Wirz. In: *Journal of the American Chemical Society* 126 (2004), pp. 4581–4595. DOI: [10.1021/ja039071z](https://doi.org/10.1021/ja039071z).
- [28] Dennis Binder et al. In: *ChemBioChem* 17 (2016), pp. 296–299. DOI: <https://doi.org/10.1002/cbic.201500609>.

- [29] Christian G Bochet. In: *Tetrahedron Letters* 41 (2000), pp. 6341–6346. DOI: [https://doi.org/10.1016/S0040-4039\(00\)01050-9](https://doi.org/10.1016/S0040-4039(00)01050-9).
- [30] Francis M. Rossi and Joseph P.Y. Kao. In: *Journal of Biological Chemistry* 272 (1997), pp. 3266–3271. DOI: [10.1074/jbc.272.6.3266](https://doi.org/10.1074/jbc.272.6.3266).
- [31] Hugo E. Gottlieb, Vadim Kotlyar and Abraham Nudelman. In: *The Journal of Organic Chemistry* 62 (1997), pp. 7512–7515. DOI: [10.1021/jo971176v](https://doi.org/10.1021/jo971176v).
- [32] Francis M. Rossi, Michael Margulis, Cha-Min Tang and Joseph P.Y. Kao. In: *Journal of Biological Chemistry* 272 (1997), pp. 32933–32939. DOI: [10.1074/jbc.272.52.32933](https://doi.org/10.1074/jbc.272.52.32933).
- [33] Kavita Manju and Sanjay Trehan. In: *J. Chem. Soc., Perkin Trans. 1* (1995), pp. 2383–2384. DOI: [10.1039/P19950002383](https://doi.org/10.1039/P19950002383).
- [34] Ulrich Widmer. EN. In: *Synthesis* (1983), pp. 135–136. DOI: [10.1055/s-1983-30253](https://doi.org/10.1055/s-1983-30253).
- [35] R.F. Abdulla and R.S. Brinkmeyer. In: *Tetrahedron* 35 (1979), pp. 1675–1735. DOI: [https://doi.org/10.1016/0040-4020\(79\)88001-1](https://doi.org/10.1016/0040-4020(79)88001-1).
- [36] Michail Tsakos, Eva S. Schaffert, Lise L. Clement, Nikolaj L. Villadsen and Thomas B. Poulsen. In: *Nat. Prod. Rep.* 32 (4 2015), pp. 605–632. DOI: [10.1039/C4NP00106K](https://doi.org/10.1039/C4NP00106K).
- [37] Brendan T. Parr, Christos Economou and Seth B. Herzon. In: *Nature* 525 (2015), pp. 507–510. DOI: [10.1038/nature14902](https://doi.org/10.1038/nature14902).
- [38] Pauli Virtanen et al. In: *Nature Methods* 17 (2020), pp. 261–272. DOI: [10.1038/s41592-019-0686-2](https://doi.org/10.1038/s41592-019-0686-2).
- [39] J. D. Hunter. In: *Computing in Science & Engineering* 9 (2007), pp. 90–95. DOI: [10.1109/MCSE.2007.55](https://doi.org/10.1109/MCSE.2007.55).
- [40] Michael P. Frank and Robert W. Powers. In: *Journal of Chromatography B* 852 (2007), pp. 646–649. DOI: <https://doi.org/10.1016/j.jchromb.2007.01.002>.
- [41] A. Defoin, R. Defoin-Straatmann, K. Hildenbrand, E. Bittersmann, D. Kreft and H.J. Kuhn. In: *Journal of Photochemistry* 33 (1986), pp. 237–255. DOI: [https://doi.org/10.1016/0047-2670\(86\)87038-1](https://doi.org/10.1016/0047-2670(86)87038-1).
- [42] E. J. Corey, Raman K. Bakshi, Saizo Shibata, Chung Pin Chen and Vinod K. Singh. In: *Journal of the American Chemical Society* 109 (1987), pp. 7925–7926. DOI: [10.1021/ja00259a075](https://doi.org/10.1021/ja00259a075).
- [43] Thomas R. Hoye, Christopher S. Jeffrey and Feng Shao. In: *Nature Protocols* 2 (2007), pp. 2451–2458. DOI: [10.1038/nprot.2007.354](https://doi.org/10.1038/nprot.2007.354).
- [44] E. J. Corey, Raman K. Bakshi and Saizo Shibata. In: *Journal of the American Chemical Society* 109 (1987), pp. 5551–5553. DOI: [10.1021/ja00252a056](https://doi.org/10.1021/ja00252a056).

- [45] E.J. Corey, Mihai Azimioara and Sepehr Sarshar. In: *Tetrahedron Letters* 33 (1992), pp. 3429–3430. DOI: [https://doi.org/10.1016/S0040-4039\(00\)92654-6](https://doi.org/10.1016/S0040-4039(00)92654-6).
- [46] Shohei Hashiguchi, Akio Fujii, Jun Takehara, Takao Ikariya and Ryoji Noyori. In: *Journal of the American Chemical Society* 117 (1995), pp. 7562–7563. DOI: [10.1021/ja00133a037](https://doi.org/10.1021/ja00133a037).
- [47] *RuCl[(S,S)-TsDPEN](mesitylen)*. <https://www.sigmaaldrich.com/DE/de/product/aldrich/708674>. Accessed: 2023-09-17.
- [48] Xiaofeng Wu and Jianliang Xiao. In: *Chem. Commun.* (24 2007), pp. 2449–2466. DOI: [10.1039/B618340A](https://doi.org/10.1039/B618340A).
- [49] Masahiko Hayashi, Tohru Matsuda and Nobuki Oguni. In: *J. Chem. Soc., Chem. Commun.* (19 1990), pp. 1364–1365. DOI: [10.1039/C39900001364](https://doi.org/10.1039/C39900001364).
- [50] Michael C. Pirrung and Steven W. Shuey. In: *The Journal of Organic Chemistry* 59 (1994), pp. 3890–3897. DOI: [10.1021/jo00093a021](https://doi.org/10.1021/jo00093a021).
- [51] Yuri N. Belokon' et al. In: *Journal of the American Chemical Society* 121 (1999), pp. 3968–3973. DOI: [10.1021/ja984197v](https://doi.org/10.1021/ja984197v).
- [52] Michael North, Dmitry L. Usanov and Carl Young. In: *Chemical Reviews* 108 (2008), pp. 5146–5226. DOI: [10.1021/cr800255k](https://doi.org/10.1021/cr800255k).
- [53] Dieter Enders, Christian R Thomas and Jan Runsink. In: *Tetrahedron: Asymmetry* 10 (1999), pp. 323–326. DOI: [https://doi.org/10.1016/S0957-4166\(99\)00003-8](https://doi.org/10.1016/S0957-4166(99)00003-8).
- [54] Yuri V. Il'ichev and Jakob Wirz. In: *The Journal of Physical Chemistry A* 104 (2000), pp. 7856–7870. DOI: [10.1021/jp000261v](https://doi.org/10.1021/jp000261v).
- [55] J A McCray, L Herbette, T Kihara and D R Trentham. In: *Proceedings of the National Academy of Sciences of the United States of America* 77 (1980), pp. 7237–7241. DOI: [10.1073/pnas.77.12.7237](https://doi.org/10.1073/pnas.77.12.7237).
- [56] T. Schmierer, S. Laimgruber, K. Haiser, K. Kiewisch, J. Neugebauer and P. Gilch. In: *Phys. Chem. Chem. Phys.* 12 (48 2010), pp. 15653–15664. DOI: [10.1039/C004025H](https://doi.org/10.1039/C004025H).
- [57] R Wieboldt, K R Gee, L Niu, D Ramesh, B K Carpenter and G P Hess. In: *Proceedings of the National Academy of Sciences of the United States of America* 91 (1994), pp. 8752–8756. DOI: [10.1073/pnas.91.19.8752](https://doi.org/10.1073/pnas.91.19.8752).
- [58] Alexander G. Russell, Maria-Eleni Ragoussi, Rui Ramalho, Christopher W. Wharton, David Carteau, Dario M. Bassani and John S. Snaith. In: *The Journal of Organic Chemistry* 75 (2010), pp. 4648–4651. DOI: [10.1021/jo100783v](https://doi.org/10.1021/jo100783v).
- [59] Alexander G. Russell, Matthew J. Sadler, Helen J. Laidlaw, Agustín Gutiérrez-Lorienté, Christopher W. Wharton, David Carteau, Dario M. Bassani and John S. Snaith. In: *Photochemical & Photobiological Sciences* 11 (2012), pp. 556–563. DOI: [10.1039/c2pp05320a](https://doi.org/10.1039/c2pp05320a).

- [60] W. Kohn and L. J. Sham. In: *Phys. Rev.* 140 (4A 1965), A1133–A1138. DOI: [10.1103/PhysRev.140.A1133](https://doi.org/10.1103/PhysRev.140.A1133).
- [61] Axel D. Becke. In: *The Journal of Chemical Physics* 98 (1993), pp. 5648–5652. DOI: [10.1063/1.464913](https://doi.org/10.1063/1.464913).
- [62] John P. Perdew, Kieron Burke and Matthias Ernzerhof. In: *Phys. Rev. Lett.* 77 (18 1996), pp. 3865–3868. DOI: [10.1103/PhysRevLett.77.3865](https://doi.org/10.1103/PhysRevLett.77.3865).
- [63] John P. Perdew, Matthias Ernzerhof and Kieron Burke. In: *The Journal of Chemical Physics* 105 (1996), pp. 9982–9985. DOI: [10.1063/1.472933](https://doi.org/10.1063/1.472933).
- [64] Carlo Adamo and Vincenzo Barone. In: *The Journal of Chemical Physics* 110 (1999), pp. 6158–6170. DOI: [10.1063/1.478522](https://doi.org/10.1063/1.478522).
- [65] A. Klamt and G. Schüürmann. In: *J. Chem. Soc., Perkin Trans. 2* (5 1993), pp. 799–805. DOI: [10.1039/P29930000799](https://doi.org/10.1039/P29930000799).
- [66] TURBOMOLE V7.3 2018, a development of University of Karlsruhe and Forschungszentrum Karlsruhe GmbH, 1989-2007, TURBOMOLE GmbH, since 2007; available from <http://www.turbomole.com>.
- [67] Manoj K. Kesharwani, Brina Brauer and Jan M. L. Martin. In: *The Journal of Physical Chemistry A* 119 (2015), pp. 1701–1714. DOI: [10.1021/jp508422u](https://doi.org/10.1021/jp508422u).
- [68] Martin Feyereisen, George Fitzgerald and Andrew Komornicki. In: *Chemical Physics Letters* 208 (1993), pp. 359–363. DOI: [https://doi.org/10.1016/0009-2614\(93\)87156-W](https://doi.org/10.1016/0009-2614(93)87156-W).
- [69] Stefan Grimme, Jens Antony, Stephan Ehrlich and Helge Krieg. In: *The Journal of Chemical Physics* 132 (2010), p. 154104. DOI: [10.1063/1.3382344](https://doi.org/10.1063/1.3382344).
- [70] Jason Quenneville Benjamin G. Levine Chaehyuk Ko and Todd J. Martínez. In: *Molecular Physics* 104 (2006), pp. 1039–1051. DOI: [10.1080/00268970500417762](https://doi.org/10.1080/00268970500417762).
- [71] Benjamin Helmich-Paris. In: *Journal of Chemical Theory and Computation* 15 (2019), pp. 4170–4179. DOI: [10.1021/acs.jctc.9b00325](https://doi.org/10.1021/acs.jctc.9b00325).
- [72] Christof Hättig and Florian Weigend. In: *The Journal of Chemical Physics* 113 (2000), pp. 5154–5161. DOI: [10.1063/1.1290013](https://doi.org/10.1063/1.1290013).
- [73] Sarah Karbalaee Khani, Alireza Marefat Khah and Christof Hättig. In: *Phys. Chem. Chem. Phys.* 20 (24 2018), pp. 16354–16363. DOI: [10.1039/C8CP00643A](https://doi.org/10.1039/C8CP00643A).
- [74] Stefan van der Walt, S. Chris Colbert and Gael Varoquaux. In: *Computing in Science & Engineering* 13 (2011), pp. 22–30. DOI: [10.1109/MCSE.2011.37](https://doi.org/10.1109/MCSE.2011.37).

- [75] „A Crash Course in Photophysics and a Classification of Primary Photoreactions“. In: *Photochemistry of Organic Compounds*. John Wiley & Sons, Ltd, 2009. Chap. 2, pp. 25–72. ISBN: 9781444300017. DOI: <https://doi.org/10.1002/9781444300017.ch2>. eprint: <https://onlinelibrary.wiley.com/doi/pdf/10.1002/9781444300017.ch2>. URL: <https://onlinelibrary.wiley.com/doi/abs/10.1002/9781444300017.ch2>.
- [76] Alexander P. Demchenko, Vladimir I. Tomin and Pi-Tai Chou. In: *Chemical Reviews* 117 (2017), pp. 13353–13381. DOI: [10.1021/acs.chemrev.7b00110](https://doi.org/10.1021/acs.chemrev.7b00110).
- [77] Simon F. Bittmann et al. In: *Phys. Chem. Chem. Phys.* 21 (33 2019), pp. 18119–18127. DOI: [10.1039/C9CP02950H](https://doi.org/10.1039/C9CP02950H).
- [78] Tomáš Šolomek, Sébastien Mercier, Thomas Bally and Christian G. Bochet. In: *Photochem. Photobiol. Sci.* 11 (3 2012), pp. 548–555. DOI: [10.1039/C1PP05308F](https://doi.org/10.1039/C1PP05308F).
- [79] Chan-Ho Park and Richard S. Givens. In: *Journal of the American Chemical Society* 119 (1997), pp. 2453–2463. DOI: [10.1021/ja9635589](https://doi.org/10.1021/ja9635589).
- [80] D. Bradley G. Williams and Michelle Lawton. In: *The Journal of Organic Chemistry* 75 (2010), pp. 8351–8354. DOI: [10.1021/jo101589h](https://doi.org/10.1021/jo101589h).

## LIST OF HAZARDOUS CHEMICALS USED

| Reagent  | GHS pictograms  | GHS hazard and precaution statements  |
|--|---|---|
| Acetic acid, glacial<br>(AcOH)                       |    | H226, H314<br>P280, P305+351+338, P310  |
| Acetic acid anhydride<br>(Ac <sub>2</sub> O)         |    | H226, H302, H314, H330<br>P210, P260, P280,<br>P304+340+310,<br>P305+351+338, P370+378  |
| Acetonitrile (MeCN)                                  |    | H225, H302, H312, H319,<br>H332<br>P210, P280, P305+351+338   |
| Acetone- <i>d</i> <sub>6</sub>                       |    | H225, H319, H336<br>P210, P261, P305+351+338  |
| 2-Aminopropan-1-ol                                   |    | H314<br>P280, P305+351+338, P310  |
| Benzene  |  | H225, H304, H315, H319,<br>H340, H350, H372, H410<br>P201, P210, P301+310,<br>P305+351+338, P308+313,<br>P331   |
| Borane-tetrahydrofuran<br>(BH <sub>3</sub> ·THF)     |  | H225, H260, H302, H315,<br>H318, H319, H335<br>P210, P223, P231+232,<br>P233, P240, P241, P242,<br>P243, P261, P264, P270,<br>P271, P280, P301+312,<br>P302+352, P303+361+353,<br>P304+340, P305+351+338,<br>P310, P312, P321, P330,<br>P332+313, P335+334,<br>P337+313 |
| 4-Bromo-<br>2-nitrobenzaldehyde<br>(4-Br-2-NBA)      |  | H302, H315, H317, H319,<br>H335, H400<br>P261, P273, P280,<br>P305+351+338  |
| <i>tert</i> -Butanol                                 |  | H225, H319, H332, H335<br>P210, P261, P305+351+338  |
| <i>tert</i> -Butyl<br>trichloroacetimidate<br>(TBTA) |  | H226, H302, H315, H319-<br>H335<br>P261-P305+351+338  |

|  |  |   |
|--|--|---|
| Celite®  |   | H319, H335<br>P261, P305+351+338  |
| Chloroform (CHCl <sub>3</sub> )  |    | H302, H315, H319, H331, H336, H351, H361d, H372<br>P201, P202, P260, P264, P270, P271, P280, P281, P301+330+331, P310, P302+352, P304+340, P311, P305+351+338, P308+313, P314, P332+313, P337+313, P362, P403+233, P235, P405, P501 |
| Chloroform- <i>d</i> (CDCl <sub>3</sub> )                                      |    | H302, H315, H319, H331, H351, H361d, H372<br>P260, P280, P301+312+330, P304+340+312, P305+351+338, P403+233   |
| Dess-Martin periodinane (DMP)  |    | H272, H315, H319, H335<br>P210, P220, P221, P305+351+338, P370+378  |
| Dichloromethane (CH <sub>2</sub> Cl <sub>2</sub> )                             |    | H315, H319, H335, H336, H351, H373<br>P261, P281, P305+351+338  |
| <i>N,N'</i> -Dicyclohexylcarbodiimide (DCC)                                    |    | H302, H311, H317, H318  |
| Diethyl ether (Et <sub>2</sub> O)  |    | H224, H302, H336<br>P210, P261  |
| 4-Dimethylaminopyridine (DMAP)   |   | H301, H310, H315, H319, H335<br>P280, P305+351+338, P337+313  |
| <i>N,N</i> -Diisopropylethylamine (DIPEA)                                      |    | H225, H301, H314, H412<br>P210, P273, P280, P301+310, P305+351+338, P310  |
| <i>N,N</i> -Dimethylformamide di- <i>tert</i> -butyl acetal (Widmer's reagent) |    | H226, H315, H319, H335<br>P261, P305+351+338  |
| Ethanol (EtOH)   |    | H225, H319<br>P210, P280, P305+351+338  |
| Ethyl acetate (EtOAc)  |    | H225, H319, H336<br>P210, P261, P305+351+338  |
| 1-Ethyl-3-(3-dimethylaminopropyl)-carbodiimide hydrochloride (EDC·HCl)         |    | H315, H318, H335<br>P261, P280, P305+351+338  |

|   |   |  |
|---|---|--|
| Formic acid (FA)                            |    | H226, H302, H314, H331<br>P210, P260, P280,<br>P304+340+310,<br>P305+351+338, P370+378   |
| <i>n</i> -Heptane                           |    | H225, H304, H315, H336,<br>H410<br>P210, P261, P273,<br>P301+310, P331   |
| Hexanes                                     |    | H225, H304, H315, H319,<br>H336, H361f, H373, H411<br>P201, P210, P273, P280,<br>P301+310, P331  |
| Hydrochloric acid, conc.<br>(HCl)           |    | H290, H314, H335<br>P260, P280, P303+361+353,<br>P305+351+338  |
| Hydrochloric acid (1 M)                     |    | H290   |
| Isopropanol ( <i>i</i> PrOH)                |    | H225, H319, H336<br>P210, P261, P305+351+338   |
| ( <i>R,R</i> )-Jacobsen's ligand<br>(salen) |    | H315, H319, H335<br>P261, P305+351+338   |
| Methanol (MeOH)                             |   | H225, H301, H311, H331,<br>H370<br>P210, P233, P240, P241,<br>P242, P243, P260,<br>P264, P270, P271,<br>P280, P301+330+331,<br>P310, P302+352, P312,<br>P303+361+353, P304+340,<br>P311, P305+351+338,<br>P307+311, P337+313, P361,<br>P363, P370+378, P403+233                                      |
| 2-Methyl-CBS-oxaza-<br>borolidine (CBS)     |  | H224, H225, H302, H304,<br>H315, H318, H319, H332,<br>H335, H336, H361, H373<br>P201, P202, P210, P233,<br>P240, P241, P242, P243,<br>P260, P261, P264, P270,<br>P271, P280, P281,<br>P301+310, P301+312,<br>P302+352, P303+361+353,<br>P304+312, P304+340,<br>P305+351+338, P308+313,<br>P310, P312 |

|  |  |  |
|--|--|--|
| Mosher's acid (MTPA)   |   | H315, H319, H335<br>P261, P264, P271, P280,<br>P302+352, P304+340,<br>P305+351+338, P312, P321,<br>P332+313, P337+313, P362,<br>P403+233, P405, P501 |
| Mosher's acid chloride (MTPA-Cl)                                     |   | H314<br>P280, P305+351+338, P310   |
| 2-Nitrobenzaldehyde (2-NBA)  |   | H302, H315, H319, H335,<br>H412<br>P261+264+270+271+280  |
| <i>n</i> -Pentane  |     | H225, H304, H336, H411<br>P210, P261, P273,<br>P301+310, P331  |
| Phenylglyoxylic acid   |   | H315, H319<br>P305+351+338   |
| Potassium cyanide (KCN)  |     | H290, H300, H310, H330,<br>H370, H372, H410<br>P260, P264, P273, P280,<br>P284, P301+310   |
| Sodium bisulfite (NaHSO <sub>3</sub> )                               |    | H302, H318<br>P280, P301+312+330,<br>P305+351+338+310  |
| Sulfuric acid (H <sub>2</sub> SO <sub>4</sub> )                      |   | H314<br>P260, P264, P280,<br>P301+330+331,<br>P303+361+353, P363,<br>P304+340, P305+351+338,<br>P310, P321, P405, P501                               |
| Tetrahydrofuran (THF)  |      | H225, H302, H319, H335,<br>H351<br>P210, P280, P301+312+330,<br>P305+351+338, P370+378,<br>P403+235  |
| Titanium chloride (1 M solution in CH <sub>2</sub> Cl <sub>2</sub> ) |      | H314, H335, H336, H351,<br>H373<br>P261, P280, P305+351+338,<br>P310   |
| Titanium isopropoxide  |    | H226, H319, H336<br>P210, P305+351+338,<br>P370+378  |
| Toluene  |      | H225, H361d, H304, H373,<br>H315, H336<br>P210, P240, P301+310,<br>P302+352, P308+313, P314,<br>P403+233   |

|                                |   |   |
|--------------------------------|---|---|
| Trifluoroacetic acid (TFA)     |  | H314, H332, H412<br>P261, P273, P280,<br>P303+361+353,<br>P304+340+310,<br>P305+351+338   |
| Trimethylsilyl cyanide (TMSCN) |  | H225, H300+310+330,<br>H410<br>P210, P260, P262, P273,<br>P280, P301+310+330,<br>P303+361+353,<br>P304+340+310, P370+378,<br>P391, P403+233 |

---

GHS pictogram key

| <b>Pictogram</b>  | <b>Code</b> | <b>Hazard</b>        |
|---|-------------|----------------------|
|    | GHS01       | Explosive            |
|    | GHS02       | Flammable            |
|   | GHS03       | Oxidising            |
|  | GHS04       | Compressed gas       |
|  | GHS05       | Corrosive            |
|  | GHS06       | Toxic                |
|  | GHS07       | Harmful              |
|  | GHS08       | Health hazard        |
|  | GHS09       | Environmental hazard |

# $^1\text{H}$ AND $^{13}\text{C}$ NMR SPECTRA OF NOVEL AND UNPUBLISHED COMPOUNDS

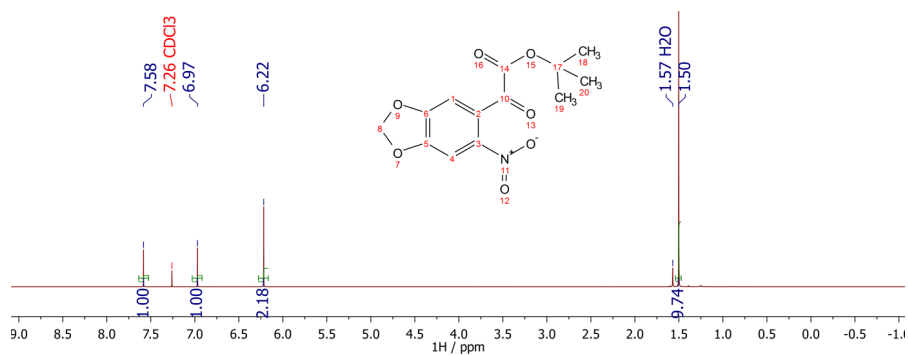


Figure I:  $^1\text{H}$  NMR (600 MHz,  $\text{CDCl}_3$ ) spectrum of  $t\text{Bu}$  CNPK.

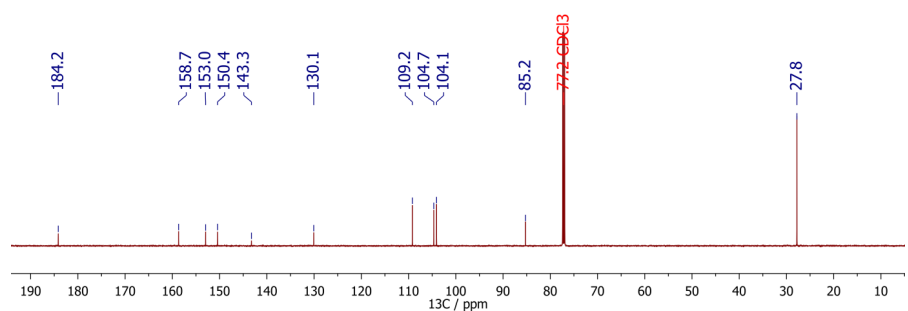


Figure II:  $^{13}\text{C}$  NMR (150 MHz,  $\text{CDCl}_3$ ) spectrum of  $t\text{Bu}$  CNPK.

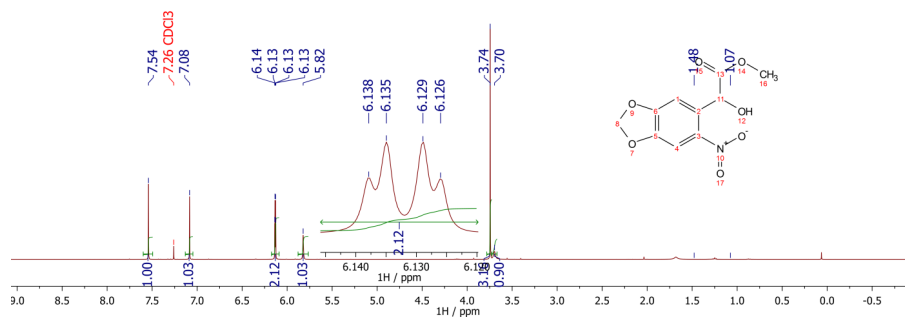
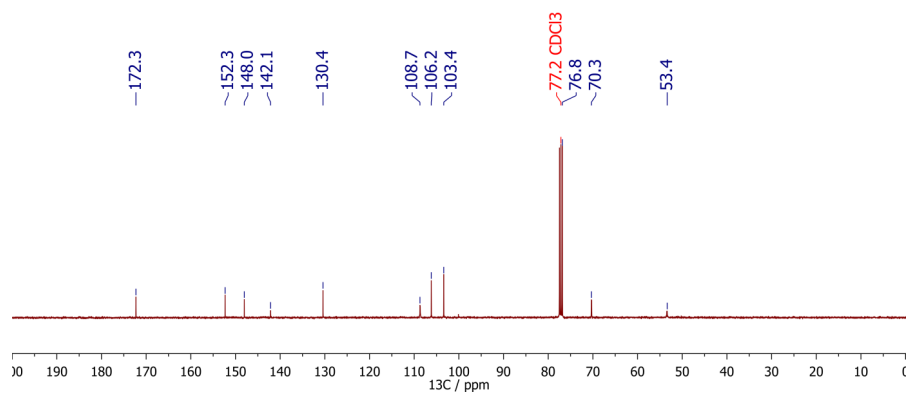
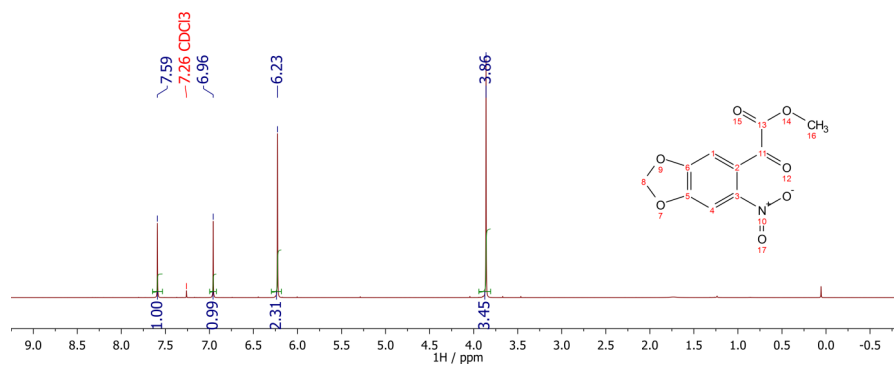
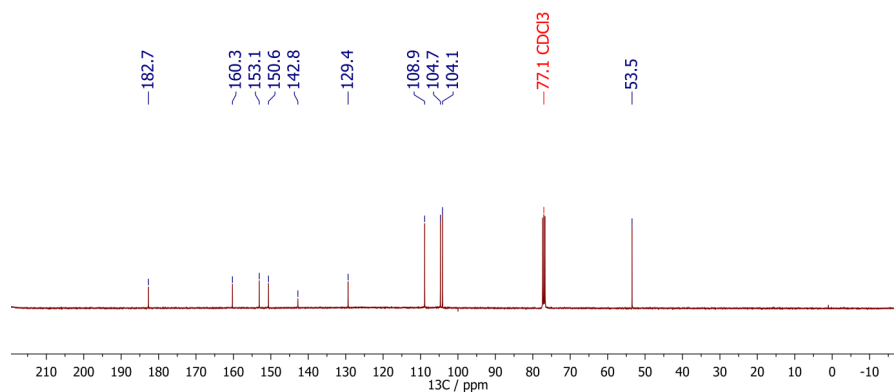


Figure III:  $^1\text{H}$  NMR (400 MHz,  $\text{CDCl}_3$ ) spectrum of  $\text{Me}$  CNP-OH.

Figure IV:  $^{13}\text{C}$  NMR (100 MHz,  $\text{CDCl}_3$ ) spectrum of Me CNP-OH.Figure V:  $^1\text{H}$  NMR (400 MHz,  $\text{CDCl}_3$ ) spectrum of Me CNPK.Figure VI:  $^{13}\text{C}$  NMR (100 MHz,  $\text{CDCl}_3$ ) spectrum of Me CNPK.

PUBLISHED  $^1\text{H}$  AND  $^{13}\text{C}$  NMR SPECTRA

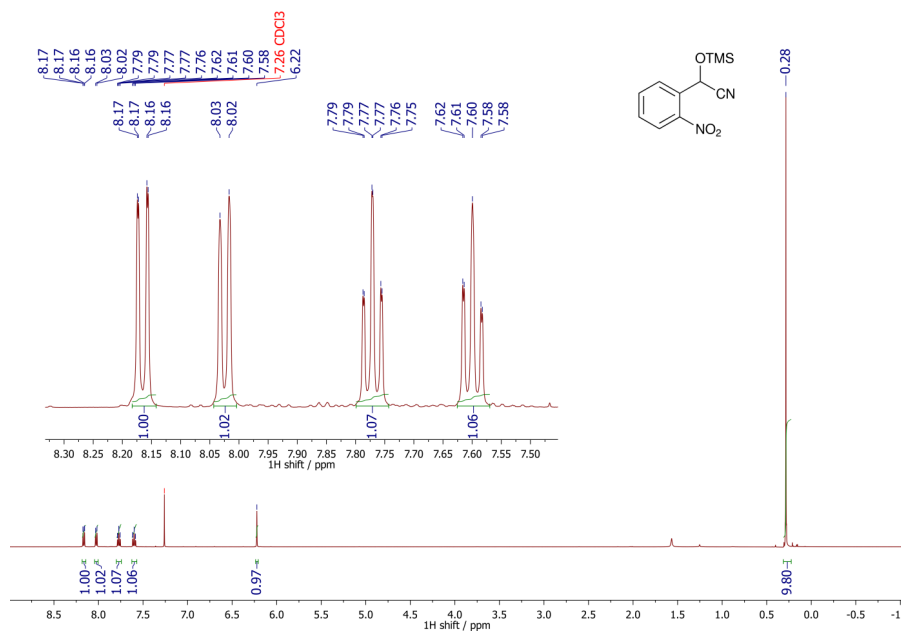


Figure VII:  $^1\text{H}$  NMR (500 MHz,  $\text{CDCl}_3$ ) spectrum of 2-NBA-TMSCN.

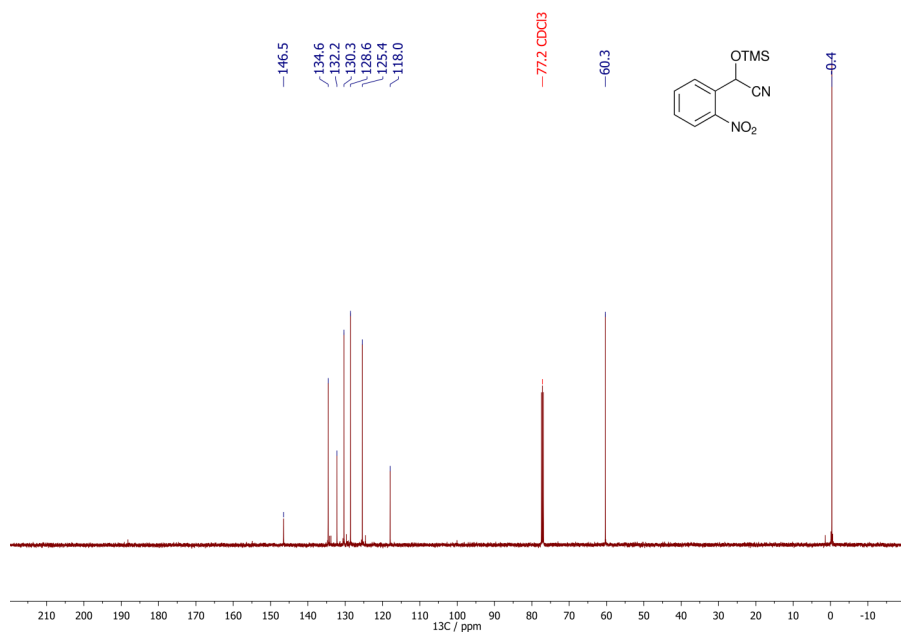
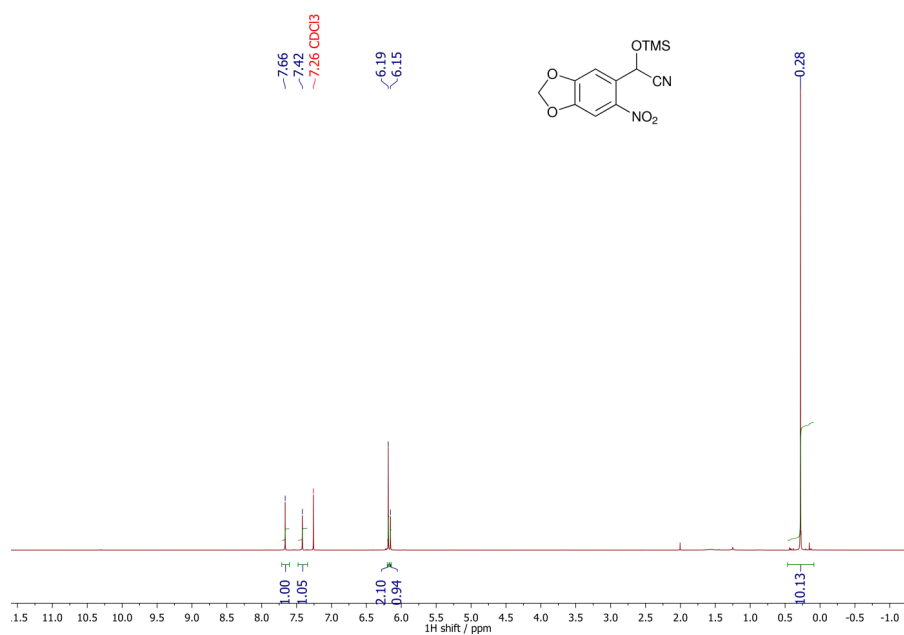
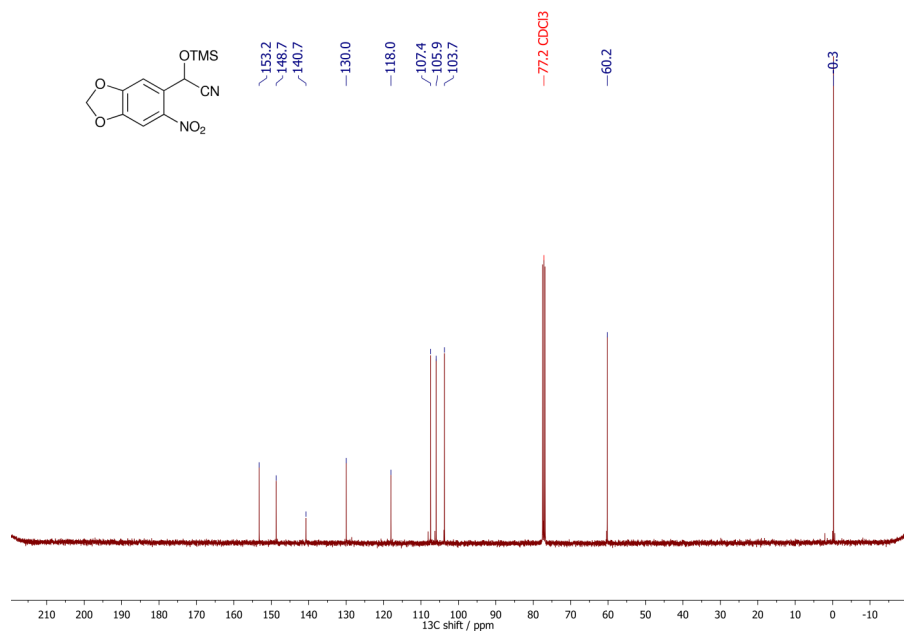
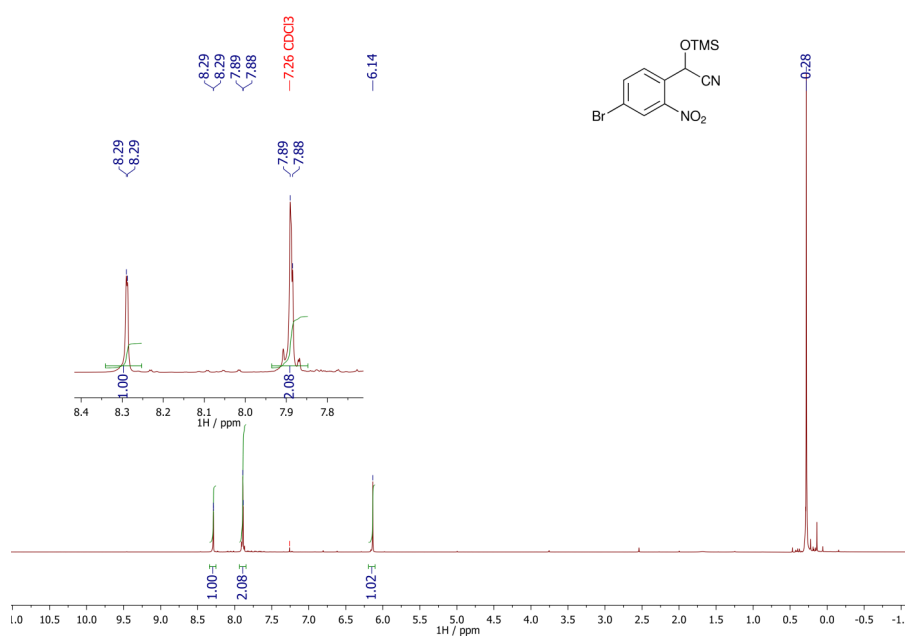
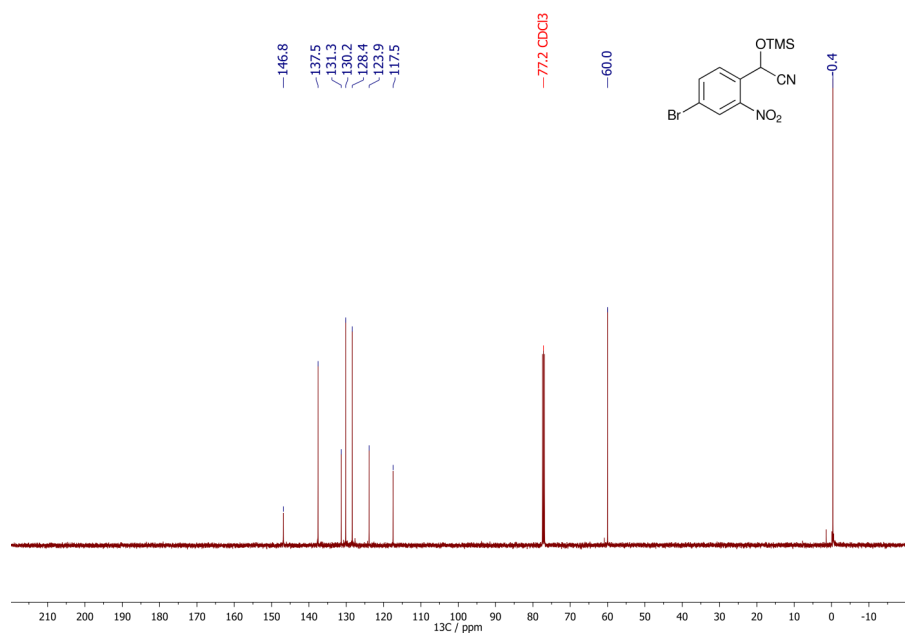
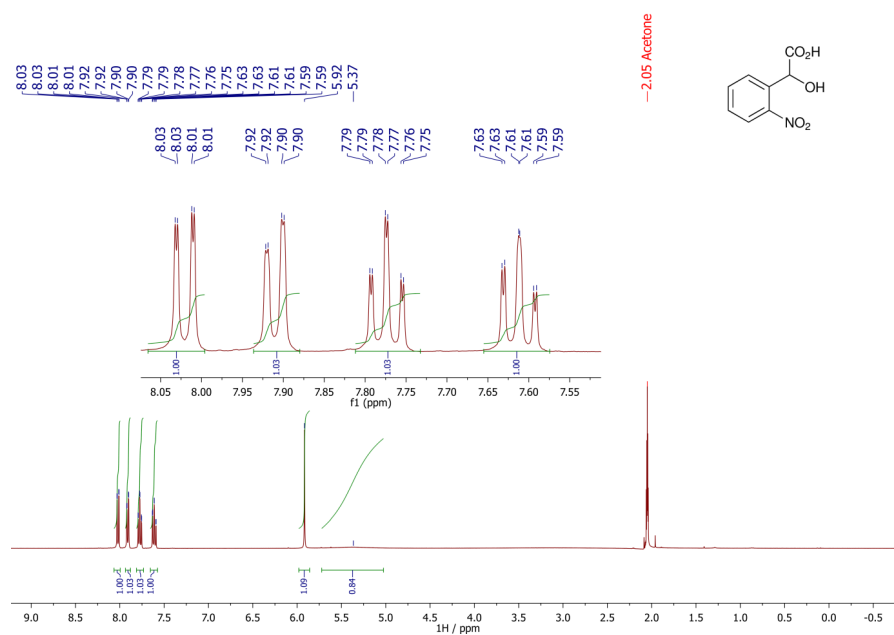
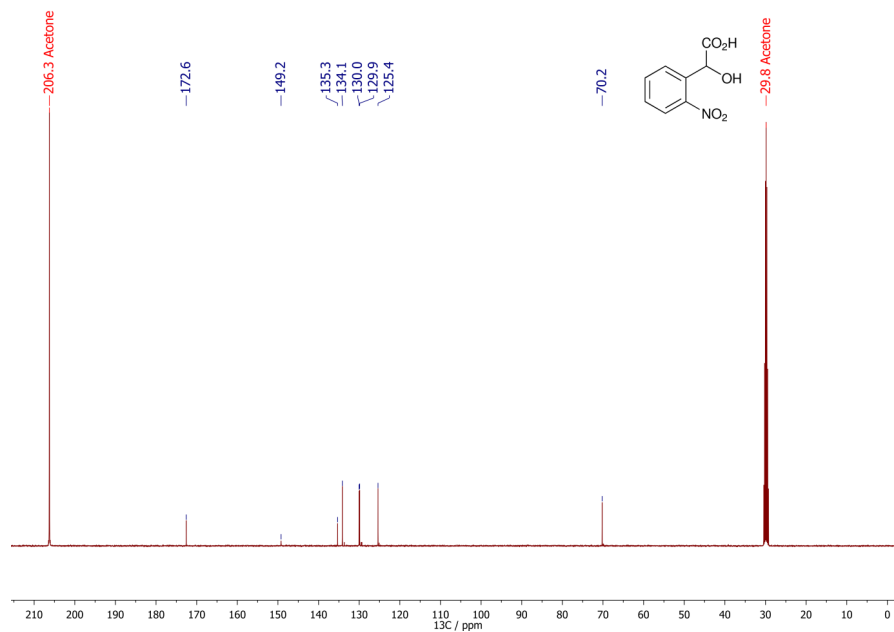


Figure VIII:  $^{13}\text{C}$  NMR (125 MHz,  $\text{CDCl}_3$ ) spectrum of 2-NBA-TMSCN.

Figure IX:  $^1\text{H}$  NMR (400 MHz,  $\text{CDCl}_3$ ) spectrum of 6-NPA-TMSCN.Figure X:  $^{13}\text{C}$  NMR (100 MHz,  $\text{CDCl}_3$ ) spectrum of 6-NPA-TMSCN.

Figure XI:  $^1\text{H}$  NMR (500 MHz,  $\text{CDCl}_3$ ) spectrum of 4-Br-NBA-TMSCN.Figure XII:  $^{13}\text{C}$  NMR (125 MHz,  $\text{CDCl}_3$ ) spectrum of 4-Br-NBA-TMSCN.

Figure XIII:  $^1\text{H}$  NMR (400 MHz, acetone- $d_6$ ) spectrum of CNB-OH.Figure XIV:  $^{13}\text{C}$  NMR (100 MHz, acetone- $d_6$ ) spectrum of CNB-OH.

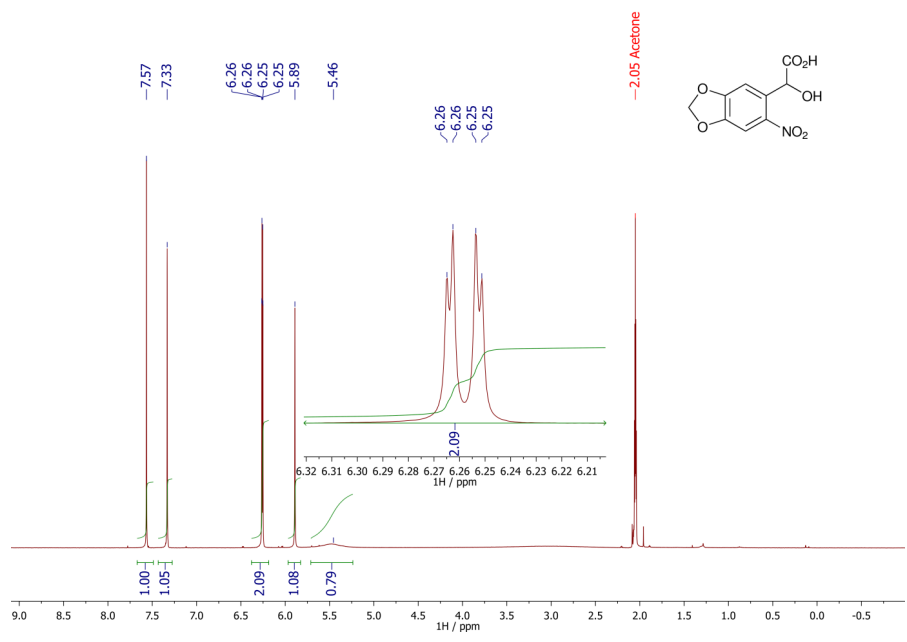


Figure XV:  $^1\text{H}$  NMR (400 MHz, acetone- $d_6$ ) spectrum of CNP-OH.

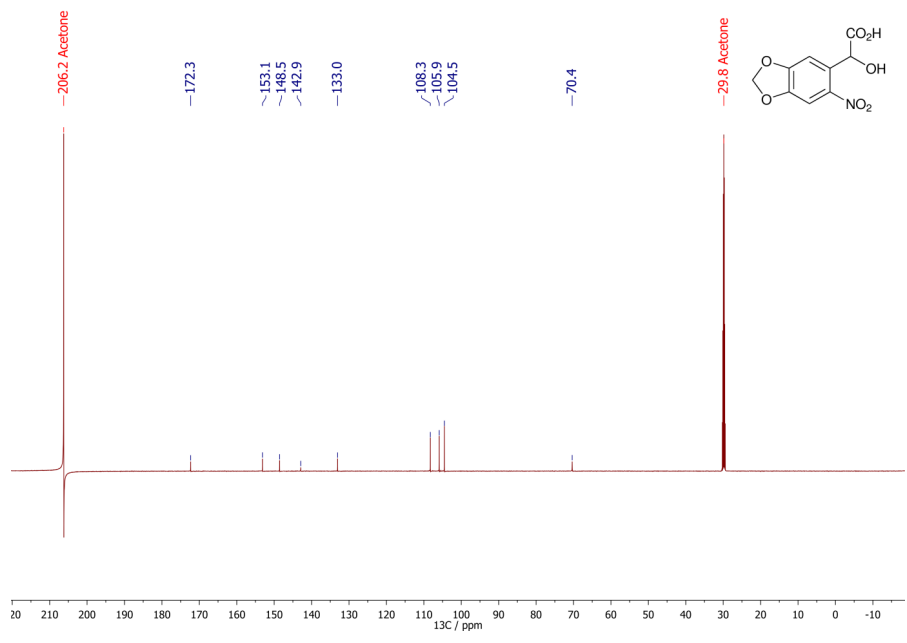
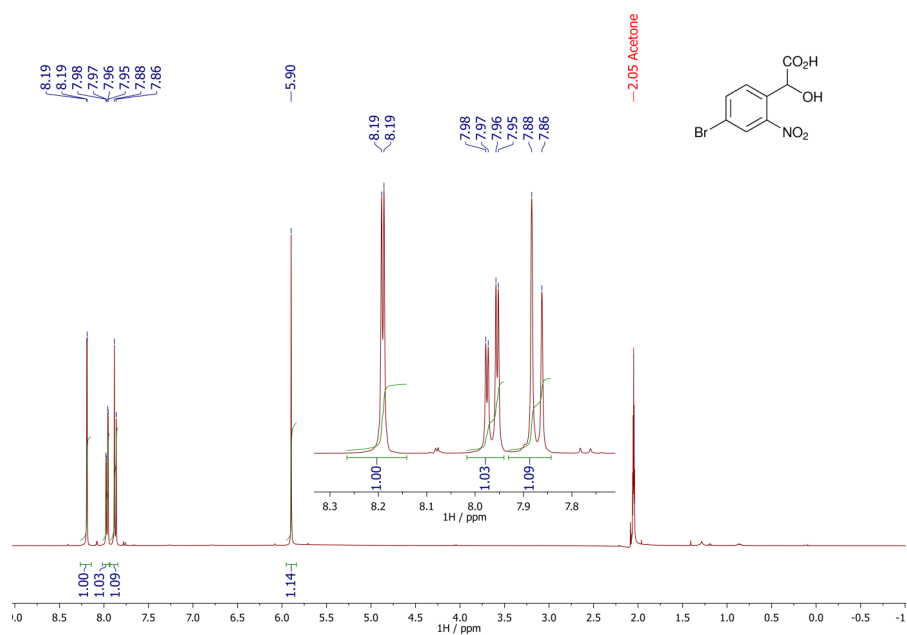
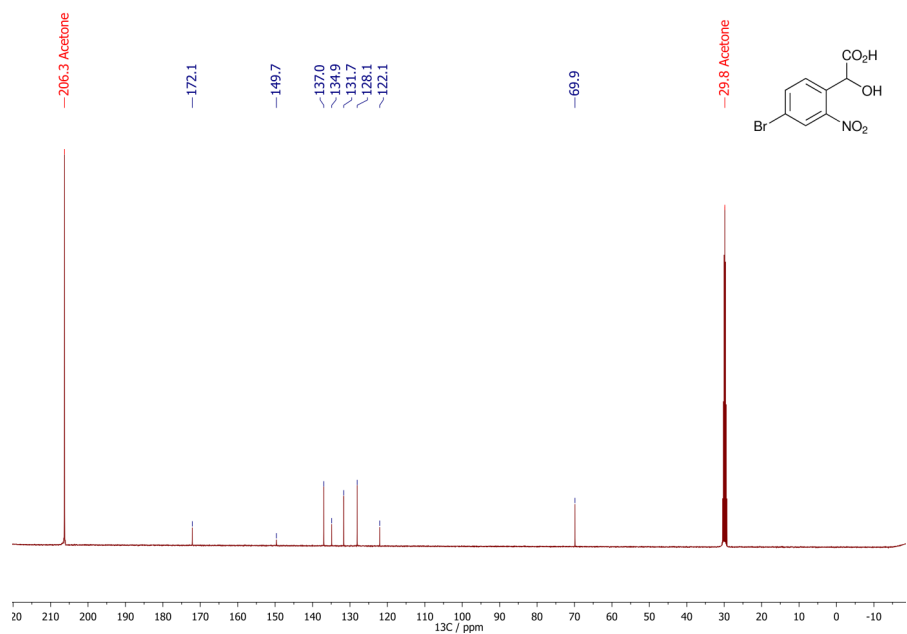


Figure XVI:  $^{13}\text{C}$  NMR (150 MHz, acetone- $d_6$ ) spectrum of CNP-OH.

Figure XVII:  $^1\text{H NMR}$  (400 MHz, acetone- $d_6$ ) spectrum of **4-Br-CNBr-OH**.Figure XVIII:  $^{13}\text{C NMR}$  (100 MHz, acetone- $d_6$ ) spectrum of **4-Br-CNBr-OH**.

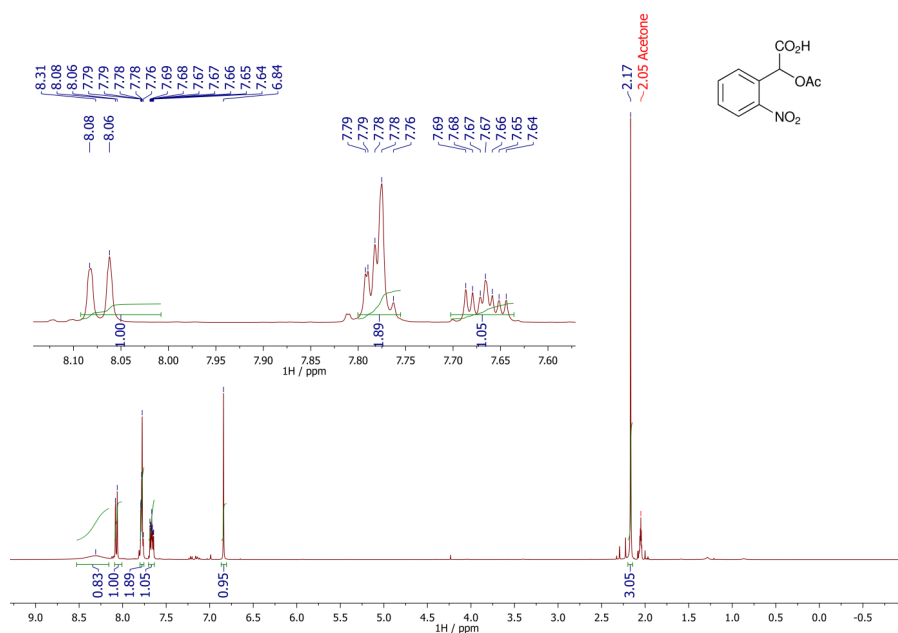


Figure XIX: <sup>1</sup>H NMR (400 MHz, DMSO-*d*<sub>6</sub>) spectrum of CNB-OAc.

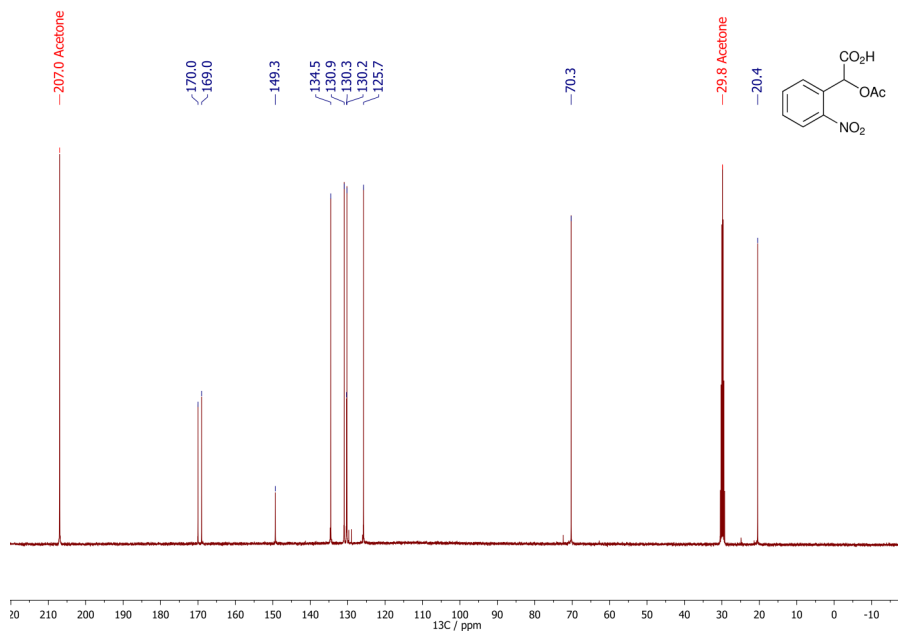
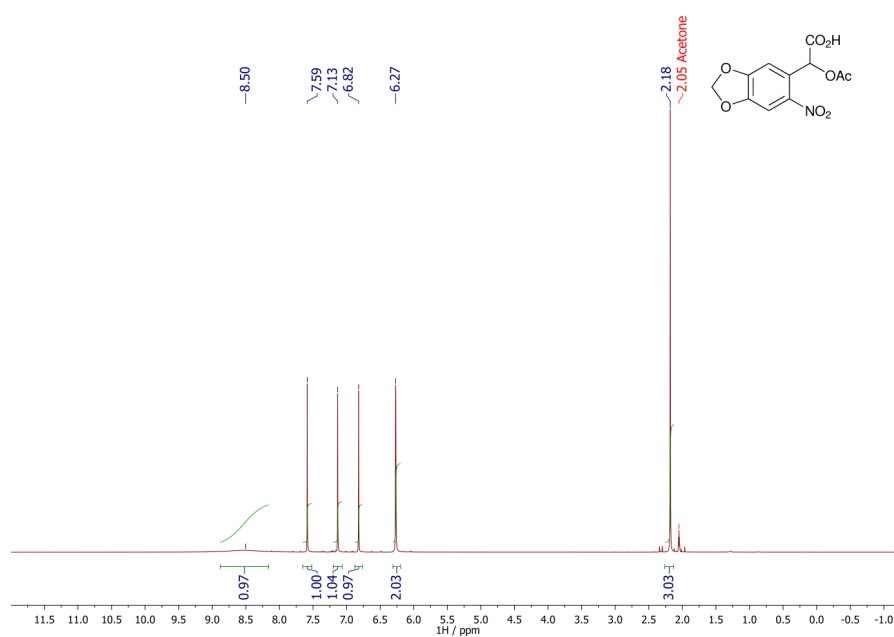
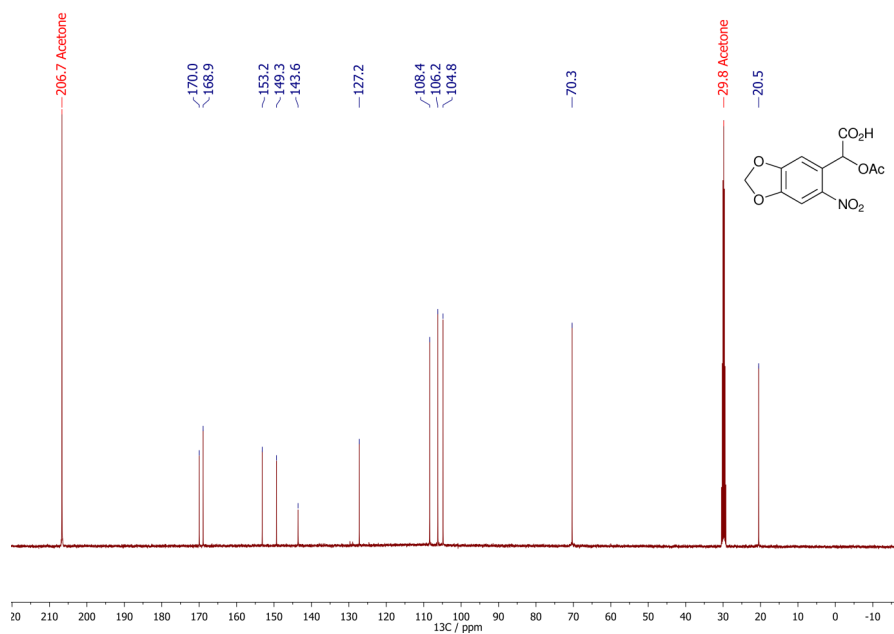


Figure XX: <sup>13</sup>C NMR (100 MHz, acetone-*d*<sub>6</sub>) spectrum of CNB-OAc.

Figure XXI:  $^1\text{H}$  NMR (400 MHz, acetone- $d_6$ ) spectrum of CNB-OAc.Figure XXII:  $^{13}\text{C}$  NMR (100 MHz, acetone- $d_6$ ) spectrum of CNB-OAc.

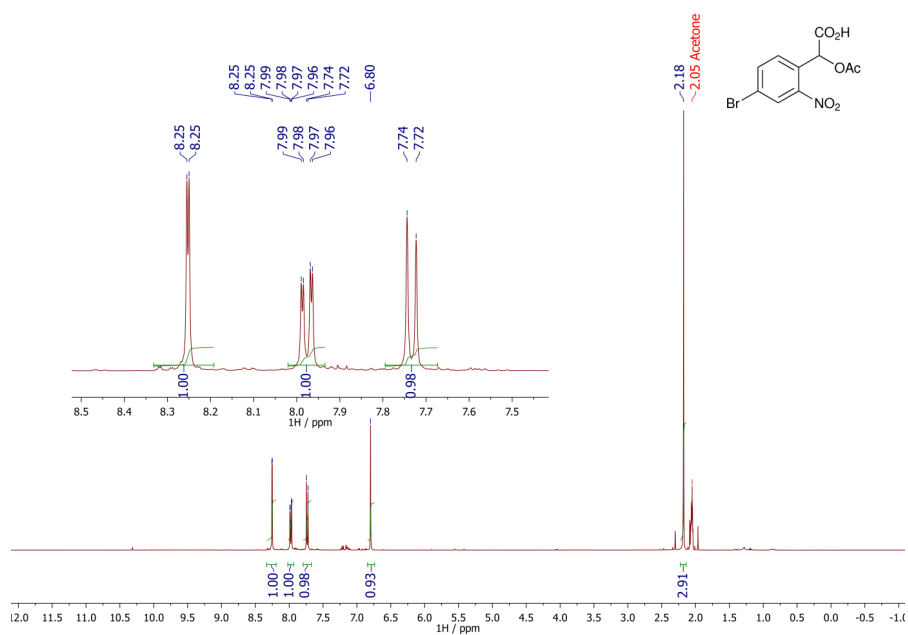


Figure XXIII: <sup>1</sup>H NMR (400 MHz, acetone-*d*<sub>6</sub>) spectrum of 4-Br-CNB-OAc.

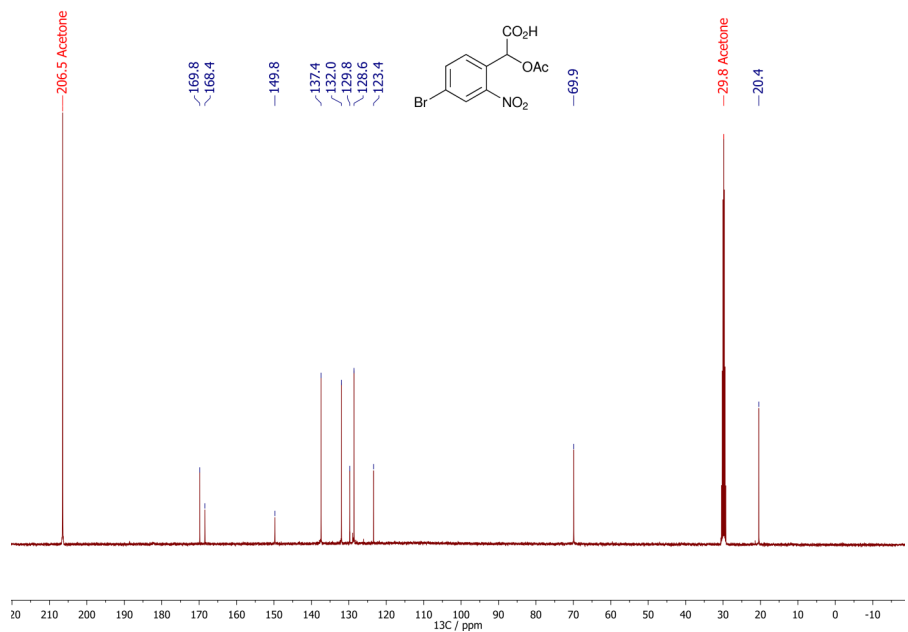
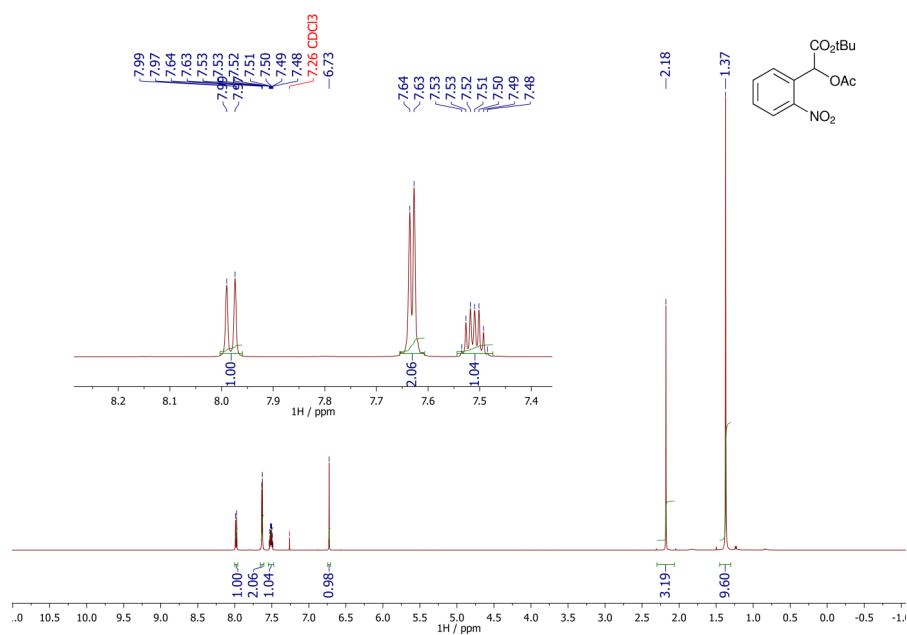
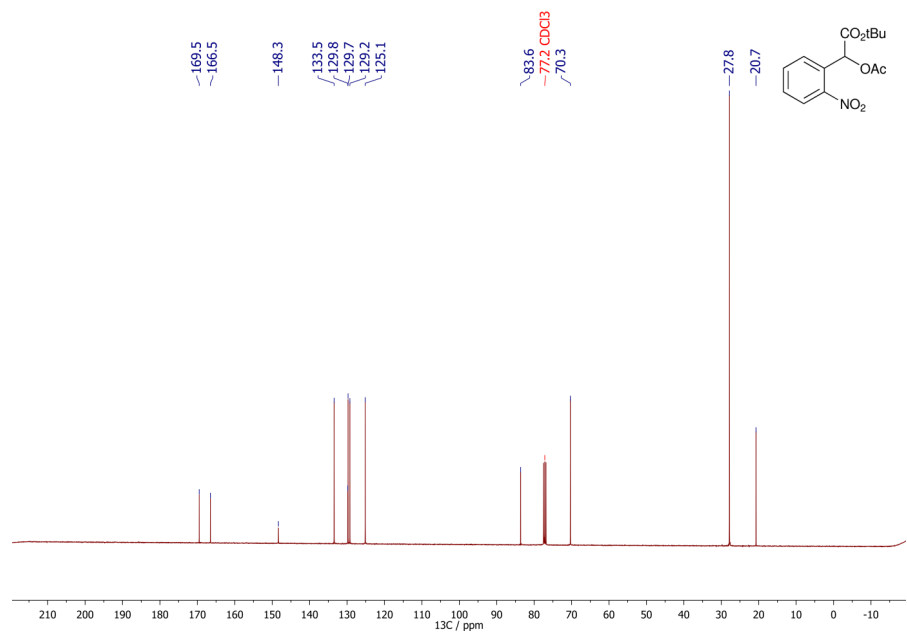


Figure XXIV: <sup>13</sup>C NMR (100 MHz, acetone-*d*<sub>6</sub>) spectrum of 4-Br-CNB-OAc.

Figure XXV:  $^1\text{H}$  NMR (500 MHz,  $\text{CDCl}_3$ ) spectrum of  $t\text{Bu CNB-OAc}$ .Figure XXVI:  $^{13}\text{C}$  NMR (100 MHz,  $\text{CDCl}_3$ ) spectrum of  $t\text{Bu CNB-OAc}$ .

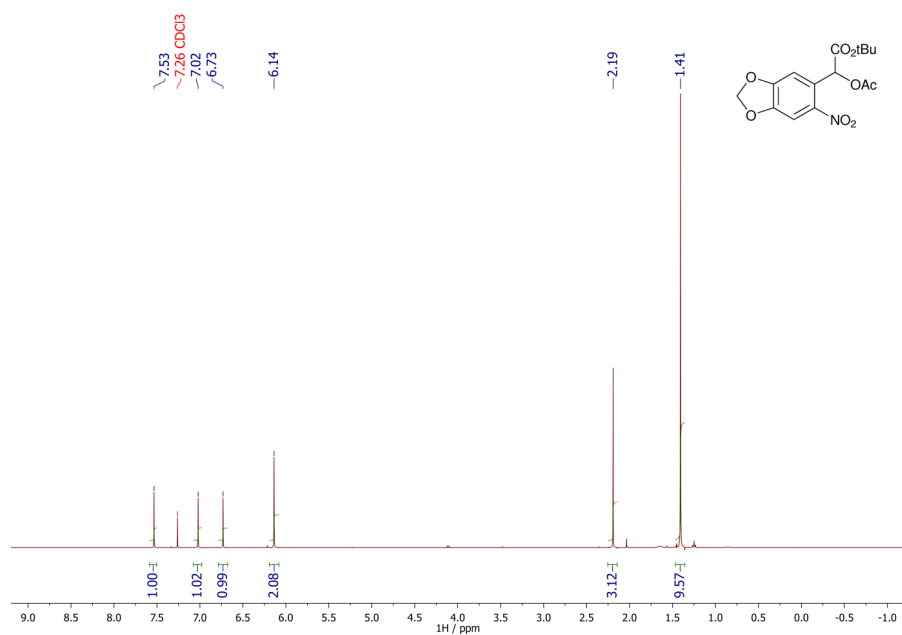


Figure XXVII:  $^1\text{H}$  NMR (400 MHz,  $\text{CDCl}_3$ ) spectrum of *t*Bu CNP-OAc.

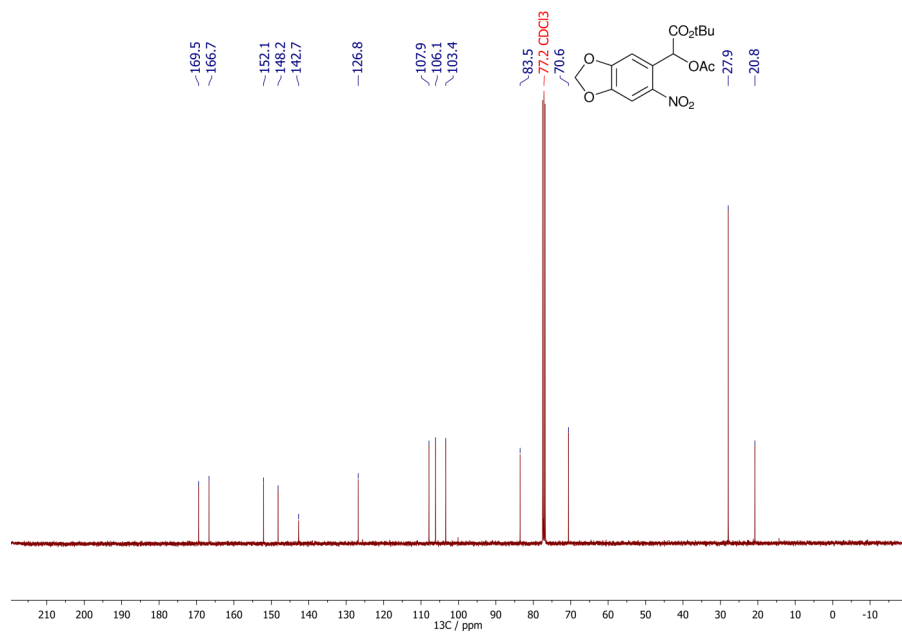
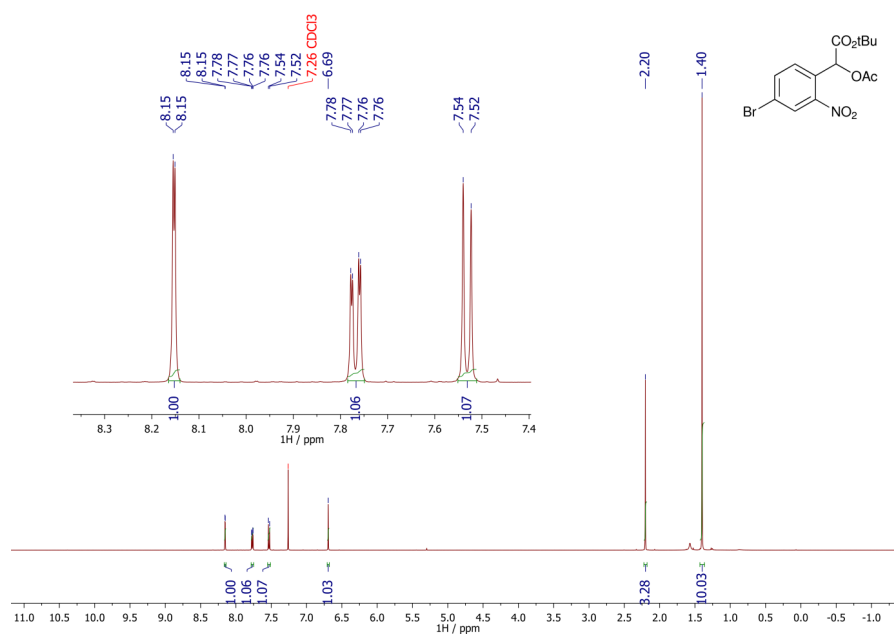
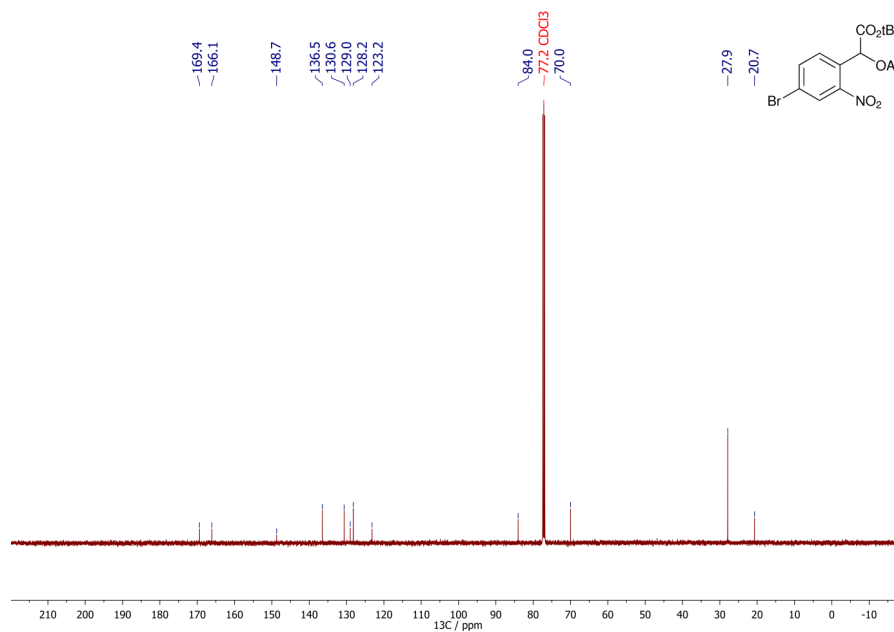
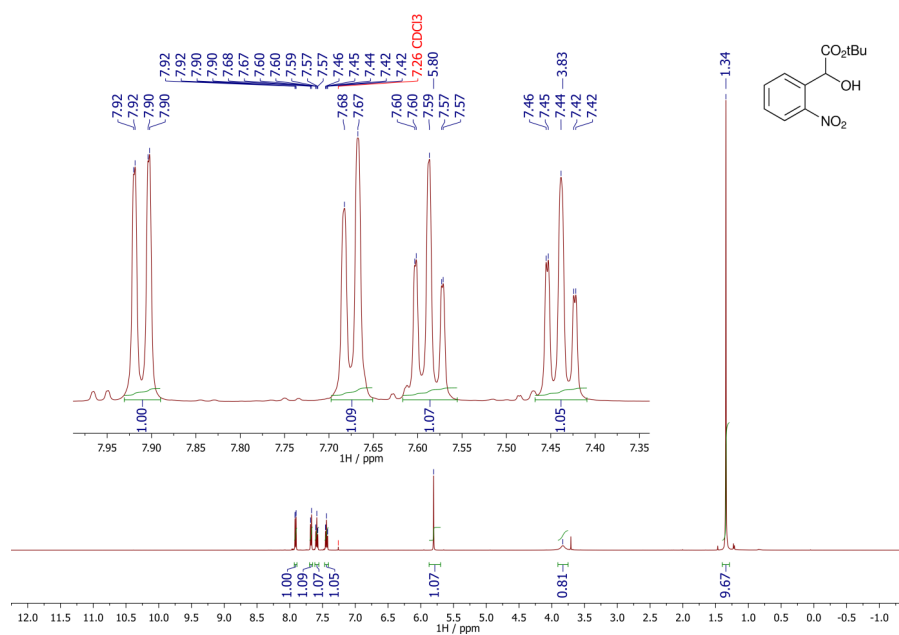
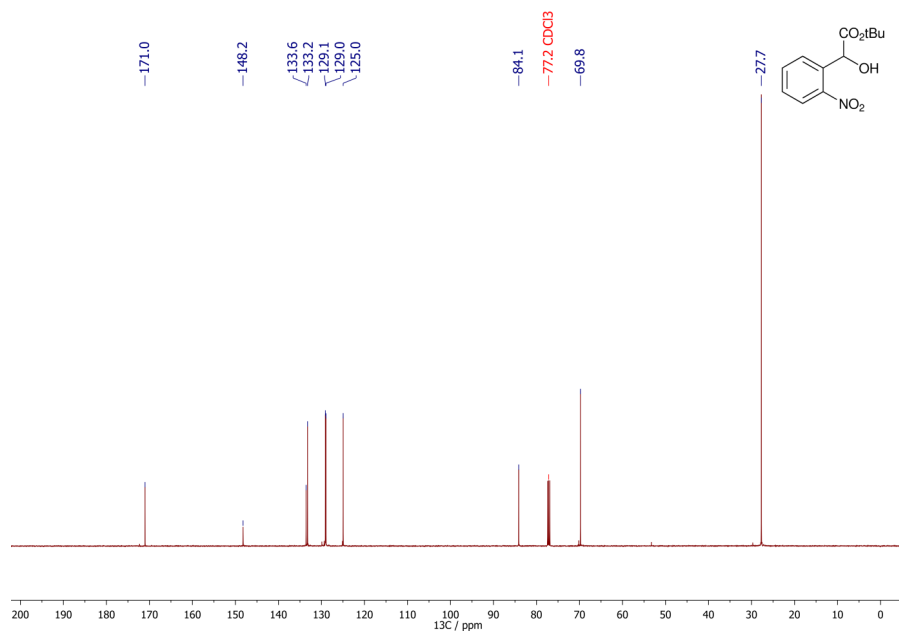
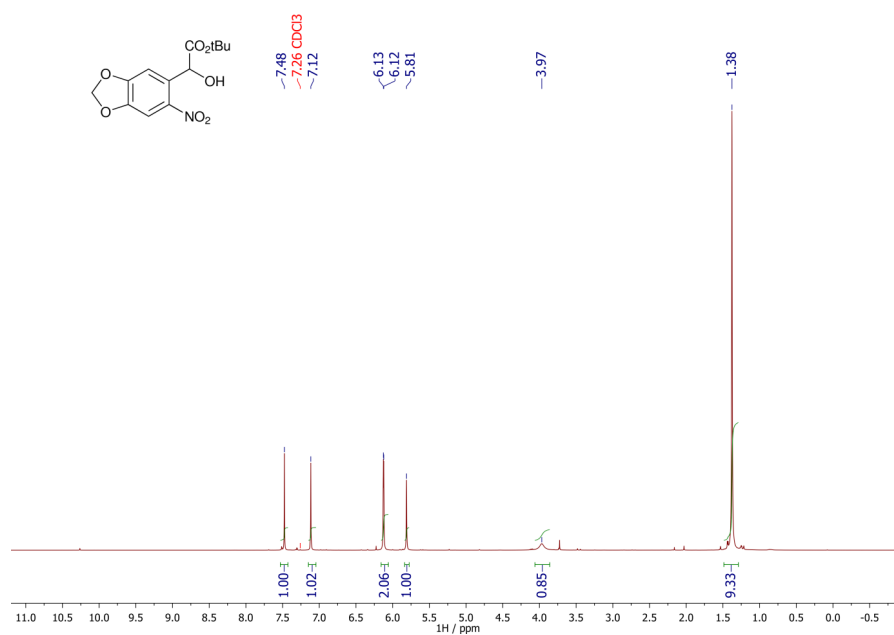
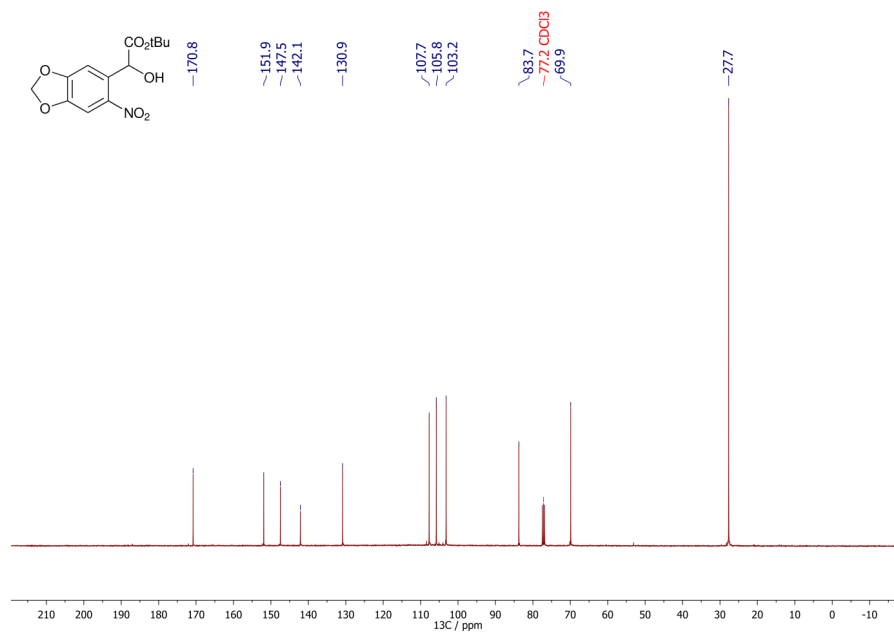
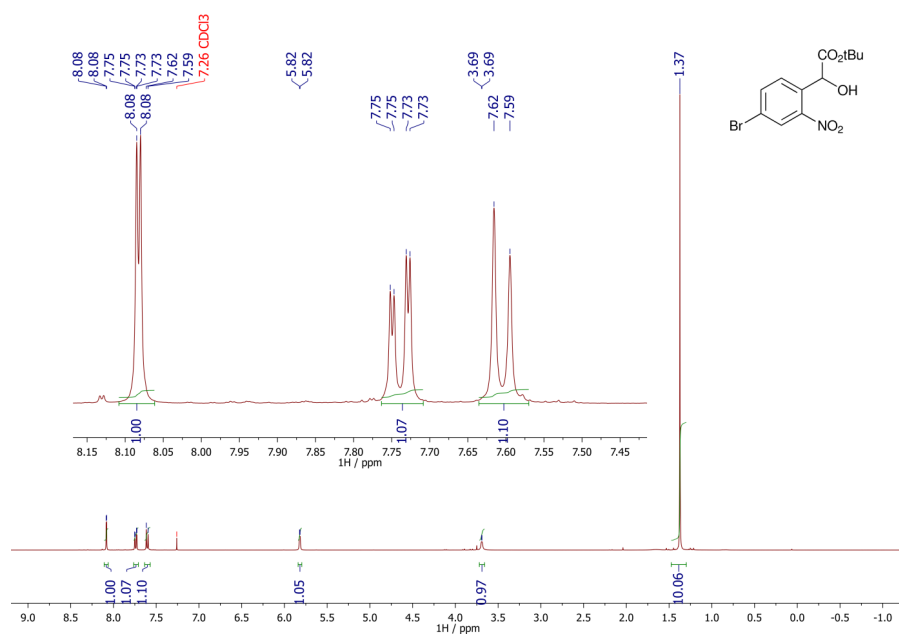
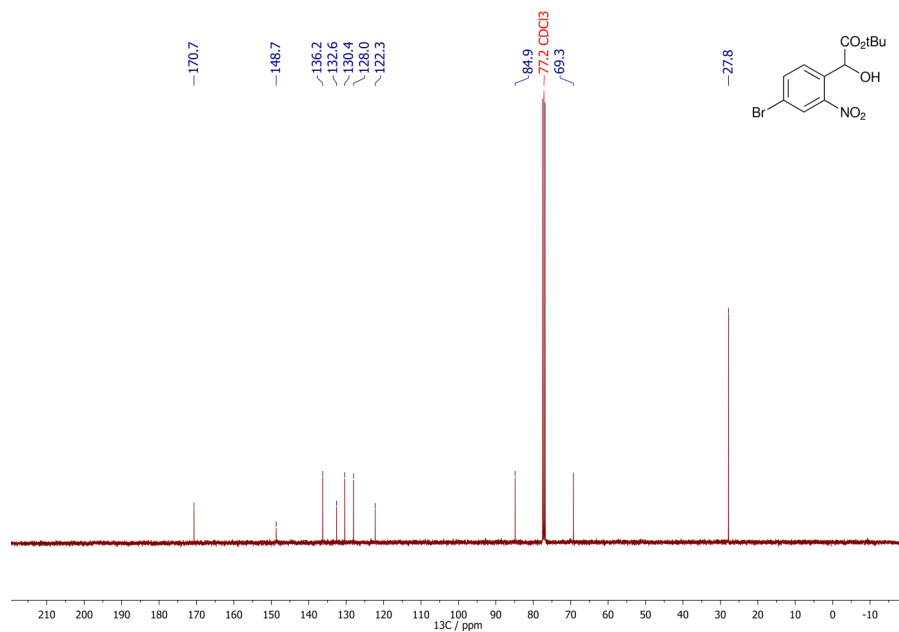


Figure XXVIII:  $^{13}\text{C}$  NMR (100 MHz,  $\text{CDCl}_3$ ) spectrum of *t*Bu CNP-OAc.

Figure XXIX: <sup>1</sup>H NMR (500 MHz, CDCl<sub>3</sub>) spectrum of *t*Bu 4-Br-CNBr-OAc.Figure XXX: <sup>13</sup>C NMR (125 MHz, CDCl<sub>3</sub>) spectrum of *t*Bu 4-Br-CNBr-OAc.

Figure XXXI:  $^1\text{H}$  NMR (500 MHz,  $\text{CDCl}_3$ ) spectrum of  $t\text{Bu}$  CNB-OH.Figure XXXII:  $^{13}\text{C}$  NMR (125 MHz,  $\text{CDCl}_3$ ) spectrum of  $t\text{Bu}$  CNB-OH.

Figure XXXIII:  $^1\text{H}$  NMR (400 MHz,  $\text{CDCl}_3$ ) spectrum of *t*Bu CNP-OH.Figure XXXIV:  $^{13}\text{C}$  NMR (100 MHz,  $\text{CDCl}_3$ ) spectrum of *t*Bu CNP-OH.

Figure XXXV:  $^1\text{H}$  NMR (400 MHz,  $\text{CDCl}_3$ ) spectrum of *t*Bu 4-Br-CNB-OH.Figure XXXVI:  $^{13}\text{C}$  NMR (100 MHz,  $\text{CDCl}_3$ ) spectrum of *t*Bu 4-Br-CNB-OH.

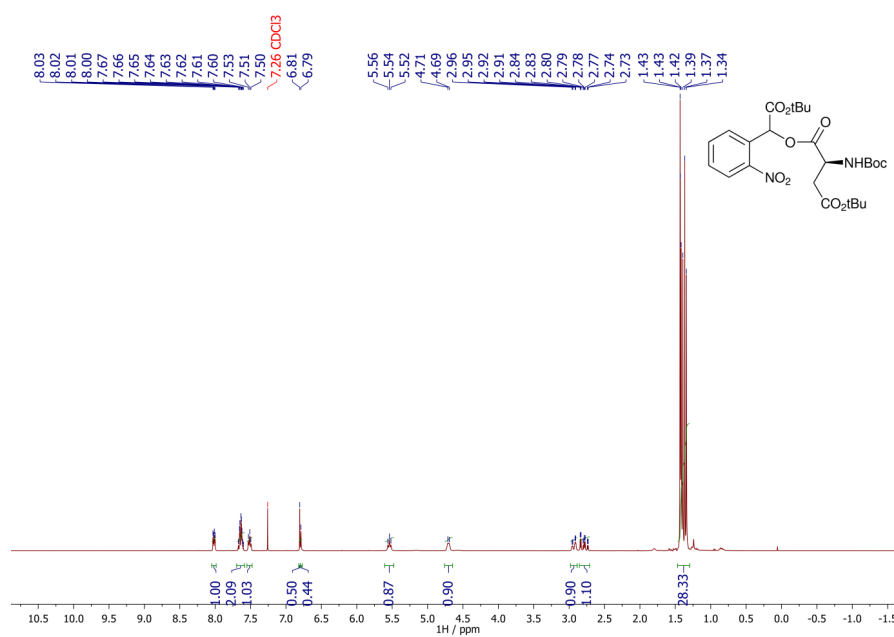


Figure XXXVII:  $^1\text{H}$  NMR (400 MHz,  $\text{CDCl}_3$ ) spectrum of di-*t*Bu N-Boc-1-CNB-L-Asp.

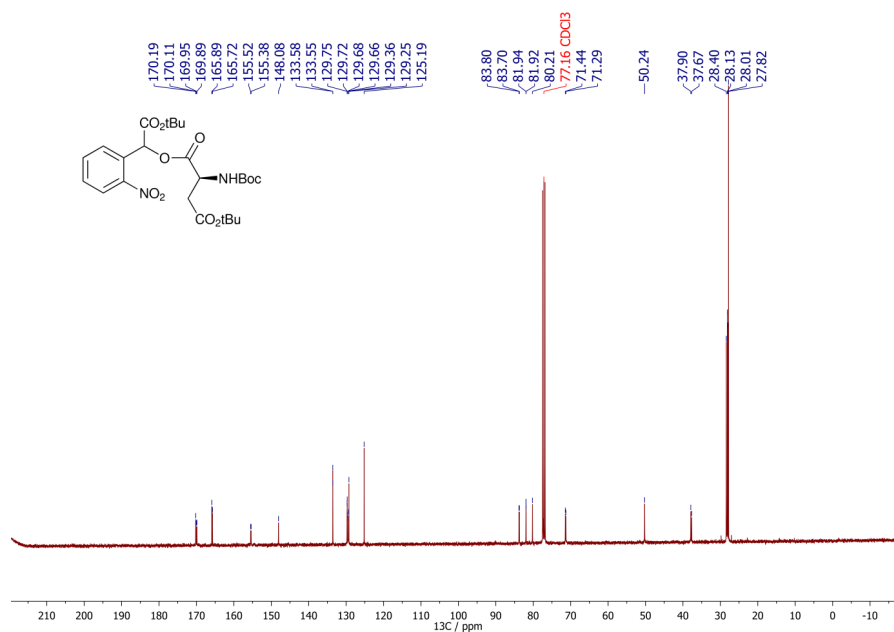


Figure XXXVIII:  $^{13}\text{C}$  NMR (100 MHz,  $\text{CDCl}_3$ ) spectrum of di-*t*Bu N-Boc-1-CNB-L-Asp.

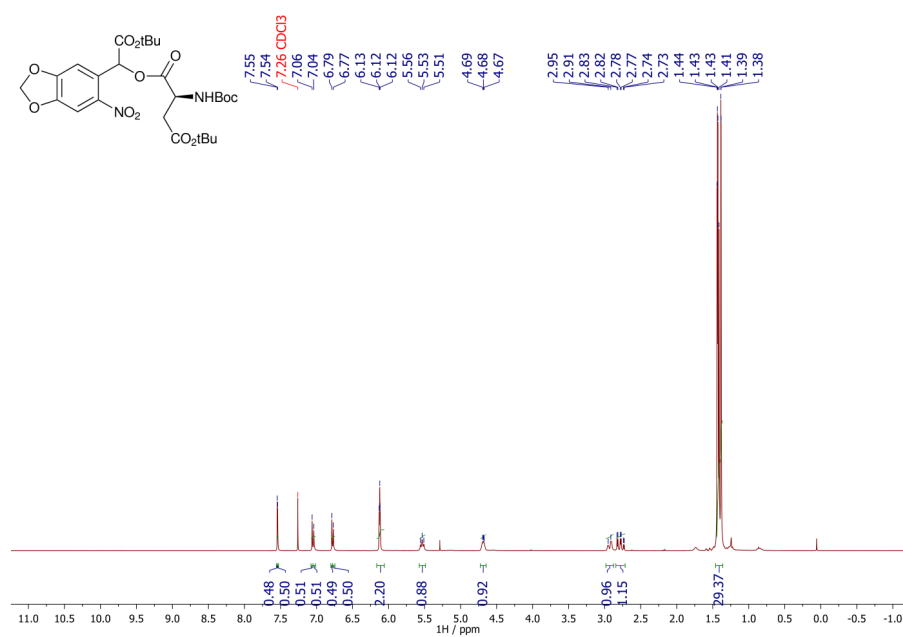


Figure XXXIX: <sup>1</sup>H NMR (400 MHz, CDCl<sub>3</sub>) spectrum of **di-<sup>t</sup>Bu N-Boc-1-CNP-L-Asp**.

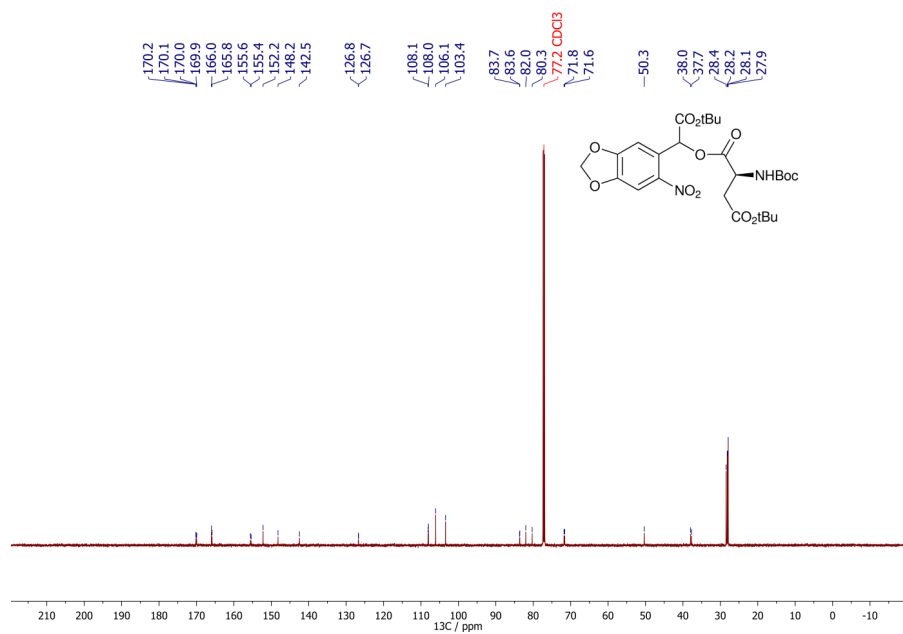


Figure XL: <sup>13</sup>C NMR (150 MHz, CDCl<sub>3</sub>) spectrum of **di-<sup>t</sup>Bu N-Boc-1-CNP-L-Asp**.

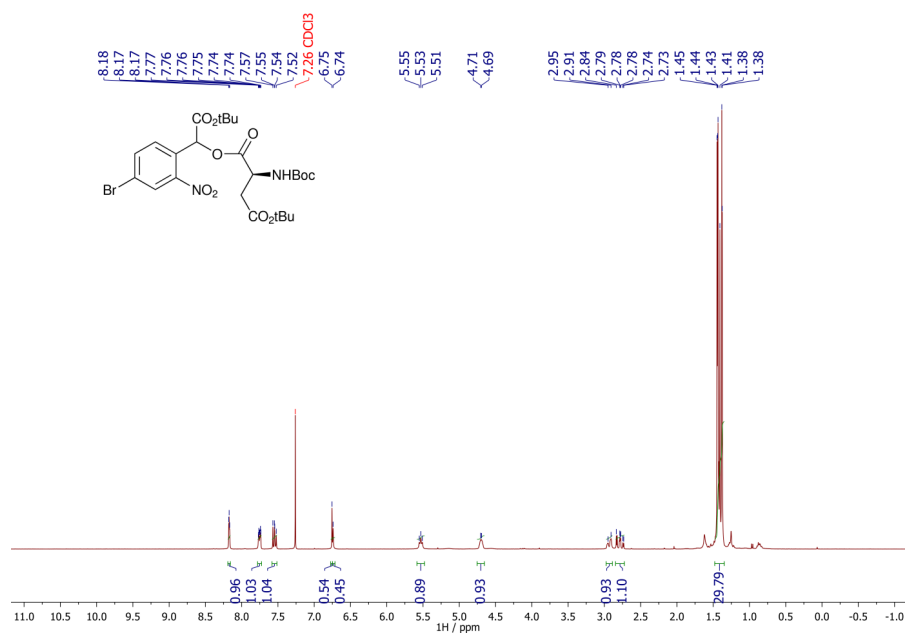


Figure XLI: <sup>1</sup>H NMR (400 MHz, CDCl<sub>3</sub>) spectrum of **di-<sup>t</sup>Bu N-Boc-1-(4-Br-CNB)-L-Asp**.

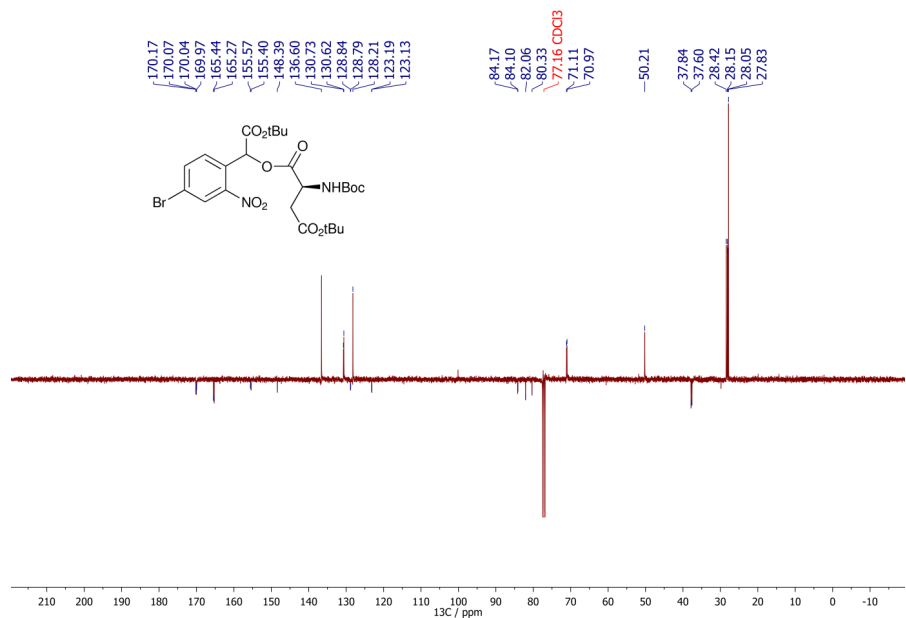
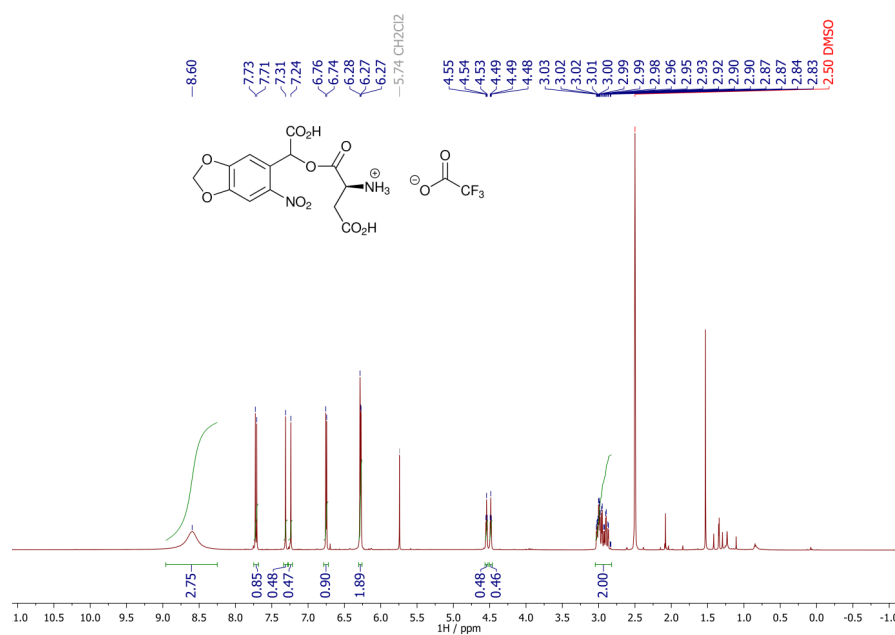
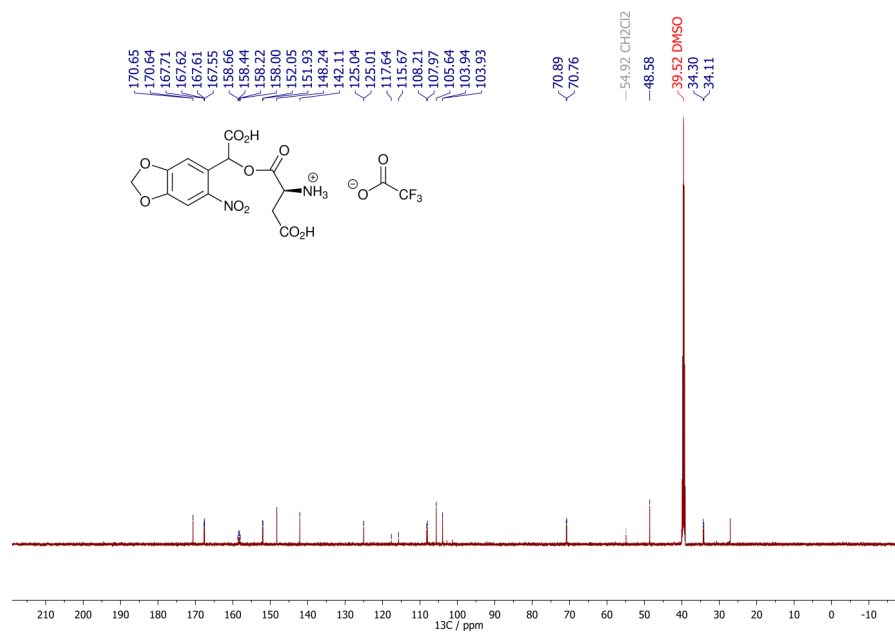


Figure XLII: <sup>13</sup>C NMR (DEPTQ-BBO, 100 MHz, CDCl<sub>3</sub>) spectrum of **di-<sup>t</sup>Bu N-Boc-1-(4-Br-CNB)-L-Asp**.



Figure XLV:  $^1\text{H}$  NMR (600 MHz,  $\text{DMSO-}d_6$ ) spectrum of **1-CNP-L-Asp**.Figure XLVI:  $^{13}\text{C}$  NMR (150 MHz,  $\text{DMSO-}d_6$ ) spectrum of **1-CNP-L-Asp**.

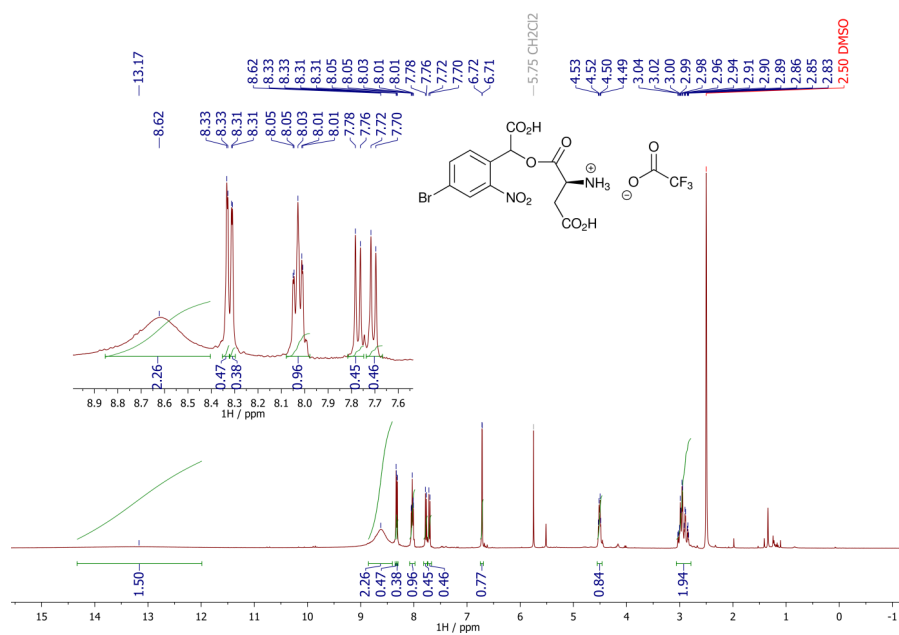


Figure XLVII: <sup>1</sup>H NMR (400 MHz, DMSO-*d*<sub>6</sub>) spectrum of **1-(4-Br-CNB)-L-Asp**.

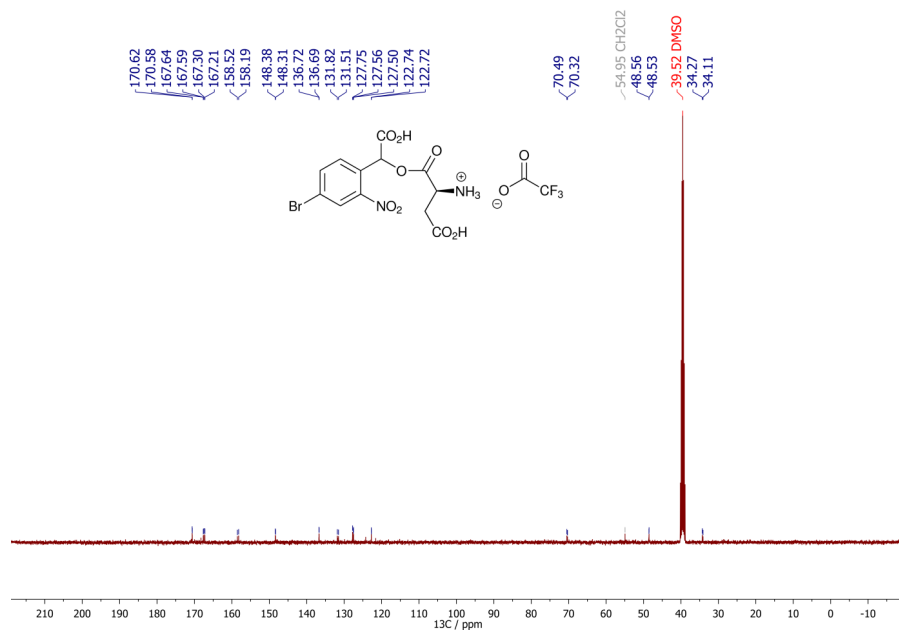


Figure XLVIII: <sup>13</sup>C NMR (100 MHz, DMSO-*d*<sub>6</sub>) spectrum of **1-(4-Br-CNB)-L-Asp**.



## PYTHON SCRIPTS

---

```
# generates Figure 3.9
import numpy as np
import scipy
import matplotlib.pyplot as plt
import scipy.optimize as opt import sys
from matplotlib.ticker import MultipleLocator, FormatStrFormatter

# function returns a tuple containing a time array (ps), a
# wavelength array (nm),
# and the absorbance matrix (mOD)
def extract_data(filename):
    raw = np.genfromtxt(filename, delimiter=',')
    # raw data contains a list of wavelengths in the first line,
    # terminated by a series of NaN
    # lines 2-4 are useless
    # matrix of absorbance values (milliOD, I think) starts at
    # raw[4:, 1:]
    # remember the format here is [columns, rows] and line 5 is
    # index 4
    # the NaNs in the wavelength list start at index 326, so
    # maybe just hardcode this cut-off
    absorbance_matrix = raw[4:, 1:326]
    wavelength_array = raw[0, 1:326] * 1000 # wavelengths are in
    # micron in the raw data, we want nm
    time_array = raw[4:, 0] / 1000 # convert from fs to ps
    return (time_array, wavelength_array, absorbance_matrix)

# function extract_wlen returns a time trace at a given
# wavelength, given the wavelength array
# and the full absorbance matrix as parameters
# desired_wlen must be in the range 300 to 900 nm
# a tuple is returned with the actual wavelength found and the
# time trace
# if the desired wavelength is outside the bounds of the
# terminal wavelengths in the dataset,
# the terminal trace is returned, otherwise, a weighted average
# of the two nearest sets is returned
# this represents a lot of time coding something cool for minor
# data smoothing which is not really necessary for thesis
def extract_wlen(desired_wlen, wavelength_array,
absorbance_matrix):
    if desired_wlen < 300 or desired_wlen > 900:
        print("wlen must be between 300 and 900")
    # find matching wavelength
    # actually we may want closest match, because some of the
    # longer wavelengths are more separated...
```

```

residual = np.sqrt(np.power(wavelength_array - desired_wlen,
    2))
# weird syntax but it does the job, np.where returns a tuple
# containing an array of min indices
index = np.where(residual == np.amin(residual))[0][0]

# in some cases, 2 arrays within the matrix will be a similar
# distance from the target # we can then take a weighted
# average of the two nearest traces
# special case if wlen is at the end or beginning of the set
if desired_wlen < wavelength_array[0]:
    return np.round(wavelength_array[0]), absorbance_matrix[:,
        0]
if desired_wlen > wavelength_array[-1]:
    return np.round(wavelength_array[-1]),
        absorbance_matrix[:, -1]

# this ensures we don't go out of bounds with the weighted
# averages
# if we're inbetween indices 0 and 1, res_prior will always
# be larger than res_next,
# if we're inbetween indices -2 and -1, res_next will always
# be larger
if index == 0:
    res_prior = 1e9
else:
    res_prior = residual[index - 1]
if index == len(residual):
    res_next = 1e9
else:
    res_next = residual[index + 1]
res_current = residual[index]

# choose which is the smaller neighbouring residual
if res_prior < res_next:
    # in this case index - 1 and index are more relevant
    res_sum = res_prior + res_current
    w = [res_sum/res_prior, res_sum/res_current]
    i = (index - 1, index + 1)
else:
    # otherwise
    res_sum = res_current + res_next
    w = [res_sum/res_current, res_sum/res_next] # weights are
    # inversely proportional to residual
    i = (index, index + 2)
return desired_wlen, np.average(absorbance_matrix[:,
    i[0]:i[1]], axis=1, weights=w)

def extract_delaytime(time_point, time, absorbance_matrix):
    for (i, t) in enumerate(iter(time)):
        if t > time_point:

```

```

        return t, absorbance_matrix[i,:] # return actual time
            point found
# couldn't find nothing mate
print("couldn't get spectrum at requested time")
sys.exit(1)

# plot_trace will be the function to plot all the stuff in a
    nice pretty graph
# will copy code from previous scripts to make this happen
def plot_traces(traces, wlen=423, img_file="out.png"):
    majorLocator = MultipleLocator(1)
    majorFormatter = FormatStrFormatter('%d')
    minorLocator = MultipleLocator(0.2)
    #set font size etc.
    font = {'family': 'calibri',
            'weight': 'normal',
            'size': '11'}
    plt.rc('font', **font)
    fig, ax = plt.subplots(figsize=(2*8/2.54,2*4/2.54))

    colours = [(73/255*1.6, 0, 146/255*1.6), (73/255*0.75, 0,
        146/255*0.75), '0.5', '0.1']
    markers = ['--', '-', '---', '-']
    # plot the actual traces
    for (i, (x, y, label)) in enumerate(iter(traces)):
        ax.plot(x, y, markers[i], label=label, color=colours[i])
    ax.legend(fontsize=11, loc=1)
        ax.xaxis.set_minor_locator(minorLocator)
        ax.xaxis.set_major_locator(majorLocator)
        ax.set_xlabel(r'$\lambda_{obs}$ / nm')
    ax.set_ylabel(r'$\Delta A$ / mOD')
    ax.set_ylim((-5, 15))
    ax.set_xlim((-1, 9))
    #ax.text(20, 0, r'$\lambda_{obs}$ = ' + str(wlen) + ' nm')
    #ax.set_yticks(np.linspace(-5, 30, num=8))
    plt.tight_layout()
    plt.savefig(img_file, facecolor=fig.get_facecolor(),
        edgecolor='none', dpi=600)
    plt.show()

# plot_trace will be the function to plot all the stuff in a
    nice pretty graph # will copy code from previous scripts to
    make this happen
def plot_spectra(spectra, img_file="out-spectral.png"):
    majorLocator = MultipleLocator(20)
    majorFormatter = FormatStrFormatter('%d')
    minorLocator = MultipleLocator(10)
    #set font size etc.
    font = {'family': 'calibri',
            'weight': 'normal',
            'size': '11'}
    plt.rc('font', **font)

```

```

fig, ax = plt.subplots(figsize=(2*8/2.54,2*4/2.54))

colours = ['0.5', (73/255, 0, 146/255), '0.1', '0.3']
markers = ['--', '-', '-', '--']
# plot the actual traces
for (i, (x, y, label)) in enumerate(enumerate(spectra)):
    ax.plot(x, y, markers[i], label=label, color=colours[i])
ax.legend(fontsize=11, loc=1)
ax.xaxis.set_minor_locator(minorLocator)
ax.xaxis.set_major_locator(majorLocator)
ax.set_xlabel(r'$\lambda$ / nm')
ax.set_ylabel(r'$\Delta A$ / mOD')
ax.set_ylim((0, 4))
ax.set_xlim((415, 615))
#ax.text(20, 0, r'$\lambda_{obs}$ = ' + str(wlen) + ' nm')
#ax.set_yticks(np.linspace(-5, 30, num=8))
plt.tight_layout()
plt.savefig(img_file, facecolor=fig.get_facecolor(),
            edgecolor='none', dpi=600)
plt.show()

# cut_trace does two things: first, it limits data to the first
    100 ps
# second, it removes everything before the CPM by removing
    everything prior to some min value
# usually, this lowest value comes at the end of the zigzaggy CPM
# BUT we also want to get rid of the negative part of the CPM,
    while the subsequent rise,
# beginning from 0 mOD, can be modelled as a (1 - exp[-t/tau])
def cut_trace(time, absorbance, end_time=100):
    # find the largest negative part of the CPM
    min_index = np.where(absorbance == np.amin(absorbance))[0][0]
    init_cut = absorbance[min_index:]
    start_index = np.where(init_cut == np.amax(init_cut))[0][0] +
        min_index

    return time[start_index:], absorbance[start_index:]

# fit function
def decay(t, A, C, tau):
    return A*np.exp(-t/tau) + C

# perform fitting,
# prints fit parameters and statistics,
# returns tuple containing a trace of the initial guess,
# and a trace of the actual fitted function at the end
def fit_trace(t, absorbance):
    guess_A = max(absorbance)
    guess_C = np.mean(absorbance[-5:-1])
    guess_tau = 3

```

```

guess = (guess_A, guess_C, guess_tau) guess_trace = decay(t,
    *guess)

try:
    fitvalues, fit_pcov = opt.curve_fit(decay, t, absorbance,
        p0=guess)
except:
    print("fitting failed!")
    return guess_trace, []

fit_trace = decay(t, *fitvalues)
fit_errors = 2*np.sqrt(np.diag(fit_pcov))

fit_A = fitvalues[0] fit_C = fitvalues[1]
fit_tau = fitvalues[2]
err_A = fit_errors[0] err_C = fit_errors[1]
err_tau = fit_errors[2]

print('A: ', str(fit_A), ' +/- ', str(err_A))
print('C: ', str(fit_C), ' +/- ', str(err_C))
print('tau: ', str(fit_tau), ' +/- ', str(err_tau))

return guess_trace, fit_trace

t, wlens, A_matrix = extract_data('raw_data.csv')
my_spectra = []
for i in iter([2, 4, 256, 900]):
    time_point, spectrum = extract_delaytime(i, t, A_matrix)
    my_spectra += [(wlens, spectrum, "{:d}
        ps".format(int(time_point)))]
plot_spectra(my_spectra)

```

---

```

#double-trace.py -- generates Figure 3.10 import numpy as np
import scipy
import matplotlib.pyplot as plt
import scipy.optimize as opt
import sys
from matplotlib.ticker import MultipleLocator, FormatStrFormatter

# function returns a tuple containing a time array (ps), a
    wavelength array (nm),
# and the absorbance matrix (mOD)
def extract_data(filename):
    raw = np.genfromtxt(filename, delimiter=',')
    # raw data contains a list of wavelengths in the first line,
        terminated by a series of NaN
    # lines 2-4 are useless
    # matrix of absorbance values (milliOD, I think) starts at
        raw[4:, 1:]
    # remember the format here is [columns, rows] and line 5 is
        index 4

```

```

# the NaNs in the wavelength list start at index 326, so
# maybe just hardcode this cut-off
absorbance_matrix = raw[4:, 1:326]
wavelength_array = raw[0, 1:326] * 1000 # wavelengths are in
# micron in the raw data, we want nm
time_array = raw[4:, 0] / 1000 # convert from fs to ps return
(time_array, wavelength_array, absorbance_matrix)

# function extract_wlen returns a time trace at a given
# wavelength, given the wavelength array
# and the full absorbance matrix as parameters
# desired_wlen must be in the range 300 to 900 nm
# a tuple is returned with the actual wavelength found and the
# time trace
# if the desired wavelength is outside the bounds of the
# terminal wavelengths in the dataset,
# the terminal trace is returned, otherwise, a weighted average
# of the two nearest sets is returned
# this represents a lot of time coding something cool for minor
# data smoothing which is not really necessary for thesis
def extract_wlen(desired_wlen, wavelength_array,
absorbance_matrix):
    if desired_wlen < 300 or desired_wlen > 900:
        print("wlen must be between 300 and 900")
    # find matching wavelength
    # actually we may want closest match, because some of the
    # longer wavelengths are more separated...
    residual = np.sqrt(np.power(wavelength_array - desired_wlen,
2))
    # weird syntax but it does the job, np.where returns a tuple
    # containing an array of min indices
    index = np.where(residual == np.amin(residual))[0][0]

    # in some cases, 2 arrays within the matrix will be a similar
    # distance from the target
    # we can then take a weighted average of the two nearest
    # traces

    # special case if wlen is at the end or beginning of the set
    if desired_wlen < wavelength_array[0]:
        return np.round(wavelength_array[0]), absorbance_matrix[:,
0]
    if desired_wlen > wavelength_array[-1]:
        return np.round(wavelength_array[-1]),
absorbance_matrix[:, -1]

    # this ensures we don't go out of bounds with the weighted
    # averages
    # if we're inbetween indices 0 and 1, res_prior will always
    # be larger than res_next,
    # if we're inbetween indices -2 and -1, res_next will always
    # be larger

```

```

if index == 0:
    res_prior = 1e9
else:
    res_prior = residual[index - 1]
if index == len(residual):
    res_next = 1e9
else:
    res_next = residual[index + 1]
res_current = residual[index]

# choose which is the smaller neighbouring residual
if res_prior < res_next:
    # in this case index - 1 and index are more relevant
    res_sum = res_prior + res_current
    w = [res_sum/res_prior, res_sum/res_current]
    i = (index - 1, index + 1)
else:
    # otherwise
    res_sum = res_current + res_next
    w = [res_sum/res_current, res_sum/res_next] # weights are
        inversely proportional to residual
    i = (index, index + 2)
return desired_wlen, np.average(absorbance_matrix[:,
    i[0]:i[1]], axis=1, weights=w)

def extract_delaytime(time_point, time, absorbance_matrix):
    for (i, t) in enumerate(iter(time)):
        if t > time_point:
            return t, absorbance_matrix[i,:] # return actual time
                point found
    # couldn't find nothing mate
    print("couldn't get spectrum at requested time")
    sys.exit(1)

# plot_trace will be the function to plot all the stuff in a
    nice pretty graph
# will copy code from previous scripts to make this happen
def plot_traces(traces, wlen=423, img_file="out.png"):
    majorLocator = MultipleLocator(1)
    majorFormatter = FormatStrFormatter('%d')
    minorLocator = MultipleLocator(0.2)
    #set font size etc.
    font = {'family': 'calibri',
        'weight': 'normal',
        'size': '11'}
    plt.rc('font', **font)
    fig, ax = plt.subplots(figsize=(2*8/2.54,2*4/2.54))

    colours = [(73/255*1.6, 0, 146/255*1.6), (73/255*0.75, 0,
        146/255*0.75), '0.5', '0.1']
    markers = ['--', '-', '--', '-']
    # plot the actual traces

```

```

for (i, (x, y, label)) in enumerate(iter(traces)):
    ax.plot(x, y, markers[i], label=label, color=colours[i])
ax.legend(fontsize=11, loc=1)
ax.xaxis.set_minor_locator(minorLocator)
ax.xaxis.set_major_locator(majorLocator)
ax.set_xlabel(r'$\lambda$ / ps')
ax.set_ylabel(r'$\Delta A$ / mOD')
ax.set_ylim((-5, 15))
ax.set_xlim((-1, 9))
#ax.text(20, 0, r'$\lambda_{obs}$ = ' + str(wlen) + ' nm')
#ax.set_yticks(np.linspace(-5, 30, num=8))
plt.tight_layout()
plt.savefig(img_file, facecolor=fig.get_facecolor(),
            edgecolor='none', dpi=600)
plt.show()

# plot_trace will be the function to plot all the stuff in a
# nice pretty graph
# will copy code from previous scripts to make this happen
def plot_spectra(spectra, img_file="out-spectral.png"):
    majorLocator = MultipleLocator(20)
    majorFormatter = FormatStrFormatter('%d')
    minorLocator = MultipleLocator(10)
    #set font size etc.
    font = {'family': 'calibri',
            'weight': 'normal',
            'size': '11'}
    plt.rc('font', **font)
    fig, ax = plt.subplots(figsize=(2*8/2.54, 2*4/2.54))

    colours = ['0.5', (73/255, 0, 146/255), '0.1', '0.3'] markers
              = ['--', '-', '-', '--']
    # plot the actual traces
    for (i, (x, y, label)) in enumerate(iter(spectra)):
        ax.plot(x, y, markers[i], label=label, color=colours[i])
    ax.legend(fontsize=11, loc=1)
    ax.xaxis.set_minor_locator(minorLocator)
    ax.xaxis.set_major_locator(majorLocator)
    ax.set_xlabel(r'$\lambda$ / nm')
    ax.set_ylabel(r'$\Delta A$ / mOD')
    ax.set_ylim((0, 4))
    ax.set_xlim((415, 615))
    #ax.text(20, 0, r'$\lambda_{obs}$ = ' + str(wlen) + ' nm')
    #ax.set_yticks(np.linspace(-5, 30, num=8))
    plt.tight_layout()
    plt.savefig(img_file, facecolor=fig.get_facecolor(),
                edgecolor='none', dpi=600)
    plt.show()

# cut_trace does two things: first, it limits data to the first
# 100 ps

```

```

# second, it removes everything before the CPM by removing
    everything prior to some min value
# usually, this lowest value comes at the end of the zigzaggy CPM
# BUT we also want to get rid of the negative part of the CPM,
    while the subsequent rise,
# beginning from 0 mOD, can be modelled as a (1 - exp[-t/tau])
def cut_trace(time, absorbance, end_time=100):
    # find the largest negative part of the CPM
    min_index = np.where(absorbance == np.amin(absorbance))[0][0]
    init_cut = absorbance[min_index:]
    start_index = np.where(init_cut == np.amax(init_cut))[0][0] +
        min_index

    return time[start_index:], absorbance[start_index:]

# fit function
def decay(t, A, C, tau):
    return A*np.exp(-t/tau) + C

# perform fitting,
# prints fit parameters and statistics,
# returns tuple containing a trace of the initial guess,
# and a trace of the actual fitted function at the end
def fit_trace(t, absorbance):
    guess_A = max(absorbance)
    guess_C = np.mean(absorbance[-5:-1])
    guess_tau = 3

    guess = (guess_A, guess_C, guess_tau)
    guess_trace = decay(t, *guess)

    try:
        fitvalues, fit_pcov = opt.curve_fit(decay, t, absorbance,
            p0=guess)
    except:
        print("fitting failed!") return guess_trace, []

    fit_trace = decay(t, *fitvalues)
    fit_errors = 2*np.sqrt(np.diag(fit_pcov))

    fit_A = fitvalues[0]
    fit_C = fitvalues[1]
    fit_tau = fitvalues[2]

    err_A = fit_errors[0]
    err_C = fit_errors[1]
    err_tau = fit_errors[2]

    print('A: ', str(fit_A), ' +/- ', str(err_A))
    print('C: ', str(fit_C), ' +/- ', str(err_C))
    print('tau: ', str(fit_tau), ' +/- ', str(err_tau))

```

```

    return guess_trace, fit_trace

t, wlen, A_matrix = extract_data('raw_data.csv')
t -= 0.4 # t0 correction for first trace, later additional
        correction of -0.5 ps aligns the CPM of both
my_spectra = []
for i in iter([2, 4, 256, 900]):
    # time_point, spectrum = extract_delaytime(i, t, A_matrix)
    # my_spectra += [(wlen, spectrum, "{:d}
                    ps".format(int(time_point)))]
plot_spectra(my_spectra)
traces = []
for wlen in (423, 565):
    wlen_actual, A_wlen = extract_wlen(wlen, wlen, A_matrix)
    t_cut, A_wlen_cut = cut_trace(t, A_wlen)
    guess, fit = fit_trace(t_cut, A_wlen_cut)
    if len(fit) > 0:
        if wlen_actual > 500:
            traces += [(t-0.5, A_wlen, str(wlen_actual)+" nm"),
                       (t_cut-0.5, fit, str(wlen_actual)+" nm, fit")]
        else:
            traces += [(t, A_wlen, str(wlen_actual)+" nm"), (t_cut,
                                                               fit, str(wlen_actual)+" nm, fit")]
    else:
        traces += [(t, A_wlen, "raw"+str(wlen_actual)), (t_cut,
                                                         guess, "guess"+str(wlen_actual))]
plot_traces(traces, wlen=wlen_actual,
            img_file="double-trace.png")

```

---

```

#long-trace.py -- generates Figure 3.11 import numpy as np
import scipy
import matplotlib.pyplot as plt
import scipy.optimize as opt
import sys
from matplotlib.ticker import MultipleLocator, FormatStrFormatter

# function returns a tuple containing a time array (ps), a
    wavelength array (nm),
# and the absorbance matrix (mOD)
def extract_data(filename):
    raw = np.genfromtxt(filename, delimiter=',')
    # raw data contains a list of wavelengths in the first line,
        terminated by a series of NaN
    # lines 2-4 are useless
    # matrix of absorbance values (milliOD, I think) starts at
        raw[4:, 1:]
    # remember the format here is [columns, rows] and line 5 is
        index 4
    # the NaNs in the wavelength list start at index 326, so
        maybe just hardcode this cut-off
    absorbance_matrix = raw[4:, 1:326]

```

```

wavelength_array = raw[0, 1:326] * 1000 # wavelengths are in
    micron in the raw data, we want nm
time_array = raw[4:, 0] / 1000 # convert from fs to ps
return (time_array, wavelength_array, absorbance_matrix)

# function extract_wlen returns a time trace at a given
    wavelength, given the wavelength array
# and the full absorbance matrix as parameters
# desired_wlen must be in the range 300 to 900 nm
# a tuple is returned with the actual wavelength found and the
    time trace
# if the desired wavelength is outside the bounds of the
    terminal wavelengths in the dataset,
# the terminal trace is returned, otherwise, a weighted average
    of the two nearest sets is returned
# this represents a lot of time coding something cool for minor
    data smoothing which is not really necessary for thesis
def extract_wlen(desired_wlen, wavelength_array,
    absorbance_matrix):
    if desired_wlen < 300 or desired_wlen > 900:
        print("wlen must be between 300 and 900")
    # find matching wavelength
    # actually we may want closest match, because some of the
        longer wavelengths are more separated...
    residual = np.sqrt(np.power(wavelength_array - desired_wlen,
        2))
    # weird syntax but it does the job, np.where returns a tuple
        containing an array of min indices
    index = np.where(residual == np.amin(residual))[0][0]

    # in some cases, 2 arrays within the matrix will be a similar
        distance from the target
    # we can then take a weighted average of the two nearest
        traces

    # special case if wlen is at the end or beginning of the set
    if desired_wlen < wavelength_array[0]:
        return np.round(wavelength_array[0]), absorbance_matrix[:,
            0]
    if desired_wlen > wavelength_array[-1]:
        return np.round(wavelength_array[-1]),
            absorbance_matrix[:, -1]

    # this ensures we don't go out of bounds with the weighted
        averages
    # if we're inbetween indices 0 and 1, res_prior will always
        be larger than res_next,
    # if we're inbetween indices -2 and -1, res_next will always
        be larger
    if index == 0:
        res_prior = 1e9
    else:

```

```

    res_prior = residual[index - 1]
if index == len(residual):
    res_next = 1e9
else:
    res_next = residual[index + 1]
res_current = residual[index]

# choose which is the smaller neighbouring residual
if res_prior < res_next:
    # in this case index - 1 and index are more relevant
    res_sum = res_prior + res_current
    w = [res_sum/res_prior, res_sum/res_current]
    i = (index - 1, index + 1)
else:
    # otherwise
    res_sum = res_current + res_next
    w = [res_sum/res_current, res_sum/res_next] # weights are
        inversely proportional to residual
    i = (index, index + 2)
return desired_wlen, np.average(absorbance_matrix[:,
    i[0]:i[1]], axis=1, weights=w)

def extract_delaytime(time_point, time, absorbance_matrix):
    for (i, t) in enumerate(enumerate(iter(time))):
        if t > time_point:
            return t, absorbance_matrix[i,:] # return actual time
                point found
    # couldn't find nothing mate
    print("couldn't get spectrum at requested time")
    sys.exit(1)

# plot_trace will be the function to plot all the stuff in a
    nice pretty graph
# will copy code from previous scripts to make this happen
def plot_traces(traces, wlen=423, img_file="out.png"):
    majorLocator = MultipleLocator(100)
    majorFormatter = FormatStrFormatter('%d')
    minorLocator = MultipleLocator(10)
    #set font size etc.
    font = {'family': 'calibri',
        'weight': 'normal',
        'size': '11'}
    plt.rc('font', **font)
    fig, ax = plt.subplots(figsize=(2*8/2.54,2*4/2.54))

    colours = [(73/255*1.6, 0, 146/255*1.6), (73/255*0.75, 0,
        146/255*0.75), '0.5', '0.1']
    markers = ['--', '-', '--', '-']
    # plot the actual traces
    for (i, (x, y, label)) in enumerate(enumerate(iter(traces))):
        ax.plot(x, y, markers[i], label=label, color=colours[i])
    ax.legend(fontsize=11, loc=1)

```

```

ax.xaxis.set_minor_locator(minorLocator)
ax.xaxis.set_major_locator(majorLocator)
ax.set_xlabel(r'\itt$ / ps')
ax.set_ylabel(r'\Delta$A / mOD')
ax.set_ylim((0, 5))
ax.set_xlim((-10, 1000))
#ax.text(20, 0, r'\lambda_{obs}$ = ' + str(wlen) + ' nm')
#ax.set_yticks(np.linspace(-5, 30, num=8))
plt.tight_layout()
plt.savefig(img_file, facecolor=fig.get_facecolor(),
            edgecolor='none', dpi=600)
plt.show()

# plot_trace will be the function to plot all the stuff in a
# nice pretty graph # will copy code from previous scripts to
# make this happen
def plot_spectra(spectra, img_file="out-spectral.png"):
    majorLocator = MultipleLocator(20)
    majorFormatter = FormatStrFormatter('%d')
    minorLocator = MultipleLocator(10)
    #set font size etc.
    font = {'family': 'calibri',
            'weight': 'normal',
            'size': '11'}
    plt.rc('font', **font)
    fig, ax = plt.subplots(figsize=(2*8/2.54, 2*4/2.54))

    colours = ['0.5', (73/255, 0, 146/255), '0.1', '0.3']
    markers = ['--', '-', '-', '--']
    # plot the actual traces
    for (i, (x, y, label)) in enumerate(iter(spectra)):
        ax.plot(x, y, markers[i], label=label, color=colours[i])
        ax.legend(fontsize=11, loc=1)
        ax.xaxis.set_minor_locator(minorLocator)
        ax.xaxis.set_major_locator(majorLocator)
        ax.set_xlabel(r'\lambda$ / nm')
        ax.set_ylabel(r'\Delta$A / mOD')
        ax.set_ylim((0, 4))
        ax.set_xlim((415, 615))
        #ax.text(20, 0, r'\lambda_{obs}$ = ' + str(wlen) + ' nm')
        #ax.set_yticks(np.linspace(-5, 30, num=8))
        plt.tight_layout()
        plt.savefig(img_file, facecolor=fig.get_facecolor(),
                    edgecolor='none', dpi=600)
        plt.show()

# cut_trace removes the first 100 ps
def cut_trace(time, absorbance):
    for (i, t) in enumerate(iter(time)):
        if t > 90:
            break
    start_index = i

```

```

        return time[start_index:], absorbance[start_index:]

# fit function
def decay(t, A, C, tau):
    return A*np.exp(-t/tau) + C

def rise(t, A, C, tau):
    return A*(1 - np.exp(-t/tau)) + C

# perform fitting,
# prints fit parameters and statistics,
# returns tuple containing a trace of the initial guess,
# and a trace of the actual fitted function at the end
def fit_trace(t, absorbance):
    guess_A = np.mean(absorbance[-5:-1])
    guess_C = 0
    guess_tau = 3000

    guess = (guess_A, guess_C, guess_tau)
    guess_trace = rise(t, *guess)

    try:
        fitvalues, fit_pcov = opt.curve_fit(rise, t, absorbance,
                                             p0=guess)
    except:
        print("fitting failed!")
        return guess_trace, []

    fit_trace = rise(t, *fitvalues)
    fit_errors = 2*np.sqrt(np.diag(fit_pcov))

    fit_A = fitvalues[0]
    fit_C = fitvalues[1]
    fit_tau = fitvalues[2]

    err_A = fit_errors[0]
    err_C = fit_errors[1]
    err_tau = fit_errors[2]

    print('A: ', str(fit_A), ' +/- ', str(err_A))
    print('C: ', str(fit_C), ' +/- ', str(err_C))
    print('tau: ', str(fit_tau), ' +/- ', str(err_tau))

    return guess_trace, fit_trace

t, wlen, A_matrix = extract_data('raw_data.csv')
t -= 0.6 # t0 correction for first trace, later additional
         # correction of -0.5 ps aligns the CPM of both
my_spectra = []
for i in iter([2, 4, 256, 900]):
    # time_point, spectrum = extract_delaytime(i, t, A_matrix)

```

```
# my_spectra += [(wlens, spectrum, "{:d}
    ps".format(int(time_point)))]
#plot_spectra(my_spectra)
traces = []
#for wlen in (460):
wlen = 460
wlen_actual, A_wlen = extract_wlen(wlen, wlens, A_matrix)
t_cut, A_wlen_cut = cut_trace(t, A_wlen)
guess, fit = fit_trace(t_cut, A_wlen_cut)
if len(fit) > 0:
    if wlen_actual > 500:
        traces += [(t-0.5, A_wlen, str(wlen_actual)+" nm"),
            (t_cut-0.5, fit, str(wlen_actual)+" nm, fit")]
    else:
        traces += [(t, A_wlen, str(wlen_actual)+" nm"), (t_cut,
            fit, str(wlen_actual)+" nm, fit")]
else:
    traces += [(t, A_wlen, "raw"+str(wlen_actual)), (t_cut,
        guess, "guess"+str(wlen_actual))]
plot_traces(traces, wlen=wlen_actual, img_file="long-trace.png")
```

---



## DECLARATION

---

Hiermit versichere ich an Eides statt, die vorliegende Dissertation selbst verfasst und keine anderen als die angegebenen Hilfsmittel benutzt zu haben. Die eingereichte schriftliche Fassung entspricht der auf dem elektronischen Speichermedium. Ich versichere, dass diese Dissertation nicht in einem früheren Promotionsverfahren eingereicht wurde.

*Hamburg, September 2024*

---

Joanna Irina  
Zaitseva-Kinneberg

*The English translation of the declaration, below, is provided for information purposes only, and is not legally binding. <https://www.deepl.com/> was used as a translation aid.*

I hereby declare that I have written this dissertation myself, and have not used any aids other than those stated. The written version submitted corresponds to the version on the electronic storage medium. I certify that this dissertation has not been submitted in a previous doctoral procedure.

*Hamburg, September 2024*

---

Joanna Irina  
Zaitseva-Kinneberg



## COLOPHON

This document was typeset using the typographical look-and-feel classicthesis developed by André Miede and Ivo Pletikosić.

First publication edition as of 3rd September 2024.